

An Ultra Low-Noise Micropower PPG Sensor

Présentée le 5 juin 2020

à la Faculté des sciences et techniques de l'ingénieur
Laboratoire de circuits intégrés
Programme doctoral en microsystemes et microélectronique

pour l'obtention du grade de Docteur ès Sciences

par

Antonino CAIZZONE

Acceptée sur proposition du jury

Prof. H. Shea, président du jury
Prof. C. Enz, Dr A. Boukhayma, directeurs de thèse
Prof. D. Demarchi, rapporteur
Prof. P. Mercier, rapporteur
Prof. Q. Huang, rapporteur

Give the ones you love wings to fly,
roots to come back
and reasons to stay.

— Dalai Lama

(Dona a chi ami ali per volare,
radici per tornare
e motivi per rimanere.

— Dalai Lama)

To my parents...
(Ai miei genitori...)

Acknowledgements

First of all, my acknowledgements go to my PhD thesis director ChristianENZ. I had the privilege to meet Christian when I was a master student at EPFL and his style and methodology has inspired me from the first moment. Particularly, I would like to thank him for having understood (before me!) that I could have found the PhD journey interesting and motivating! Indeed, Christian is the person who convinced me to start the PhD (and frankly, I don't have any regret!). I also thank him for his guidance and patience, above all in correcting my papers and always finding the weaknesses and how to make them better.

Since September 2016, I had the chance to work closely with Dr. Assim Boukhayma, my thesis co-director, who had just finished his PhD at that time. I must admit that calling him "Dr. Assim Boukhayma" makes me feel weird. The reality is that, on that month, I have not only met a great scientist, from whom I have learnt a lot of things, but above all a real friend. I will always feel grateful to Assim for his endless support and friendship!

My acknowledgements also go to the ICLAB colleagues for the nice vibes and "endless (noisy) babyfoot matches". Particularly, I would like to thank Lysiane for all the administrative support throughout my time at ICLAB.

I cannot finish this section without thanking my friends, who are, unfortunately, spread all over the world.

Last, but not the least I would like to thank the people I will always bring with me in my heart: my father Franco, my mother Angelita, my brother Andrea and a special dedication goes to my two grandparents, Ciccio and Concettina, who are always in my thoughts. Grazie!

Ops, I was forgetting someone. *Merci Ludivine, a toi qui a rendu ma vie belle à en mourir, qui réussis à rendre la fatigue un immense plaisir, a toi qui es mon grand amour et mon amour grand, a toi qui a pris ma vie et qui en as fait beaucoup plus, a toi qui as donné du sens au temps sans le mesurer, a toi mon grand amour et mon amour grand...*

Bôle, 22 January 2020

Antonino Caizzzone

Abstract

Nowadays, efficient and remote health monitoring is becoming increasingly important, given both the ageing of population and the combined action of an increase in obesity level and cardiovascular diseases. The healthcare industry is becoming more reliant on new methods to monitor and treat patients. This, along with an increased interest in fitness and wellness, is calling for more affordable, precise and wearable health monitoring devices. In this context, photoplethysmography (PPG) appears to be a key technology allowing non-invasive monitoring of vital biological indicators such as the heart rate, the blood oxygen saturation, the respiration rate and the arterial blood pressure. A standard PPG system comprises pulsed LEDs synchronized with a photosensor and a processing chain. The LEDs diffuse light in the human skin. Processing the signal held by the diffused light allows the extraction of the vital parameters. Despite the great potentials behind the PPG technology, the fairly large power burnt by the LEDs still represent a serious challenge towards truly continuous PPG operations, limiting its practical exploitation. State-of-the-art PPG sensors, both in academia and in commercial products, still follow a quite standard design paradigm. Indeed, they rely on off-chip photodiodes and relatively standard circuitry. The commercially available smart-watches and wearables fall short of meeting customer requirements in terms of reliability, precision and battery lifetime. In this regard, we should not expect any dramatic improvement unless there are fundamental changes in the PPG sensor technology. This is particularly true on the photosensor side, since its parasitic capacitance represents one of the limiting factor in terms of power/noise. Pinned-photodiode (PPD) are today the key ingredients of CMOS image sensors, thanks to the low dark current, low noise and large sensitivity operations. Several markets including security, scientific and medical imaging are relying today on this technology. The excellent performance of a PPD makes it particularly interesting for the PPG application. Indeed, the LED power can be reduced provided the noise floor is decreased proportionally. In this work a truly micropower PPG sensor combining an array of double transfer gates (TG) PPDs together with an ultra-low noise read-out chain is presented. Compared to conventional solution, this work achieves the same signal-to-noise ratio (SNR) at a significantly lower LED power. The use of an array additionally enables spatial averaging leading to further noise reduction and easing the engineering trade-off between the possible achievable dynamic range and the overall noise performance. Consequently, the LED power can be reduced dramatically. The micropower PPG sensor is implemented in a $0.18\ \mu\text{m}$ CMOS image sensor process (CIS), achieving $4.6\ \mu\text{W}$ total power consumption, including $1.97\ \mu\text{W}$ LED power, at 1.38 bpm HR average error. Compared to the most recent state-of-the-art work

Acknowledgements

this means more than an order of magnitude in power reduction. A PPG signal usually suffer from a relatively low AC/DC ratio, being the AC component the one carrying the majority of the biomedical information. Therefore, any PPG sensor has to integrate a proper AC/DC ratio enhancement technique. An additional advantage coming from the PPD array structure, and its double TG, is its excellent control of the integrated charge. This can also be exploited for enhancing the perfusion index of the PPG signal. Unlike state-of-the-art works, this can be performed without any power or silicon area overhead, by properly tuning the TG control voltage and the charge transfer time. The increasing demand for embedding more and more light sensors in portable and wearable devices is calling for higher integration and reuse of the sensor interface electronics. In this perspective, this work has tried to assess whether the extremely sensitivity and low noise operation of the proposed PPG sensor could have been enough to open to new applications, far from the PPG one. ToF distance ranging is key in several applications from consumer electronics such as drones, cameras and smartphones to industrial metrology. Without any lens, the micropower PPG sensor can be operated for indirect ToF operations, requiring less than 2 mA average laser current, during exposure, and only 10 μ W for the sensor chip enabling a 2 mm resolution for 130 cm range. Moreover, the presented architecture is implemented in a standard CIS process which presents a considerable advantage for large volume consumer applications and for miniaturization. The CMOS implementation also allows the integration of digital processing or machine learning for specific applications on the same die opening the way for edge computing. Eventually, the sensor architecture presented in this work not only offers the advantage of covering ALS, PPG and ToF using the same device, but it also brings significant performance improvement in each application field. This architecture represents a promising step towards all-in-one miniaturized photonic sensors, thanks to low-cost high-volume production and integration in portable and wearable devices.

Key words: PPG, ToF, Array, Photodetector, PPD, CMOS, CIS, LED, low-power, low-noise, wearable.

Résumé

De nos jours, la mesure des paramètres vitaux, d'une manière continue et en dehors des centres hospitaliers, devient particulièrement importante. Le vieillissement de la population, l'augmentation de l'obésité et des maladies cardiovasculaires en sont les causes. L'industrie de la santé se montre de plus en plus ouverte à de nouvelles méthodes de soin pour les patients. De plus, l'intérêt de la population pour sa condition physique et son bien-être est croissant. C'est pour toutes ces raisons que la demande en systèmes innovants de mesure est grande. Dans ce contexte, la technologie nommée photoplethysmographie (PPG) représente un pilier important du changement de méthode. Un capteur PPG permet de mesurer divers paramètres vitaux comme la fréquence cardiaque, l'oxygénation sanguine, la respiration ainsi que la pression artérielle. Un système PPG est caractérisé par une source lumineuse (LED) rythmée, synchronisée avec un photodétecteur et une chaîne électronique de lecture. La LED diffuse des photons, donc de la lumière, à travers la peau humaine. Le photodétecteur capture la lumière réfléchie à partir de laquelle l'extraction des paramètres vitaux peut avoir lieu. Malgré l'énorme potentiel de la technologie PPG, la consommation de la LED représente toujours un défi important dans le développement des systèmes PPG capables de mesurer d'une façon continue. Ceci en limite l'utilisation effective. L'état de l'art des capteurs PPG, soit au niveau académique, soit au niveau commercial, suit un paradigme de développement éprouvé, mais répétitif; des photodétecteurs externes et des circuits de lecture relativement ordinaires sont utilisés. Les dispositifs portables aujourd'hui sur le marché, comme les montres connectées, ont tendance à décevoir les attentes des clients quant à la durée de la batterie et la précision des données fournies. Pour pouvoir améliorer ces deux caractéristiques, il faudra attendre des changements importants de la technologie PPG. Ce changement sera crucial surtout pour la technologie du photodétecteur dont la capacité parasite représente une limite importante pour le bruit et la puissance. Le photodétecteur "pinned" (PPD) est de nos jours à la base de la technologie des capteurs d'image CMOS grâce à son courant "dark" réduit et sa formidable sensibilité. Plusieurs applications commerciales comme la sécurité, les images scientifiques et médicales sont aujourd'hui basées sur cette technologie. Les excellentes prestations des dispositifs PPD les rendent particulièrement intéressants pour l'application PPG. En fait, la puissance de la LED peut être réduite si le niveau de bruit est réduit proportionnellement. Dans ce travail de thèse, un capteur PPG à micropuissance, combinant une matrice de PPDs à double grille de transfert avec un circuit de lecture à très basse consommation et à faible bruit, a été présenté. Comparé à l'état de l'art, ce travail réduit considérablement la puissance de la LED sans compromettre le rapport signal/bruit

Acknowledgements

(SNR). L'utilisation de la matrice introduit la possibilité de réaliser une moyenne spatiale permettant une réduction supplémentaire du bruit. De plus, la matrice facilite le compromis technique entre la dynamique d'entrée et la performance du bruit; ceci réduit drastiquement la puissance de la LED. Le capteur PPG à micropuissance a été fabriqué dans une technologie à capteur d'image CMOS à 180 nm, obtenant un niveau de consommation de puissance totale de 4.6 μ W, y compris 1.97 μ W utilisée par la LED. Ceci a été obtenu avec une erreur moyenne sur la détection de la fréquence cardiaque de 1.38 bpm par rapport à une bande thoracique. Par rapport à l'état de l'art le plus récent, ces performances représentent une réduction entre un et deux ordres de grandeur de la puissance consommée. Un signal PPG normalement présente un rapport AC/DC particulièrement réduit. Il est très important de considérer ce rapport car on trouve au sein de la composante AC la majorité des informations médicales; c'est la raison pour laquelle chaque capteurs PPG doit intégrer une stratégie interne d'augmentation de ce rapport. La structure matricielle et la double grille de transfert permettent une excellente capacité de contrôler la quantité de charge intégrée par le PPD. Contrairement à l'état de l'art, le rapport AC/DC peut être augmenté sans aucune pénalité de puissance ou surface de silicium, ceci en optimisant la tension de contrôle de la grille de transfert et du temps de transfert de la capacité intégrée. La demande toujours croissante d'intégration des capteurs de lumière dans les dispositifs portables nécessite la réutilisation des interfaces et des capteurs pensés pour des applications différentes. Dans cette optique, ce travail de thèse a essayé d'étudier la possibilité d'utiliser les excellentes performances du capteur PPG décrit ci-dessus dans des applications différentes que celles du PPG. Les capteurs à temps de vol (ToF) sont de plus en plus importants dans diverses applications comme les drones, les automobiles à conduite autonome ou les applications industrielles. Sans l'utilisation de lentilles, le capteur PPG à micropuissance décrit ci-dessus peut être utilisé pour des mesures indirectes du temps de vol, avec moins de 2 mA de courant moyen utilisé par les lasers et consommant seulement 10 μ W dans la chaîne de lecture. Le capteur a été caractérisé pour cette performance jusqu'à 130 cm, où il a montré une résolution de 2 mm. Indépendamment de l'application, l'architecture proposée est fabriquée dans un processus à capteur d'images qui est particulièrement avantageux par rapport aux coûts, en particulier pour des productions de consommation. La technologie CMOS permet aussi l'intégration, sur le même silicium, de circuits digitaux avec ou sans intelligence artificielle, vers des systèmes totalement automatisés. Finalement, il est important de souligner que l'architecture proposée dans ce travail de thèse ne permet non seulement son utilisation dans diverses applications, comme le PPG ou le ToF, mais également de dépasser l'état de l'art dans toutes ses applications. Cette dernière caractéristique combinée à l'intégration de la technologie CMOS à large échelle, fait de l'architecture décrite ci-dessus un tournant technologique vers des capteurs intégrés dans diverses applications.

Mots clefs : PPG, ToF, Matrice, Photodétecteur, PPD, CMOS, CIS, LED, faible-consommation, faible-bruit, portable.

Sommario

Oggigiorno la misurazione di parametri vitali, in maniera continua e al di fuori dei centri ospedalieri, sta acquisendo particolare importanza. I fattori trainanti sono l'invecchiamento della popolazione e l'azione combinata dell'aumento dei livelli di obesità e delle malattie cardiovascolari. L'industria sanitaria sta mostrando importanti segni di apertura verso nuovi metodi di cura dei pazienti. Questo, combinato con un interesse sempre crescente verso la forma fisica ed il benessere, chiama a gran voce dei sistemi innovativi di misura. In questo contesto, la tecnologia chiamata fotoplethysmografia (PPG) rappresenta un pilastro importante di rinnovamento. Un sensor PPG permette di misurare diversi parametri vitali come il battito cardiaco, l'ossigenazione sanguigna, la respirazione e perfino la pressione arteriosa. Un sistema PPG è caratterizzato da una sorgente luminosa (LED) ritmata, sincronizzata con un fotorilevatore ed una catena elettronica di lettura. Il LED diffonde i fotoni, quindi la luce, attraverso la pelle umana. Il fotorilevatore rileva la luce riflessa dalla quale l'estrazione dei segnali vitali ha luogo. Nonostante l'enorme potenziale dietro la tecnologia PPG, la considerevole potenza dissipata dal LED rappresenta una sfida importante nello sviluppo di sistemi PPG che operino in maniera continua, limitandone l'effettivo utilizzo. Lo stato-dell'arte dei sensori PPG, sia a livello accademico, quanto a livello commerciale, segue un paradigma di sviluppo collaudato, ma alquanto ripetitivo; si sfruttano fotorilevatori esterni e circuiti di lettura alquanto ordinari. I dispositivi indossabili oggi sul mercato, come orologi connessi, hanno la tendenza a deludere le aspettative dei clienti in termini di precisione dei dati forniti e tempo di vita della batteria. In quest'ottica non dovremmo aspettarci nessun miglioramento sostanziale fintantoché un importante cambiamento della tecnologia PPG abbia luogo. Questo è particolarmente rilevante per quanto concerne la tecnologia del fotorilevatore, la cui capacità parassita rappresenta uno dei limiti in termini di rumore e quindi di potenza. I fotorilevatori pinned (PPD) sono oggi alla base della tecnologia dei sensori di immagine CMOS, grazie alla loro ridotta corrente dark, rumore generato e stupefacente sensibilità. Diverse applicazioni commerciali come la sicurezza, immagini scientifiche o medicali si basano oggi su questa tecnologia. Le eccellenti prestazioni dei dispositivi PPD li rendono particolarmente interessanti per l'applicazione PPG. Infatti, la potenza dissipata dal LED può essere ridotta se il livello di rumore è ridotto proporzionalmente. In questo lavoro di tesi un sensore PPG a micropotenza, combinante una matrice di PPDs a doppio gate di trasferimento con un circuito di lettura a bassa potenza e basso consumo, è presentato. Rispetto allo stato-dell'arte, questo lavoro riduce considerabilmente la potenza del LED senza compromettere il rapporto segnale rumore (SNR). L'utilizzo di una matrice introduce la possibilità di realizzare una media

spaziale che permetta un'addizionale riduzione del rumore. In aggiunta, la struttura matriciale facilita il compromesso ingegneristico tra la dinamica d'ingresso e le prestazioni di rumore; questo porta ad una riduzione importante della potenza dissipata dal LED. Il sensore PPG a micropotenza è stato implementato in una tecnologia a sensore d'immagine CMOS a 180 nm, raggiungendo un livello di consumo di potenza totale di $4.6 \mu\text{W}$, includendo i $1.97 \mu\text{W}$ dissipati dal LED. Il tutto è stato raggiunto con un errore medio sulla stima del battito cardiaco di 1.38 bpm, rispetto ad una fascia toracica. Con riferimento allo stato-dell'arte piu' recente, queste prestazioni rappresentano una riduzione da 1 a 2 ordini di grandezza del consumo di potenza totale. Un segnale PPG di norma presenta un rapporto AC/DC particolarmente ridotto. Tenerne conto è particolarmente importante dal momento che la componente AC porta con se la maggior parte delle informazioni biomediche. Percio', ogni sensore PPG deve obbligatoriamente integrare una strategia interna di aumento del suddetto rapporto. In questo senso la struttura matriciale, e soprattutto il doppio gate di trasferimento, porta con se un ulteriore vantaggio, cioè l'eccellente capacità di controllare la quantità di carica integrata nel PPD. Contrariamente allo stato-del'arte, il rapporto AC/DC puo' essere aumentato senza nessuna penalità in termini di potenza o area di silicio, andando ad ottimizzare la tensione di controllo del gate di trasferimento ed il tempo di trasferimento della carica integrata. La domanda sempre crescente d'integrazione di sensori di luce in dispositivi portatili ed indossabili urge il riutilizzo delle interfacce, anche di sensori concepiti per applicazioni diverse. In quest'ottica, questo lavoro di tesi ha cercato di studiare la possibilità di utilizzare le eccellenti prestazioni del suddetto sensore PPG in applicazione ben lontane da quella PPG. I sensori a tempo di volo (ToF) sono sempre piu' importanti in diverse applicazioni come quelle di consumo, basti pensare ai droni o alle automobili a guida autonoma, o industriali. Senza l'utilizzo di alcuna lente, il sensore PPG a micropotenza descritto sopra puo' essere operato per misure indirette di tempo di volo, con meno di 2 mA di corrente media dissipata dal laser e consumando solamente $10 \mu\text{W}$ in lettura. Il sensore è stato caratterizzato, per le suddette prestazioni, fino a 130 cm, in cui ha mostrato una risoluzione di 2 mm. Indipendentemente dall'applicazione, l'architettura proposta è implementata in un processo a sensore d'immagine CMOS, quindi particolarmente vantaggioso, in termini di costo, per volumi di produzioni di consumo. La tecnologia CMOS permette anche l'integrazione, sullo stesso silicio, di circuiti digitali con o senza intelligenza artificiale, verso sistemi totalmente automatizzati. In fine è importante sottolineare che l'architettura proposta in questo lavoro di tesi non solamente permette il suo sfruttamento in ambiti applicativi diversi, come il PPG o il ToF, ma in tutti gli ambiti ha raggiunto prestazioni superiori rispetto allo stato-dell'arte. Quest'ultima caratteristica, insieme all'integrazione della tecnologia CMOS su larga scala, rende la sopra citata architettura una svolta tecnologia verso sensori integranti in diverse applicazioni.

Parole chiave: PPG, Tempo-di-Volo, Matrice, Fotorilevatore, PPD, CMOS, CIS, LED, bassa-potenza, basso-rumore, indossabile

List of abbreviations

IoT	Internet-of-Things
IoMT	Internet-of-Medical-Things
CAGR	Compound-annual-growth-rate
BMI	Body-Mass-Index
CVDs	Cardiovascular-Diseases
PPG	Photoplethysmography
ToF	Time-of-Flight
LED	Light-Emitting-Diode
PD	Photodetector
PI	Perfusion-Index
IR	Infrared
HR	Heart-Rate
BPM	Beats-per-Minute
SA	Sinoatrial-Node
ECG	Electrocardiogram
RR	ECH(R)-peak to ECG(R)-peak
PP	PPG-peak to PPG-peak
HRV	Heart-Rate-Variability
IBI	Inter-Beats-Intervals
PRV	Pulse-Rate-Variability
SD	Standard-Deviation
RMSSD	Root-Mean-Square-Successive-Difference
LF	Low-Frequency
VLF	Very-Low-Frequency

Acknowledgements

HF	High-Frequency
AFib	Atrial-Fibrillation
AI	Artificial-Intelligence
SpO2	Oxygen-Saturation
BR	Breathing-Rate
THM	Traube-Hering-Mayer
BPRM	Breaths-per-Minute
FFT	Fast-Fourier-Transfer
MAE	Mean-Absolute-Error
EMD	Empirical-Mode-Decomposition
IMF	Intrinsic-Moe-Functions
BP	Blood-Pressure
SBP	Systolic-Blood-Pressure
DBP	Systolic-Blood-Pressure
MBP	Mean-Blood-Pressure
ICG	Impedance-Cardiography
BCG	Ballistocardiogram
CO	Cardiac-Output
SV	Stroke-Volume
PWV	Pulse-Wave-Velocity
PEP	Pre-Ejection-Period
PTT	Pulse-Transient-Time
VPPG	PPG-First-Derivative
APPG	PPG-Second-Derivative
CT	Crest-Time
NN	Neural-Network
TIA	Transimpedance-Amplifier
CTIA	Capacitive-Feedback-Transimpedance-Amplifier
ZTIA	RC-Feedback-Transimpedance-Amplifier
ADC	Analog-to-Digital-Converter

SH	Sample-and-Hold
SNR	Signal-to-Noise-Ratio
ALC	Ambient-Light-Cancellation
AM	Amplitude-Modulation
DRE	Dynamic-Range-Enhancer
TDC	Time-to-Digital-Converter
CS	Compressive-Sampling
FSM	Finite-State-Machine
LDC	Light-to-Digital-Converter
FIFO	First-Input-First-Output
SPI	Serial-Peripheral-Interface
MA	Motion-Artefacts
SMR	Signal-to-Motion-Ratio
MAC	Motion-Artefacts-Cancellation-Techniques
ANC	Adaptive-Noise-Cancellation
FIR	Finite-Impulse-Response
PSD	Power-Spectral-Density
ENBW	Equivalent-Noise-Bandwidth
STD	Standard-Deviation
OTA	Operational-Transconductance-Amplifier
CCD	Charge-Coupled-Device
EQE	Effective-Quantum-Efficiency
TG	Transfer-Gate
CIS	CMOS-Image-Sensors
WI	Weak-Inversion
SI	Strong-Inversion
AFE	Analog-Front-End
PCB	Printed-Circuit-Board
AL	Ambient-Light
FPGA	Field-Programmable-Gate-Array

Acknowledgements

UART	Universal-Asynchronous-Receiver-Transmitter
ENOB	Effective-Number-of-bit
SINAD	Signal-to-Noise-and-Distortion-Ratio
SPAD	Single-Photon-Avalanche-Detector
ALS	Ambient-Light-Sensing
VCSEL	Vertical-Cavity-Surface-Emitting-Laser
LIDAR	Light-Detection-And-Ranging

Contents

Acknowledgements	i
Abstract (English/Français/Italian)	iii
List of abbreviations	ix
List of figures	xvii
List of tables	xxi
1 Introduction	1
1.1 The Digital Health: the next big Thing	1
1.2 Driving factors	3
1.2.1 Increase of cardiovascular diseases	3
1.2.2 Healthcare costs	6
1.3 The increasing need of reliable and continuous health monitoring	7
1.4 Thesis organization	9
2 The photoplethysmography (PPG)	11
2.1 History of PPG	11
2.2 What is the PPG?	12
2.3 What is the physics behind? The Beer-Lambert law	13
2.4 Light-tissue interaction: some optical considerations	15
2.5 Tricks to enhance the PPG (AC) magnitude	19
2.5.1 Measurement sites	21
3 PPG applications in physiological measurements	23
3.1 Heart rate	23
3.2 Inter-beats-interval and heart rate variability	25
3.2.1 Atrial fibrillation	27
3.2.2 Stress monitoring	28
3.3 Oxygen saturation	29
3.4 Breathing rate	33
3.5 Blood pressure	34
3.5.1 Pulse wave velocity and pulse transient time	35
	xiii

3.5.2	PPG decomposition analysis and features extraction	41
4	A classic PPG readout chain	45
4.1	Description of the basic readout chain	45
4.2	Challenges and bottlenecks	48
4.2.1	Ambient light: static and dynamic interferers	49
4.2.2	Dynamic range and DC offset cancellation	50
4.3	State-of-the-art: academic works	52
4.4	State-of-the-art: commercial works	64
5	Noise and artefacts in PPG sensors	69
5.1	Noise types	69
5.1.1	Thermal noise	70
5.1.2	Shot noise	72
5.1.3	Flicker noise	74
5.2	Noise analysis in PPG readout chains	74
5.2.1	ZTIA	76
5.2.2	CTIA	78
5.2.3	ZTIA and CTIA comparison	80
5.2.4	Correlated double sampling: a kTC analysis	82
5.3	Beyond the CTIA: the CIS readout chain	90
5.3.1	The pinned photodiode	92
5.3.2	The CIS readout chain	93
5.3.3	The CIS readout chain noise analysis	93
5.4	Artefacts: the motion-induced signal corruption	101
5.4.1	Motion artefacts sources	101
5.4.2	Wavelength dependency	102
5.4.3	Proposed techniques to reduce motion artefacts	103
6	A micropower PPG sensor	107
6.1	The double TG pinned photodiode structure	107
6.2	The micropower PPG sensor architecture	109
6.2.1	Array of PPDs	110
6.2.2	One big pixel versus an array of pixels?	111
6.2.3	Switched-cap averaging and amplifier	112
6.2.4	A low-power incremental ADC	115
6.2.5	Micrograph picture and measurement set-up	116
6.2.6	The characterization of the micropower PPG sensor	119
6.3	AC/DC ratio enhancement	131
6.3.1	Working principle	132
6.3.2	Measurements results	132
6.3.3	Discussion on the AC/DC ratio enhancement technique	135

7	A low-power and mm-resolution 1D ToF sensor	139
7.1	Towards "all-in-one" photonic sensors	139
7.2	Direct and indirect ToF operations	140
7.3	A low-power 1D indirect ToF sensor	141
7.3.1	Characterization of the low-power 1D ToF sensor	144
7.4	Discussion and comparison to the state-of-the-art	146
8	Conclusions	151
8.1	Future perspectives	156
A	Appendix	161
	Bibliography	195
	Curriculum Vitae	197

List of Figures

1.1	IoT connected devices from 2015 to 2025 (billion)	2
1.2	Obesity and Body Mass Index	4
1.3	Rising overweight rates	5
1.4	Population ageing	6
1.5	Young children and older people	7
1.6	Healthcare spending	7
1.7	Current technologies for health monitoring	8
2.1	Smartwatch with PPG sensor on	12
2.2	PPG set-up	13
2.3	Beer-Lambert law	14
2.4	Beer-Lambert law and PPG	15
2.5	Absorption spectrum of Melanin, Haemoglobin and Water	16
2.6	Skin composition	17
2.7	Elastic and inelastic scattering	18
2.8	Reflective PPG: photon travelling path in tissue at different wavelengths	19
2.9	External light barriers in PPG modules helping the reduction of the direct optical crosstalk	21
3.1	Parasympathetic and sympathetic cardiac nerves	24
3.2	ECG and PPG	25
3.3	ECG and PPG with the three characteristic points for IBI detection	26
3.4	Heart section and ECG with and without atrial fibrillation	28
3.5	Arterial and venous blood and oxygenated and deoxygenated haemoglobin	30
3.6	A commercial pulse oximetry	30
3.7	Extinction coefficients of Hb and HbO ₂	31
3.8	PPG in time and frequency domain with both the HR and BR visible	34
3.9	Synchronous ECG, ICG/BCG and PPG	36
3.10	Simplified arterial tree	39
3.11	Microcirculation	40
3.12	PPG decomposition and features extraction	42
3.13	PPG morphology	43
4.1	A classic PPG readout chain	46

List of Figures

4.2	Two possible TIA configurations: ZTIA and CTIA	47
4.3	Spectral power distribution of solar radiation	49
4.4	Percentage reduction of a 50 Hz interfere thanks to CDS	51
4.5	Dynamic range requirement for different PI with respect to the $S_p O_2$	52
4.6	State-of-the-art academic works: Tavakoli et al.	53
4.7	State-of-the-art academic works: Patterson et al.	54
4.8	State-of-the-art academic works: Glaros et al.	55
4.9	State-of-the-art academic works: Winokur et al.	56
4.10	State-of-the-art academic works: Gubbi et al.	57
4.11	State-of-the-art academic works: Pamula et al.	58
4.12	State-of-the-art academic works: Schönle et al.	59
4.13	State-of-the-art academic works: Kim et al.	60
4.14	State-of-the-art academic works: Lee et al.	61
4.15	State-of-the-art academic works: Lin et al.	62
4.16	State-of-the-art commercial works: TI4403	64
4.17	State-of-the-art commercial works: MAX86140	65
4.18	State-of-the-art commercial works: AS7026GG	66
5.1	The different noisy components in a PPG chain	70
5.2	Low pass filter	71
5.3	Integration of a white noise	73
5.4	Schematic of a classical PPG readout chain	75
5.5	SNR of both CTIA (solid line) and ZTIA (dashed line) based design versus the input photocurrent, for three different PD parasitic capacitance values	82
5.6	Three proposed CDS circuits	83
5.7	Noise small signal schematic of CDS2 and CDS3: (a) CDS2, (b) CDS3, (c) switch equivalent model.	84
5.8	Simulated and calculated RMS noise vs C_1 for CDS1.	88
5.9	Simulated and calculated RMS noise vs C_3 for CDS2.	88
5.10	Simulated and calculated RMS noise vs C_1 for CDS3.	89
5.11	PPD device: (a) PPG cross section, (b) PPD hydraulic equivalent model, (c) PPD EQE, (d) Conventional PPD readout timing diagram, (e) PPD timing diagram for PPG.	91
5.12	Conventional source follower based CIS readout chain	93
5.13	CIS vs CTIA at 0.2% PI and for three different PD parasitic capacitances	97
5.14	CIS vs CTIA at 1% PI and for three different PD parasitic capacitances	98
5.15	CIS vs CTIA at 10% PI and for three different PD parasitic capacitances	99
5.16	Effect of motion artefacts on simultaneously recorded reflective PPG signals at different wavelengths	102
5.17	Block diagram of the adaptive noise cancellation technique	103
5.18	Motion artefacts cancellation based on two PPG sensors	104

6.1	PPD device: (a) double TG PPG cross section, (b) PPD hydraulic equivalent model, (c) PPD EQE, (d) Conventional PPD readout timing diagram, (e) Modified timing diagram for ALC.	108
6.2	Block diagram of the proposed monolithic PPG sensor. The implemented ASIC consists of an array of macro-pixels, as photosensitive area, an averaging block, an amplifier and an ADC.	109
6.3	An array of pixels versus a single big pixel.	113
6.4	(a) Ratio of the single pixel current and the array one versus the (W/L) of the single pixel SE, (b) Ratio of the currents versus the inversion coefficient of the single pixel SE	114
6.5	Architecture of the monolithic PPG sensor and detailed schematic of the OTA used in the amplifier, the averaging block, together with the timing diagram. . .	115
6.6	Full schematic of the on-chip incremental ADC with the related timing diagram.	115
6.7	(a) PCB 1.0, (b) PPG set-up and optical signal, highlighting the DC and AC components , (c) Micrograph of the monolithic PPG sensor, 4 mm by 5 mm. . .	118
6.8	(a) PCB 2.0: measurement set-up consisting of an FPGA device interfacing with an application running on a computer and the monolithic PPG sensor on a compact board, (b) Zoom on the compact evaluation board of 2 cm by 3 cm. . .	119
6.9	Measured chip light-to-digital conversion linearity.	120
6.10	Total noise STD shown both at the output of the ADC and an off-chip 11 taps FIR digital low-pass filter.	121
6.11	Total noise STD, reported both at the output and input-referred, as a function of the gain.	122
6.12	Output DN with and without the ALC vs the AL.	122
6.13	Correlation of HR data between this work and a commercial ECG chest strap. The experiment has been carried out at $4.6 \mu\text{W}$ total power (LED+AFE+ADC) on three healthy individuals (each color representing one person).	125
6.14	Measured PPG raw signals at the finger for two emitting wavelengths, green and red. The real-time HR , HRV , S_pO_2 are displayed from the top to the bottom, respectively. The measured SNR is related to the green channel.	125
6.15	Measured PPG raw signals at the wrist for the green channel. The real-time HR , HRV and SNR are displayed from the top to the bottom, respectively.	126
6.16	Measured SNR vs f_s and logarithmic fit.	127
6.17	Measured sensor efficiency vs f_s and logarithmic fit.	128
6.18	The double TG PPD device and the three most important phases: Integration, PI Enhancement and Sink. The PI Enhancement illustrates a PPD readout in which only a part of the integrated photo-generated electrons reaches the SN.	131
6.19	Measured DC and AC components of the emulated PPG wave vs the TG control voltage for several transfer times.	133
6.20	Measured PI vs the TG control voltage for several transfer times.	134
6.21	Measured PI vs the TG control voltage at three different emulated PPG PI, 10%, 5% and 1%, for $t_{transfer}$ of 100 ns.	134

List of Figures

6.22	Measured SNR vs the TG control voltage for several transfer times.	135
7.1	Indirect and direct ToF operations.	141
7.2	The PPD-based sensor: (a) block diagram of the proposed sensor, (b) Architecture of the sensor and detailed schematic of the OTA, used in the amplifier, and the averaging block.	142
7.3	PPG timing diagram related to Fig. 7.2b. (a) Readout chain, (b) Transfer gates and source control for first acquisition and (c) second acquisition.	143
7.4	ToF measurement set-up showing the sensor and the VCSEL without any lenses and the labview interface displaying the real time measured distance.	145
7.5	(a) Sensor output versus source pulse delay steps of 100 ps up to 2 ns and 1 ns after with a zoom onto the 100 ps steps. (b) The target versus measured distance with steps of 1 cm up to 35 cm and 1 cm after measured with the sensor chip and light emitted from a VCSEL and reflected back from the target.	147
A.1	Maximum acceptable ratio of R for the oxygen saturation	162
A.2	Single pixel current consumption versus the array one, at the same SF bandwidth.	165

List of Tables

4.1	Summary of the academic works.	63
4.2	Summary of the commercial works.	67
5.1	ZTIA and CTIA-based PPG readout chains design parameters as for the noise analysis	81
5.2	Simulation parameters	87
5.3	CTIA and CIS-based PPG readout chains design parameters as for the noise analysis	96
5.4	Noise analysis summary comparing CTIA and CIS readout chain.	100
6.1	ADC characterization	123
6.2	Summary of the PPG sensor performance with comparison to state-of-the-art.	130
7.1	ToF Sensor Performance	146
7.2	ToF Sensing Comparison Table	148
A.1	Extinction coefficients of oxygenated and deoxygenated hemoglobins	162

1 Introduction

Nowadays, the Digital Health is becoming the next big Thing. Modern lifestyle often comes at the cost of increased stress levels, uncontrolled diets and little time devoted to medical prevention. Moreover, in a short term future, there will be more connected devices than human beings [1]. Indeed, as shown in Fig. 1.1, the number of Internet-of-Things (IoT) devices is expected to reach more than 70 billion by 2025. Out of this, 22% is the expected market share of connected health devices, the Internet-of-Medical-Things (IoMT). By 2020, 40% of IoT technology will be health related, more than any other category [2]. In parallel, [3] indicates that the global population could grow to around 8.5 billion in 2030, 9.7 billion in 2050, and 10.9 billion in 2100. These numbers lead to incredible business and societal transformation, but also possible threats. In this framework, the healthcare industry is becoming more reliant on new methods to monitor and treat patients. This, along with an increased interest in fitness and wellness, is calling for more affordable, precise and wearable health monitoring devices. This chapter aims at introducing the great opportunities and challenges behind the digital health and also the driving factors sustaining the urgent need of change in the modern healthcare system. The motivations behind this work are pointed out and the organisation of this manuscript is presented.

1.1 The Digital Health: the next big Thing

Digital Health is a collective term bringing together the electronic health (eHealth) and the mobile health (mHealth). The eHealth covers the systematized collection of patients' medical records into a digital format. The mHealth, instead, complements the eHealth by deploying health services and information via mobile platforms such as smartphones, tablets and personal computers [4]. Generally speaking, the Digital Health has been uniquely considered "the next big Thing", in other words the largest technology breakthrough of our modern times. It is also one of the biggest drivers for healthcare delivery innovations: wearable or implantable sensors, big data and artificial intelligence, augmented reality and medical robots are breakthrough technologies dramatically changing the way people think and act about healthcare. The digital health's dawn is mainly driven by the fast innovative developments

of the three technological pillars of mHealth: telecommunications, computing and medical sensing. Billion of smartphones and internet devices connected to tens of thousands of mobile health applications are used worldwide by patients, clinicians and healthcare providers. This constellation of devices comes with huge business potential: in 2017, the IoT healthcare market was valued at 41 billion dollars and is projected to more than 150 billion by 2022, at a compound-annual-growth-rate (CAGR) of more than 30% [5]. Such number of connected devices is continuously generating enormous datasets, which are already changing the way patients, scientists or physiologists today perceive the eHealth. The eHealth is becoming the "big data Health". The big data will, on one hand, come with severe challenges such as privacy issues [6]. In addition, data collection is still complicated: so far only about 10% of unstructured generated data is worth being saved and one-third of IoT solutions are abandoned due to the lack of data management and analytic skills [2]. On the other hand, this will also disclose new healthcare insights opportunities and may give rise to new industrial and service sectors with massive impact on the worldwide employment. We should also take into account that the patients of tomorrow, the *millennials*, are getting used to streaming (personal) data over the clouds. Moreover, they want to book appointments using their smartphones and securely message their health providers between visits. They also want to receive their medical records

Internet of Things - number of connected devices worldwide 2015-2025

Internet of Things (IoT) connected devices installed base worldwide from 2015 to 2025 (in billions)

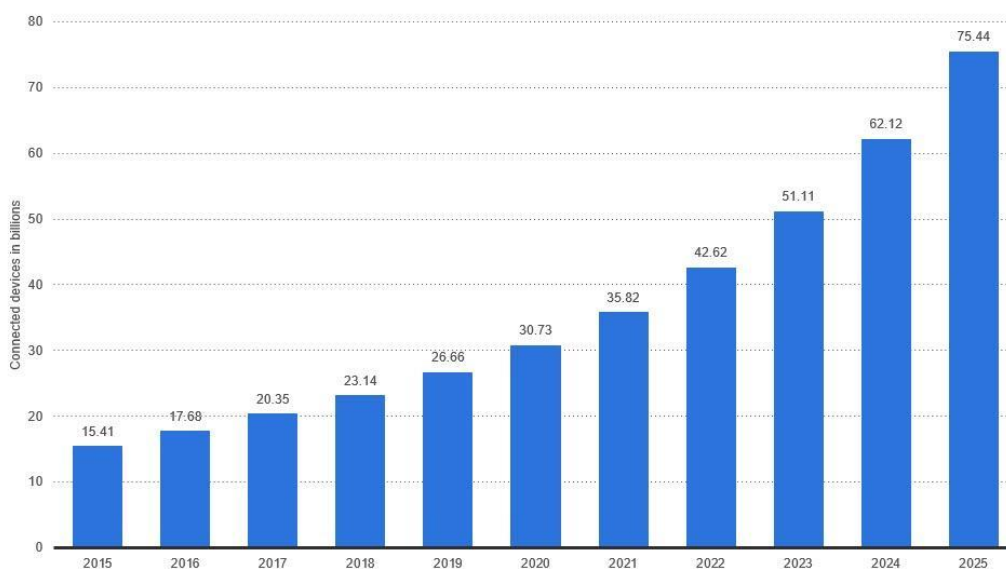


Figure 1.1 – Internet of things connected devices installed base worldwide from 2015 to 2025 (billion), [1].

over the cloud and above all skip the travel time and see their doctors through e-visits wherever possible. In other words, the healthcare industry, that has largely resisted consumer-centric change, can no longer ignore the rapidly growing population of mobile-powered patients, who likely researched their condition on the Internet before their visit.

1.2 Driving factors

The previous section has clearly shown that the modern society is irreversibly changing and with it the way people perceive the healthcare. The objective of this section is to deepen the driving factors ultimately triggering the digital health revolution.

1.2.1 Increase of cardiovascular diseases

Cardiovascular diseases (CVDs) are the number 1 cause of death globally: more people die annually from CVDs than from any other cause [7]. An estimated 17.9 million people died from CVDs in 2016, representing 31% of all global deaths. Out of these deaths, 85% are due to heart attack and stroke.

Most CVDs can be prevented by addressing behavioural risk factors such as smoking, obesity and physical inactivity. People with CVDs or who are at high cardiovascular risk (due to the presence of one or more risk factors such as hypertension or diabetes) need early detection and management using counselling and medicines, as appropriate.

The estimated direct and indirect cost of heart disease in the US from 2014 to 2015 (average annual) was 218.7 billion dollars, where heart attack alone accounts for more than 12 billion dollars [8].

Increasing obesity and population ageing are boosting those numbers. Unhealthy diets and obesity are among the most important driving factors behind CVDs. People aged 65 and older are much more likely than younger people to suffer a heart attack, to have a stroke, or to develop coronary heart disease and heart failure. In the next paragraphs, these two triggering factors are independently examined.

Increase in obesity level

Overweight and obesity are defined as uncontrolled or abnormal fat accumulation which may result dangerous to the person's health. Generally speaking, any overweight state (including obesity) is classified by the body mass index (BMI). The BMI, shown in Fig. 1.2 is a simple index of weight-for-height which is universally used today, by doctors, to classify obesity. Historically, the basis of the BMI was introduced by Adolphe Quetelet (1796-1874), a Belgian mathematician and sociologist [9]. Quetelet's aimed at defining the features of "normal man" and fitting the distribution around the Gaussian one. Doing so, he developed what he called

"social physics": he demonstrated for the first time how important is the comparative statistics in understanding human physical characteristics and social aptitudes. In his principal work "A Treatise of Man and the development of his faculties" published in 1835, he proposed that the normal body weight in kilograms was proportional to the square of the height in meters, generally known in the small circle of experts as the Quetelet Index.

Despite Quetelet's pioneering work, only after World War II the relationship between weight and mortality, particularly diabetes and cardiac diseases, became a serious medical concern and so the subject of deep medical studies. In one of these studies, Ancel Keys (1904-2004) confirmed the validity of the Quetelet index and named it BMI [11]. From Keys's work to our modern time, worldwide obesity has nearly tripled [12]. In 2016, the World Health Organization has revealed that, in 2016, more than 1.9 billion adults, 18 years plus, were overweight. Of these, more than 650 million were obese. In terms of percentage with respect to the global population, this means 39% and 13% of adults were overweight and obese, respectively. This trend is dramatically biased by the G8 countries, US at first, on which the obesity rate is in average more than 20% [13] with respect to the population, Fig. 1.3.

Excessive body weight is fundamentally caused by an energy imbalance between calories consumed and calories expended. Specifically, the increasingly sedentary nature of many works is causing an increase in physical inactivity. Raised BMI is a major risk factor for various diseases, particularly CVDs, diabetes type II, sleep apnoea, musculoskeletal disorders, especially osteoarthritis, and some cancers, such as breast, liver, kidney and colon. As a result, obesity reduces significantly life expectancy: it is the sixth most important risk factor contributing to the overall burden of disease worldwide [14].

Luckily, overweight and obesity, as well as their related noncommunicable diseases, are largely preventable. Indeed, raising awareness in social environments is key in shaping people's choices, by making the choice of healthier foods and regular physical activity the easiest choice

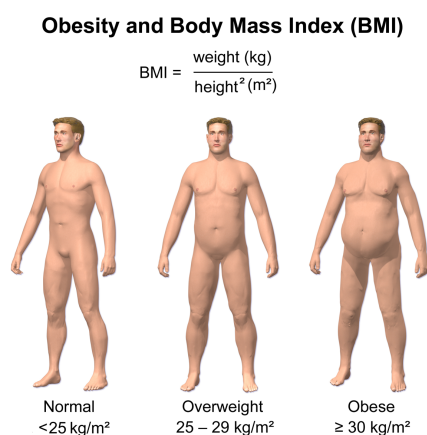


Figure 1.2 – ,
Obesity and Body Mass Index [10].

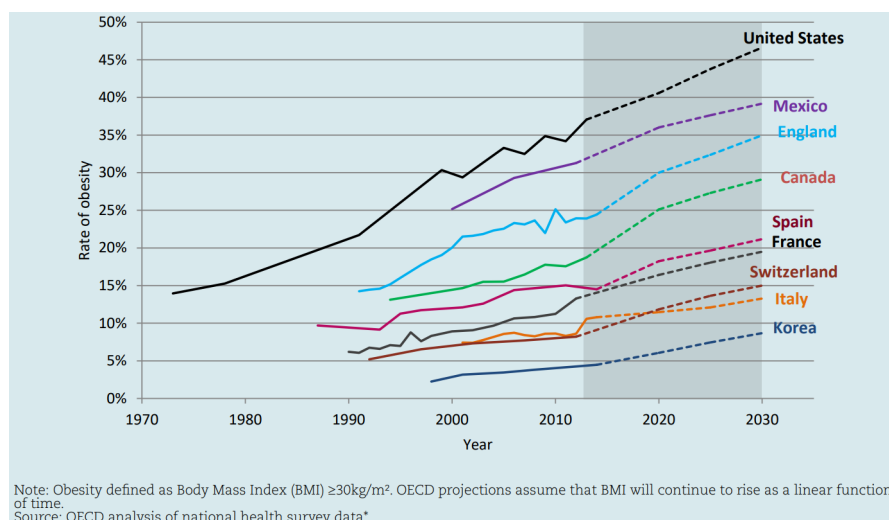


Figure 1.3 – ,
Rising overweight (including obesity) rates in adults aged 15-74 years [13].

(the choice that is the most accessible, available and affordable), and therefore preventing overweight and obesity. In addition, the modern social tissue should seriously take advantage of this billion of connected device, as presented in section 1.1, to get a faster (preventive) health screening or interactive support during regular physical activity.

Population ageing

Global population is getting older and older. At the actual rate, the implications of this trend cannot be dismissed. According to [15], the population aged 60 or over is the fastest growing one. In the most developed countries, the 60+ population will grow at 2.4% annually until 2050 and is expected to increase by more than half over the next forty years: from 274 million in 2011 to 418 million in 2050, Fig. 1.4. Population ageing is the result of the combined action of two leading factors: the increased longevity and declining fertility. The former raises the average age of population, whilst the latter reduces the number of babies and consequently the younger pie of the population. The median age of population is higher in countries that have been experiencing low fertility for a long time, such as Japan or Italy. According to [15] and as shown in Fig. 1.5, from 2020 onwards, there will be more seniors, i.e. 65+, than juniors, i.e. 5-.

The societal implications of an ageing population are important, in several sectors. Among those, the social security system is particularly concerned. Indeed, pension systems have begun to experience serious problems as the extension of the pension period has not been accompanied by an increase in pension contributions. Moreover, the declined fertility and consequently the fewer babies will generate lower tax income leading to public budgets issues.

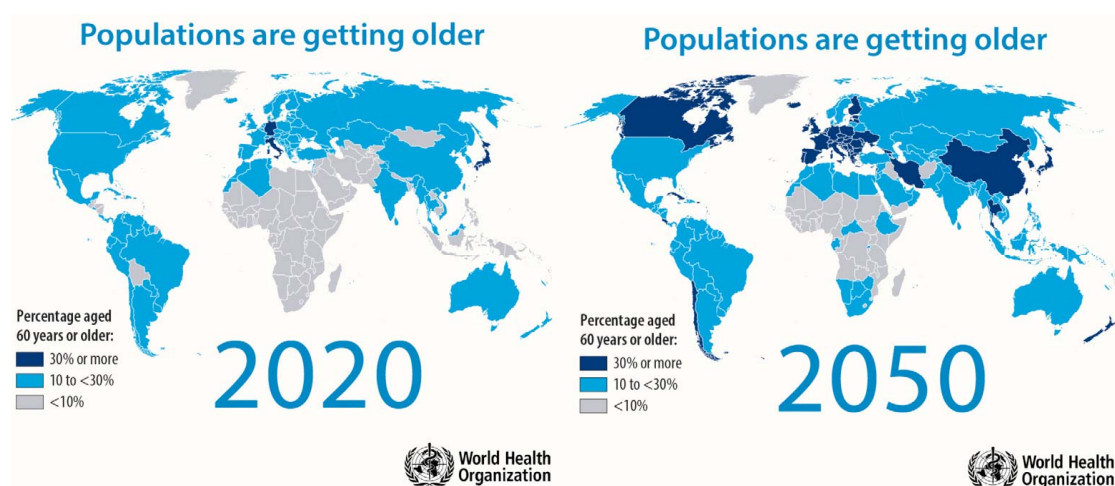


Figure 1.4 – ,
Populations are getting older: comparative study between 2020 and 2050 [15].

1.2.2 Healthcare costs

The economic implications of increasing CVDs, obesity and population ageing are huge. The adage, "what goes up, must come down", is not likely to apply to the global healthcare, which is the resulting largest area of expenditure. The societal implications of such trend may result being dramatic and without a significant change of the modern lifestyle the healthcare costs are expected to explode the countries' budgets. According to [16], the global healthcare spending is supposed to increase at an annual rate of 5.4% between 2018 and 2022. A considerable increase compared to the 2.9% in 2013-2017. In this scenario, the global healthcare spending is expected to surpass 10 trillion dollars by 2022, Fig. 1.6. This forces the healthcare providers to envisage cost reduction and increase their efficiency.

The digital health is sustaining health systems' efforts to transition to new models of patient-centered care and "smart health" approaches. Its innovation is expected to increase healthcare's access and affordability, improve its quality, and lower its costs. Digital solutions also have the potential to enable better use of health data in research and innovation. Consequently, the healthcare can be fully personalized leading to better health interventions and services. Indeed, ageing populations and increasing obesity level and their consequent rise of non-communicable diseases are pushing an industry shift away from curing disease in the short term toward preventing and managing disease and promoting overall well-being in the long term. In order to enable such transition we have to move the healthcare outside hospital walls: scientists, engineering R&D centers and hospitals have to start working together providing new sensors, systems, medical platforms intercepting customers' and societal needs and winning prejudices. Likely, health systems around the world are already investing in the digital health, with varying degrees of success and conviction [16]. Among these countries, China issued the 13th Five Year National Science and Technology Innovation Plan, which aims at developing new technologies for precise e-medicine and creating a national platform to

1.3. The increasing need of reliable and continuous health monitoring

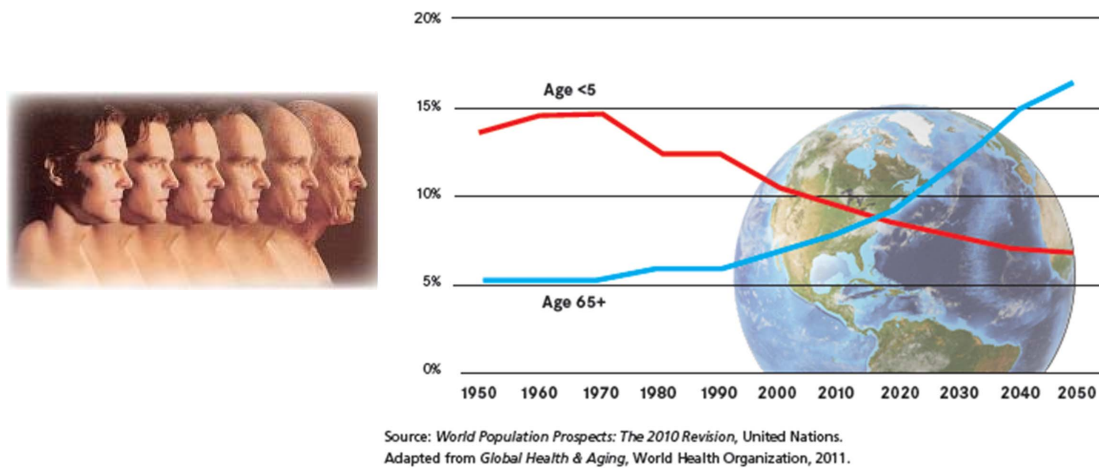


Figure 1.5 – ,
Young children and older people as a percentage of the global population: 1950-2050 [15].

share biomedical big data. The existence of already unified national platforms is reassuring: the next (ambitious) step will be an international standardized platform.

1.3 The increasing need of reliable and continuous health monitoring

In the previous sections the reasons why, nowadays, efficient and remote health monitoring is becoming increasingly important have been disclosed. The healthcare industry is becoming more reliant on new methods to monitor and treat patients. This, along with an increased interest in fitness and wellness, is calling for more affordable, precise and wearable health

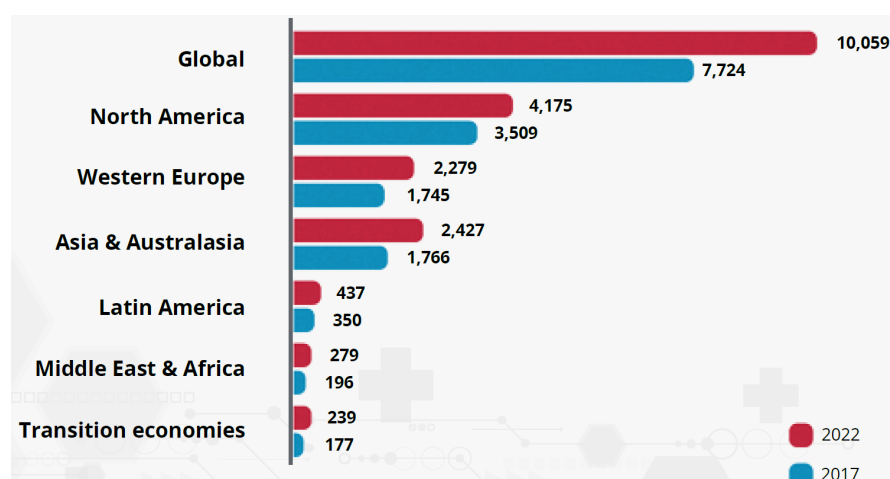


Figure 1.6 – ,
Healthcare spending (USD billion), and CAGR 2017-2022 [16].

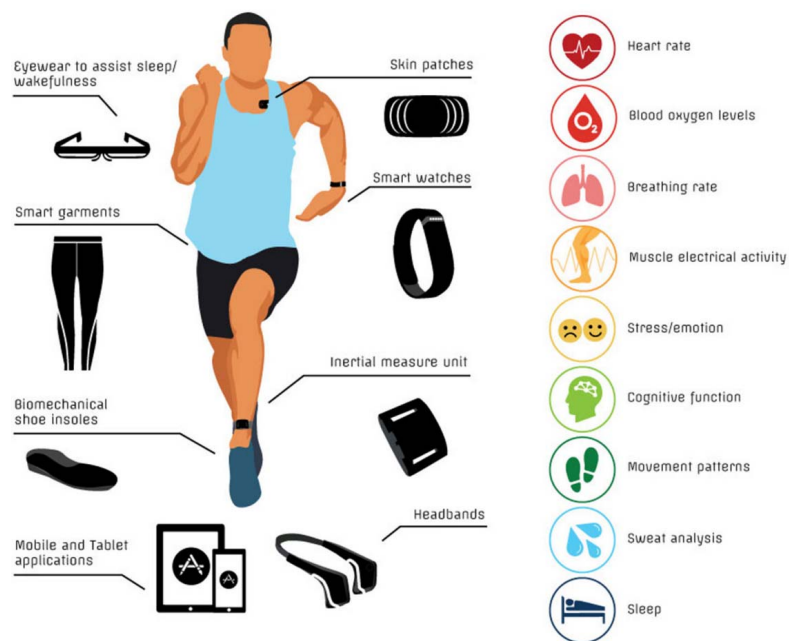


Figure 1.7 – ,
Summary of current technologies for monitoring health/performance [17].

monitoring devices. Generally speaking, the number of available consumer technologies for evaluating physical and physiological health has increased dramatically in the last ten years, as shown in Fig. 1.7: some of them focus on monitoring heart rate or its variability, other on sleep, stress or specific metabolic functions.

Despite the number of available devices is huge, few of them have been independently tested to determine their validity or reliability. In addition, some of their key functionalities are often released after their commercialization [17]. In this perspective, commercially available smartwatches and wearables fall short of meeting customer requirements when it comes to reliability, precision and battery lifetime. This is particularly true when it comes to heart rate monitoring. A big chunk of these heart rate sensors uses optical transduction. The science and sensing scheme behind the optical heart rate monitors is the so called Photoplethysmography (PPG). A PPG sensor measures the artery volume change thanks to the light reflected from the tissue. PPG appears to be a key technology allowing non-invasive monitoring of vital biological indicators such as the heart rate, the blood oxygen saturation, the respiration rate and the arterial pressure. The popularity of optical heart rate monitors in smartwatches, smartphones or smartrings is largely due to the convenience and low cost of these devices. On the other hand, accurately estimating a person's heart rate using these devices still remains challenging and we should not expect dramatic improvements in reliability unless there are fundamental changes in the sensor technology. As above mentioned, optical sensors tend to elicit consumer expectations. An example is the 2018 class action in California against Fitbit whose sensors were accused to be "grossly inaccurate and frequently fail to record any heart rate at all".

The optical pulse sensors market is expected to witness a CAGR of 9.3%, over the forecast period 2019-2024 [18]. The capability of the sensors to improve accuracy, and increase functionality and efficiency of several applications, along with the growth in the use of wearable, will produce a significant demand for optical pulse sensors. In this scenario, any fundamental change in the today PPG sensor technology leading to better performance and longer lifetime measurements would be simply welcomed as a serious game changer. Indeed, thanks to the "readiness" of such sensors into wearable platforms, any game changer in this business will dramatically change the modern healthcare by generating big quantity of health data that will be key in exploring new medical frontiers.

1.4 Thesis organization

Chapter 2 aims at introducing the history and physics behind the PPG sensor. Questions such as "how does a PPG sensor work?" or "what is the physics behind a PPG signal?" are answered. Particular attention is devoted to the light absorbance and the optical considerations of the origins of the PPG waveform, so the light-tissue interactions, and the sensing probe.

Chapter 3 focuses on the PPG clinical applications. Specifically, this chapter illustrates what are the vitals that can be directly or indirectly extracted out of a PPG waveform in applications ranging from fitness/wellness to medical.

Chapter 4 illustrates the PPG instrumentation in terms of readout circuits. Particular attention is devoted to the challenges and bottlenecks while designing a PPG sensor. The chapter ends with a state-of-the-art analysis of PPG sensors.

Chapter 5 complements chapter 4 by deepening the noise and artefacts types affecting a PPG reading. The chapter focuses on the electronic noises, such as the thermal or the flicker, but also on the noise which is naturally brought by the light itself, i.e. the shot noise. The chapter also presents some of the artefacts, e.g. motion, ultimately limiting the PPG signal quality. Eventually, taking advantage of the state-of-the-art analysis in chapter 4, this chapter compares two possible readout chains in terms of signal-to-noise performance.

Chapter 6 is the center chapter presenting the heart of this work: a micropower PPG sensor. The basic recipe behind this innovative sensor is disclosed and its fundamental ingredients presented. The chapter ends with some performance metrics and comparison versus the state-of-the-art.

Chapter 7 presents an alternative application complementing the PPG one in the today portable business: the time-of-flight (ToF). In particular, the possibility of having an "all-in-one" sensor is further illustrated. The ToF performance of the chip presented in chapter 6 are illustrated and benchmarked versus commercially available devices.

Chapter 8 concludes this manuscript.

Conclusions

The modern society is changing and with that the way people perceive the healthcare. Specific factors such as the increase of CVDs, as a consequence of increased obesity and population ageing, are changing the modern healthcare needs and already impacting on the countries' budgets. In this perspective, efficient and remote health monitoring is becoming increasingly important.

The popularity of PPG sensors in smartwatches, smartphones or smartrings is largely due to the convenience and low cost of these devices. On the other hand, accurately estimating people's vitals by the means of these devices still remains challenging and we should not expect dramatic improvements in reliability unless there are fundamental changes in the sensor technology.

Thanks to the "readiness" of such sensors into wearable platforms, any fundamental change in the today PPG sensor technology leading to better sensing would be simply welcomed as a serious game changer. This has been the constant motivating factor behind this work whose organization, chapter-wise, has been also presented.

2 The photoplethysmography (PPG)

Nowadays, the duo between wearable devices and optical heart rate sensor is becoming a must. Indeed, roughly no fitness trackers or smartwatches are today sold without an optical heart rate sensor, Fig. 2.1. The technology behind these sensors is called Photoplethysmography (PPG), which is an optical measurement technique used to detect blood volume changes in living tissues. A PPG sensor requires few optoelectronics components, such as a light source, e.g. light-emitting-diode (LED) to shine the living tissue, a photodetector (PD) to track any light intensity variation due to the blood volume change and an analog front-end (AFE) for signal conditioning and processing. Today, the importance of PPG for medical monitoring is proven by the number of primary vital signs directly or indirectly recordable out of it [19]. The vital signs are a group of four most important signs that indicate the status of the patient's vital functions. These are the body temperature, the blood pressure, the heart rate and the respiration rate. With the exclusion of the body temperature, a PPG sensor can be used to record all the others.

It is objective of this chapter to deepen the basic principle of PPG, the light-tissue interaction and the physics behind it. The chapter starts with a brief overview of the history of PPG.

2.1 History of PPG

The PPG was first explored in the 1930's. In 1936 two research groups at Merck Institute of Therapeutic Research, New Jersey, and at Stanford University School of Medicine disclosed the experiments of monitoring the blood volume changes in rabbits' ears by the means of similar instrumentations to the PPG's ones [20]. A pioneer of the PPG was Alrick Hertzman (1898-1991) from the Department of Physiology at St.Louis University. In 1937, Hertzman published a paper describing the use of reflective PPG to measure induced blood volume changes. In particular, only one year later [21], Hertzman already identified the most important challenges related to the PPG sensing, e.g. the movement of the measurement probe against the tissue, the content of which is further described in the next chapters of the manuscript. Hertzmann's observations have significantly contributed to shaping the modern PPG technology.

Chapter 2. The photoplethysmography (PPG)

In the last three decades, the growing wave of small, low-cost, reliable and easy-to-use cardiovascular monitoring systems have also concerned the design of modern PPG sensors. Specifically, PPG sensors have gained popularity thanks to the great advancement in optoelectronics. The development of new semiconductor technology, e.g. LED, has contributed to shrink the size and to increase the sensitivity and reliability of those sensors. In the 1970's, a major push to the use of PPG sensors also came from the development of the pulse oximetry [22] and its universal adoption in medical institutions as a non-invasive method of monitoring patients' oxygen level.

2.2 What is the PPG?

A PPG signal is obtained by shining light from an LED at a given wavelength, in the visible or near-infrared range, into an human tissue, e.g. finger, forehead, ear lobes. As shown in Fig. 2.2, a PD detects the light transmitted through (transmissive PPG) or reflected (reflective PPG) from the tissue and transforms it into a photogenerated current.

The transmissive PPG sensors are usually placed near finger tips to reduce the needed light intensity to penetrate through the tissue. On the contrary, reflective PPG sensors can be placed wherever the tissue is properly perfused, e.g. presence of blood vessels close to the skin surface. The detected signal, i.e. PPG, consists of two different components: a large DC (quasi-static) component corresponding to the light diffusion through tissues and non-pulsatile blood layers, and a small AC (pulsatile) part due to the diffusion through the arterial blood. The AC component is only a very small fraction (typically 0.2% to 2%) of the DC one, meaning an AC being 500 to 50 times smaller than the DC, respectively. This mostly depends on the body location and the LED wavelength and weakly on the skin tone [23, 24, 25, 26, 27]. Such small AC/DC ratio is often called perfusion-index (PI).

The AC component shows changes in the blood volume that occurs between the systolic and



Figure 2.1 – Apple watch with the PPG sensor on.

the diastolic phases of the cardiac cycles. In other words, the fundamental frequency of the AC component depends on the heart rate, e.g. 1 Hz equal to 60 beats per minute. The DC component instead slowly changes with the respiration, Mayer waves, vasomotor activity and also thermoregulations [28, 29, 30, 31].

2.3 What is the physics behind? The Beer-Lambert law

The science behind the PPG technology was mostly understood by 1854 when the German physicist August Beer (1825-1863) proved that the amount of light transmitted through a solution varies based on the concentration of the solute. His findings, together with those of Johann Heinrich Lambert (1728-1777) and Pierre Bouguer (1698-1758), gave rise to the Beer-Lambert law.

The Beer-Lambert law describes the attenuation of monochromatic light travelling through an uniform medium containing an absorbing substance. If an incident light at a given wavelength and intensity I_0 enters the medium, a part of this light is transmitted through the medium, whilst another part is absorbed. The intensity I of the transmitted light decreased exponentially with the distance, as shown in Fig. 2.3.

The light transmission (T) through the medium is defined as the ratio of the impinging light (I_0) and the transmitted one (I)

$$T = \frac{I}{I_0} = e^{-\epsilon(\lambda)cd}, \quad (2.1)$$

where $\epsilon(\lambda)$ is the extinction coefficient, usually in $L\text{ mmol}^{-1}\text{ cm}^{-1}$, of the absorbing substance at a given emitting wavelength, c , usually in mmol L^{-1} , the concentration of the substance in the medium and d , usually in cm , the optical path through the medium. In other words, the

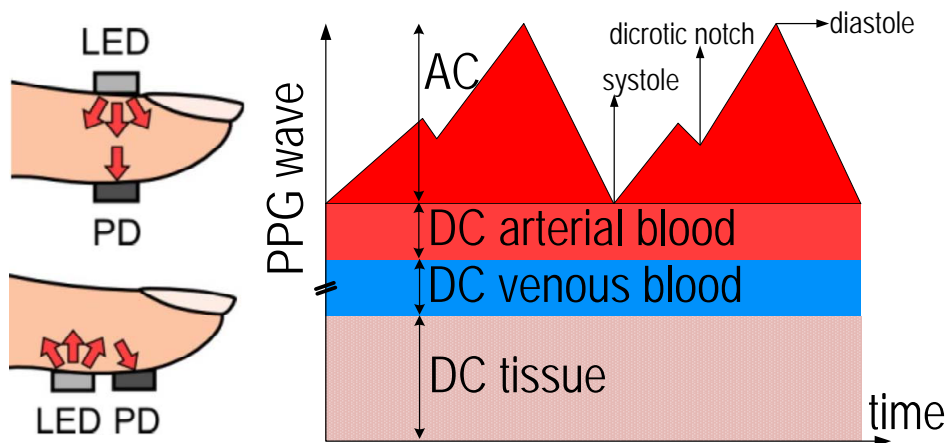


Figure 2.2 – PPG sensor set-up (transmissive and reflective) and the DC and AC components of a PPG signal.

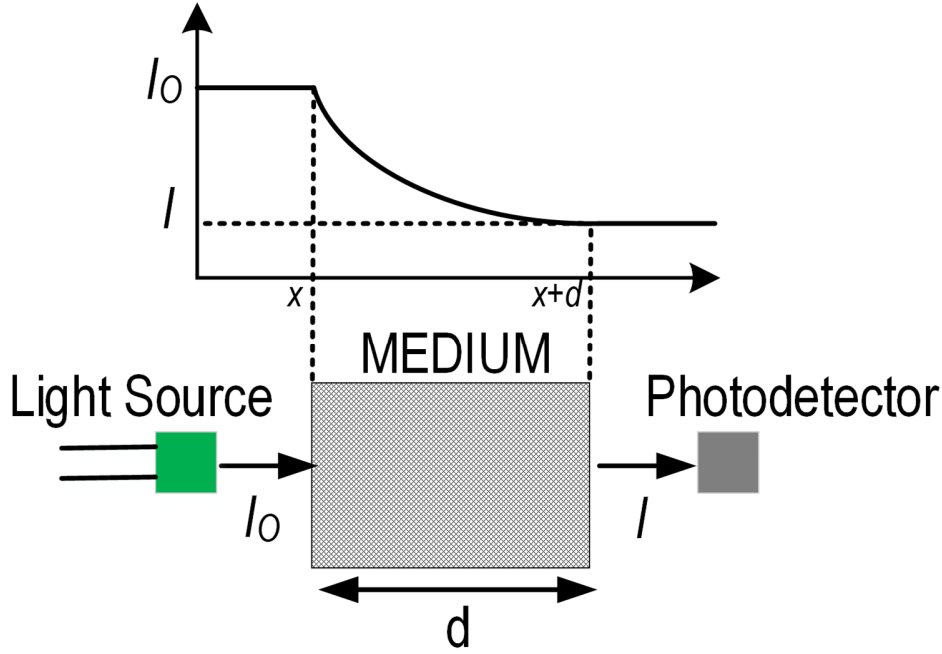


Figure 2.3 – Illustration of the Beer-Lambert law.

Beer-Lambert law is based on the assumption that the sum of the transmitted and absorbed light equals the impinging one. Indeed, it doesn't account for any physical process which may include scattering of light in the medium or reflection at the surface. The (unscattered) absorbance (A) is defined as the negative natural logarithm of the light transmission

$$A = -\ln T = \epsilon(\lambda)cd. \quad (2.2)$$

The Beer-Lambert law is valid even in the presence of matter with multiple absorbants. In this case, supposing the presence of n absorbing substances, the resulting total absorbance A_t is the sum of the n independent absorbances. In other words, (2.1) results to

$$T = \frac{I}{I_0} = e^{-A_t} = e^{-\sum_{i=1}^n \epsilon_i(\lambda)c_i d_i}, \quad (2.3)$$

where ϵ_i , c_i , d_i is the extinction coefficient, the concentration of the substance and the optical path, respectively, of the individual absorbing substance i .

A living tissue consists of several absorbing substances. These substances are called chromophores. The most common chromophores encountered in the skin are: the haemoglobin, the melanin and the water, being the first two the main light absorber in human blood at the wavelengths used in PPG [32], e.g. visible or near-infrared, as shown in Fig. 2.5.

Fig. 2.4 shows how the PPG signal is, with good approximation, generated from the Beer-Lambert law. Indeed, the effective optical path seen by the impinging light, i.e. d , results

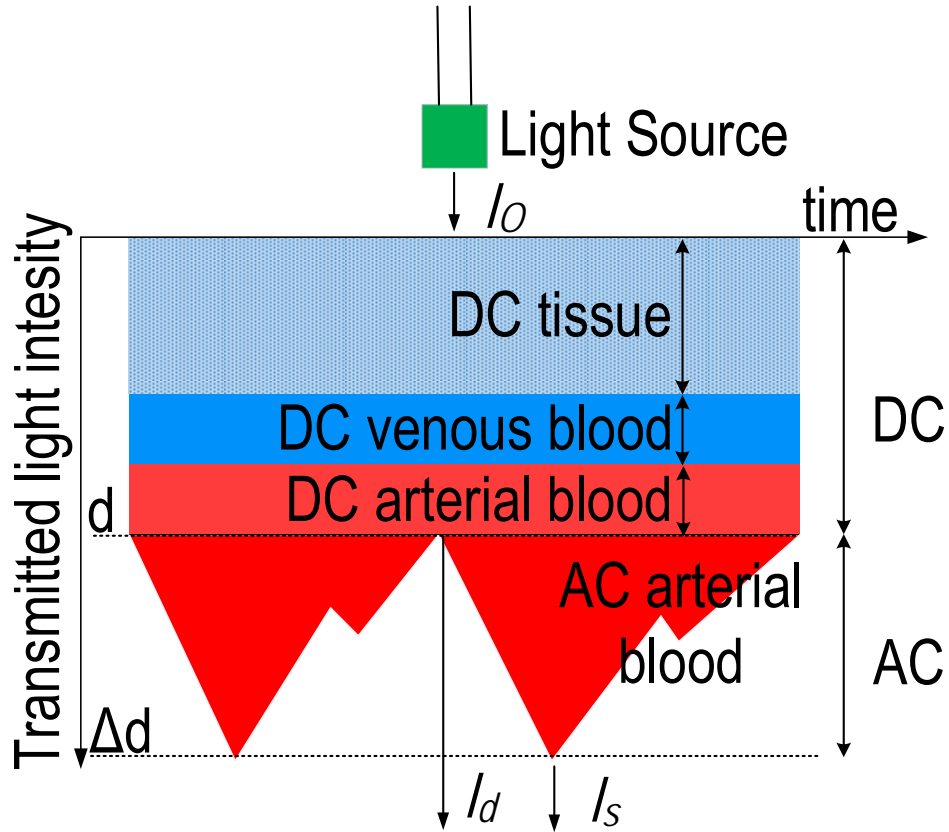


Figure 2.4 – Illustration of how the PPG signal is generated from the Beer-Lambert law.

being time dependent and modulated by the cardiac activity. At systole, the arteries contain more fresh blood and therefore their diameter increases due to the increased pressure. In other words, the systolic transmission is lower due to the larger optical path. On the contrary, during the cardiac diastole the transmission is at its maximum, equal to the non-pulsatile (DC) one, thanks to the shorter optical path. The notch between the systolic minima and the diastolic maxima is called dicrotic notch or incisura. This notch is associated with the isovolumetric relaxation happening at the end of the cardiac systole. Indeed, the end of the systole is accompanied by the valve closure. This is associated with a small backflow of blood into the ventricles giving rise to the characteristic notch [33].

In Chapter 3 we will see that the reasons behind the characteristic features of the PPG signal are slightly more complex and also take into account other mechanisms beyond the Beer-Lambert law.

2.4 Light-tissue interaction: some optical considerations

We have seen that the most common chromophores encountered in the skin, at the PPG wavelengths, are the haemoglobin and the melanin. Fig. 2.6 shows how complex the human

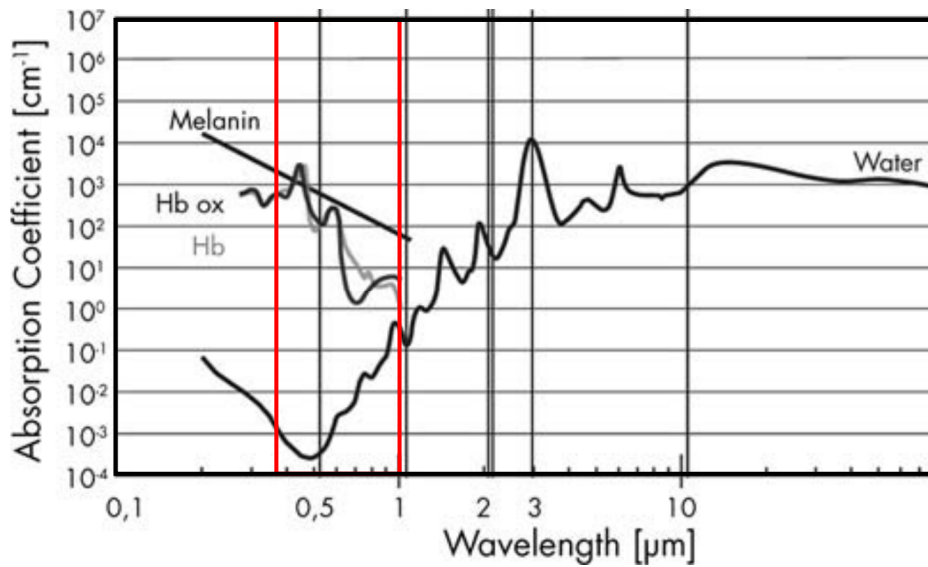


Figure 2.5 – Absorption spectrum of melanin, haemoglobin and water versus the emitting wavelength [37]. Highlighted in red the PPG optical spectrum.

skin is. Indeed, it consists of several layers: from the surface, the epidermis, the dermis and the subcutis. The epidermis is the outermost layer of the skin and contains no blood vessels. It is the shallowest skin layer: in average $100\ \mu\text{m}$. In the PPG optical spectrum, melanin is the major absorber in the epidermis, especially at shorter wavelengths [34, 35]. The dermis is the layer beneath the epidermis and consists of hair follicles, different glands and blood vessels (and its haemoglobin). The dermis largely defines the overall light absorbance and its optical penetration depth since it extends for roughly $2\ \text{mm}$. Indeed, the penetration of any optical radiation in the tissue is wavelength dependent. For instance, only the epidermis would result exposed to blue or shorter (UV) wavelengths. As the emitting wavelength gets larger and larger, the deeper this penetrates into the tissue, so reaching the dermis and beneath. The work in [34] shows, for the same subject, a factor 6 of difference in penetration depth between a $500\ \text{nm}$ and a $800\ \text{nm}$ impinging light. For this reason, infrared light (IR) has been a reference in PPG devices. However, PPG sensors based on green-wavelengths are becoming increasingly popular due to the larger effective PI, at a given LED emission [24, 36, 27]. Indeed, the shorter green penetration means that the reflected signal includes less information from various non-pulsatile media than IR PPG.

The light interaction with biological tissues is more complex than what is described by the Beer-Lambert law. Indeed, such interaction includes the optical processes of scattering, reflection, transmission and fluorescence [34]. In addition, the LEDs don't emit monochromatic light. In other words, the absorbance of light is not only proportional to the concentration of melanin and haemoglobin or the optical path length. This becomes even more complex as the skin penetration depth increases [36], explaining why modern PPG sensors are more and more employing green LEDs.

2.4. Light-tissue interaction: some optical considerations

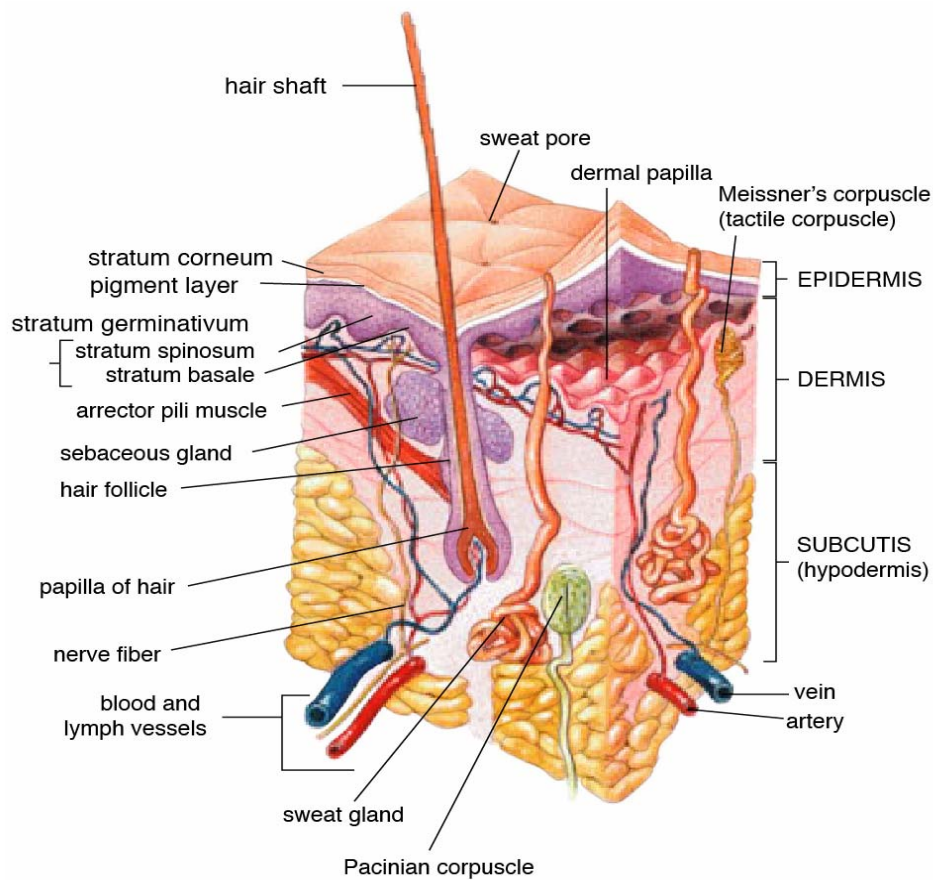


Figure 2.6 – Skin composition: epidermis, dermis and subcutis [38].

Light scattering causes the deviation of the light beam from the target direction. Scattering is due to material inhomogeneities or more precise to physical inhomogeneities resulting into refractive index discontinuities in the medium. The spatial distribution and intensity of scattered light depends on the size and shape of these inhomogeneities, ultimately determining a change in the direction of propagation. Scattering may be either elastic, which means that the frequency of the scattered wave is equal to the frequency of the incident wave (no energy change) or inelastic, which brings a frequency shift so an energy variation. Among the elastic one we need to account for the Rayleigh and Mie scattering, Fig. 2.7. Raman scattering (Stokes and Anti-Stokes) is an example of inelastic one. For molecules or small particles whose dimensions is smaller than roughly one-tenth of the light wavelength, scattering is generally weak, nearly isotropic and varies with the inverse of the 4th power of the incident wavelength. This is the Rayleigh scattering. For particles with larger dimensions on the same order as the impinging wavelength, scattering is much stronger, more forward-directed and depending on the inverse of the wavelength. This is the Mie scattering. When the particle size greatly exceeds the incident wavelength scattering becomes weaker and strongly forward-directed.

A tissue consists of a mixture of Rayleigh and Mie scattering, but Mie scattering seems to

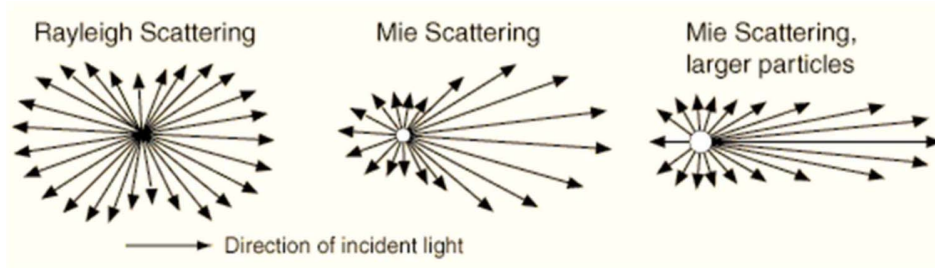


Figure 2.7 – Representation of the possible scattering events: Rayleigh, Mie and Mie for larger particles [39].

dominate in the dermis due to the presence of collagen (proteins) [39]. In addition, in biological tissues, several scattering (or multiple scattering) sites exist. First of all, the whole blood. The blood consists of about 45% of red blood cells, about 54.3% of plasma and 0.7% of white cells. In whole blood, haemoglobin is not dissolved in the plasma, but is mostly present in the red blood cells. The red blood cell shape, disc, is dependent on the flow-velocity [40]. Indeed, their major diameter is aligned parallel to the direction of the flow during diastole and perpendicular during systole. In other words, during systole there will be more absorption and this goes on top of the increase in the optical path due to the arteries' diameter [41]. The second scattering site is the tissue itself. Although, the light loss due to the tissue scattering is supposed to be constant, it does interfere with the PPG measurements since changing the path on which the photons travel through the tissue. More specifically, [25] describes the detected light as an ensemble of independent photon paths. Some of the detected photons have travelled shorter paths in the tissue and others scattered further without being absorbed. The longer travelled photon path provides more interaction with the whole blood or tissue. As the photons penetrate more in the medium, their survival rate (probability not to be absorbed) reduces. One possible model to describe such behaviour is the random walk model, which is a combination of (multi)scattering and absorption. In other words, the final detected signal at the level of the PD comprises a mixture of all surviving photon paths and convolves informations coming from all the paths. To account for these effects, [25] has proposed to modify the Beer-Lambert law expressed in (2.1), by replacing the optical path d with the effective photon mean path length $\langle d \rangle$. Several other theories have tried to model the scattering effect in the tissue. Twersky's multiple scattering theory [42, 43, 44] seems to be the one getting more consensus: the total absorbance of whole blood can be expressed as the sum of the absorbance as described by the Beer-Lambert law, (2.2), and a second term representing the effect of scattering (superimposition). In other words, the scattering increases the photons' absorption and consequently the light interaction with the matter.

The expected photons' propagation path into a tissue can be simulated by the means of Monte Carlo simulations [45, 46]. In a typical Monte Carlo model, virtual photon packets are simulated as they propagate through a given medium volume. The medium is both highly scattering and absorbing.

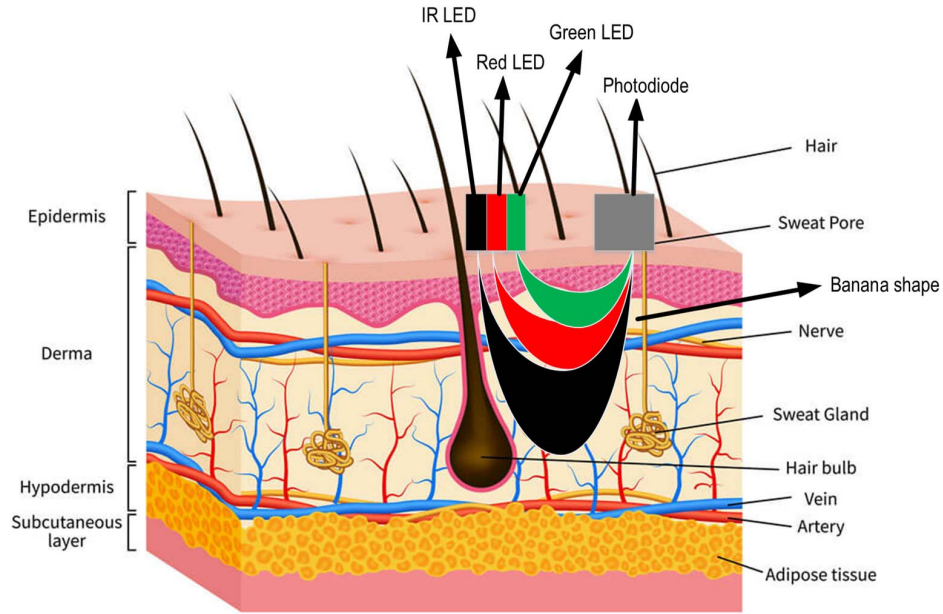


Figure 2.8 – Reflective PPG: photon travelling path in tissues for three different emitting wavelengths, IR, red and green, assuming almost equal LED-PD distance. The characteristic banana shape is larger as the photons’ penetration depth increases. Reprinted from [47] and adapted.

Fig. 2.8 shows the typical photons’ travelling path in a tissue. From the figure, the typical photons’ banana shape distribution can be seen. Longer wavelengths lead to wider banana shapes [48, 49], meaning a larger probability of photons undergoing a random walk, i.e. multiscattering or absorption events (lower survival rate). However, the tissue volume with the highest travelling probability still consists of the direct path between the LED and the PD, which is independent of the emitting wavelength.

2.5 Tricks to enhance the PPG (AC) magnitude

As described in section 2.2, the pulsatile AC component is only a small fraction of the whole PPG signal. On the other hand, almost all the relevant medical features rely on the AC component. So, a good PPG sensor has to be built with the aim of maximizing the PI, i.e. the AC versus the DC, without any significant power, area and system’s complexity overhead. In Chapter 3 we will see that a good PPG morphology is key to enable wide vital signs monitoring.

A PPG sensor, as above-explained, consists of one or more LEDs, a broad-band PD and an AFE. These three ingredients define together a PPG module. A PPG module comes with several degrees of freedom. As far as the PI is concerned, this can be enhanced either at the optical side or at the electronic side (or at both!). The objective of this section is to focus on the optical side, so describing how to design the optical part of the PPG module in order to maximize the

PI.

The PI strongly depends on the emitting wavelength, on the LED-PD distance, on the LED-PD relative height and as well on the tissue perfusion. Apart from the last one, all the others are design variables fully tunable to enhance the PPG signal quality.

As already presented in section 2.4, the IR comes with a larger irradiation volume than the green light [24, 36]. Being the pulsatile blood a very small percentage of the whole absorbing matter, this means intrinsically a larger DC component or a smaller PI. Indeed, the reflection and scattering from deeper tissue produce a much more complex signal. In other words, the green light PPG is affected by noise to a much lesser extent.

The LED-PD distance is one of the most important design variables. If we place the LED too close to the PD, the latter will immediately saturates due to the large DC component resulting from the direct cross-talk or the multiscatterings taking place at the epidermis. For a constant LED emitting power, the light intensity detected by the PD decreases roughly exponentially as the LED-PD distance increases. This applies for both the AC and DC components, but at a different rates. Indeed, as the LED-PD distance increases, the DC component decreases faster than the AC one, resulting into a larger PI. On the other hand, LED-PD distances larger than 10 mm tends to enhance the PI, at the cost of larger LED power [26]. Indeed, the probability of photons (survival rate) is decreased with the increasing distance. Depending on the choice of the emitting wavelength, the LED-PD distance should change accordingly. The reason still relies on the optical consideration described in section 2.4: the green photons, carrying less energy than the IR ones, propagate less in the tissue, meaning that the LED-PD distance has to be reduced accordingly. The work in [49] has tried, by the means of Monte Carlo simulations, to identify the optimum LED-PD separation distance as a function of the emitting wavelength. Maximum PI has been found at the LED-PD distance of 1.85 and 2.75 mm for the 530 nm and 940 nm, respectively.

As discussed above, the direct crosstalk between the LED and the PD has to be minimized. Direct reflection from the skin adds to this crosstalk. In order to enhance the PPG signal quality, it is good practice to incorporate external light barriers and elevating the PD with respect to the LED, as shown in Fig. 2.9. At the same LED shining power, the external light barriers can increase the PI by a factor of almost 4 [50].

The skin perfusion also changes with the environment. Whenever the skin is either cooled or heated, the skin perfusion varies the AC and DC components. Especially in the case of a large blood volume, the blood absorption increases and the signal decreases. For the reflective PPG, the influence is weaker with the green light compared to IR light because the change in light irradiation volume is smaller [36].

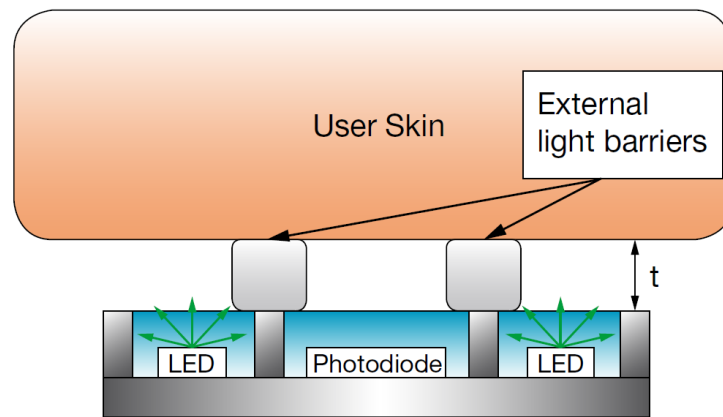


Figure 2.9 – External light barriers in PPG modules helping the reduction of the direct optical crosstalk and consequently reducing the DC component [50].

2.5.1 Measurement sites

The body location of the PPG sensor is an important issue affecting the signal quality or the sensor's resilience to artefacts, e.g. motions. In the last years, different measurement sites, beyond the classic finger one, have been explored, including the wrist, earlobe, ear canal. Even the esophageal region has been explored in clinical tests [51]. The work in [52] has compared 52 anatomical sites in healthy subjects in terms of perfusion values. It has shown that the finger, the palm, the face and the ears offer much better perfusion than other sites.

Conclusions

PPG sensors are nowadays integral parts of wearable devices. The importance of PPG for medical monitoring is proven by the number of primary vital signs directly or indirectly recordable out of it, such as the heart rate, the respiration rate and the blood pressure.

A PPG signal consists of a tiny AC component, fully synchronous with respect to the cardiac period, which is superimposed on a large quasi-static baseline. The majority of the medical information are brought by the AC component. For this reason, it is key to build PPG sensors maximizing the AC part of the PPG signal.

The physics behind a PPG signal is the Beer-Lambert law which describes the attenuation of monochromatic light travelling through an uniform medium containing an absorbing substance. On the other hand, despite the Beer-Lambert law gives a good understanding of how a PPG signal is generated, the interaction of light with biological tissues is more complex than what is actually described by the Beer-Lambert law. Indeed, such interaction includes the optical processes of scattering, reflection, transmission and fluorescence.

Building a performing PPG sensor requires some attention. For instance, the choice of the light wavelength has implications on the light-tissue interaction and generated artefacts.

Chapter 2. The photoplethysmography (PPG)

Moreover, the distance from the PD and the LED (and relative height) is key in enhancing the AC component of the PPG signal.

3 PPG applications in physiological measurements

PPG has been extensively used to monitor several physiological measurements such as the heart rate and the blood oxygen saturation. Several studies have also developed theories or methods to use the PPG for monitoring the respiration rate and the blood pressure. In addition, PPG has also been applied for vascular states' assessment, including arterial stiffness and ageing, and for autonomic function monitoring, such as the heart rate variability and the stress level.

The objective of this chapter is to review each of these vitals with the ultimate aim of demonstrating the widespread possible use of the PPG technology in vital signs monitoring.

3.1 Heart rate

The heart rate (HR) is a very important vital for a variety of possible applications, including fitness and wellness and ambulatory patient monitoring. It reports the cardiac period or in other words the number of cardiac contraction per minute, i.e. beats-per-minute (bpm).

The HR can vary according to different factors, including air temperatures, body position, increased respiration, stress, physical exercises or drugs' ingestion [53]. Normal resting HRs range from 60 to 100 bpm. Heart rate abnormalities, also called heart arrhythmias, are often linked to cardiovascular diseases (CVDs), such as heart failures [53, 54]. Possible arrhythmia types are a slower rhythm, also called bradycardia, or a faster one, named tachycardia.

The HR is generated by the sinoatrial node (SA), which is the heart's natural pacemaker [54]. The HR is also influenced by the autonomic nervous system, through the sympathetic and parasympathetic nerves, as shown in Fig. 3.1. The nervous system over the HR is controlled by the cardiovascular centres of the medulla oblongata, which is a part of the cerebellum responsible for autonomic (involuntary) functions. Specifically, the brain, through the nervous system, can alter the HR thanks to the vagus and the sympathetic cardiac nerves. The former participates in inhibiting the heart activity (parasympathetic stimulation), while the latter stimulates it (sympathetic stimulation). Intrinsic HR is measured in the conditions of no

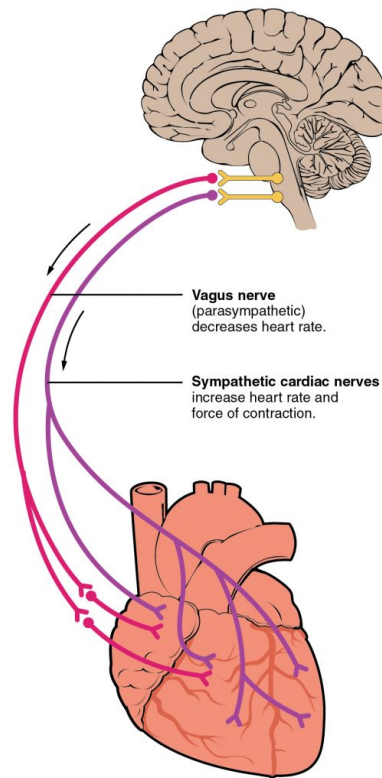


Figure 3.1 – Parasympathetic and sympathetic cardiac nerves: cardioaccelerator and cardioinhibitory at the basis of the heart rate modulation [58].

autonomic nervous system influence. In this case, a healthy heart is supposed to pump at about 100 bpm [55], which tends to get lower as the age increases. Since resting HR is lower than this value, it is evident that the parasympathetic stimulation inhibits the cardiac period. On the other hand, whatever HR beyond the intrinsic one would require sympathetic stimulation.

As presented in section 2.3 of the previous chapter, the PPG wave consists of a small AC component superimposed on a large (quasi) DC one, being the former fully synchronous with the cardiac period. As shown in Fig. 3.2, the periodicity of the AC part of a PPG wave corresponds to the periodicity of the R-peaks of the QRS complex in the synchronous ECG trace. This demonstrates the validity of the PPG technique for HR monitoring. Indeed, even for wrist PPG monitoring, a percentage as high as 99.44 % of PPG corrected beats versus the ECG has been reported [56]. Of course, any artefact, e.g. motion, on the PPG sensing probe would seriously impact the reliability of these data. It should also be mentioned that, unlike ECG, PPG is an electrode-free and fully wearable technique which leads to better patient comfort and easier measurements. Indeed, an ECG recording requires placement of typically 3 to 12 electrodes [57].

3.2. Inter-beats-interval and heart rate variability

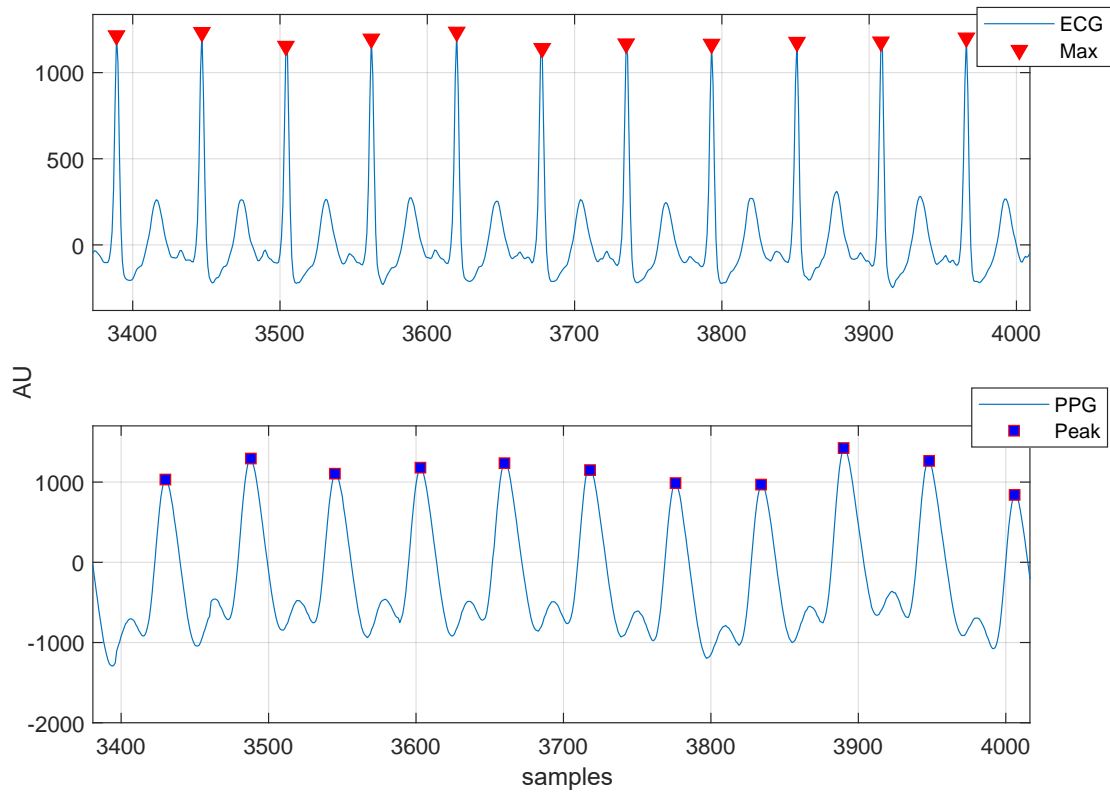


Figure 3.2 – ECG and PPG signals: the RR intervals of the ECG trace correspond to the PP interval of the PPG one.

3.2 Inter-beats-interval and heart rate variability

The HR variability (HRV) represents the variation of the HR between consecutive beats. The HRV analysis has been the subject of numerous clinical studies concerning cardiological diseases and the function of the autonomous nervous system. Indeed, HRV is a marker of cardiac autonomic nervous system function, and has been reported to reflect cardiac health, cardiac mortality and morbidity and overall mortality risk [59]. For instance, reduced HRV is correlated with the risk of myocardial infarctions, congestive heart failure or sudden cardiac death [60]. An elevated HRV can also reflect physical fitness and social integration [61].

The gold standard technique for HRV monitoring relies on analysing the RR intervals from an ECG signal, Fig. 3.2. On the other hand, as above-mentioned, these intervals can also be extracted out of the PPG wave, being the AC component synchronous with respect to the ECG time intervals. Extracting the HRV from the PPG wave is often called pulse rate variability (PRV) [60, 62]. The extracted intervals are called inter-beats-intervals (IBI) [63]. Several studies have investigated the accuracy of PRV as an estimate of HRV in healthy subjects. In particular, PRV has been shown to be sufficiently accurate to estimate the HRV in healthy subjects at rest or during night sleep [60, 62, 64, 56]. On the other hand, it should also be highlighted that the agreement between ECG and PPG in terms of IBI deteriorates during upright position or

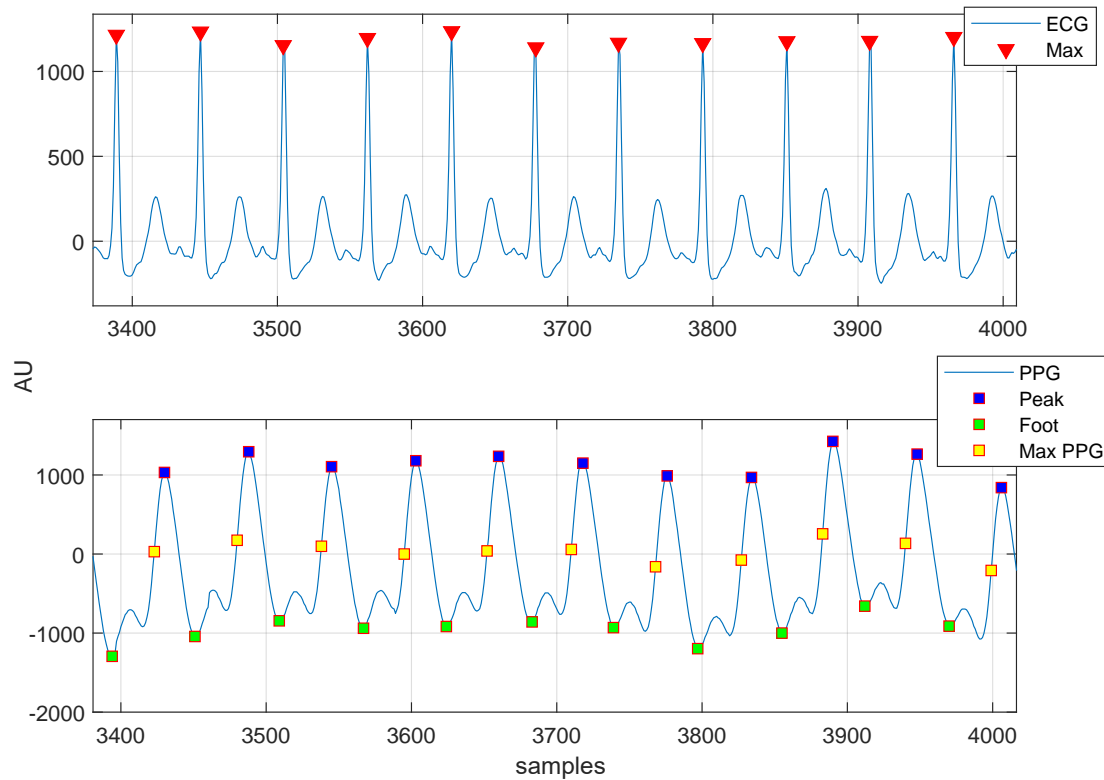


Figure 3.3 – ECG and PPG signals. The three characteristic points of the PPG used for IBI detection are shown: the peak, the foot and the maximum first derivative.

exercises [60, 65].

The methodology associated with the PPG processing for PRV and IBI detection is important. First of all, the IBI can be extracted at different PPG locations, where the exact location depends on the used processing algorithm. Indeed, three alternatives are possible, as shown in Fig. 3.3: the peak to peak time distance, the foot to foot distance or the distance between two consecutive inflection points (maximum first derivative). In the existing literature the three methods have been independently used and a comparative study can be found in [66]. Some works have shown results working on peaks or foot [62, 67, 63], other based on the maximum first derivative [64]. The latter seems to be more robust since the maximum first derivative point is far away in time from any possible second peak coming from elevated diastolic notches. Indeed, we will see in the next sections that increased arterial stiffness, elevated blood pressure and respiration can change the PPG morphology bringing the diastolic notch very close to the PPG peak.

The PRV and IBI extracted from the PPG are evaluated in terms of time and frequency domains according to the standard definitions of HRV [68]. In the time domain, the mean RR and IBI intervals (mean NN interval), the standard deviation of all the RR and IBI intervals (SDNN) and the root mean square of the difference of successive RR or IBI intervals (RMSSD) are often

proposed. The percentage of corrected, extra and missed beats, versus the ECG RR, is also often considered [63, 56]. In the frequency domain, the ratio of the low-to-high frequency spectra (LF/HF) is often used. Indeed, the HRV embeds three frequency bands of interest: very low (< 0.04 Hz, VLF), low (0.04-0.15 Hz, LF) and high (0.15 - 0.4 Hz, HF). The LF reflects the sympathetic action, whilst the HF the parasympathetic one [68].

It should also be mentioned that both the ECG and PPG are sampled signals. The value of the sampling rate has an influence into the PRV and IBI detection. It has been shown that PRV and HRV deteriorates with decreasing sampling rate from 1000 Hz to 10 Hz, although the effect is not noticeable until well below 100 Hz [69]. The work presented in [70] suggests a minimum of 39.5 Hz sampling frequency for heart rate variability monitoring.

In the next two sub-sections, two important applications related to the HRV are further explained and discussed.

3.2.1 Atrial fibrillation

Atrial fibrillation (AFib) is an abnormal cardiac rhythm which is characterized by rapid and irregular beating of the heart's atria. It is the most common cardiac arrhythmia, affecting between 2.7 million and 6.1 million adults in the US only [71]. Even worse, about 60% of these people don't even know when they have an AF episode. Worldwide, AFib has an estimated prevalence of 3% in the adult population that is projected to more than 4% by 2050 [72, 73]. AFib is a serious risk factor for blood clots and strokes. Today, the AFib is diagnosed with an ECG. Characteristic findings are the absence of P-waves and irregular RR intervals, i.e. HRV [54]. Unfortunately, AFib is often asymptomatic, meaning that it can dramatically benefit from any wearable and continuous monitoring solution.

In this section, we have shown that a PPG signal can effectively track the HRV. An AFib event is often accompanied by irregular conduction of impulses to the heart's ventricles giving rise to irregular RR intervals [53], as shown in Fig. 3.4. These intervals are detectable thanks to the PRV or IBI analysis of PPG waves.

The work presented in [75] has used a smartphone camera to detect AFib on patients pre- and post- electric stimulation, i.e. cardioversion. The PPG signal is recorded by placing a finger over the camera and illuminating the tissue by the means of the flash light. The AFib detection is based on the RMSSD, Shannon Entropy and Sample Entropy of the extracted IBIs. The achieved sensitivity, specificity and accuracy is very promising above all for a fully portable device.

The more recent works presented in [63, 56, 67] has also come with promising results, suggesting that the PPG can provide, during low motions or sleep conditions, a comfortable alternative to ECG for continuous screening of AFib episodes.

The dawn of the artificial intelligence (AI) and deep learning is also a trigger in developing PPG-

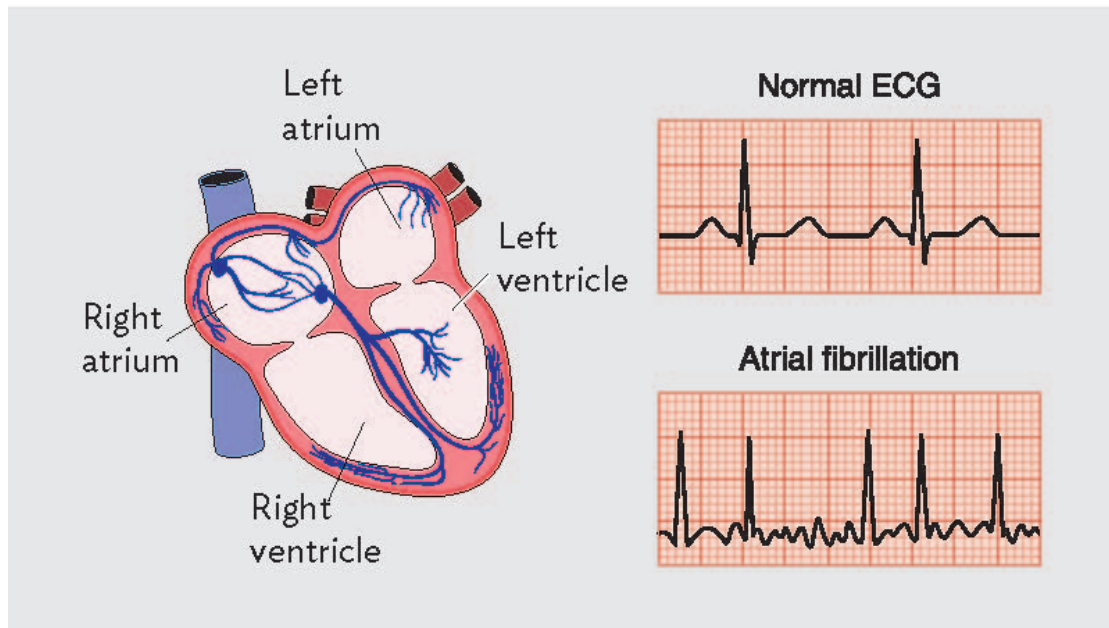


Figure 3.4 – Heart's sections with the four elementary chambers, atria and ventricles. Two ECG traces are shown: without and with an atrial fibrillation event. The atrial fibrillation comes with an irregular ECG behaviour [74].

based systems for continuous and accurate AFib detection. AI can also enhance the robustness of AFib detection in conditions where the regular methods tend to suffer, e.g. during exercise or motions. In this direction, the work presented in [76] has proposed a 50-layer convolutional neural network achieving 95% of correct classification (AFib versus no-AFib) on the test data.

3.2.2 Stress monitoring

Human stress has been shown to be strongly correlated with increased risk of cardiac problems, such as the myocardial infarction [77]. The modern society moves relatively fast and short time recovery from workload and other daily stressing elements is a serious trigger to CVDs.

Nowadays, measuring stress still requires special laboratory equipments and body samples, e.g. saliva [59]. On the other hand, the increasing number of people experiencing stressed conditions and their extensive effects deserves the research and development of portable and wearable devices capable of real-time stress monitoring.

An effective and convenient method of deriving stress information from a person is to extract from a PPG signal information related to the stress itself. As above presented, HRV is a marker of the autonomous nervous system whose operations ultimately determines the rising of the stress. Indeed, low HR and large HRV are related to relaxed situations dominated by the parasympathetic system. On the contrary, elevated HR and low HRV report sympathetic conditions, i.e. stress. The work presented in [59] has proposed to use a PPG sensor by

comparing an individual's normal baseline resting level of HR and HRV with respect to the HR and HRV responses in real life conditions. The results have suggested that, particularly, the SDNN and the LF of the IBI capture best the effect of stress to a subject.

The work presented in [78] has aimed at identifying specific features of the PPG signal whose dynamic can identify the mental stress. In particular, specific haemodynamic changes occur at the PPG as a consequence of the stress. Three PPG features have been chosen, since the most resilient to the measuring site: the time from the pulse onset to the peak, named the crest time (CT), the diastolic duration, meaning the time from the dicrotic notch to the pulse end, and the instantaneous HR.

3.3 Oxygen saturation

In Chapter 2 we have seen that the melanin and the haemoglobin are the largest light absorbants in tissues. The haemoglobin plays a key role in transporting the oxygen via the blood to the cell. Haemoglobin is a respiratory pigment contained within the red blood cells. One red blood cell contains roughly 256 million molecules of haemoglobin. Haemoglobin consists of heme units, which are molecules containing iron, and globin units, polypeptide chains [26]. One haemoglobin molecule contains four heme and four globin units, where each heme and globin unit can carry one molecule of oxygen. In other words, one haemoglobin molecule can carry four molecules of oxygen. Haemoglobin changes color when oxygenated: the oxygenated haemoglobin (HbO₂), bound to the oxygen, is bright red, while the deoxygenated one (Hb) is dark red, as shown in Fig. 3.5. The difference in color is used in the application of pulse oximetry to measure the oxygen saturation in the blood. Haemoglobins that are able to bind reversibly with oxygen molecules are called functional haemoglobin.

Nowadays, the oxygen saturation is widely measured by the means of the so called pulse oximetry, Fig. 3.6. Indeed, already in the early 1990's, pulse oximetry became an universally accepted standard for monitoring oxygen levels during anaesthesia. Today, pulse oximetries can measure the oxygen saturation using both transmissive and reflective PPG sensors.

The functional oxygen saturation (functional SO₂) is defined as the percentage of HbO₂ with respect to the overall haemoglobin, Hb and HbO₂. Another way to define it is to use the concentration of HbO₂ with respect to the sum of the overall Hb

$$\text{Functional } SO_2 \% = \frac{HbO_2}{Hb + HbO_2} \cdot 100\% = \frac{c_{HbO_2}}{c_{Hb} + c_{HbO_2}} \cdot 100\%. \quad (3.1)$$

The oxygen saturation of the arterial blood is called S_aO_2 and its normal physiological value has to be larger than 90 %.

The functional oxygen saturation, as shown in (3.1), considers only the haemoglobin bounded to the oxygen. Actually, the haemoglobin can also bound to other molecules, some of them even dangerous. Indeed, it is usually defined as a dysfunctional haemoglobin whatever

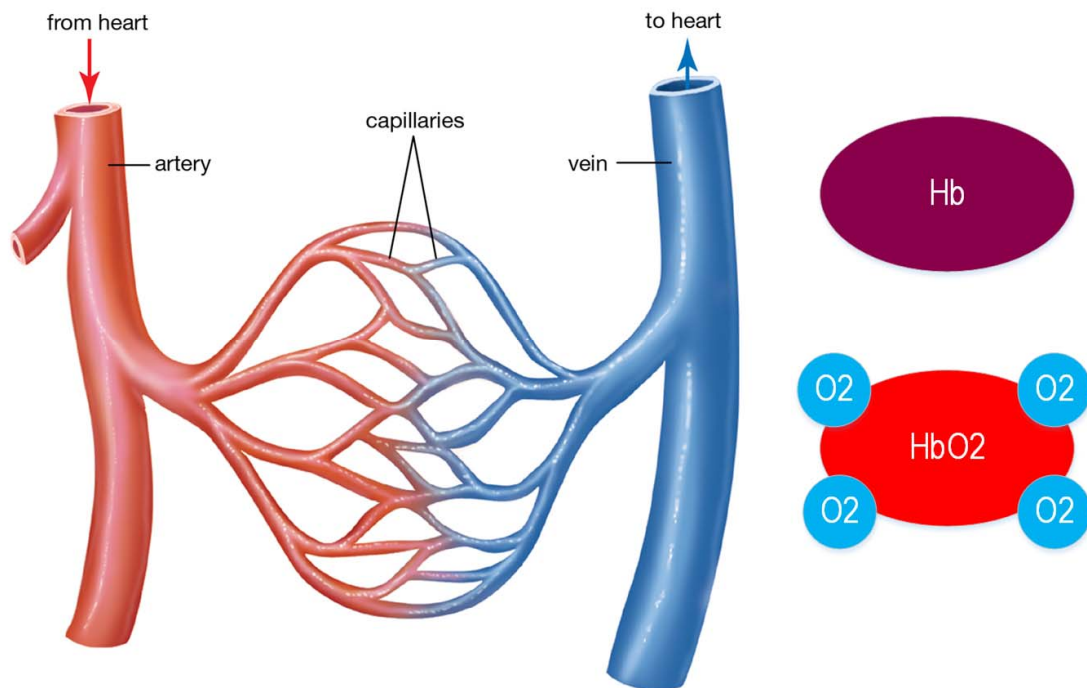


Figure 3.5 – Haemoglobin molecules are contained within red blood cells. The oxygenated haemoglobin is dark red and usually associated to the fresh blood pumped through the arteries. On the contrary, the deoxygenated haemoglobin is dark red and related to the exhausted venous blood.



Figure 3.6 – A commercially available pulse oximetry exploiting the transmissive PPG technique.

haemoglobin that doesn't support the oxygen transport in the blood. The four most common dysfunctional haemoglobins are the methemoglobin (MetHb), carboxyhaemoglobin (COHb),

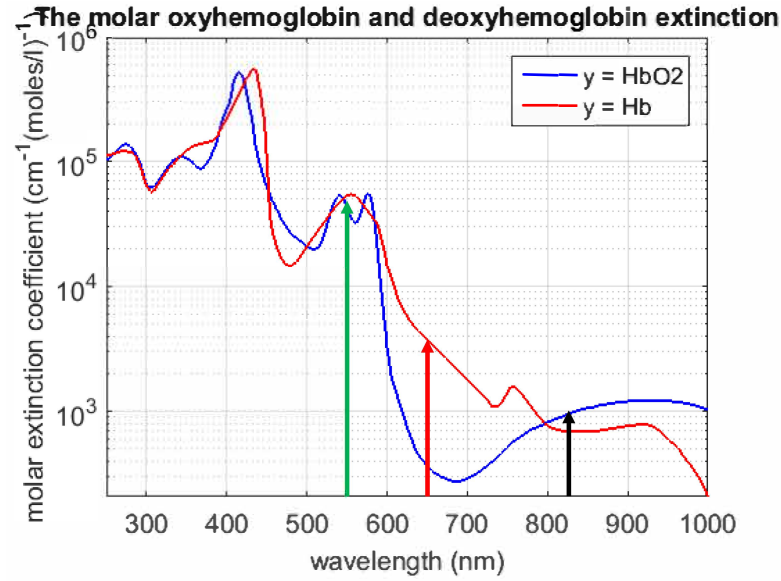


Figure 3.7 – Extinction coefficients of the functional haemoglobins versus the wavelength: Hb and HbO₂. The classic three PPG wavelengths are highlighted: green, red and near-infrared.

sulfhemoglobin (SulfHb) and carboxysulfhemoglobin (COSulfHb). Apart from the last ones, whose concentrations in human blood are usually negligible [26], the other two, i.e. MetHb and COHb, can be present in the blood in few percentages. For instance, in non-smokers the level of COHb is usually below 2%, but this value can increase depending on the local environment, e.g. pollution. The fractional haemoglobin saturation is defined as the percentage of the HbO₂ with respect to all the haemoglobin families

$$\text{Fractional } SO_2 \% = \frac{HbO_2}{Hb + HbO_2 + MetHb + COHb} \cdot 100\%. \quad (3.2)$$

Neglecting the dysfunctional haemoglobins, the Hb and HbO₂ have different absorptivities at green, red and IR light, as shown in Fig. 3.7. In other words, they absorb the light differently depending on the wavelength. A pulse oximetry works by exploiting this mechanism. Two PPG signals, at two different wavelengths, are recorded in time division multiplexing (the LEDs never shine together). Measuring at two wavelengths allows to distinguish the concentrations of Hb and HbO₂. Commercially available pulse oximeters usually embed red and near-IR lights [26]. The recent works in [79, 80] have presented pulse oximeters embedding visible light LEDs only. Indeed, by looking at Fig. 3.7, it is clear that the difference in the extinction coefficients between Hb and HbO₂ at green is comparable to the one at near-IR. In addition, as explained in Chapter 2, the visible light, and particularly the green, comes with important advantages versus the IR, mostly determined by the shorter penetration depth. This is particularly true in the case of pulse oximetry since the oxygen saturation is very often measured at the finger.

According to the Beer-Lambert law, presented in Chapter 2, the total absorbance A_t of a

solution containing only Hb and HbO₂ is equal to

$$A_t = \epsilon_{HbO_2}(\lambda) c_{HbO_2} d + \epsilon_{Hb}(\lambda) c_{Hb} d, \quad (3.3)$$

assuming the optical path to be the same, i.e. $d_{HbO_2} = d_{Hb} = d$. Rewriting (2.1) in terms of the total absorbance A_t and normalizing the diastolic transmitted light with respect to the systolic one gives rise to

$$T_n = e^{-(\epsilon_{HbO_2} c_{HbO_2} + \epsilon_{Hb} c_{Hb}) \Delta d}, \quad (3.4)$$

where $\Delta d = d_{max} - d_{min}$, so quantifying the maximum arterial diameter oscillation during a cardiac period, i.e. systolic and diastolic phases. The normalization is necessary since the LEDs may emit light with different intensities or the sensitivity of the photodetector may slightly change. Moreover, the absorbing characteristics of the DC component might differ for the two separate wavelengths. In other words, normalizing the transmitted light during diastole with respect to the one during systole corresponds to deriving the total absorbance due to the AC component only. In order to do so the natural logarithm of the normalized transmitted light level is considered. Eventually, it is possible to define a ratio R of the normalized logarithmic of the transmitted light levels at the two chosen wavelengths depending only on the light absorbers present in the arterial blood

$$R = \frac{\ln(T_n(\lambda_1))}{\ln(T_n(\lambda_2))}, \quad (3.5)$$

where in the case of visible LEDs, λ_1 and λ_2 correspond to the red and green, respectively. Finally, by deriving the concentrations as a function of the oxygen saturation, (3.3), (3.5) can be rearranged in a form where the functional oxygen saturation SO_2 is a function of R

$$SO_2 \% = \frac{\epsilon_{Hb}(\lambda_1) - \epsilon_{Hb}(\lambda_2) R}{\epsilon_{Hb}(\lambda_1) - \epsilon_{HbO_2}(\lambda_1) + [\epsilon_{HbO_2}(\lambda_2) - \epsilon_{Hb}(\lambda_2)] R} \cdot 100\%. \quad (3.6)$$

By replacing the extinction coefficient values of (3.6) with the tabular values, the arterial oxygen saturation (S_aO_2) can be derived.

The reading of the pulse oximeter, usually named S_pO_2 is an empiric estimation of the arterial oxygen saturation S_aO_2 . Most of the commercial pulse oximeters use a calibration curve based on empirical data. Indeed, modelling the light-tissue interaction as described in Chapter 2 is very complicated. These oximeters are usually calibrated from in vitro data. A large set of data obtained in clinical studies is collected. In particular, the oxygen saturation S_pO_2 , as calculated by the pulse oximeter, is compared with the arterial oxygen saturation S_aO_2 measured by a gold standard, i.e. CO-oximeter [26]. To relate the measured value of R to the S_pO_2 , (3.6) can be modified to

$$S_pO_2 = \frac{k_1 - k_2 R}{k_3 - k_4 R}, \quad (3.7)$$

where k_i are calibration constants determined by clinical studies. Polynomials of different orders are also often employed as empirical calibration curves. For instance, a 1st order simple relationship of the form

$$S_pO_2 = 110 - 25R, \quad (3.8)$$

has been suggested in the literature [26].

3.4 Breathing rate

The pioneering work in [81] and many others following have shown the potential of PPG in assessing respiratory events. Indeed, the breathing rate (BR) has shown to modulate the PPG signal in both amplitude (AM) and frequency (FM). In addition, the BR tends to drift periodically the baseline (DC component) of the PPG signal.

The respiratory rate of adults at rest ranges from 5 to 24 breaths-per-minutes (BRPM), meaning from 0.08 to 0.4 Hz. Neonates, instead, breath between 10 and 80 BRPM, corresponding to 0.17 and 1.33 Hz, respectively [81]. Another slow modulation of the PPG wave comes from the Traube-Hering-Mayer (THM) waves, which are caused by the sympathetic control of the tones of the vascular tree. THM have a rate of about 0.1 Hz, corresponding to an equivalent 6 BRPM [82].

Fig. 3.8 shows a PPG signal both in time and frequency domain. By looking at the time domain, the effect of respiration is visible. Indeed, the PPG, positive and negative, envelopes are modulated by the BR. The corresponding frequency component is reported by the same PPG signal in the frequency domain. The Fast-Fourier-Transform (FFT) shows two main components: the BR at about 0.25 Hz (15 BRPM) and the HR at roughly 2 Hz (120 BPM).

Different studies have tried to extract the BR out of the PPG signal. The work presented in [83] has proposed a fully automatized algorithm for BR extraction out of the PPG signal. The PPG signal is decomposed three times via Morlet wavelet transform to produce three different breathing signals. The best signal is chosen as the one that, for a 5 seconds window, shows the smallest mean absolute error (MAE) with respect to the gold standard. Despite the achieved MAE is quite low (<0.35 BRPM), it is highly dependent on the reference signals, which are not always available above all in domestic environments. Another relevant work is the one presented in [84], not only for the achieved results, but also for the motivating factors. Indeed, the motivation of this work is the more than 2 million children under five years killed by pneumonia. An easy to use diagnostic device pre-identifying pneumonia on children would increase their survival rate, above all in poor countries. [84] has proposed a method, called Smart Fusion, for estimating the BR from the PPG signal. The method extracts the three respiratory-induced variations from PPG, i.e. FM, AM and DC modulation, and the frequency content of each parameter is analysed in the frequency domain. Despite the interesting proposed method, it suffers from poor specificity at low BR due to the effect of THM waves and

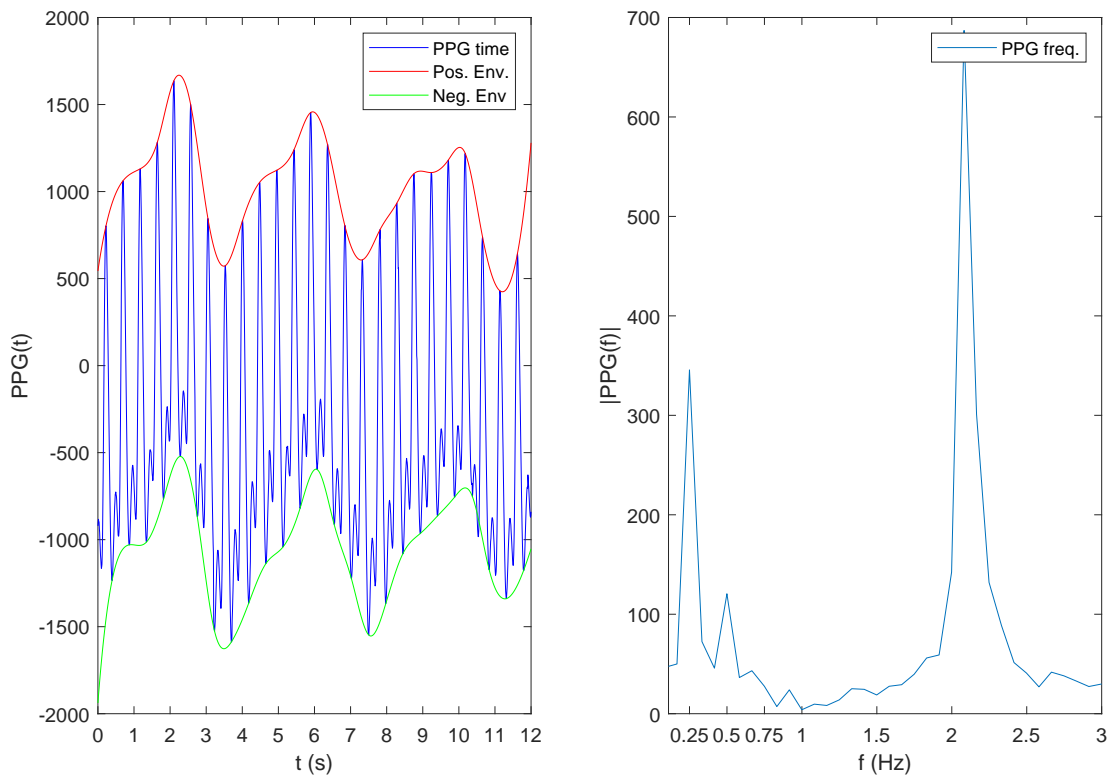


Figure 3.8 – PPG in both time and frequency domain. The effect of breathing rate can be assessed by looking at the PPG time domain envelope modulation. This corresponds to a 0.25 Hz frequency components or 15 BRPM.

artefacts. The more recent work in [85] has utilized the Empirical Mode Decomposition (EMD) for estimating BR from the PPG signal. The EMD is an adaptive time-frequency data analysis which extracts the Intrinsic Mode Functions (IMF). The IMF is a function that represents an oscillating mode embedded in the signal. Using a certain sliding window, a PPG signal can be divided into its IMF. For each IMF, the frequency peak with the highest power is evaluated. In this way, the HR and the BR can be easily evaluated.

3.5 Blood pressure

Hypertension is a medical pathology associated with elevated blood pressure (BP). Hypertension is diagnosed if, when it is measured on two different days, the systolic blood pressure (SBP) readings on both days is larger than 140 mmHg and/or the diastolic blood pressure (DBP) readings on both days is larger than 90 mmHg. Elevated BP is a serious medical condition which significantly increases the risk of heart, brain and kidney-related diseases. An estimated 1.13 billion people worldwide have hypertension, most (two-thirds) living in low- and middle-income countries [86].

Hypertension is called a "silent killer". Most people with hypertension are unaware of the

problem because it may have no warning signs or symptoms. Even worse, hypertension is the major cause of premature death worldwide: it causes each year more than 7.5 million deaths, about 13% of the total death [86]. For this reason, it is essential that the blood pressure is measured regularly.

Continuous BP recordings are still not easy to implement in daily life. Indeed, discontinuous BP measurements by the means of arm cuff based devices (either auscultatory or oscillometric-based) is still the method routinely applied [87]. Although these techniques have seriously contributed in increasing the people awareness about the risks associated with uncontrolled BP, they present two major limitations. First of all, any continuous BP monitoring is simply impossible. In other words, it is not possible to follow the dynamic evolution of BP over the time. Second, the readings are often disturbed by white coat effects or simply the discomfort due to the inflatable cuff, which may ultimately affect the quality of the measures. This is particularly important for BP monitoring during sleep which has shown to be particularly relevant for clinical information. Indeed, during normal sleep the mean BP (MBP) is supposed to decrease from 10% to 20%. Lack or diminished night BP trends are strong and independent predictors of cardiovascular diseases [88]. In this framework, any system capable of truly continuous BP monitoring would represent a game-changer.

Alternative methods of measuring the BP trying to overcome those challenges have gained traction in recent years, particularly thanks to the advent of more performing and wearable sensors. BP management is one of the most prominent applications for PPG sensors. Indeed, a PPG signal hides several haemodynamic features that can be traced back to BP.

In the following, two research tracks on the extraction of BP out of the PPG signal are presented. First, the pulse wave velocity-based method and, second, the pulse decomposition one.

3.5.1 Pulse wave velocity and pulse transient time

In recent years, the arterial wave propagation theory has attracted the interest of many researchers. It is based on the simultaneous collection of the ECG, the ICG (impedance-cardiography) (or BCG, i.e. ballistocardiogram) and the PPG signal, Fig. 3.9. Some works have preferred using the ECG, ICG and PPG [89], others the ECG, BCG and the PPG [90, 91]. The ICG is a very important technique measuring the total electrical conductivity of the thorax. Any blood flow through the body would change its impedance. Objective of the ICG is to estimate the amount of fresh blood being effectively released at each cardiac cycle. Indeed, the ICG is nowadays used to measure important cardiac vitals such as the cardiac output (CO) and the stroke volume (SV). The BCG measures the acceleration of the heart as the result of the cardiac phases. The arterial wave propagation theory refers to the propagation of the pressure wave through the vessels as the result of the heart pumping. Indeed, at the closing of the aortic valve, the sudden rise of aortic pressure is absorbed by the aorta's walls and a pulse wave naturally propagates towards the peripheral sites as the result of the energy exchange between the aorta's wall and the blood flow.

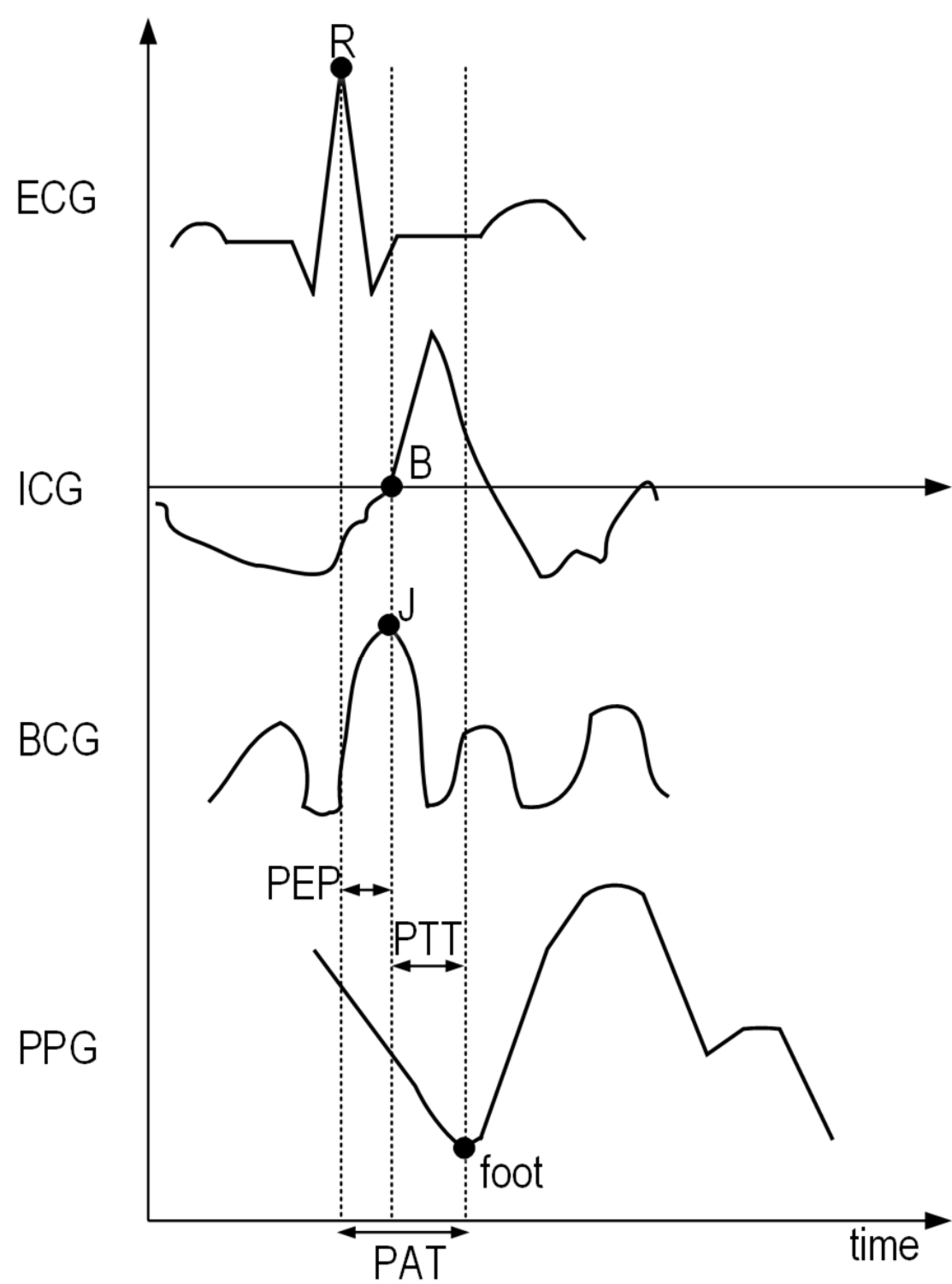


Figure 3.9 – Simultaneous recording of the ECG, the ICG or BCG and the PPG. The PAT and the PPT are identified as the time from the R-peak of the ECG and the PPG minimum and the time from the R-peak of the ECG and the zero crossing of the ICG (B-point) or the J-peak of the BCG, respectively.

The pulse wave velocity (PWV) is usually assessed using the pulse arrival time (PAT) of the pressure wave at a given distance (L) with respect to the heart. As shown in Fig. 3.9, the PAT refers to the timing between the R-peak of the ECG and the foot of the PPG wave, the latter measured at a distal position, i.e. the finger or the wrist. The PAT is the sum of two time intervals

$$PAT = PEP + PTT, \quad (3.9)$$

the pre-ejection-period (PEP) and the pulse transient time (PTT). The PEP refers to the timing of an isometric contraction of the heart, meaning the time needed to convert the electric signal coming from the SA node into a mechanical pumping ultimately contracting the ventricles and opening the aortic valve [87]. The PTT is the effective time the pressure wave has taken to propagate to the sensing location, after the opening of the aortic valve, and shows high correlation to the BP [92]. In other words, the PWV is defined as

$$PWV = L/PTT, \quad (3.10)$$

with L being the distance between the peripheral sensing location and the heart. The PEP depends on the electrical activity of the heart and can move in opposite direction with respect to PTT. For this reason, the PEP has shown a negative impact when using the PAT to estimate the BP [93]. Moreover, the PEP changes with various factors such as the stress and the age [94]. Studies have also shown that the PEP changes with the heart rate and can account for the 7% of the PTT [95]. The impact of the PEP decreases with the increasing distance from the heart, since the PTT is expected to grow accordingly. The negative impact of the PEP forces its subtraction from the PAT in order to compute the PWV.

Using the PWV in order to estimate the BP requires some attention and has been the objective of several studies over many years. Indeed, understanding how the pressure wave propagates through the vessels requires at first to model the relationship between BP and the arterial elasticity and, second, the relationship between the arterial elasticity and the PTT [92].

Relationship between BP and arterial elasticity

The pressure wave propagates along the arterial tree thanks to the continuous energy exchange between the wall and the fluid. Therefore, determining the dynamic properties of the arteries' wall is key. The arterial wall consists mostly of four components, each one having different properties: endothelium, collagen, elastin and smooth muscle (SM), [96]. In other words, depending on the applied stress, i.e. the pressure so the BP, the arteries' elastic properties, i.e. the Young's modulus (Y), can change considerably, leading to non-linearity. Endothelium contributes little to the arterial wall mechanics, while the collagen is roughly 400 times stiffer than the elastin. This means that the resulting arteries' Young's modulus is highly non-linear: at low BP, elastin ultimately determines the arterial elasticity and so the Young's modulus, while collagen takes over at larger BP. SM, both on elongation and relaxation, can also modulate

arterial elasticity, by making the arterial wall viscous in addition to elastic. In other words, stress-strain hysteresis is low in relaxed condition, but pronounced visco-elasticity is observed if the SM are contracted [97].

The relative contributions of these components differ throughout the arterial tree. Indeed, central arteries, e.g. aorta, largely consists of elastin, which makes their response to the applied pressure quite linear and more resilient to SM. On the contrary, SM is mostly dominated in the peripheral sites, making their dynamic tougher to model. This is the reason why central arteries and peripheral ones are usually named elastic and muscular arteries, respectively. In addition, the arteries' Young's modulus is found to be heart rate, so frequency, dependant. In other words, it is possible to identify a frequency, i.e. corner frequency, above which the Young's modulus cannot increase. The value of this corner frequency has been long debated. Some studies have indicate a corner frequency around 1 Hz [97], other even above [96].

The arteries dynamically evolve, suffering from ageing. This contributes to arteriosclerosis, which is the process of wall thickening and stiffening with the ageing. Arteriosclerosis mostly interests elastic arteries and is characterized by an increase of collagen against the elastin. A stiffer artery gives rise to a larger BP due to the larger wall stiffness. Fig. 3.10 shows how the pressure wave and the relative flow velocity change with respect to the body location. Central arteries come with reduced flow velocity due to the larger elasticity. On the contrary, the increased stiffness of peripheral arteries accelerates the blood flow due to the lower energy exchange.

The (central) arteries' Young's modulus has been shown to be related to the BP as follows

$$Y(BP) = Y_0 e^{\alpha BP}, \quad (3.11)$$

where α is a subject specific parameter and Y_0 the Young's modulus at no pressure.

Relationship between arterial elasticity and PTT/PWV

The relationship between arterial elasticity and PWV (so PTT) is defined by the Moens-Korteweg equation

$$PWV = \frac{L}{PTT} = \sqrt{\frac{Yh}{2r\rho}} = \sqrt{\frac{Y_0 e^{\alpha BP} h}{2r\rho}}, \quad (3.12)$$

where h is the wall thickness, r the artery's radius and ρ the density of the fluid. Rewriting (3.12) in terms of BP leads to

$$BP = K_1 + K_2 - \beta \ln(PTT), \quad (3.13)$$

where $K_1 = \frac{1}{\alpha} \ln(\frac{2r\rho}{hY_0})$, $K_2 = \frac{2\ln L}{\alpha}$ and $\beta = \frac{2}{\alpha}$ are calibration constants.

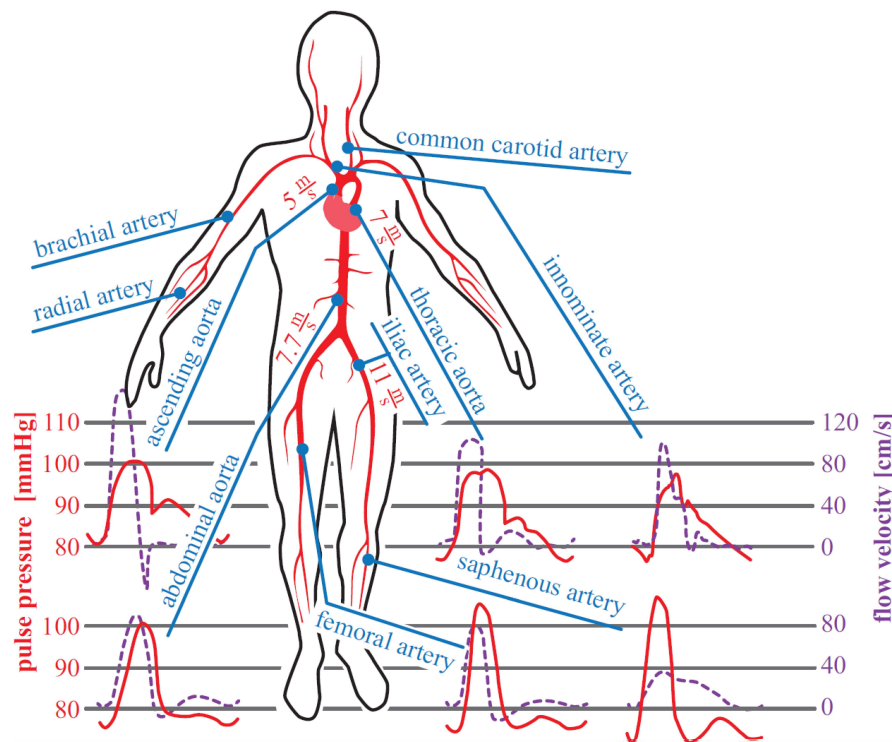


Figure 3.10 – Simplified arterial tree showing how the pulse pressure and the flow velocity change along the body [46].

As presented above, the arterial system is quite complex, which reduces the applicability of (3.12) to healthy people and central arteries only. Indeed, (3.12) relies on the fact that its variables are time independent. Actually some of these variables, such as the blood density can be considered constant with good approximation. On the contrary, this is not true for the arteries' radius and thickness. Unfortunately, for muscular vessels, such as the brachial artery in the arm, it is not easy to extract a good relationship between PWV/PTT and BP. Indeed, as above-mentioned, these vessels are not elastic and the effect of vasomotion is quite limiting [89]. Vasomotion considers the effect of change of resistance and thickness due to the applied pressure. Not surprisingly, this is more and more evident as we move further from the central arteries.

Increasing wall stiffness also leads to a gain in pulse amplitude towards the periphery. As shown in Fig. 3.11, the blood circulation accounts for several transitions from big arteries to arterioles and eventually capillaries (microcirculation). Mechanically speaking, any arterial branching can be associated to an impedance mismatch which ultimately causes wave reflection. Indeed, wave reflection takes place at all these sites introducing any consistent change into the arterial morphology or geometry [92].

The work presented in [98], and supported by others [99], demonstrated the existence of two major reflection sites to travelling pressure waves. As shown in Fig. 3.11, the first reflection site

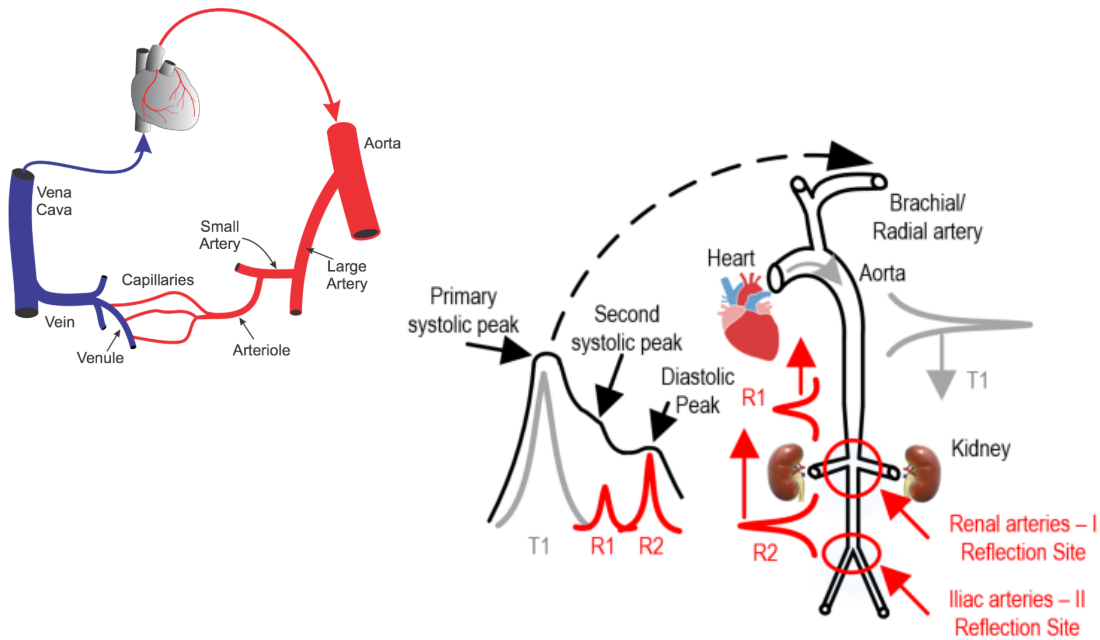


Figure 3.11 – Microcirculation: the heart pumps the blood through the aorta, then the large arteries, the small arteries, the arteriole, the capillaries and then back through the venous systems, consisting of, in sequence, the venules, the veins and the vena cava [33].

corresponds to the renal arteries' branching, while the second comes from the iliac bifurcation. With respect to Fig. 3.11, any downward primary pressure wave, T1, generated from the closing of the left ventricle gives rise to upward reflected pressure waves, R1 and R2. Any pressure wave measured at the radial sites, i.e. the arm, would consist of the superimposition of those reflected waves on the primary wave that has directly reached the site. The reflected waves reach the peripheral site with some delay due to the larger travelled distance.

In conclusion, wave reflection deeply impacts on the shape of pressure waves. This is particularly true with the increasing distance from the heart due to stiffer arteries and increased reflections. Fig. 3.10 also shows the impact of the propagation on the wave's morphology. Indeed, with respect to the central arteries, as we move to the peripheral site, the waveforms become progressively amplified with the increasing distance. Hence, proximal and distal waveforms are not different from the time delay only, but also from the different morphologies. This phenomenon tends to affect SDB much more than DBP [92]. Indeed, isolated systolic hypertension often occurs in the elderly which results into an elevated SBP at a fairly constant DBP [87].

Finally, any PTT/PWV-BP model can be effectively used under continuous recalibration and specific assumptions, ultimately limiting its applicability to real conditions. Moreover, there are challenges to have independent determination of SBP and DBP. Indeed, any PTT-BP model can refer to one BP value only, either the SBP or the DBP. Prior works have shown a better correlation with respect to DBP, since more stable for peripheral measurements [92, 100, 87].

3.5.2 PPG decomposition analysis and features extraction

In Chapter 2 the origin of the PPG wave have been discussed in details starting from the Beer-Lambert law. In particular, a characteristic point of the PPG wave has been identified and named as dicrotic notch. This phenomenon is often attributed to the closure of the aortic valve [101]. On the other hand, the impedance mismatches introduced by the microcirculation, presented in the previous paragraph, suggest a causation by reflection of the pressure peak from small arteries in the trunk and lower limbs [102]. The goodness of the two theories suggests having both of them actually valid.

A PPG signal consists of two major phases: the systolic or anacrotic and the diastolic or catacrotic one [103]. The systolic ejection phase of the cardiac cycle is actually a two-stage phenomenon. At first, it comprises a rapid increase in intraventricular pressure due to the high electric myocardial excitability. Second, it is characterized by a slow decrease in intraventricular pressure due to reduction in excitation. Hence, the complete phase is marked by the presence of two systolic peaks in the PPG signal, as shown in Fig. 3.11. The diastolic phase takes place after the dicrotic notch and is characterized by one major wave, named diastolic peak, which is characterized by a slowly decreasing pressure thanks to the cushioning reservoir effect introduced by the big elastic arteries of the trunk [46].

The progressive time-domain PPG waveform has been empirically modelled as the summation of two or more Gaussian functions, accounting for the overall systolic and diastolic peaks [104, 105, 106], as shown in Fig. 3.12.

We have seen both in this chapter and in the previous one that a PPG signal is the result of several factors, including the light-tissue interaction and the local perfusion, the respiration, the autonomous nervous system and many others [107]. More specifically to the BP, the dynamic evolution of the superimposition of the forward and reflected waves, as above mentioned, is ultimately related to some factors affecting the BP, such as the atherosclerosis and the ageing [103, 78]. In this perspective, it is important to identify the critical points of the PPG signal. Features of the first and second derivative of the PPG signal, VPPG and APPG, respectively, have also been used to accurately recognized those critical points [108, 109]. Third derivative has also been proposed [78]. Fig. 3.12 shows the PPG, VPPG and APPG signals, together with some of those critical points.

The objective of the next paragraphs is to deepen those critical points emphasizing how they can be used to monitor the BP. A more comprehensive set of features can be found in [103, 78]. Eventually, some works exploiting AI for extracting indexes from PPG signals are also presented.

PPG features

The amplitude of the first systolic peak is an indicator of the pulsatile changes in blood volume. It has been related to SV and to the local vascular extensibility. An elevated peak has shown to

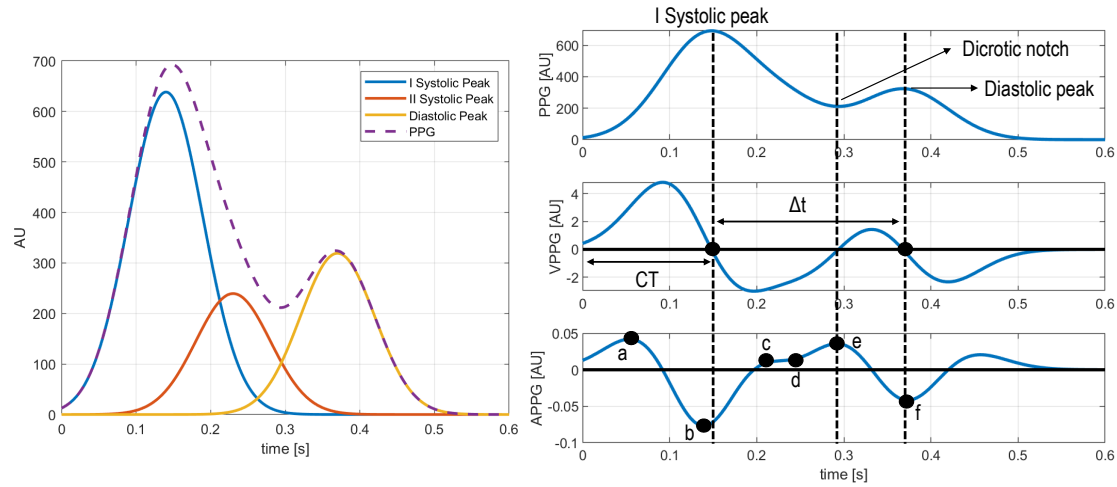


Figure 3.12 – PPG decomposition into the fundamental waves, i.e. I systolic, II systolic and diastolic wave. Extracting the PPG features from the PPG, VPPG (PPG') and APPG (PPG'').

be correlated to increased BP.

The systolic component of the waveform arises mainly from a forward-going pressure wave transmitted from the left ventricle to the finger. The diastolic component mostly arises from pressure waves transmitted along the aorta to small arteries in the lower body, from where they are then reflected back along the aorta as a reflected wave which then travels to the finger. As shown in Fig. 3.12, the time delay, Δt , between the first systolic peak and the diastolic peak (or, in the absence of this, the dicrotic notch) is related to the transit time of pressure waves from the root of the subclavian artery to the apparent site of reflection and back to the subclavian artery. The time delay between the systolic and diastolic peaks decreases with the age as a consequence of the increased arterial stiffness and the increased pulse wave velocity of pressure waves in the aorta and large arteries [107]. The work in [110] has demonstrated that 98% of patients with overt arteriosclerosis undergo a diminution or disappearance of the dicrotic notch and diastolic peaks. Thanks to this result, [111] has proposed the classification of pressure waves (including PPG) into four classes. With increasing age and/or the presence of CVDs, the waveform moves from class 1 to class 4, as shown in Fig. 3.13.

VPPG features

VPPG is commonly used in literature. Fig. 3.12 shows the VPPG with respect to the PPG. The time from the rising of the PPG wave from the first systolic peak is called crest time (CT). CT has shown to be key for CVDs classification [103]. The CT can be easily detected by the means of VPPG. Indeed, CT is the time from the onset of the PPG pulse to the first zero crossing of VPPG.

VPPG can also be useful in determining the diastolic point and the Δt .

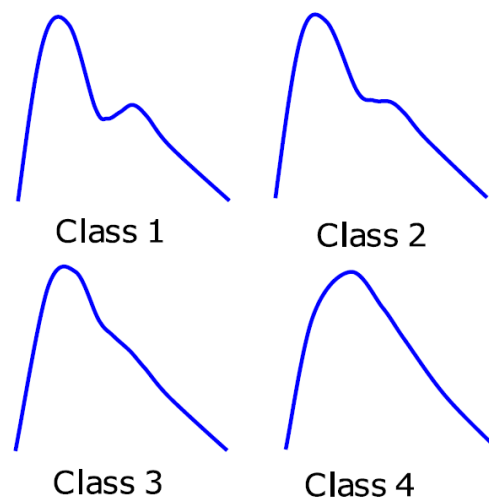


Figure 3.13 – PPG morphology and classification according to [111]. The morphological change of the PPG wave can be interpreted in terms of earlier arrival of the reflected waves. Increasing stiffness accelerates the reflected waves which arrive earlier to the distal point and so closer to the forward wave [112].

APPG features

APPG is even more used than VPPG. As shown in Fig. 3.12, the APPG includes four systolic waves and two diastolic waves. These are: the a-wave (early systolic positive wave), b-wave (early systolic negative wave), c-wave (late systolic re-increasing wave), d-wave (late systolic re-decreasing wave), e-wave (early diastolic positive wave) and f-wave (diastolic negative wave). The e-wave represents the dicrotic notch, while the f-wave the position of the diastolic peak. The combination of these waves can also enhance the correlation with respect to CVDs. For instance, the ratio b/a has shown to reflect increased arterial stiffness: it increases with the age. On the contrary, the ratios c/a and d/a decrease with the arterial stiffness, so the age [108, 109]. The work in [113] has classified the APPG morphology as an indicator of the good/bad circulation.

Features extraction and artificial intelligence

Nowadays artificial intelligence through machine learning has been used in research for BP prediction and cuffless BP measurement. The general approach is to initially extract specific features from physiological signals that show high correlation to BP. These features are given to a neural network (NN) for training and testing. The features extracted from PPG, VPPG and APPG and presented above are often used.

The work in [114] has used 21 features extracted from the PPG signal. A feed-forward NN with two hidden layers, 35 neurons on the first layer and 20 on the second has been used. The obtained results are promising and fulfil the maximal accepted error of 5 ± 8 mmHg, as

defined by the American National Standards of the Association for the Advancement of Medical Instrumentation. The number of used features has increased in the last years. The work in [115] has used 42 features out of the PPG, VPPG and APPG, achieving an average error of roughly 2 mmHg, for both SBP and DBP. Time domain features can also be complemented by frequency domain ones. In [116], 233 features were extracted, both in time and frequency domain.

Despite these promising results, none of these solution has been scaled up to a large population of users, limiting its applicability on the daily life.

Conclusions

PPG is a key player of the digital health revolution. The advent of more performing and wearable sensors is increasing the number of medical data which can be extracted out of a PPG sensor.

PPG has been extensively used to monitor several physiological measurements such as the heart rate and the blood oxygen saturation. On the other hand, a PPG signal carries additional information related to stress, respiration rate and blood pressure. In this perspective, several works have proposed in literature very promising methods for extracting as many vitals as possible from a PPG sensor.

Among those vitals, blood pressure has a prestigious role. Hypertension is the major cause of premature death worldwide: it causes each year more than 7.5 million deaths, about 13% of the total death and an estimated 1.13 billion people worldwide have hypertension. For this reason, it is essential that the blood pressure is measured regularly and continuously. A PPG signal carries several information that are directly or indirectly linked to hypertensive pathologies. The advent of artificial intelligence through machine learning and deep learning is changing the paradigm increasing the probability of seeing fully wearable and non-invasive blood pressure monitoring systems.

4 A classic PPG readout chain

In the previous chapters, we have seen that a PPG signal is at the heart of any wearable system, from the wellness/fitness to the medical space. Indeed, the PPG signal can be extensively used to monitor several physiological measurements.

The objective of this chapter is to describe a typical PPG readout chain. Specific design challenges and bottlenecks, such as the dynamic range and the DC offset, are also introduced and treated from a design perspective. Finally, state-of-the-art's solutions, both academic and commercial, are presented, with special regards with respect to those challenges.

4.1 Description of the basic readout chain

A simplified block diagram of a classic PPG readout chain is presented in Fig. 4.1. A PPG readout chain receives the weak PPG optical signal, converts it, and amplifies it into a strong electrical signal. The optical signal is usually converted into an electrical current by the means of a photodiode (PD). The PD's size is key (often few mm²) in order to collect most of the PPG optical signal, given the large tissue attenuation [117, 118]. This attenuation pushes the final PPG power bottlenecks on the LED driving current, which should emit enough light to build up a signal on the PD side. A low-noise, high-gain closed loop transimpedance-amplifier (TIA) usually follows the PD to amplify the weak photocurrent into a strong voltage. The main requirements of a TIA are high sensitivity, high gain and wide dynamic range. The combined action of the large DC component of the PPG signal and the ambient light reduces the possible feedback amplification, not to saturate the amplifier's output for large photocurrents. In this regard, a typical PPG readout chain usually embeds the possibility of reducing the DC component of the photogenerated current, by the means of feedback loops. This operation can be performed both in the analog and in the digital domain.

The TIA is the most important block of a PPG readout chain since it directly determines the receiver sensitivity and bandwidth. The TIA feedback operation minimizes the impact of the PD capacitance thanks to the lower TIA input impedance, introduced by the closed loop gain

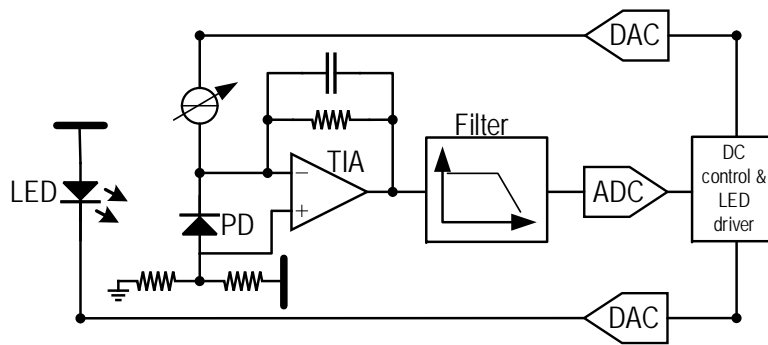


Figure 4.1 – A classic PPG readout chain, embedding the LED, the PD and the electronic processing circuitry.

[119]. This allows the measurement of fast changes in the detected photocurrent, despite the PD parasitic capacitances which can be of the order of a few pF [46, 118]. This feature is particularly important since the LED light is usually modulated with very short pulses in order to reduce the power consumption. The PD junction capacitance limits the signal bandwidth, particularly at larger PD size [120, 118, 121]. PD reverse-operations (photoconductive mode) reduce the impact of the parasitic capacitance thanks to the larger depletion area, at the cost of more dark current [121]. In the next chapter, we will see how the PD capacitance also affects the TIA noise performance.

A TIA amplifier is usually operated in two possible ways, as shown in Fig. 4.2, being both the solutions commonly used. In a capacitive TIA (CTIA), the feedback element consists of a capacitor, which defines, together with the integration time, the TIA gain. In other words, a CTIA integrates the input photocurrent. On the contrary, a RC TIA (ZTIA) embeds both a resistor and a capacitor as feedback elements and simply converts the photocurrent into a voltage by the means of the feedback resistor. State-of-the-art works have used both ZTIA [122, 123, 124, 125, 126, 127] and CTIA configurations [128, 122, 129, 130, 131].

In the ZTIA, the feedback capacitor ensures stability and lower noise operations, at the cost of the TIA bandwidth [121]. For smaller gains operations a ZTIA is usually preferred, since a CTIA would require a large capacitor and consequently larger silicon area. On the contrary, a CTIA allows to cover a wide range with fine resolution without the need of configurable circuitry. The CTIA feedback capacitor is always accompanied by a parallel switch which resets the capacitor to avoid the monotonic increase of the output voltage. In this way, the effective CTIA gain depends only on the integration time and the feedback capacitance. This operation is called autozero which, in parallel of resetting the feedback capacitor, also reduces the low frequency noise and the offset of the amplifier [132].

State-of-the art's work usually embeds programmable feedback elements to avoid any possible saturation, which is particularly important given the small PPG perfusion index (PI). Next chapter will compare these two possible configurations in terms of noise and power. We will see that the integration of the photocurrent reduces both the effect of the wideband noise

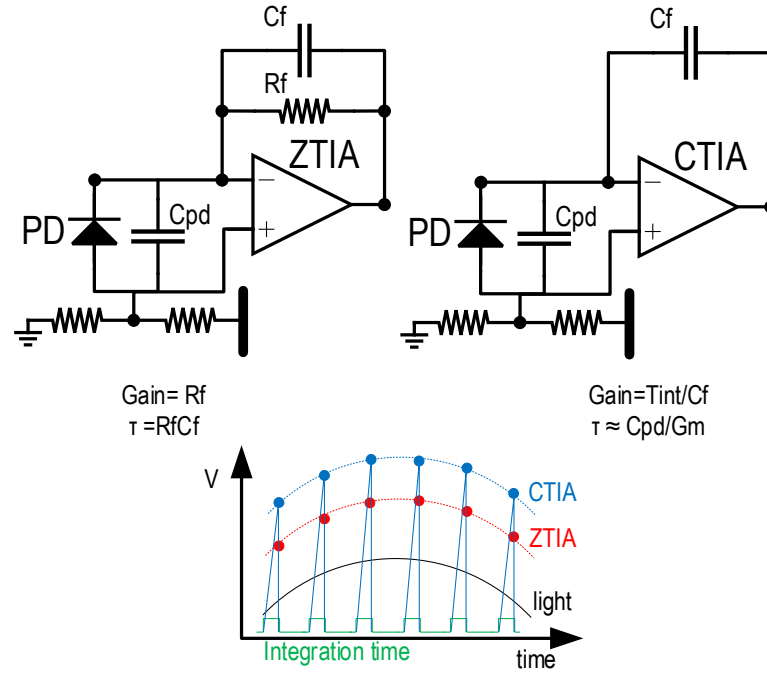


Figure 4.2 – Two possible TIA configurations: ZTIA and CTIA.

and the necessary bandwidth, as also shown in [130]. The ZTIA and CTIA have also been compared in [46] in terms of achievable dynamic range for a given power. In particular, the limitations introduced by the ZTIA settling time should tip the balance in favour of the CTIA, unless incomplete settling operations are envisaged. In this case, the introduced gain loss corresponds to a proportional increase in the amplifier noise and consequently a dynamic range drop. Another possibility, as presented in [118], is to have a TIA with resistive feedback immediately followed by a switched integrator. This solution takes advantage of a TIA larger bandwidth thanks to the pure resistive feedback. The noise penalties introduced by the purely resistive feedback [121] are compensated by the integrator which operates as a low-pass filter reducing the wideband noise. Moreover, the integrator can also be used as anti-aliasing filter before the analog-to-digital-converter (ADC). Logarithmic TIA implementations have also been proposed in order to boost the achievable dynamic range [133, 134]. A logarithmic TIA can also take advantage of the natural logarithmic operations behind the Beer-Lambert law, as shown in Chapter 2. In other words, employing a logarithmic amplifier allows a faster calculation of the R parameter, (3.5), and so of the $S_p O_2$. Moreover, the logarithmic operations leads to a wide range of input signal intensity at almost uniform signal-to-noise-ratio (SNR). The downside of this solution is the intrinsic lower sensitivity and speed.

Independently of the feedback elements, the TIA is almost always designed as a broadband amplifier. As mentioned above, the LED light is ultimately the power bottleneck. For this reason it is usually modulated with narrow pulses in order to reduce the power consumption. This also leads to most of the signal power being distributed to a large number of harmonics

with respect to the fundamental modulating frequency [117, 135]. In other words, a broadband amplifier let most of the input signal power enter the front-end. We recall that among the most important features of a TIA amplifier we find the bandwidth and the speed. The wide bandwidth is key to ensure fast settling given the short LED pulse, while the gain ultimately defines the amplifier sensitivity. Achieving a wide bandwidth while keeping the TIA gain high is a difficult problem [121], which has been faced in several state-of-the-art's work in order to lower the PPG sensor power consumption. Another solution which has also been presented is to use a narrowband TIA, in other words an amplifier having a response tuned to a particular harmonic of the modulation frequency, whose advantage would be a lower input noise bandwidth.

With respect to Fig. 4.1, a TIA is usually followed by a filtering stage, which is a key element of the signal conditioning. For instance, low-pass filters are often used for anti-aliasing purposes before the signal is sampled by the ADC or by a sample-and-hold (SH) prior to the ADC. Several circuit topology have been proposed including active-RC biquadratic filters or correlated-double-sampling (CDS) implementations [120]. The work in [136] has compared several possible filter types and orders in order to get the optimal PPG filtering.

ADCs are also key in PPG readout chains. Different ADC topologies have been proposed, such as the SAR [131, 46, 122], the $\Delta\Sigma$ [137, 138], the dual slope [129] and the incremental [139, 80]. The advances in the technology and design of ADCs are making them even more important in the latest PPG readout chains. For instance, some designs make the ADC follow directly the TIA without any signal conditioning or DC removal [131, 140]. Other designs directly digitize the PD output [141, 142]. This design choice shifts most of the signal processing in the digital domain with the downside of an ADC with quite large number of bits, so requiring more power and more silicon area. Generally speaking, any design with extensive analog signal conditioning would result into an ADC with lower number of bits.

LED drivers are also important building blocks in building a PPG sensor front-end. Indeed, particularly for wearable applications, the battery lifetime can be extended by reducing the LED on time. A key characteristic for the PPG LED driver circuit is its low noise: indeed, any introduced in-band noise would corrupt the SNR. LED drivers are very often part of a more complex feedback loop. The LED driving current is often adapted in real-time not to saturate the TIA or to keep the signal within a given scale.

For applications such as the S_pO_2 , PPG readout chains have to be multiplexed. Indeed, most designs use a single wideband PD, meaning that switches or SHs are employed to decompose the received signals into the corresponding input wavelengths.

4.2 Challenges and bottlenecks

Any electronic design comes with challenges and bottlenecks. Indeed, it is the task of the designer to ensure that the specifications in terms of noise, dynamic range and power are

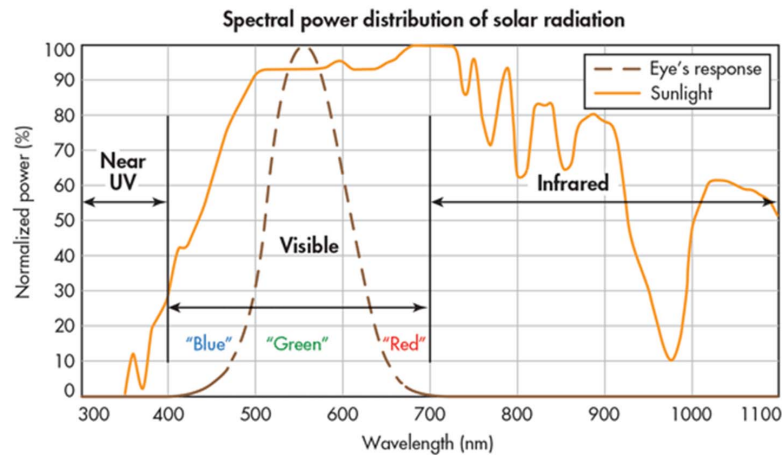


Figure 4.3 – Spectral power distribution of the solar radiation.

eventually fulfilled. The design of a PPG readout chain doesn't escape from this. While postponing the discussion about the noise on PPG front-ends for the next chapter, the objective of this section is to deepen two main challenges while designing the readout circuitry for PPG sensors: the ambient light and the dynamic range. We will see that the two are also linked.

4.2.1 Ambient light: static and dynamic interferers

Ambient light artefacts are induced by both the sun light (static interferer) and the indoor fluorescent/incandescent lighting conditions (dynamic interferers). The first and more straightforward approach to reduce these artefacts is an effective optical screening, which is, unfortunately, not always possible considering the probe-tissue displacement and, as well, the miniaturization of the sensor probe.

Depending on the environment, the ambient light can be quite different. In a clinical or laboratory environment, the dominant ambient light is the indoor one coming from the bulbs. This is likely to be generated from the main supply, meaning at 50 Hz in EU and 60 Hz in US. When accounting for both 50 and 60 Hz power frequencies, the irradiated spectrum becomes very crowded due to the existence of harmonics. This is due to the often non-linear relationship between input current and output irradiated light.

Outdoor activities are dominated by the sun light, whose spectral power distribution is shown in Fig. 4.3. Sun light also tends to have a much higher intensity than LED light sources. In other words, it has to be seriously considered in the design of a PPG systems. Fig. 4.3 also shows that a big portion of the spectral power is distributed in the IR. This is particularly dangerous for the PPG sensors given the high penetration of IR photons in the skin, as shown in Chapter 2. One possibility would be to build a PPG module with an IR blocker as done in [142].

One additional limitation of the sun light comes from its static nature. Indeed, it contributes

in increasing the already large PPG DC component. This is a major concern in pulse oximetry, since the signal has to include its DC, as shown in section 3.3. Although efforts are made to ensure optical shielding by the mechanical design of the sensor probe, the residual ambient light incident to the photodiode can be large enough to distort S_pO_2 readings.

Removal of time-varying interferers from the PPG signal is another difficult design challenge. As mentioned above, most lamps irradiate a quite broad spectrum. On the other hand, LED are often driven at very short pulse time (less than $100\mu s$) which imposes the PPG front-end bandwidth to be quite large in order to enable correct settling operations. This is even worse, as the LED duty cycle gets smaller and smaller [117], since the receiver bandwidth has to increase accordingly. This can cause harmonics of the ambient light at multiple of the driving frequency to alias into the PPG bandwidth of interest if they are not filtered properly [131]. For example, a PPG system that samples at 100 Hz will modulate 120 Hz from fluorescent lights down to 20 Hz and 60 Hz from incandescent lights down to 40 Hz.

Correlated-double-sampling

A quite effective way to perform the ambient light cancellation (ALC) is the CDS: an ambient sample is taken, which is then subtracted from the LED sample, meaning the PPG signal. If the time between the two samples, Δ , is comparable with the LED pulse time width, T_{ON} , an (almost) ambient light free PPG signal is obtained. Typical CDS is performed by the means of a SH stage. We will see that the CDS has also an important impact on the noise. Indeed, together with any offset, e.g. the ambient light, it dramatically reduces the low frequency noise, such as the flicker noise.

Designing a PPG system with a CDS stage requires careful analysis of the expected frequency content of the ambient light. Indeed, the two samples should be quite close not to have the ambient light changing meanwhile. This means that the sampling rate must be set high enough. A higher sampling rate, at constant LED duty cycle, requires higher bandwidth LED drivers and photodetectors which inherently are more complicated and have higher current consumptions. Fig. 4.4 reports how efficient the cancellation introduced by the CDS is versus the Δ between the two samples. It shows, for a 50 Hz artificial light, that more than 90% of light attenuation can be achieved if the time between the two samples is shorter than $300\mu s$. From a design perspective, this means that, supposing the LED pulse equal to Δ , the PPG front-end should have enough bandwidth to settle in about one tenth of that time, meaning $30\mu s$, which corresponds to more than 5 KHz bandwidth. A shorter Δ would increase the CDS efficiency at the cost of larger required bandwidth, so power consumption.

4.2.2 Dynamic range and DC offset cancellation

As explained in Chapter 2, the PPG signal consists of a large DC (static) component with on top a small AC (pulsatile) one. The ratio between these two components, i.e. PI, has serious

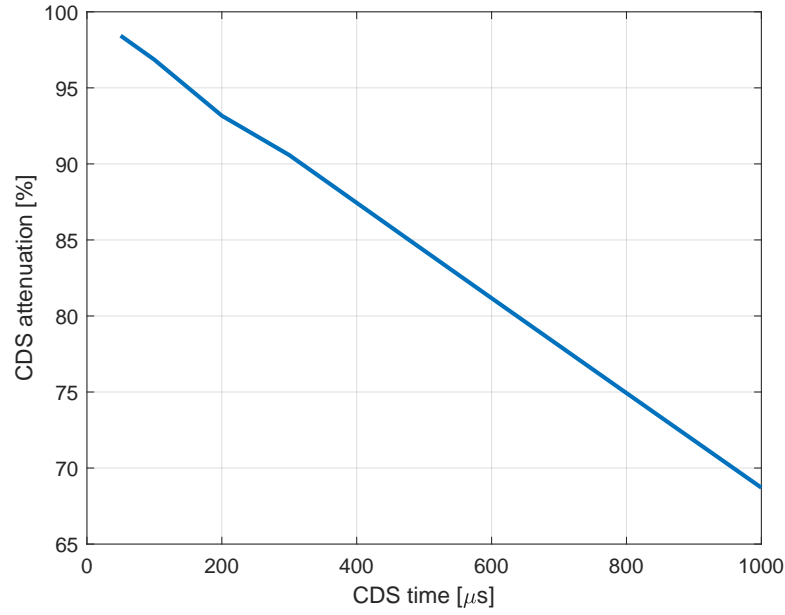


Figure 4.4 – Percentage reduction of a 50 Hz interfere thanks to CDS. More than 90% attenuation requires the two samples to be shifted not more than 300 μ s. No reduction takes place for samples distant more than 3 ms.

implications on the dynamic range constraints of the PPG readout chain. In addition, ambient light can further increase the overall dynamic range requirements.

This is particularly important for clinical application, such as the S_pO_2 , requiring particular resolution. As demonstrated in [46, 122], the required DR for a certain target noise depends on the PI and the oxygen saturation value, as shown in Fig. 4.5.

Fig. 4.5 shows that for a worst case PI condition (0.1 %) and worst case oxygenation level (70 %), a DR as close to 90 dB is needed. For the full derivation, the reader should refer to appendix A. From an electronic design point of view, the PI determines one of the most severe challenges in the design of pulse oximetry. Indeed, such large DC may result both on the saturation of the signal amplifiers and power hungry dynamic range conditions and also ADC resolution. For instance, let's suppose to directly digitize, with a 12-bit ADC, a PPG signal with a 5 V full scale (FS) and PI of 1%. This means setting the DC equal to 2.5 V and the AC equal to 25 mV. A 12-bit ADC leads to a maximum 4096 levels. Considering the AC to be just 1% of the DC, the former will use only 20 levels, leaving 4076 levels to the latter. Such scenario would lead to weak SNR due to the impact of quantization noise [26].

In literature, two techniques have been proposed to extend the TIA dynamic range: automatic gain control and signal compression. The automatic gain can be implemented by using a variable resistor changing with the input optical signal power[143]. The variable feedback resistor can be implemented with a MOSFET operating in the linear region, connected in parallel with a fixed resistor to improve the linearity and to limit the maximum resistance.

As far as the signal compression is concerned, this can be implemented by the means of a logarithmic TIA [134, 133].

Any effort in boosting the dynamic range at the level of the TIA has been always accompanied by DC offset reduction loops which dynamically subtract, from the input photocurrent, a current proportional to the wanted DC reduction. A differential output TIA with a DC photocurrent rejection loop has been presented in [144]. An error amplifier integrates over time an offset depending on the differential TIA output. The amplifier's output drives a transistor which operates as a variable current sink that eliminates the DC photocurrent from the TIA input signal path. Despite the robustness of these feedback loops in reducing the DC photocurrent level, they come with significant power and area overhead.

4.3 State-of-the-art: academic works

The objective of this section is to revise the state-of-the-art of academic works in PPG sensing. A total of 10 works will be presented, spanning over more than 10 years. Each work will be presented with a special focus on how the PPG sensor challenges, as presented above, have been handled, from a design perspective. Eventually, a table summarizing these works is also presented.

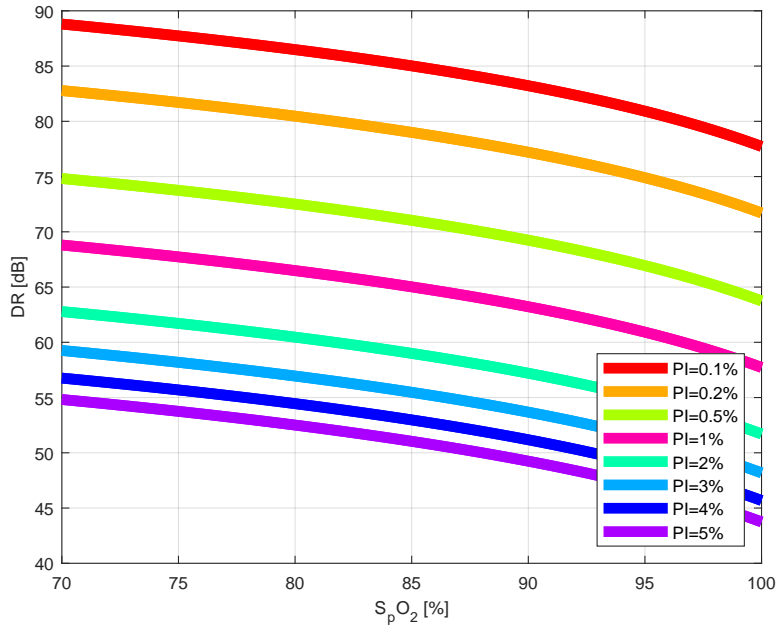


Figure 4.5 – Dynamic range requirement for different PI with respect to the S_pO_2 level.

Tavakoli et al. [133]

This work is, to the best author's knowledge, the only fully analog PPG front-end. It is based on a logarithmic TIA, that thanks to a feedback loop and multi-stages operations, achieves large dynamic range (thanks to the inherent logarithmic features) together with good sensitivity. The proposed solutions comes with two interesting points. First, in the feedback loop a capacitive divider, thanks to a sinh resistance, amplifies the AC component of the PPG $\frac{1}{\beta}$ times more than the relative DC, β being the feedback factor (equal to 1 in DC and progressively decreasing for larger frequencies). In other words, the feedback loop already performs a DC offset reduction. Secondly, it relies on multi-stages operations. The settling time of the TIA has been identified to be a limiting factor for lowering the LED duty cycle. The gain has been distributed over three stages rather than one only, this intended to boost the Gain-Bandwidth. This work shows that up to a certain number of stages the amplifier cascade extends the total gain-bandwidth of the amplifier, for almost the same total power consumption. In fact both a large bandwidth and a large gain are important. The structure presented in Fig. 4.6 is complemented by trans-linear analog circuits, generating a single output current corresponding to the R parameter, (3.5), and so the oxygen saturation value. In other words, the output current will result being proportional to the oxygen saturation. This is the reason why this solution is considered a fully analog one. A total power consumption of 4.8 mW was achieved for the whole system.

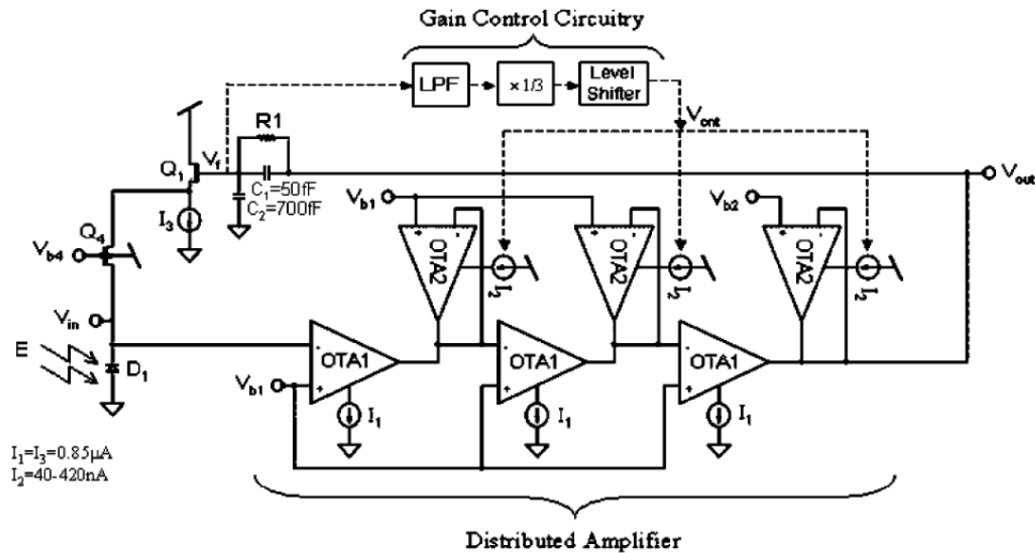


Figure 4.6 – Logarithmic TIA and multi-stages operations as in [133].

Patterson et al. [130]

This work has proposed to use a CTIA as first stage to lower both the power consumption and the wideband noise of the front-end, the latter built by off-the-shelf components. It has used a digitally-assisted analog technique to subtract ambient light from the PD, as shown in Fig. 4.7. The current is subtracted at >10 Hz intervals, and the subtraction steps are digitally tuned. This work is mostly centered on the sensor placement and artifacts reduction. Indeed, it focuses on signal processing techniques for the compensation of motion artifacts and ambient light offsets and also on LED modulation schemes to reliably cancel fixed pattern noise. The proposed paradigm exploits the fact that a ratiometric comparison of the IR and red hemoglobin absorption characteristics cancels out noise that is multiplicative in nature. The algorithm is supposed to be simple enough to be implemented in a microcontroller unit (MCU), without computationally costly conversions into the logarithmic domain, while also being robust against ambient light induced and systematic offsets between the multi-channels PPG. This work also proposes an alternative method to CDS for removing fixed pattern noise and DC offset. Indeed, as above-mentioned, the CDS is an attractive method as soon as the two samples are close enough. Moreover, this can result into a larger LED sampling frequency to compensate for time-varying ambient interferes. This work has proposed to modulate the LED emission with a sine wave, unlike a standard square wave method. This generates an amplitude-modulated (AM) image of the LED sine wave at frequency equal to the sum and the difference with respect to the carrier. Careful selection of the LED modulation frequency places it not to overlap with any frequencies present in the noise signal, otherwise the noise would also be mixed down into the low frequency band so corrupting the absorption signal. The demodulation happens in an homodyne fashion since the carrier signal is fully controlled. The reported front-end consumes in total approximately 13 mW.

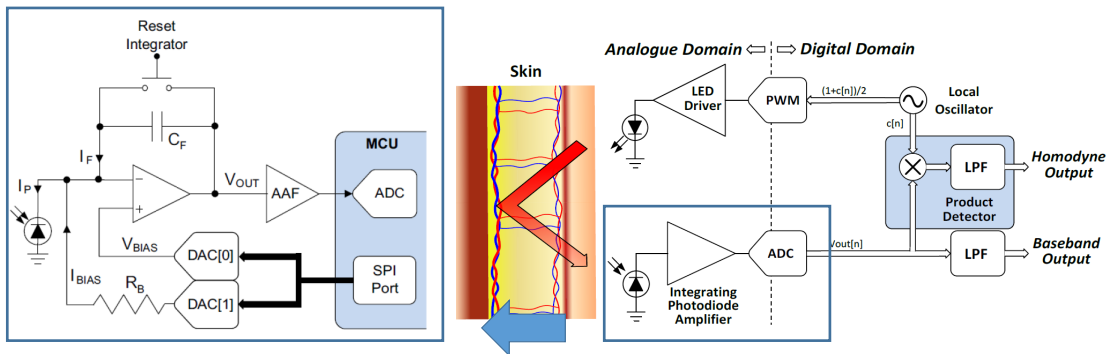


Figure 4.7 – ZTIA topology with a digitally assisted DC offset cancellation loop and homodyne demodulation as in [130].

Glaros et al. [117]

This work has been the first academic one reaching near sub-mW operations. The readout circuitry, shown in Fig. 4.8, consists of two paths: the first one, i.e. forward path, measures the PD current, while the second one, i.e. feedback path, is employed to control the LED drive current so to achieve a desired average (DC) photocurrent level at the PD. Instead of measuring the DC and the AC photocurrents, the system, by the means of the feedback-path, sets the DC photocurrent to a desired value, called I_{ref} , which is the same for both the visible and the IR channels. This DC tuning happens via a feedback mechanism at regular intervals, i.e. calibration phases, during the normal operation of the system. In other words, once the LED is switched on, the front-end is directly connected to the LED driver and more precisely to the gate of the transistor acting as a transconductance to provide the LED driving current. Knowing a priori the average expected photocurrent allows for the removal of the DC in a quite easy way, which is to say exploiting the differential operation of an electronic amplifier. With respect to Fig. 4.8 the reference current will be converted into a reference voltage which is supplied to the positive terminal of the switched integrator following the TIA: the integrator both limits the (thermal) noise bandwidth of the TIA, so reducing the corresponding noise power, and behaves as anti-aliasing filter before the sampling, SH stage. As above-mentioned, having the switched integrator directly following a TIA with resistive feedback leads to a larger bandwidth. Indeed, a ZTIA usually embeds a resistor and a capacitor in the feedback for a better noise performance [121], at the cost of lower bandwidth, which becomes, on the other hand, independent of the PD capacitance. In this work, the pure resistive feedback comes with little noise penalties thanks to the low-pass filter operations of the integrator. The reported front-end consumes in total approximately 837 μ W.

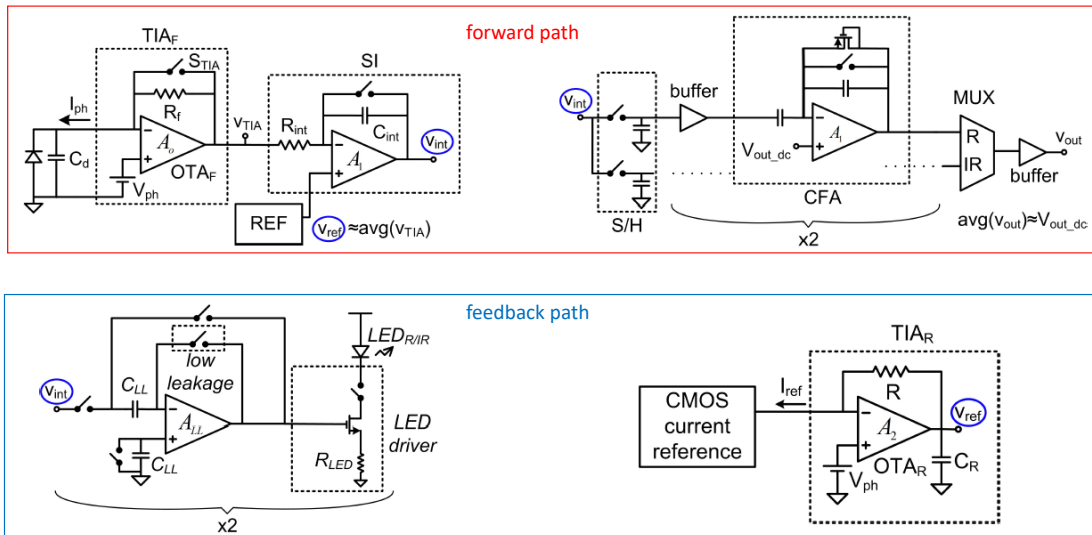


Figure 4.8 – TIA followed by a switched integrator and feedback loop controlling the LED light for controlling the DC photocurrent level [117].

Winokur et al. [131]

In this work, shown in Fig. 4.9, the photocurrent is integrated by a CTIA and then transposed into the digital domain by a 9-bit SAR ADC. In other words, a big portion of the signal conditioning happens in the digital domain. The digital core has three main functions: digital filtering, PPG demodulation and control signal managements. The proposed front-end embeds a “Dynamic-Range Enhancer” (DRE), whose algorithm, shown in Fig. 4.9, subtracts a static current (up to $100\ \mu\text{A}$) from the photogenerated one, so to keep the output of the TIA within a wanted range. This work also shows an interesting way of reducing the impact of time-varying interferences, in a low power manner, without employing a CDS. It exploits the intrinsic modulation of the PPG signal coming from the LED drivers: indeed, the PPG signal gets modulated at integer multiples of the LED frequency, f_{led} , whereas the interferences stay at low frequency (they are not modulated). By the means of digital FIR filters, the PPG spectrum is filtered around the second image (at $2f_{led}$) and then eventually decimated to bring the image to baseband. The value of f_{led} has been properly chosen so to reduce as much as possible the intermodulation with the time varying interferences. This work reports the 300-360 Hz in the US and 300-350 Hz in EU as the best sampling frequency ranges to minimize the effect of time varying interferences, such as the artificial light. The reported front-end consumes in total roughly $336\ \mu\text{W}$.

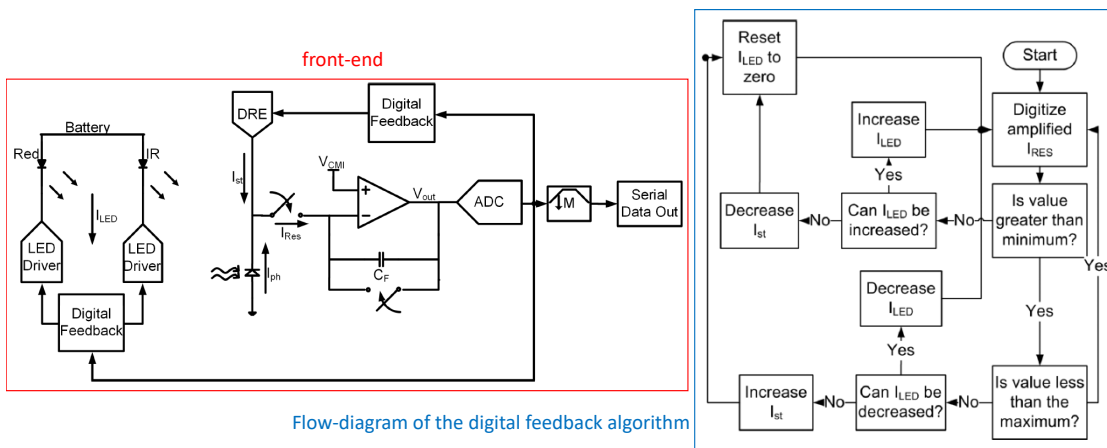


Figure 4.9 – CTIA followed by a 9-bit SAR and digital processing. The front-end embeds a DRE to reduce the input of the DC offset [131].

Gubbi et al. [128]

This work, shown in Fig. 4.10, has used off-the-shelf component and embedded a CTIA followed by two comparators and a time-to-digital-converter (TDC). The CTIA converts the photocurrent into a voltage ramp. The amplified ramp is then thresholded against two voltage references thanks to two comparators. Eventually, the TDC measures the difference between the times when the amplified ramp hits the two reference voltages. Measuring the difference helps suppressing the flicker noise of the CTIA, similarly to a CDS. Unlike other works, the LED driving current is kept fixed so to enable the LED to always operate at its highest efficiency. The photocurrent is then controlled by dynamically tuning the LED duty cycle, at a constant current. A TDC is proposed instead of an ADC, since it is relatively easier to obtain large dynamic range in TDCs rather than ADCs, particularly at lower supply voltages. This work also focuses on two techniques in order to minimize the PPG sensor power consumption, namely the "Minimum SNR tracking" and the "PLL tracking". The former measures the SNR of the acquired PPG signal and dynamically adjust the LED duty cycle so that the system operates at just sufficient SNR. The latter, reduces the duration for which the LED is on, by taking fewer samples. Indeed, for the oxygen saturation measurements, only the peaks and troughs of the PPG signal are needed. In other words, the sampling can be performed only just before the time when these events are expected to occur. The reported front-end consumes in total roughly 800 μW .

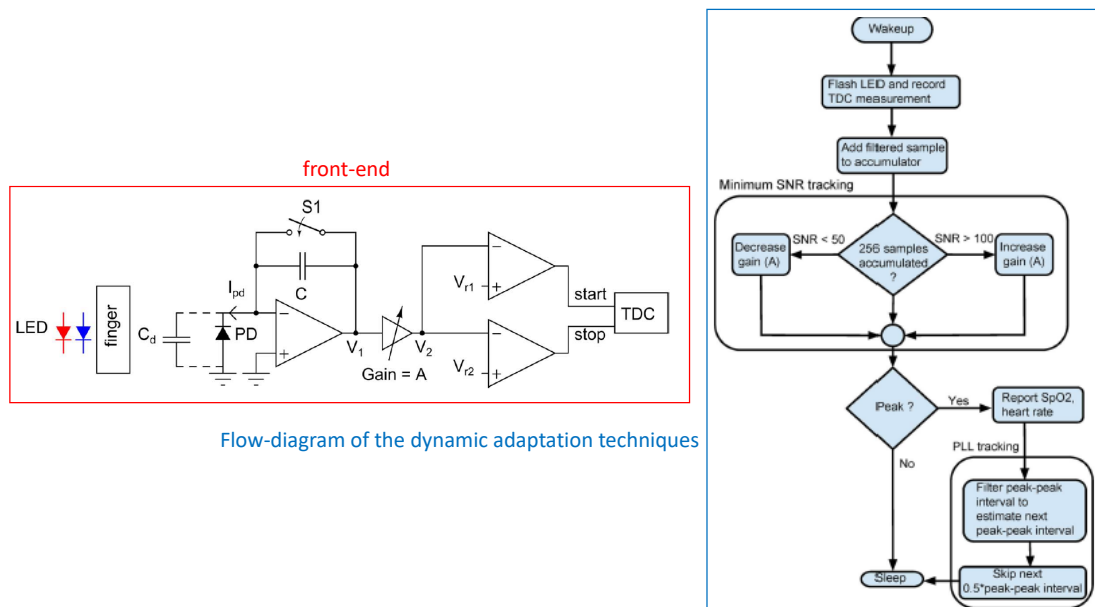


Figure 4.10 – CTIA followed by two comparators and a TDC and the diagram of the dynamic adaptation techniques [128].

Pamula et al. [125]

This work, shown in Fig. 4.11, has exploited the compressive sampling (CS) technique to reduce the LED power consumption. The PPG signal is naturally sparse in the frequency domain. This can be exploited to achieve a strong reduction of the LED duty-cycle and generally speaking of the average sampling frequency by the means of sub-sampling operations. A duty-cycle as low as 0.0125% and an effective sampling frequency of 4 Hz have been obtained. The proposed PPG front-end embeds a ZTIA, with programmable gain, followed by a switched integrator. The switched integrator, with programmable feedback capacitor, improves further the gain programmability and behaves as an anti-aliasing filter. A feedback loop is capable of subtracting up to 10 μA of current from the TIA input to improve the dynamic range by reducing the DC offset. A digital back-end block samples, at non-uniform sampling times, the output of a 12-bit SAR for further digital processing. It also generates the control signals required for the LED driver, the ZTIA, the switched integrator and the ADC. The digital back-end calculates the HR on the processed data which has been stored, after the digital processing, into a local memory. The reported front-end consumes in total roughly 172 μW .

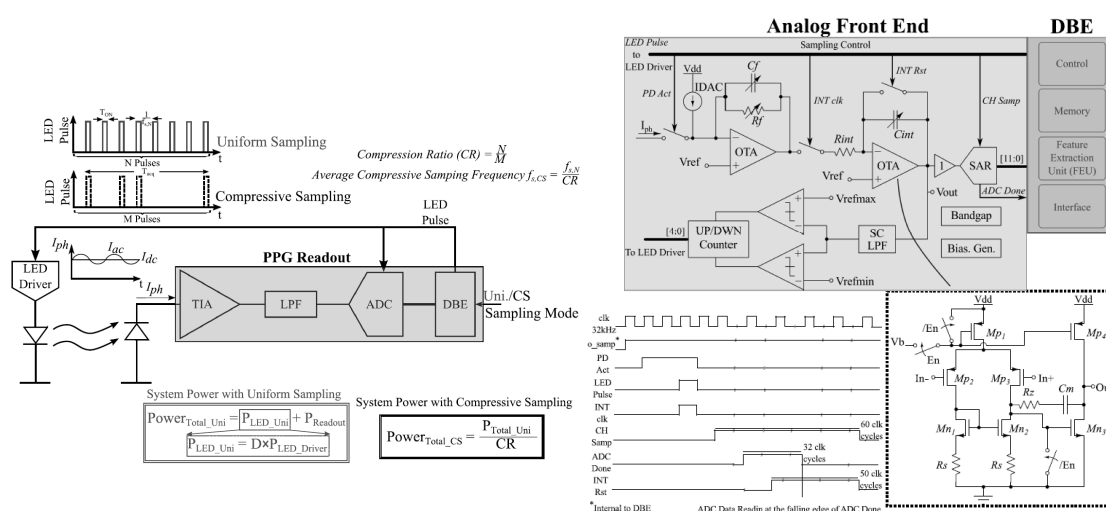


Figure 4.11 – CS based PPG readout chain [125].

Schönle et al. [122]

Fig. 4.12 shows the proposed analog front-end. The reported PPG sensor supports probes with up to 32 LEDs and 4 PDs. The analog front-end is based on a differential TIA and switched capacitor summation for analog ALC. The TIA is operated either as a ZTIA or a CTIA thanks to different clocking. In the ZTIA operations, a differential DC current, up to $10\ \mu\text{A}$ is subtracted from the amplifier input, based on an initial estimate of its DC level. In the CTIA operations, the DC offset compensation happens by pre-charging the feedback capacitor. The DC value is restored digitally in order to compute the oxygen saturation. A 14-bit SAR ADC is used to convert the TIA output. The LED driver array and the electronics are coordinated by a digital finite state machine (FSM) that provides all control and clock signals for the analog circuits. The proposed solutions achieves a dynamic range of 96 dB at slightly more than 5.5 mW total power.

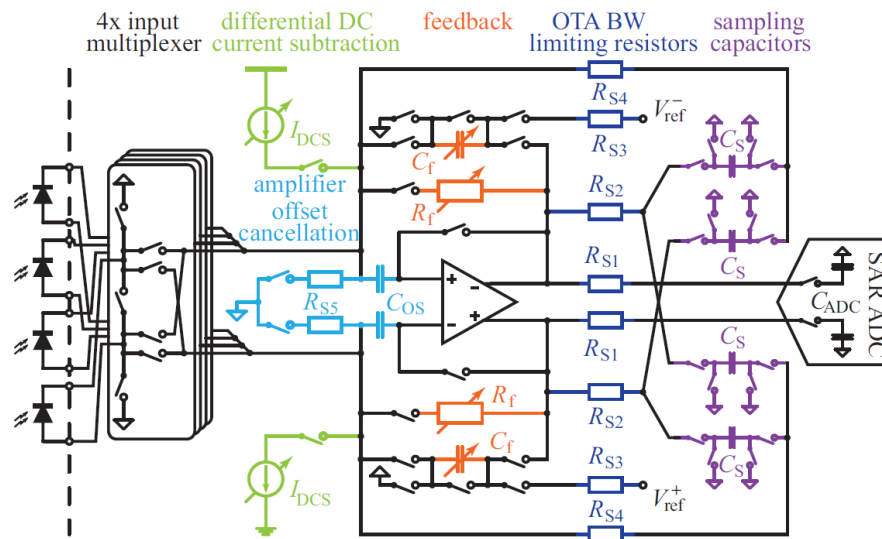


Figure 4.12 – Proposed PPG front-end as in [122].

Kim et al. [137]

This work, shown in Fig. 4.13, has presented a CMOS monolithic PPG sensor. A monolithic PPG sensor refers to the integration of the PD together with the analog front-end, on the same silicon. As described earlier in the chapter, and further deepen in the next chapter, a PD comes with large parasitic capacitance which ultimately limit the power and noise performance of the readout chain. Integrating the PD on the same silicon with respect to the front-end would reduce the power consumption and noise. The proposed work takes advantage of a distributed array of 1-bit $\Delta\Sigma$ light-to-digital-converter (LDC). The chip embeds 128 LDCs. Each LDC integrates a PD in reverse mode whose anode voltage is converted to a $\Delta\Sigma$ modulated 1-bit stream. Simple addition of the 128 LDCs outputs finalizes the reading. Off-chip digital filter removes high frequency noise taking advantage of the noise shaping mechanism. The dynamic range requirement of each LDC is relaxed thanks to the light being distributed over 128 LDCs. Proposed monolithic and distributed architecture minimizes the effect of noise and improves the dynamic range of the sensor. The proposed solutions achieves a power consumption lower than $25 \mu\text{W}$, without accounting for the LED.

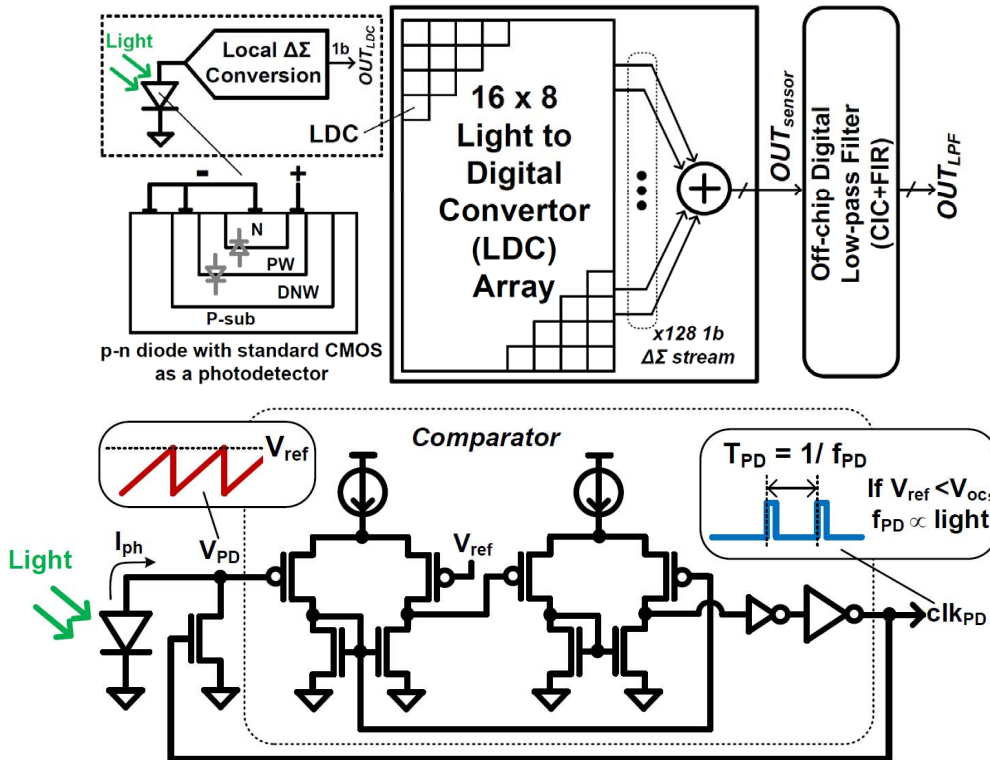


Figure 4.13 – Proposed monolithic PPG front-end as in [137].

Lee et al. [127]

This work has aimed at reducing as much as possible the LED power, which is, as mentioned earlier in the chapter, the most power hungry element of a PPG sensor. The work is shown in Fig. 4.14. It is based on a heartbeat-locked loop (HBLL) that turns on the LED only during the PPG peaks, thus achieving an effective duty cycle of 0.0175%. The readout chain consists of analog and digital blocks. On the analog side, the chip integrates a DC offset cancellation circuit, a ZTIA with programmable gain, a switched capacitor low pass filter, two SHs, and a comparator. The comparator compares two consecutive samples. Its output is high when the PPG signal increases and low when it decreases. Consequently, a high-to-low transition is created when there is a peak in the PPG signal, which results in a digital clock signal, synchronized with the PPG signal and the HR. This creates a periodic window, in phase with respect to the HR, in which the electronic operates. Beyond the window, the PPG is expected not to show any peak and so the electronic is switched off, further reducing the power consumption. On the digital side, the HBLL block receives the clock converted from the PPG signal from the comparator and measures the peak-to-peak interval by using a counter. Thanks to a variable moving average filter it also estimates the heartbeat interval (HBI). Based on the HBI algorithm, the digital circuit centres the observation window at the estimated peak location and locks it for the next samples. The size of the window is set to 100 ms. The LED shines only in this window. If the peak doesn't occur within two consecutive windows, then the HBLL increases the window size to 400 ms. If the peak is still not visible, then the window is disabled and the LED is duty cycled continuously, without the window. In this case, the HBI algorithm will look for two consecutive peaks to reactivate the "windowing" process. The proposed solution achieves a total power consumption lower than $45 \mu\text{W}$.

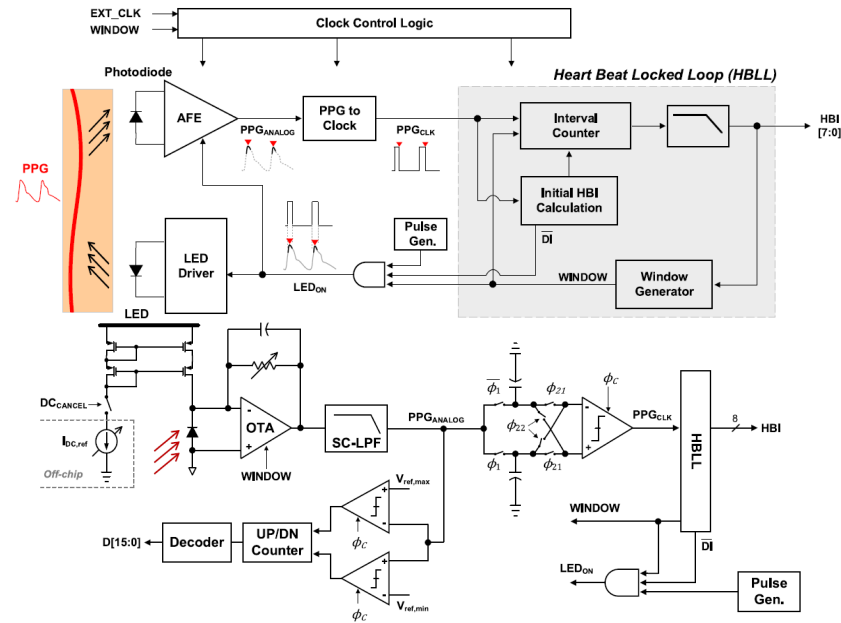


Figure 4.14 – PPG front-end as in [127].

Lin et al. [129]

This work, shown in Fig. 4.15, has used a LDC based PPG sensor. The LDC converts light into the time domain with a dual-slope mode integrator, which is then followed by a counter-based TDC. The input stage consists of a periodically reset CTIA and a reference current source, I_{ref} , which generates the dual-slope output voltage. The amplifier is followed by a dynamic comparator and a counter, converting the integrator output directly into a digital code. The readout operations are based on two phases: the integration and the conversion phase. In the integration phase, the LDC integrates the ambient light signal on the feedback capacitor C_f during t_1 . This is performed by closing the switch I_{INSW} . Then the LED is pulsed, and both signal current and ambient light current are integrated on the feedback capacitor C_f . Since the LED pulse width is exactly the same as t_1 , the polarity of C_f is swapped just before the LED pulse in order to effectively cancel the ambient light in each sampling period. This is the same technique as shown in [122]. After the LED pulse, the integrated signal is automatically sampled on C_f . As mentioned earlier in the chapter, the switched integration also acts as a low pass, anti-aliasing filter. In the conversion phase, I_{INSW} is disabled and I_{REFSW} is enabled. Then, the voltage stored on C_f is converted into a digital code by counting the number of needed time intervals to discharge C_f to the initial reference V_{REF} by the means of a predetermined I_{ref} . In order to remove the large baseline component from the input PPG signal, before the integration, two 7-bit current DACs synchronized with the LED pulses provide compensation current, enhancing the dynamic range. The LED driver can provide up to 100 mA peak current for two LEDs. The proposed solutions achieves 196 μ W total power consumption.

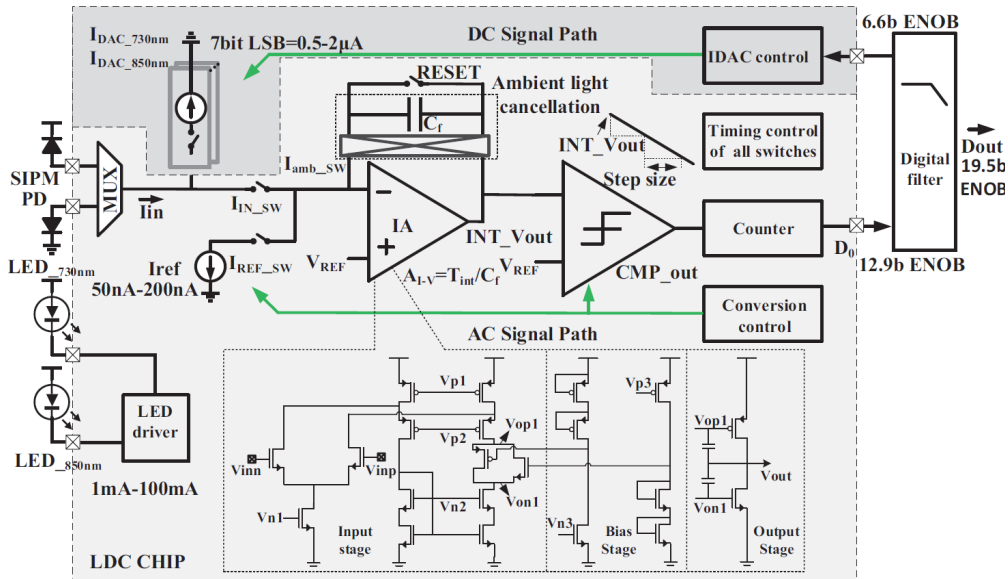


Figure 4.15 – PPG front-end as in [129].

Table 4.1 – Summary of the academic works.

Reference	[133]	[130]	[117]	[131]	[128]	[125]	[122]	[137]	[127]	[129]
Year	2010	2009	2013	2015	2015	2017	2017	2017	2018	2019
Technology [<i>nm</i>]	1500	NA ^a	350	180	NA ^b	130	180	180	180	180
Supply Voltage [V]	5	3	3.3	1.8	NA	1.2/3.3	1.2	NA	3.3	1.2/3.3
Sampling Frequency [Hz]	100	1000	100	165	NA	600	4	160000	100	2000
LED Duty Cycle [%]	3	NA	3	0.7	NA	1.7	0.0125	10 ^c	0.0175	NA
Full Integration ^d	NO	NO	NO	NO	NO	NO	NO	YES	NO	NO
Max HR Error [<i>bpm</i>]	NA	NA	NA	NA	NA	NA	10	NA	2.1	NA
LED Power [μW] ^e	4400	NA	309	120	NA	5500	43	NA	16	107
Circuit Power [μW]	400	NA	528	216	NA	370	172	13 ^f	27.4	89
TOT Power [μW]	4800	13000	837	336	800	5870	215	NA	43.4	196
Main Feature	Log TIA	Homodyne ^g	TIA+SI ^h	DRE+ALC ⁱ	Min SNR+PLL	CTIA+ZTIA	CS ^j	Monolithic ^k	HBLI ^l	LDC ^m

^aoff-the-shelf components^boff-the-shelf components^cReported data for pulsed operations^dpD+Circuit^eBest case from the given data^fPulsed LED^gLed modulated by a sine wave and homodyne demodulation^hTIA with resistive feedback followed by a programmable gain switched integrator for anti-aliasingⁱTime varying interferers removal^jSub-Nyquist compressive sampling operations^kArray consisting of 128 1-bit $\Delta\Sigma$ LDC^lHeart-beat-lock-loop, the readout chain tracks only the PPG peaks^mLight-to-digital conversion based on a dual-slope mode integrator

4.4 State-of-the-art: commercial works

Objective of this section is to revise the state-of-the-art of commercial products in PPG sensing. As shown in Chapters 2 and 3, the duo between wearable devices and optical heart rate sensor is becoming a must. Consequently, the number of PPG sensors on the market is significantly increasing.

Texas Instruments: TI4403 [138]

The TI4403 PPG sensor is presented in Fig. 4.16. It consists of 4 main blocks: a differential ZTIA, an ambient cancellation block, a low pass filter and an ADC. The output of the ZTIA is sourced to a second stage with consists of a current DAC sourcing the cancellation current, up to $10\ \mu\text{A}$, and an amplifier which amplifies the ZTIA voltage subtracted by the DC offset. This second amplification is tunable. The output of the second amplifier is then low pass filtered, with 500 Hz cut-off, and buffered for the 22-bit $\Delta\Sigma$ ADC. The 22-bit ADC converts the LED samples and the ambient signals sequentially. In other words, for each conversion it provides a single digital code at the ADC output. The ALC takes place in the digital domain.

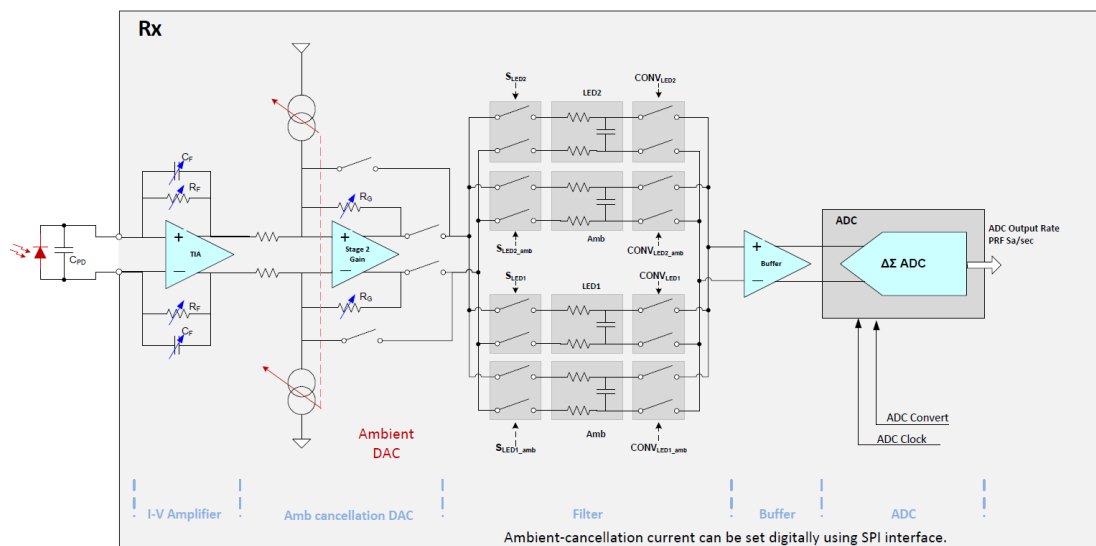


Figure 4.16 – TI4403 front-end as in[138].

Maxim Integrated: MAX86140 [141]

Fig. 4.17 shows the MAX86140 from Maxim integrated. The PD output is digitized by the means of a 19-bit current ADC. An ALC and picket fence detect and replace algorithm are integrated on chip for up to 70 dB artificial light (120 Hz) resilience. Thanks to a digitally controlled feedback loop, the dynamic range can be enhanced by subtracting more than $100\ \mu\text{A}$ from the PD current. The MAX86140 embeds a 128-words first-input-first-output (FIFO) register and supports a standard serial peripheral interface (SPI) and fully autonomous operations.

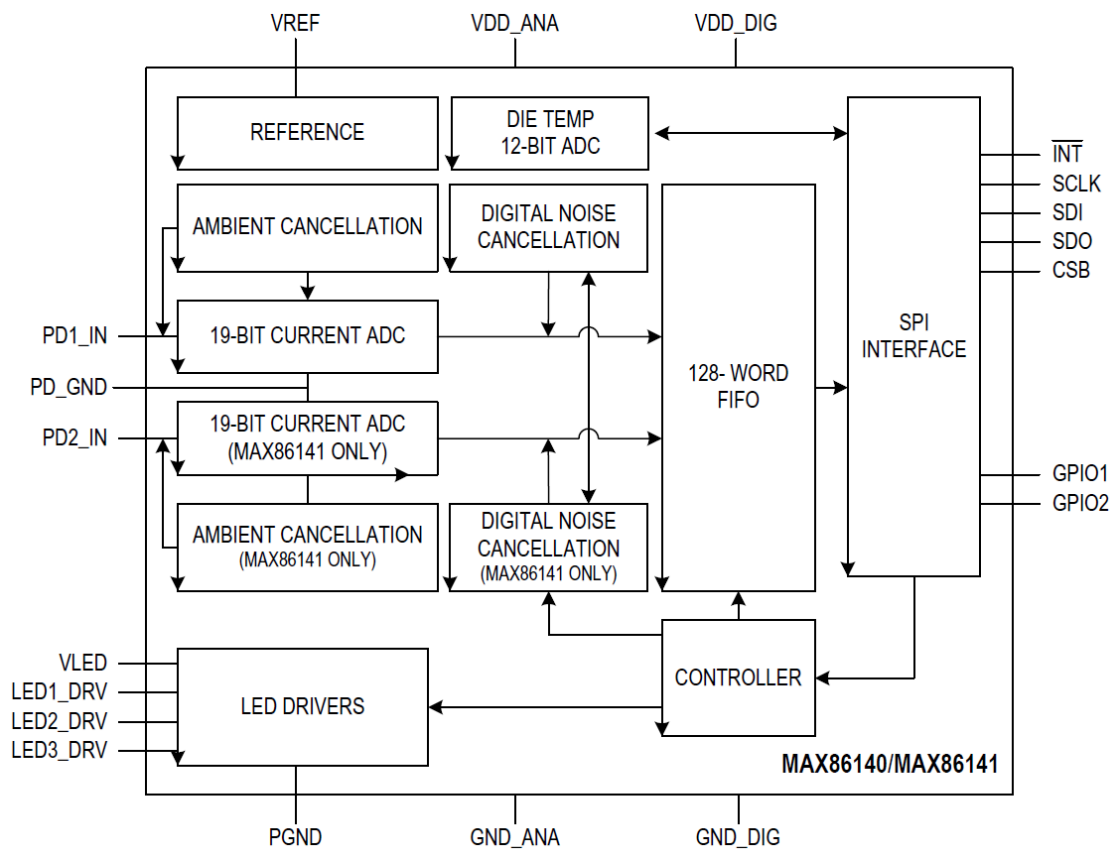


Figure 4.17 – MAX86140 front-end as in [141].

AMS: AS7026GG [140]

Unlike the AFE4403 and the MAX86140, the AS7026GG from AMS, shown in Fig. 4.18, is a module integrating 5 PDs on chip and the 3 LEDs off chip. A TIA, either in ZTIA or CTIA configuration, reads the output of the PD. After the TIA, the system allows multiple configurations. One possibility is to directly digitize the TIA output by the means of a 14-bit ADC. Another possibility is to perform some signal conditioning before the ADC. Several filters are available such as low pass, high pass and band pass. This is used to remove unwanted components, e.g. noise or DC offset, from the PPG signal and it allows further amplification.

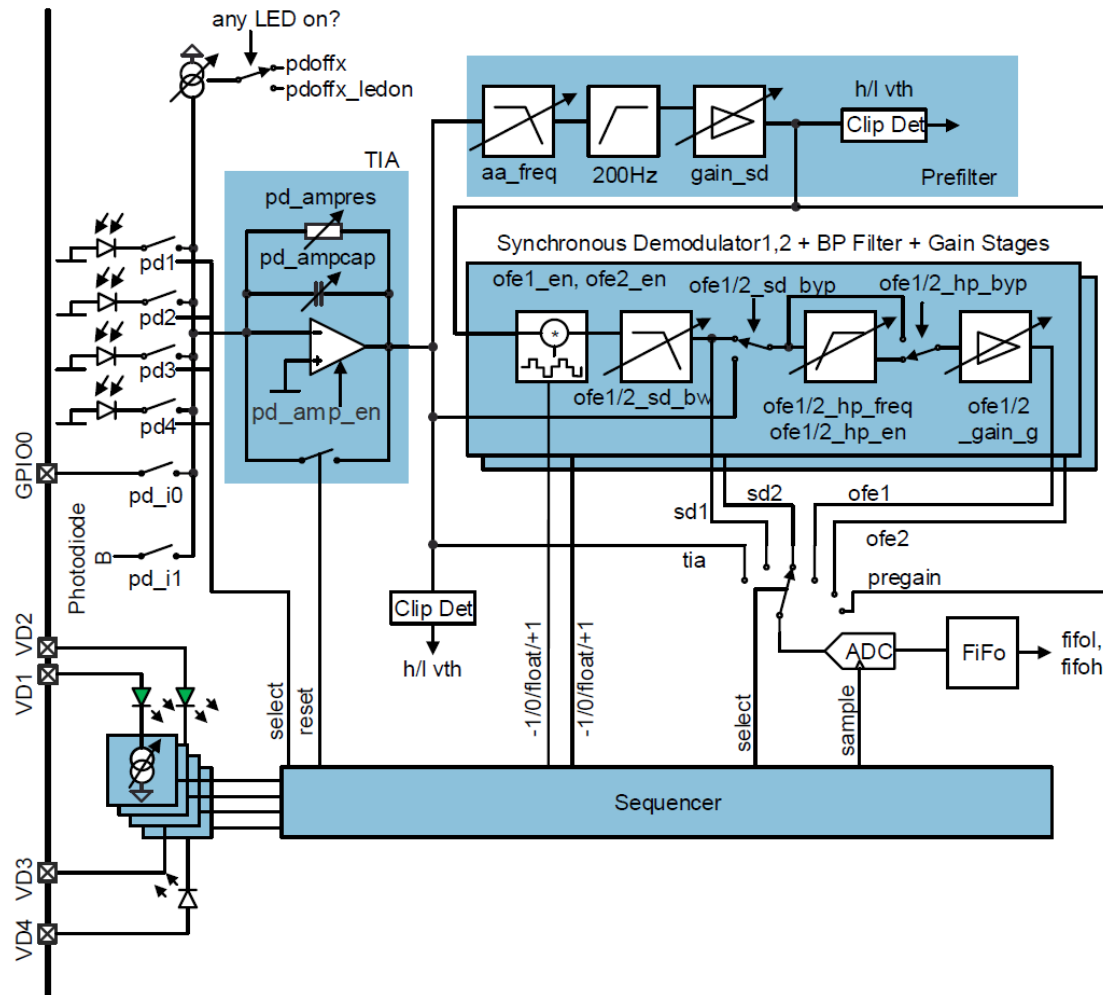


Figure 4.18 – AS7026GG front-end as in[140].

Table 4.2 – Summary of the commercial works.

Reference	[138]	[141]	[140]
Company	Texas Instruments	Maxim Integrated	AMS
Year	2014	2017	2017
Supply Voltage [V]	3/5	1.8/5	2.7/5.5
Sampling Frequency [Hz]	62.5/2000	8/4096	1000
LED Duty Cycle [%]	25	0.037 ^a	10
Full Integration^b	NO	NO	YES
Communication protocol	SPI	SPI	I2C
LED Power [μW]^c	18000 ^d	116.7 ^e	7.75 ^f
Circuit Power [μW]	700	15.3 ^g	600 ^h
TOT Power [μW]	18700	132	8350
Cost [\$]ⁱ	3.25	3.94	4.5
Package size [mm^2]	3.07 x 3.07	2.048 x 1.848	2.75 x 6.2 ^j
Main Feature	22-bit ADC	19-bit Current ADC	Integrated PD & LEDs

^aAt 25 Hz sampling frequency^bPD+Circuit^cBest case from the given data in datasheets^dAt 25mA, 3 V and 25% duty cycle^eAt 62mA, 5 V, 25 Hz sampling frequency and 0.037% duty cycle^fAt 25mA, 3.1 V and 10% duty cycle^gAt 25 Hz sampling frequency^hAt 3 V and 200 μA ⁱDistributor's price for 1000 pieces^jIncluding 5 PDs and 3 LEDs

Conclusions

Designing a good PPG sensor undergoes several bottlenecks and engineering trade-offs. The LED power, due to its few tens of mAs driving current, is still the largest power hungry element. State-of-the-art PPG sensors, both in academia and in commercial products, still follows a quite standard design paradigm. Indeed, they rely on off-chip PDs and relatively standard circuitries.

In the last 10 years, we have seen the PPG circuit power scaling down at an almost constant LED power. This ultimately limits the applicability of PPG sensors in platforms for continuous monitoring. One possible solution relies on reducing as much as possible the LED duty cycle to values well below 1%. The downside of this is the increased complexity of the analog front-end. Indeed, in order to cope with those very short pulse, the TIA has to be capable of settling within a short amount of time. From a design perspective, this means a larger bandwidth and consequently more power consumption and larger (thermal) noise. Additional complexity may also come from sub-Nyquist sampling operations which effectively reduce the duty cycle and sampling frequency at the cost of more processing power. Reducing the LED duty cycle also means distributing the signal power over a very large number of harmonics so increasing the needed bandwidth to recover the signal power. For this reason, wideband TIAs are often chosen, followed by analog or digital filters.

The majority of PPG sensors still utilize off chip PDs. The parasitic capacitance of those devices degrades the speed and noise performance of the front-end. For this reason, some few works have proposed to integrate the PD together with the processing chains for better performance.

Despite a PPG sensor always comes with an optical shielding, handling the ambient light is not easy. The large IR power of the natural light can saturate the front-end due to the large IR penetration in the skin. The artificial light often comes with large order of harmonics whose effect cannot be easily cancelled by CDS blocks, otherwise using a large sampling frequency which increases the LED and circuit power consumption.

The extremely low PI of a PPG signal makes the design of a PPG sensor even more complicated. First of all, the DC has to be properly corrected at the input by the means of feedback loops, bringing power and area overheads. Secondly, for applications requiring strict resolutions, such as the oxygen saturation, the extremely low PI imposes a minimum dynamic range at the front-end, which is usually larger than 90 dB in the worst PI conditions. Designing a PPG sensor for a large dynamic range, low noise and low power operations is not an easy task and very often requires some engineering trade-offs. For instance, the dynamic range can be traded versus the power for applications, such as the HR, not requiring a strict resolution or large SNR.

5 Noise and artefacts in PPG sensors

In the previous chapters, we have seen that the PPG technology can provide valuable information about the cardiovascular system. Indeed, a PPG sensor can be used to monitor the HR, the HRV, the oxygen saturation and the blood pressure. Moreover, the PPG technology is intrinsically suitable for wearable sensing, as long as its power consumption is reduced.

Despite the advantages of the PPG, this technique is known to be susceptible to noise and artefacts. It is the objective of this chapter to deepen the noise and artefacts analysis of PPG sensors.

5.1 Noise types

Whatever analogue signal processed by an integrated circuit, it is corrupted by two different noise types: the electronic noise coming from the circuit itself and the noise coming from the environment. The environmental noise may result being quite generic. Indeed, it may refer to both the random disturbances introduced in the circuits by the power lines or the substrate and also to the noise introduced by the light. Despite the importance of those random disturbances, this chapter will focus on the noise introduced by the circuit only.

As described earlier in this manuscript, a PPG sensor is a full opto-electronics system. Indeed, it can be decomposed in two elementary blocks: the optical part, related to the LED and PD, and the electronics part, meaning the readout circuits. As shown in Fig. 5.1, the noise finds its way both on the optical and the analog part. It is then important to identify the main noise sources ultimately limiting the PPG sensor performance. As pointed out in Chapter 4, the power consumption of PPG systems is limited by the LED driving current. However, the LED power can be reduced provided the noise floor of the readout electronics is decreased proportionally to achieve the same SNR.

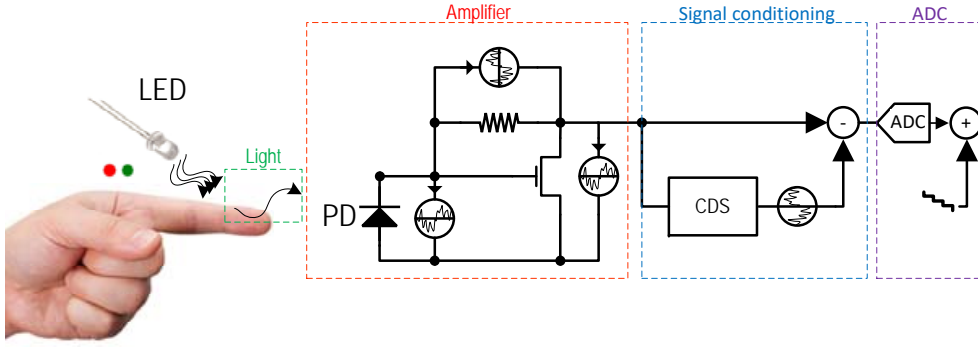


Figure 5.1 – The different noisy elements of a PPG readout chain: the light, the amplifier, the signal conditioning and the ADC.

5.1.1 Thermal noise

The thermal noise is a fundamental phenomenon which is observable in whatever conducting device at absolute positive temperature. The origin of the thermal noise goes back to the fluctuations of the charge carriers velocity in a conductor due to thermal excitation. This noise has usually been microscopically modelled as a carrier ensemble whose exchange energy happens either by collisions or by thermal process, very similarly to an ideal gas. The resulting random electrons' motion, called Brownian motion, in the conducting device gives rise to voltage fluctuations across the conductor itself. In the case of a resistor, this voltage fluctuations can be modelled by a series voltage source whose power-spectral density (PSD) is

$$S_v = 4kTR, \quad (5.1)$$

where k is the Boltzmann constant equal to $1.38 \cdot 10^{-23} J/K$ and T the absolute temperature. The thermal noise of a resistor can also be modelled by a parallel current source with PSD of $4kT/R$. Eq. (5.1) suggests that the thermal noise is frequency independent, so corresponding to a white PSD. Actually, this is true with good approximation up to roughly 100 THz. Since the circuits bandwidth is usually much lower with respect to this intrinsic cut-off frequency, the thermal noise can be considered as a purely white noise.

In the case of MOS transistors, each slice of its channel can be considered to have a local resistance ΔR with a PSD equal to $4kT/\Delta R$. Using the EKV formalism [145] and accounting for the contribution of this current noise source to the total drain current gives rise to the following current PSD

$$S_i = 4kT\gamma G_m, \quad (5.2)$$

where G_m is the MOS gate transconductance and γ the thermal excess noise factor, defined as $G_m R_n$ (R_n is the input referred thermal noise resistance) [145]. For a long-channel transistor γ is equal to $n/2$ and $2n/3$ in weak inversion and strong inversion operations, respectively, where n is the EKV model parameter defining the slope factor. In other words, similarly to a

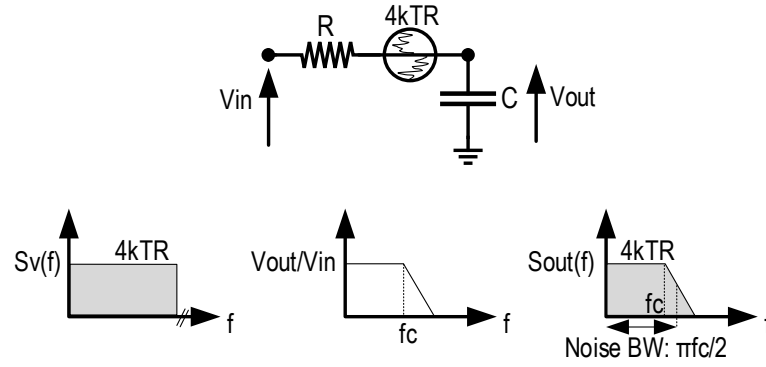


Figure 5.2 – The noise spectrum is shaped by the transfer function. Particularly, in the case of a RC low pass filter, this gives rise to a KT/C output noise power.

resistor, the thermal noise in the case of a MOS transistor can be modelled by a parallel current source whose power-spectral density (PSD) is defined by (5.2).

KT/C noise

The noise spectrum, i.e. PSD, is shaped by the system transfer function, as defined by the Wiener-Kintchine theorem. It is possible to define an equivalent noise bandwidth (ENBW) which defines the maximum PSD frequency extent with regard to the system bandwidth. If the input noise is white, then the ENBW depends on the system transfer function only. So, in this case, the noise power can be defined as

$$\sigma_n^2 = V_n^2 = S_n \cdot ENBW, \quad (5.3)$$

where ENBW is defined as

$$ENBW = (1/H_n^2(0)) \cdot \int_0^\infty |H_n(f)|^2 df. \quad (5.4)$$

In (5.4), $H_n(f)$ is the noise transfer function. The noise transfer functions, for noise calculations, are usually of three types: 1st-order low-pass (LP), 2nd-order LP (with zero) and 2nd-order band-pass (BP)

$$H_n|_{1^{st}}(f) = \frac{1}{1 + \frac{jf}{f_c}} \quad H_n|_{2^{nd}LP}(f) = \frac{1 + \frac{jf}{f_z}}{1 + \frac{jf}{f_0 \cdot Q} + \left(\frac{jf}{f_0}\right)^2}$$

$$H_n|_{2^{nd}BP}(f) = \frac{\frac{jf}{f_0}}{1 + \frac{jf}{f_0 \cdot Q} + \left(\frac{jf}{f_0}\right)^2}, \quad (5.5)$$

for which the ENBW is equal to

$$ENBW|_{1st} = \frac{\pi}{2} f_c \quad ENBW|_{2nd_{LP}} = \frac{\pi}{2} f_0 Q \left[1 + \left(\frac{f_0}{f_z} \right)^2 \right]$$

$$ENBW|_{2nd_{BP}} = \frac{\pi}{2} \frac{f_0}{Q}, \quad (5.6)$$

respectively.

What was stated so far can be applied in the case of an RC low pass filter, as shown in Fig. 5.2. The thermal noise originated by the resistor can be modelled by a series voltage source with a $4kTR$ PSD filtered by the RC circuit. Exploiting the ENBW given by (5.6), the noise variance across the capacitor C can be calculated as

$$\sigma_n^2 = V_n^2 = S_n \cdot ENBW = 4kTR \frac{\pi}{2} f_c = 4kTR \frac{\pi}{2} \frac{1}{2\pi RC} = \frac{kT}{C}. \quad (5.7)$$

(5.7) implies that the output thermal noise power is independent of the value of R. Indeed, for smaller values of R, the ENBW increases while the associated noise per unit bandwidth decreases, so keeping the overall noise power constant. On the contrary, larger capacitors are related to smaller noise power. This introduces some design issues since larger capacitors come with more power consumption and silicon area.

5.1.2 Shot noise

The shot noise is a statistical phenomenon which appears in nature for physical processes resulting from a series of independent random events occurring at any time with the same probability. If we consider a lamp irradiating a given photon flux, Φ , the probability of receiving n photons in the interval $[0, t]$ tends to a Poisson distribution as

$$p_n(t) = \frac{(\Phi t)^n}{n!} \cdot e^{-\Phi t}, \quad (5.8)$$

where Φ is supposed to be constant. The most peculiar property which characterizes the shot noise is the fact that the variance of the number of received particles is equal to the constant average number. In other words, supposing the lamp shining N photons in the interval $[0, t]$, the associated shot noise standard deviation (STD) is equal to \sqrt{N} , meaning that the resulting SNR is equal to \sqrt{N} . The quantized nature of light and charge makes a photon or electron flux obeying this Poisson process. In optical devices, shot noise dominates whenever a large number of particles are detected. In this case, the Poisson distribution approaches a normal distribution about its mean, resulting into the elementary events, e.g. photons or electrons, no longer individually observed. This makes the shot noise in actual observations indistinguishable from the true Gaussian noise.

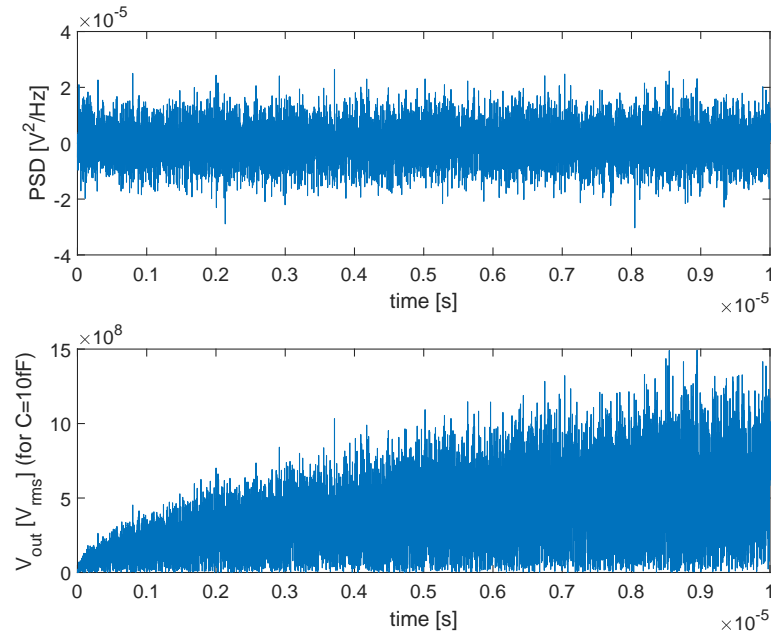


Figure 5.3 – The integration of the white noise over a capacitor gives rise to noise voltage output increasing with the square root of the integration time.

In the case of a p-n junction, as a PD, the shot noise is dependent on the DC current value. Indeed, large photon fluxes result into large electron-hole recombination and consequently larger number of photogenerated electrons. The (current) shot noise PSD is expressed as

$$S_i = 2qI, \quad (5.9)$$

where q is the electrons' charge, equal to $1.6 \cdot 10^{-19} \text{C}$, and I the photogenerated current.

Integrated white noise - Wiener process

The integration of a stationary white (current) noise over a capacitor is usually associated with a Wiener process [146]. This applies to both the thermal and the shot noise, since both can be considered as white noises. As shown in (5.3), supposing to start integrating, at the time t_0 , a white PSD S_i over a capacitor C , the noise power is linearly increasing with the integration time t_{int} as

$$\sigma_n^2 = V_n^2 = \frac{S_i}{C^2} t_{int}. \quad (5.10)$$

5.1.3 Flicker noise

The flicker noise, or $1/f$ noise, is a very important noise source whose exact mechanism is still a matter of debate. Indeed, its origin is still not precisely understood. The most common physical model behind the flicker noise refers to the interface between the gate oxide and the conductive channel in a MOS transistor. Since the silicon crystal reaches an end at this interface, many dangling bonds appear. A dangling bond is usually referred to free radicals, meaning atoms, molecules or ions with unpaired valence electrons and consequently highly chemically reactive. In the oxide-silicon interface, those dangling bonds give rise to extra energy states. This can randomly trap and later release charge carrier moving at the interface, resulting into a device conductance fluctuation introducing flicker noise in the drain current. This model has been introduced by McWhorter [147]. Historically speaking, another model has been introduced by Hooge [148] which, unlike McWhorter, explains the MOS conductance fluctuation as a result of the mobility fluctuation of the free carriers. Although both models have been accepted, a long debate still exist.

What can be surely said about the flicker noise is that, unlike the thermal noise, its average power cannot be predicted that easily. Depending on the MOS manufacturing process and technologies, the flicker noise PSD can assume different order of magnitude. For instance, in some older technologies PMOS devices exhibit less flicker noise than NMOS because the holes flow into a buried channel at a further distance with respect to the oxide-silicon interface. In other words, the probability of conductance fluctuation due to trapping and detrapping is lower.

The flicker noise is also named $1/f$ noise since its PSD decreases with respect to the frequency. This noise can be modelled as a voltage source in series with the gate having a PSD given by

$$S_v(f) = K_F / (C_{ox}^\alpha W L f), \quad (5.11)$$

where K_F is the flicker (technological) noise parameter, C_{ox} the gate oxide capacitance per unit area, α is 1 for the Hooge's model and 2 for the McWhorter's one, and WL the MOS channel area. For a 180 nm process $K_F = 1 \cdot 10^{-27} [\frac{J \cdot F}{m^2}]$ and $C_{ox} = 8.46 \cdot 10^{-3} [\frac{F}{m^2}]$. We should also notice that (5.11) doesn't depend on the bias current. Actually, the PSD is slightly bias dependent, but, to first order, it can be considered as bias independent when referred to the gate.

5.2 Noise analysis in PPG readout chains

In Chapter 4 several possible PPG readout chains, as presented in the state-of-the-art, have been proposed. The readout chain that has been used the most is the one embedding a transimpedance amplifier (TIA), a SH-based CDS block and an ADC. For this reason, the noise analysis of this chapter will be focused on the latter.

It has been mentioned earlier that the power consumption of PPG systems is limited by the

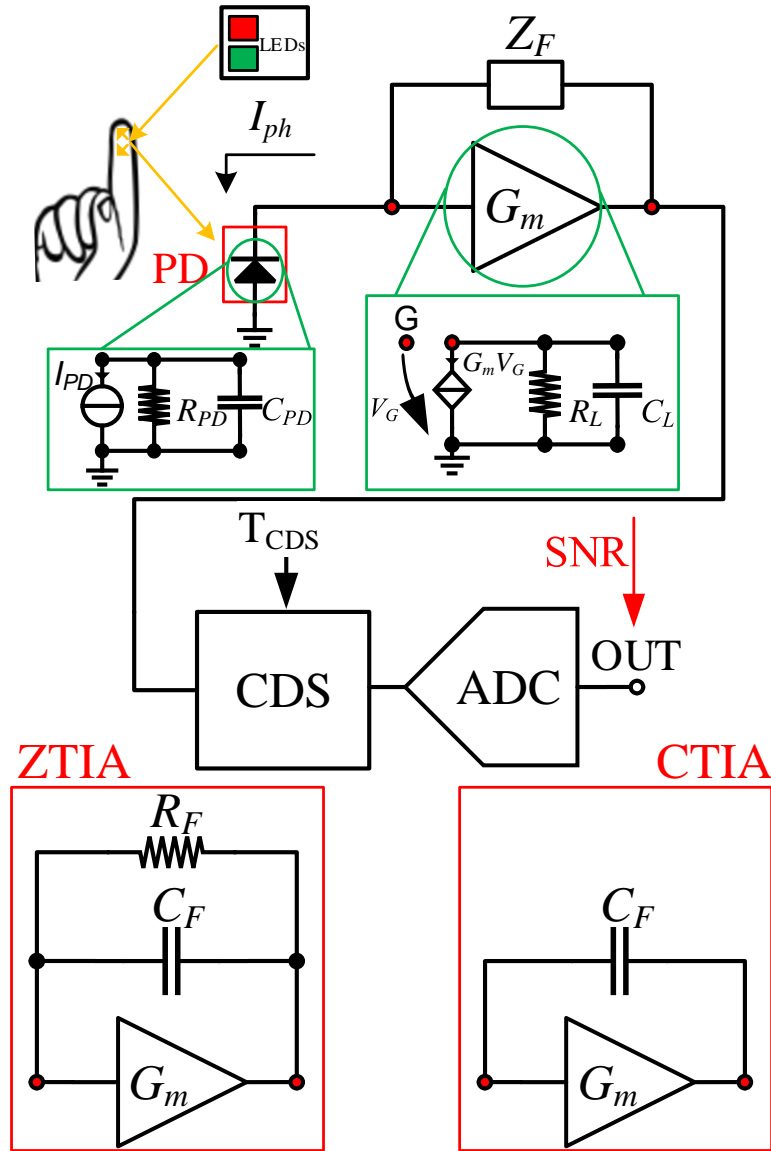


Figure 5.4 – Schematic of a classical PPG readout chain showing the two possible implementations, i.e. ZTIA-based or CTIA-based.

LED driving current. However, the LED power can be reduced provided the noise floor of the front-end electronics is decreased proportionally. In this regards, it is important to define analytically how the noise sources affect the SNR. Indeed, the proposed analysis clarifies, by the means of analytical equations, the impact of the input photocurrent, the PD parasitic capacitance, the feedback impedance and the system bandwidth on the SNR of the a PPG readout, as shown in Fig. 5.4. Several noise sources have been considered including the shot noise associated with the input light and the thermal, flicker and quantization noise of the readout chain. Since, as mentioned in Chapter 4, the TIA is usually proposed either with an RC feedback (ZTIA) or a purely capacitive one (CTIA), the noise analysis has been independently

carried out for both.

With respect to Fig. 5.4, the PD shunt resistance, R_{PD} , can be usually neglected since typically large enough to be considered as an open circuit. The overall noise variances contributions has been evaluated at the output of the ADC and eventually used to compare the two proposed structures in terms of SNR vs photogenerated current, I_{ph} . Moreover, the comparison highlights the trade-off between the SNR and the power consumption. Note that I_{ph} is roughly linearly proportional to the LED current, i.e. LED power, through a constant representing the tissue attenuation, whose values range from 10^{-3} to 10^{-4} , [117]. The TIA has been modelled as an operational transconductance-amplifier (OTA).

As already mentioned in Chapter 4, the PD also absorbs ambient light photons whose associated photocurrent has to be compensated in the readout chain. The simplest and usual way to do it is to perform CDS. As mentioned earlier in this manuscript, typical CDS is performed by the means of SH stage and the CDS has an important impact on the noise. Indeed, it cancels the offset, e.g. the ambient light, and dramatically reduces low frequency noise, such as the flicker noise. The CDS transfer function can be expressed as

$$|H_{CDS}(f)|^2 = 4 \sin^2(\pi T_{CDS} f), \quad (5.12)$$

[150], where T_{CDS} is the time between two consecutive CDS samples [149, 150]. For a generic noise source, having a PSD $S_n(f)$, its corresponding noise variance, accounting for the effect of CDS, is equal to

$$\sigma_n^2 = \int_0^\infty S_n(f) \cdot |H_n(f)|^2 \cdot |H_{CDS}(f)|^2 df, \quad (5.13)$$

where $H_n(f)$ and $H_{CDS}(f)$ are the noise transfer function and the CDS transfer function, given in (5.12), respectively. It has been shown in [150] that the CDS has no impact on the noise variance.

5.2.1 ZTIA

Shot noise

Since the shot noise current appears in parallel to the photocurrent source, the noise transresistance is identical to the signal transresistance

$$H_{n,shZTIA}(f) = R_F \cdot \frac{1 - jf/f_{z_{sh}}}{(1 + jf/f_{p1})(1 + jf/f_{p2})}, \quad (5.14)$$

where $f_{p1} = \frac{G_m}{2\pi(C_{PD} + C_F G_m R_F)}$, $f_{p2} = \frac{(C_{PD} + C_F G_m R_F)}{2\pi C_F C_{PD} R_F}$ and $f_{z_{sh}} = \frac{G_m}{2\pi C_F}$. For noise calculations the noise transresistance (5.14) can be approximated by a first order response, whose cut-off frequency is f_{p1} . Indeed, in practical cases $f_{p1} \ll f_{p2} \ll f_{z_{sh}}$. Using (5.13), the shot noise

variance for the ZTIA case becomes

$$\sigma_{sh_{ZTIA}}^2 \cong \alpha_{sh_{ZTIA}} \cdot 2qI_{ph} \cdot ENBW_{n,sh_{ZTIA}} \cdot R_F^2, \quad (5.15)$$

where $ENBW_n$ is, for the ZTIA shot noise case, approximately equal to

$$ENBW_{n,sh_{ZTIA}} \cong \frac{\pi}{2} f_{p1} \quad (5.16)$$

and $\alpha_{sh_{ZTIA}}$ is an unit-less circuit design parameter, accounting for the effect of CDS, given by

$$\alpha_{sh_{ZTIA}} = \frac{1}{ENBW_{n,sh_{ZTIA}}} \int_0^\infty \frac{4 \sin^2(\pi T_{ON} f)}{1 + (f/f_{p1})^2} df \cong 2. \quad (5.17)$$

This integral has been numerically calculated and is simply equal to 2, when $2\pi T_{ON} f_{p1} > 5$ (which is the condition for sufficient settling of the signal) [150]. Indeed, the shot noise behaves as a white noise. Hence, the CDS corresponds to the differentiation of two uncorrelated noise samples, which results in doubling the noise variance.

Thermal noise

Two thermal noise contributions should be taken into account: the one related to the MOS channel and the one coming from the feedback resistance, R_F . Nevertheless, the noise variance related to the channel dominates over the feedback resistance's, which means that the latter will be neglected. For the channel thermal noise the corresponding noise transresistance is

$$H_{n,th_{ZTIA}}(f) = \frac{1}{G_m} \cdot \frac{1 + jf/f_{z_{th}}}{(1 + jf/f_{p1})(1 + jf/f_{p2})}, \quad (5.18)$$

where $f_{z_{th}} = \frac{1}{2\pi R_F(C_F + C_{PD})}$. From (5.13), the channel thermal noise variance for the ZTIA case becomes

$$\sigma_{th_{ZTIA}}^2 \cong \alpha_{th_{ZTIA}} \cdot \frac{4kT\gamma}{G_m} \cdot ENBW_{n,th_{ZTIA}}, \quad (5.19)$$

where $\alpha_{th_{ZTIA}}$ is

$$\alpha_{th_{ZTIA}} = \frac{1}{ENBW_{n,th_{ZTIA}}} \int_0^\infty \frac{4 \sin^2(\pi T_{ON} f) \left[1 + \left(\frac{f}{f_{z_{th}}} \right)^2 \right]}{\left[1 + \left(\frac{f}{f_{p1}} \right)^2 \right] \left[1 + \left(\frac{f}{f_{p2}} \right)^2 \right]} df \cong 2 \quad (5.20)$$

and $ENBW_{n,th_{ZTIA}}$ is

$$ENBW_{n,th_{ZTIA}} \cong \frac{\pi}{2} f_{p2} \cdot \frac{(C_{PD} + C_F)^2 (G_m R_F)^2}{(C_{PD} + C_F G_m R_F)^2}, \quad (5.21)$$

considering $f_{z_{th}} \ll f_{p1} \ll f_{p2}$.

So far we have shown that, no matter the PSD source, the CDS simply doubles the thermal noise variance. This result is expected since, as far as the thermal noise is concerned, the CDS subtracts two samples which are uncorrelated. We will see that the same considerations apply to the CTIA case.

Flicker noise

Regarding the ZTIA circuit, the flicker noise transresistance is the same than the channel thermal noise, (5.18). Using (5.13), the flicker noise variance for the ZTIA case becomes

$$\sigma_{1/f_{ZTIA}}^2 \cong \alpha_{1/f_{ZTIA}} K_F / (C_{ox}^2 WL), \quad (5.22)$$

where $\alpha_{1/f_{ZTIA}}$ is

$$\alpha_{1/f_{ZTIA}} = \int_0^\infty \frac{1}{f} \frac{4 \sin^2(\pi T_{ON} f) \left[1 + \left(\frac{f}{f_{z_{th}}} \right)^2 \right]}{\left[1 + \left(\frac{f}{f_{p1}} \right)^2 \right] \left[1 + \left(\frac{f}{f_{p2}} \right)^2 \right]} df \cong 4.5, \quad (5.23)$$

under the assumption of $f_{z_{th}} \ll f_{p1} \ll f_{p2}$. $\alpha_{1/f_{ZTIA}}$ is the CDS parameter, increasing (logarithmically) with the ratio between T_{CDS} and the signal settling-time. Assuming that T_{CDS} is roughly equal to the settling time, $\alpha_{1/f_{ZTIA}}$ is, as shown by (5.23), approximately equal to 4.5.

Quantization noise

The variance due to the quantization process in the ADC is given by

$$\sigma_{ADC}^2 = \Delta^2 / 12, \quad (5.24)$$

where, in (5.24), Δ is the quantization step (assuming uniform quantization) which depends on the reference voltage V_{ref} and the resolution N_{bit} and typically ranges from $50 \mu V_{rms}$ to $150 \mu V_{rms}$ [151].

5.2.2 CTIA

Shot noise

Unlike the ZTIA case, in the case of the CTIA, the PSD of the shot noise gets fully integrated by the feedback capacitance, C_F . The shot noise transresistance of the CTIA is

$$H_{n,sh_{CTIA}}(f) = \frac{1}{j2\pi f C_F} \frac{1 - jf/f_{z_{sh}}}{1 + jf/f_p}, \quad (5.25)$$

where f_{zsh} and f_p are the zero and the pole (signal BW), respectively, related to the shot noise transresistance. For noise calculations the transresistance in (5.25) can be approximated by a first order response, whose cut-off frequency is given by

$$f_p = G_m / 2\pi C_{PD}. \quad (5.26)$$

Using (5.13), the shot noise variance for the CTIA case becomes

$$\sigma_{sh_{CTIA}}^2 \cong \alpha_{sh_{CTIA}} \cdot 2qI_{ph}T_{ON} \cdot \frac{1}{C_F^2}, \quad (5.27)$$

where $\alpha_{sh_{CTIA}}$ is

$$\alpha_{sh_{CTIA}} = \frac{1}{T_{ON}} \int_0^\infty \frac{1}{(2\pi f)^2} \cdot \frac{4 \sin^2(\pi T_{ON} f)}{1 + \left(\frac{f}{f_p}\right)^2} df \cong \frac{1}{2}. \quad (5.28)$$

This integral has been numerically calculated and is simply equal to 1/2, when $2\pi T_{ON} f_p > 5$. Thus, the shot noise for the CTIA case corresponds to a Wiener process for which the variance increases linearly with T_{ON} [146], as shown in (5.27).

Thermal noise

Regarding the CTIA based circuit, the only thermal noise contribution is the one related to the transconductor, whose transresistance is

$$H_{n,th_{CTIA}}(f) = \frac{1}{G_m} \cdot \frac{C_{PD} + C_F}{C_F} \cdot \frac{1}{1 + jf/f_p}, \quad (5.29)$$

where f_p is the pole (signal BW) related to the channel thermal noise transresistance. Using (5.13), the thermal noise variance for the CTIA case becomes

$$\sigma_{th_{CTIA}}^2 \cong \alpha_{th_{CTIA}} \cdot \frac{4kT\gamma}{G_m} \cdot ENBW_{n,th_{CTIA}}, \quad (5.30)$$

where $\alpha_{th_{CTIA}} \cong 2$ (same calculation as in $\alpha_{sh_{ZTIA}}$) and $ENBW_{n,th_{CTIA}}$ is

$$ENBW_{n,th_{CTIA}} = \frac{\pi}{2} f_p \cdot \left(\frac{C_{PD} + C_F}{C_F} \right)^2. \quad (5.31)$$

Flicker noise

As for the ZTIA case the 1/f noise shares the same transresistance than the transconductor thermal noise, (5.29). The flicker noise variance for the CTIA is given by

$$\sigma_{1/f_{CTIA}}^2 \cong \alpha_{1/f_{CTIA}} \frac{K_F}{C_{ox}^2 WL} \left(\frac{C_{PD} + C_F}{C_F} \right)^2, \quad (5.32)$$

where $\alpha_{1/f_{CTIA}}$ is

$$\alpha_{1/f_{CTIA}} = \int_0^\infty \frac{1}{f} \cdot \frac{4 \sin^2(\pi T_{ON} f)}{1 + \left(\frac{f}{f_p}\right)^2} df \cong 4.5. \quad (5.33)$$

Quantization noise

The quantization noise analysis of the CTIA is the same as in the ZTIA case.

5.2.3 ZTIA and CTIA comparison

This section compares the two readout structures, i.e. ZTIA and CTIA, in terms of noise and power trade-off. Specifically, the comparison is driven with respect to the minimum SNR value to ensure an accuracy within 2% of the $S_p O_2$. As shown in [117], this value is equal to 28.5 dB.

The SNR at the output of the ADC can be expressed as

$$SNR = 10 \log_{10} \frac{S^2}{N^2} = 10 \log_{10} \frac{V_{out}^2}{\sigma_{sh}^2 + \sigma_{th}^2 + \sigma_{1/f}^2 + \sigma_{ADC}^2}. \quad (5.34)$$

The ZTIA and CTIA readout chains are compared assuming the same signal bandwidth

$$f_p = f_{p1} = BW = \frac{1}{2\pi\tau}. \quad (5.35)$$

In the case of the ZTIA, the output voltage is given by

$$V_{out} = PI \cdot R_F \cdot I_{ph}, \quad (5.36)$$

where PI is the perfusion index, i.e. $\frac{AC}{DC}$, as introduced in Chapter 2. In this comparison PI has been considered equal to 0.2% in order to account for the worst case (perfusion) condition. The output voltage in the CTIA case is given by

$$V_{out} = PI \cdot T_{ON} \cdot I_{ph} / C_F, \quad (5.37)$$

where T_{ON} is the ON-time of the LED (LED time duration).

Fig. 5.5 shows the SNR of both circuit topologies as function of the average input photocurrent, i.e. LED power, for different PD parasitic capacitances, pointing out the shot noise and the electronic read noise limited regions. The analysis has been performed based on the parameters given in Tab. 5.1 (these parameters are related to $C_{PD} = 100$ pF). Assuming full shot noise limitation, i.e. large I_{ph} condition, the ratio between the two SNR is

$$\frac{SNR_{CTIA}}{SNR_{ZTIA}} \cong 2\pi \cdot BW \cdot T_{ON} = \frac{T_{ON}}{\tau}. \quad (5.38)$$

$2\pi \cdot BW \cdot T_{ON}$ must be much larger than 1 to ensure enough signal settling. The condition to ensure efficient signal settling is $2\pi \cdot BW \cdot T_{ON} \cong 10$. This means that the SNR of the CTIA based configuration is at least 10 times better than the ZTIA based one. Indeed, Fig. 5.5 shows exactly 10 dB difference between the two cases in the shot noise dominated region.

Assuming the same signal bandwidth between the two compared structures, a ZTIA-based readout chain comes with both larger LED power(8 times more) and a larger Gm , compared to a CTIA-based one. This advantage is attributed to the integration feature of the CTIA. Indeed, the CTIA comes intrinsically with a larger bandwidth than the ZTIA. Comparing the two for the same bandwidth means, in other words, having a larger signal gain for the CTIA than the ZTIA. Moreover the ZTIA shows a larger read noise than the CTIA, which is, on the contrary, intrinsically more shot noise limited. A ZTIA solution should be preferred only when low gain operations are needed. Indeed, the CTIA gain being inversely proportional to the feedback capacitance, this results into a large silicon area for low gain operations. It should also be noticed that for the target SNR, both solutions show still an important electronic read noise level, calling for further design optimizations.

Analogies with other works

Other works have tried to compare the ZTIA-based readout chain versus the CTIA-based one. For instance, the work in [46] has compared them in terms of the achievable dynamic range for a given power. In particular, the limitations introduced by the ZTIA settling time should tip the balance in favour of the CTIA, unless incomplete settling operations are envisaged. In this case, the introduced gain loss corresponds to a proportional increase in the amplifier noise and consequently a dynamic range drop. The work in [130] has also shown that the integration of the photocurrent reduces both the effect of the wideband noise and the necessary bandwidth, similarly to what is presented in this work.

Table 5.1 – Design Parameters

Parameter	Value	Parameter	Value
$G_{m_{CTIA}}$	$10 \mu S$	T_{ON}	$100 \mu s$
$G_{m_{ZTIA}}$	$100 \mu S$	R_L	$100 M\Omega$
R_F	$1 M\Omega$	W	$5 \mu m$
C_F	$9 pF$	L	$2 \mu m$
C_L	$1 pF$	Δ	$100 \mu V_{RMS}$
C_{ox}	$8.46 fF/\mu m^2$	K_F	$10^{-27} C^2$

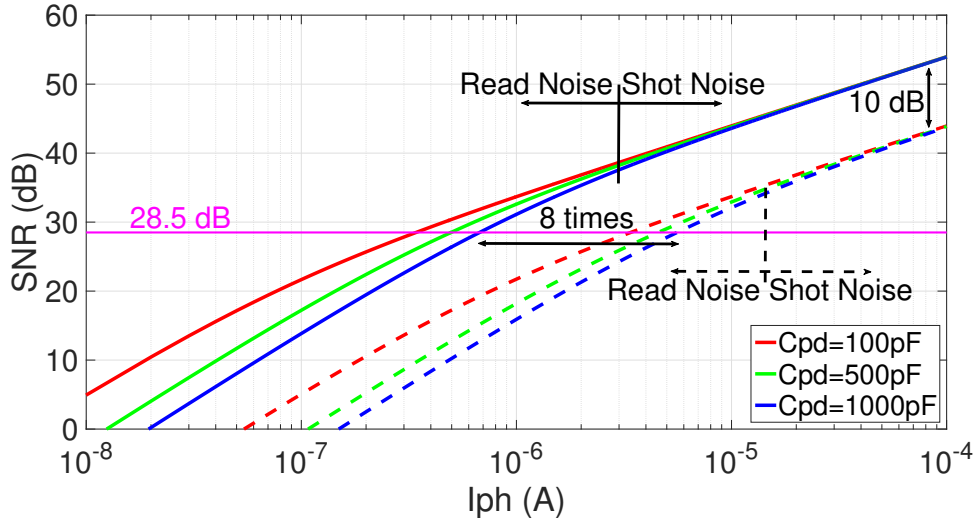


Figure 5.5 – SNR of both CTIA (solid line) and ZTIA (dashed line) based design versus the input photocurrent, for three different PD parasitic capacitance values.

5.2.4 Correlated double sampling: a kTC analysis

Despite CDS circuits reduce dramatically the low frequency noise, they remain limited by circuit non-idealities. Indeed, CDS circuits are mainly limited by analog switches non-idealities (on and off resistances), charge injection and thermal noise, the latter usually referred to as kTC noise, as shown in section 5.1.1. The sampled noise voltage variance (kT/C) is, by definition, inversely proportional to the capacitance. On the contrary, both power and silicon area are directly proportional to the capacitance, resulting into a noise/power-area trade-off. From a design perspective, it is necessary to be fully aware of the capacitances ultimately limiting the circuit performance. kTC noise analysis of SC circuits is never a simple task, considering that the noise transfer function, for these circuits, changes in time. Modern CAD simulators are useful in the estimation of the overall noise features, despite they require a very high accuracy set-up, resulting into extremely long simulations. Moreover, they don't provide simple analytical expressions to optimize the SC circuit noise.

In this perspective, this section aims at presenting a simple and comprehensive kTC noise analysis of three different CDS circuits: a fully passive CDS, a voltage buffer-based CDS and an amplifier-based CDS. The three proposed CDS circuits are depicted in Fig. 5.6.

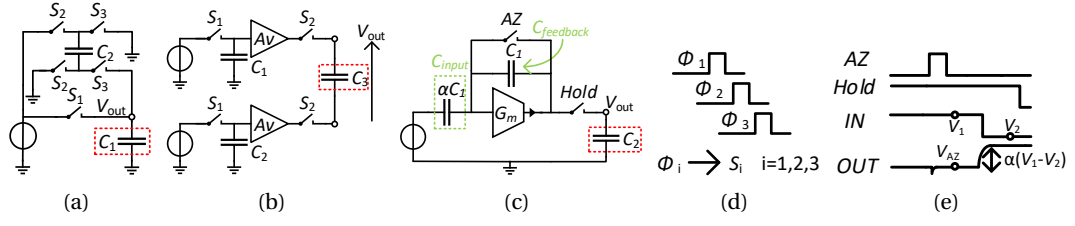


Figure 5.6 – Schematic of the three proposed CDS circuits with the timing diagrams: (a) fully-passive CDS, (b) voltage buffer-based CDS, (c) amplifier-based CDS, (d) timing diagram for (a) and (b), (e) timing diagram for (c).

Fully-passive CDS

The circuit of Fig. 5.6a embeds passive elements only. Referring to the timing diagram shown in Fig. 5.6d, during phase Φ_1 , all switches are open except switch S_1 which is closed. Then a generic input signal voltage, V_1 , is first sampled on the capacitor C_1 when switch S_1 opens, which means at the end of phase ϕ_1 . During phase ϕ_2 , the switches S_2 close and, at the end of phase ϕ_2 , a second input signal voltage, V_2 , is sampled on the capacitor C_2 . During the third phase ϕ_3 , the switches S_3 close, connecting C_1 and C_2 in parallel. The charge conservation principle applied at the output node leads to an output voltage equal to

$$V_{out} = \frac{V_1 C_1 - V_2 C_2}{C_1 + C_2} = \frac{V_1 - V_2}{2}, \quad (5.39)$$

assuming that $C_1 = C_2$. Eq. (5.39) results into a CDS action, with a loss equal to two. From now on, we will refer to the fully passive CDS of Fig. 5.6a as CDS_1 .

Due to the thermal noise originating from the on-resistance of the switches, two uncorrelated kTC noise charge are injected in the switched capacitors C_1 and C_2 at the end of phase ϕ_1 and ϕ_2 , respectively. In both phases ϕ_1 and ϕ_2 , the on-resistor, R_{on} , of the switches and the capacitor form a RC low-pass filter. Applying (5.13), (5.5), (5.6) to this case and considering $S_n = 4kTR_{on}$ results into noise voltage variances across C_1 and C_2 equal to

$$V_{nC_1}^2|_{\phi_1} = \frac{kT}{C_1} \quad V_{nC_2}^2|_{\phi_2} = \frac{kT}{C_2}. \quad (5.40)$$

During the third phase ϕ_3 the two capacitors share both their signal and uncorrelated noise charge, resulting into a noise voltage variance at the output node equal to

$$V_{out}^2|_{\phi_3} = \frac{(C_1^2 kT/C_1 + C_2^2 kT/C_2)}{(C_1 + C_2)^2}. \quad (5.41)$$

At the end of phase ϕ_3 , due to the switch S_3 , an additional kTC noise charge, uncorrelated with the one generated in the previous phases, is injected in C_1 and C_2 resulting into an overall

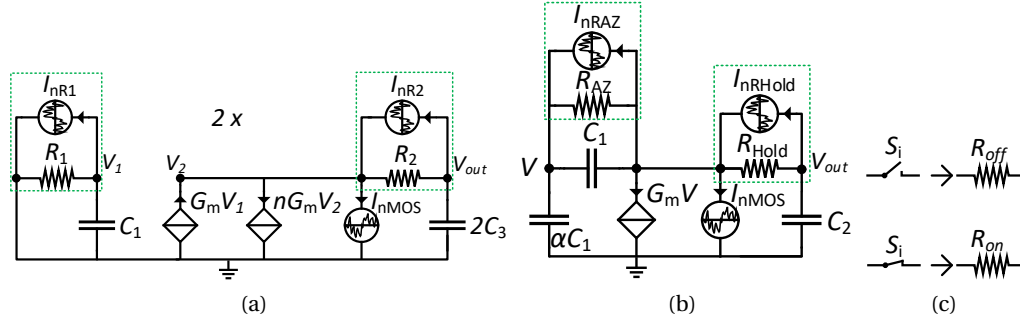


Figure 5.7 – Noise small signal schematic of CDS2 and CDS3: (a) CDS2, (b) CDS3, (c) switch equivalent model.

output voltage variance equal to

$$V_{n_{out}}^2 = \underbrace{\frac{(C_1^2 kT/C_1 + C_2^2 kT/C_2)}{(C_1 + C_2)^2}}_{\text{shared noise from } \phi_1, \phi_2} + \underbrace{\frac{kT}{C_1} \frac{C_2}{C_1 + C_2}}_{\text{added noise from } \phi_3} = \frac{kT}{C_1}. \quad (5.42)$$

If we consider the typical case where all the capacitances are equal to C , then the total voltage variance results equal to kT/C .

Voltage-buffered based CDS

The circuit depicted in Fig. 5.6b consists of a voltage buffer-based CDS. Referring to the timing diagram shown in Fig. 5.6d, two independent input signals V_1 and V_2 are sampled on C_1 and C_2 , respectively, during phase ϕ_1 . In the next phase ϕ_2 the charge previously stored in C_1 and C_2 is transferred, through the two voltage buffer of gain A_v , to the output capacitor C_3 . At the end of this phase, the voltage across C_3 is

$$V_{out} = A_v (V_1 - V_2). \quad (5.43)$$

Referring to (5.43), A_v is the gain of the voltage buffer. In case of source follower stages, featuring body effect, $A_v = 1/n$, where n is the slope factor (larger than one), accounting for the body effect in MOS transistors, [145]. A_v takes values closer to one for source to bulk connected devices. As in the previous case, (5.43) represents a CDS, with a loss accounting for the source follower non-idealities, i.e. $n > 1$. From now on, we will refer to the CDS of Fig. 5.6b as CDS_2 .

Under the assumption that $C_1 = C_2$ and exploiting the fully-differential structure, the small signal schematic of CDS_2 , from a noise perspective, simplifies to the half circuit shown in Fig. 5.7a. The total output noise voltage variance of the circuit of Fig. 5.6b is then simply equal to twice the output voltage variance of Fig. 5.7a. With reference to the small signal schematic, three noise sources have to be accounted for: the on and off resistances of the two switches,

S_1 and S_2 , and the saturated MOS transistor in the source-follower. The noise coming from the off-resistor R_{off} can be neglected as long as the corresponding time constant is much larger than the fraction of the period over which it is integrated (typically 1/3). As shown above, the thermal noise (current) PSD of the transconductor is $4kT\gamma G_m$. Referring to Fig. 5.7a, the voltage-controlled current source $nG_m V_2$ accounts for the additional transconductance due to the body effect [145]. During phase ϕ_1 , R_1 is equal to the on-resistor, R_{on} , while R_2 is equal to the off-resistor, R_{off} . Evaluating the noise transfer functions related to the noise sources I_{nMOS} , I_{nR1} and I_{nR2} and applying (5.13), (5.5), (5.6) leads to (considering the differential structure)

$$V_{nC_1}^2|_{\phi_1} \cong \underbrace{\frac{2kT}{C_1}}_{S_1 R_{on}}. \quad (5.44)$$

Repeating the same procedure during phase ϕ_2 and exploiting again the differential structure results into a voltage variance on C_3

$$V_{nC_3}^2|_{\phi_2} \cong \underbrace{\frac{\gamma kT}{nC_3} \left(\frac{1}{1 + nG_m R_{on}} \right)}_{\text{MOS channel}} + \underbrace{\frac{kT}{C_3} \left(\frac{nG_m R_{on}}{1 + nG_m R_{on}} \right)}_{S_2 R_{on}}. \quad (5.45)$$

In this case, R_1 is equal to the off-resistor, R_{off} , while R_2 is equal to the on-resistor, R_{on} . C_3 accounts for any additional parasitic capacitance too, despite these have been initially neglected. Eventually, assuming that the noise on C_1 in ϕ_1 and on C_2 in ϕ_2 are uncorrelated, and that $G_m R_{on} \cong 0$, the overall kTC variance on the output capacitor C_3 is

$$V_{n_{out}}^2 = A_v^2 V_{nC_1}^2|_{\phi_1} + V_{nC_3}^2|_{\phi_2} \cong \frac{2kT}{C_1} + \frac{\gamma kT}{nC_3}. \quad (5.46)$$

Amplifier based CDS

Fig. 5.6c shows an amplifier-based CDS. Referring to the timing diagram of Fig. 5.6e, the amplifier (transconductor) is first autozeroed. This phase, i.e. *AZ*, reduces the low frequency noise and the offset of the amplifier [132] and resets the feedback capacitor C_1 . After this phase, in the scenario that the input signal, to the amplifier, toggles between the level V_1 and the level V_2 , the amplifier output variation, i.e. ΔV_{out} , results in

$$\Delta V_{out} = \alpha (V_1 - V_2), \quad (5.47)$$

where $\alpha \cong -C_{input}/C_{feedback}$ is the closed-loop gain assuming the OTA DC gain much larger than one. As in CDS_1 and CDS_2 , (5.47) shows the CDS operation on the input signal levels. From now on, we will refer to CDS of Fig. 5.6c as CDS_3 .

As far as the thermal noise analysis is concerned, this stage operates in two phases, namely, the *AZ* phase and the amplification phase, during which the amplifier provides a closed-

loop gain α . In both phases, the overall kTC noise at the output of CDS_3 consists of two terms, both caused by the AZ and Hold switch resistance and the OTA. First, the overall noise generated during the AZ phase which is frozen in αC_1 and eventually transferred to the feedback capacitor during the Amp phase. Secondly, the one generated during the amplification phase. Both noise variances add to the output, contributing to the overall kTC output thermal noise variance. Note that the frozen noise generated during the AZ phase could be cancelled by a second CDS stage. The noise sampled on αC_1 at the end of the AZ phase can be calculated from the schematic shown in Fig. 5.7b. In this case, R_{AZ} and R_{Hold} represent the on-resistor, R_{on} , of the switch AZ and Hold, respectively. Evaluating the noise transfer functions related to the noise sources I_{nMOS} , I_{nRAZ} and I_{nRHold} and applying (5.13), (5.5), (5.6) leads to

$$V_{n\alpha C_1|AZ}^2 \cong \underbrace{\frac{\gamma kT}{\alpha C_1 + C_2}}_{\text{transconductor}} + \underbrace{\frac{kT}{\alpha C_1} \frac{C_2}{\alpha C_1 + C_2}}_{\text{Hold } R_{on}}. \quad (5.48)$$

Referring to (5.48), it can be shown that the noise contribution of R_{AZ} is negligible with respect to the R_{Hold} one. Repeating the same procedure during the Amp phase results in

$$V_{nC_2|Amp}^2 \cong \underbrace{\frac{\gamma kT (1 + \alpha)^2}{\alpha C_1 + C_2 (1 + \alpha)}}_{\text{transconductor}} + \underbrace{\frac{kT}{C_2} \frac{\alpha C_1}{\alpha C_1 + C_2 (1 + \alpha)}}_{\text{Hold } R_{on}}. \quad (5.49)$$

In this case, R_{AZ} represents the off-resistor, R_{off} , of the switch AZ, whilst R_{Hold} the on-resistor, R_{on} . As in CDS2, the off-resistor contribution can be neglected. Assuming that the noise given by (5.48), (5.49) are uncorrelated, the overall kTC variance at the output capacitor C_2 is then given by

$$V_{nout}^2 \cong \alpha^2 V_{n\alpha C_1|AZ}^2 + V_{nC_2|Amp}^2. \quad (5.50)$$

As mentioned above, at the end of the AZ phase, the noise variance (5.48) gets frozen in the input capacitor, αC_1 , and simply added, multiplied by the square of the closed-loop gain, to the one generated in the next phase. In the above analysis, the parasitic capacitors are neglected. Note that the expression of the total output noise variance given by (5.50) includes the effect of the switches on-resistance which is usually neglected in the literature.

The work presented in [152], whose full text is reported in appendix A, reports the same results as the one proposed above for the amplifier based CDS. [152] proposes a simple method for estimating the thermal noise voltage variance at any port of passive and active circuit made of OTA with capacitive feedbacks, like the amplifier based CDS. The proposed method is based on the Bode theorem [153] and allows the calculation of the thermal noise voltage variance across any capacitor of a passive RC network by simple inspection of several equivalent schematics made of capacitors only. This avoids the evaluation of complex transfer functions and cumbersome integrals.

Simulation results

In order to confirm the analytical noise calculations presented above for the three CDS structures, we have performed noise simulations. All the presented CDS circuits have been simulated by using SpectreRF Noise and Transient Noise simulations and Eldo Transient Noise simulations. SpectreRF Noise performs AC small-signal analysis, deriving the noise transfer functions, for all the noisy elements, and eventually integrating the result (multiplied by the PSD, as in (5.13)) over the chosen frequency span. This is the same approach as reported in the above analysis. Indeed, all the equations reported above have been validated, for each phase, by the means of SpectreRF Noise simulations. On the contrary, both Eldo and SpectreRF Transient Noise simulations model each noise source as a sum of sinusoids over the frequency range of interest, with random phase, and with amplitude equal to the given noise PSD [154]. Transient noise simulations become particularly useful when the noise is large or the circuit highly nonlinear. Moreover, these simulations are the best ones to assess how the noise evolves in time, which means in the most realistic condition. All the capacitors and switches of the circuits meet the condition $f_{th,max} \gg 1/(2\pi R_{on}C)$, where $f_{th,max}$ is a simulation parameter setting the maximum noise frequency. The simulations are performed on a circuit where the OTA is modelled by a simple VCCS and the switches are modelled by an ideal switch in series with a noisy resistor of resistance $R_{on} = 50k\Omega$. The simulation results, for the three CDS circuits, are shown in Figs. 5.8 to 5.10: both SpectreRF and Eldo show an excellent match with respect the calculated noise. Particularly, for CDS3, Fig. 5.10 shows the effect of neglecting the switches on-resistance in the final computation. Their contribution is particularly important for low α or low γ . In most practical cases where $\alpha > 2$ or $\gamma > 2$, then the switches on-resistance becomes negligible with respect to the transconductor.

The noise is reported referred to the input (output noise rms divided by the gain). The simulations are performed with $f_{th,max} = 8\text{ GHz}$, 100 noise simulations, $T = 300\text{ K}$, $\gamma = 1.5$, $n = 1.2$ and $G_m = 20\text{ }\mu\text{S}$.

Table 5.2 – Simulation parameters

Parameter	Value	Parameter	Value
γ	0.9	R_{on}	50 k Ω
G_m	20 μS	$f_{th,max}$	8 GHz

Discussion

The fully passive features of CDS1 make it particularly suitable for ultra-low power applications, despite the SNR is affected by the intrinsic signal loss due to the charge sharing mechanism. Moreover, it is not affected by any signal saturation, the latter usually due to active elements. One of the main advantages of this implementation is that the SNR can be improved without limiting the input signal range and only at the cost of more silicon area (larger capacitors). On

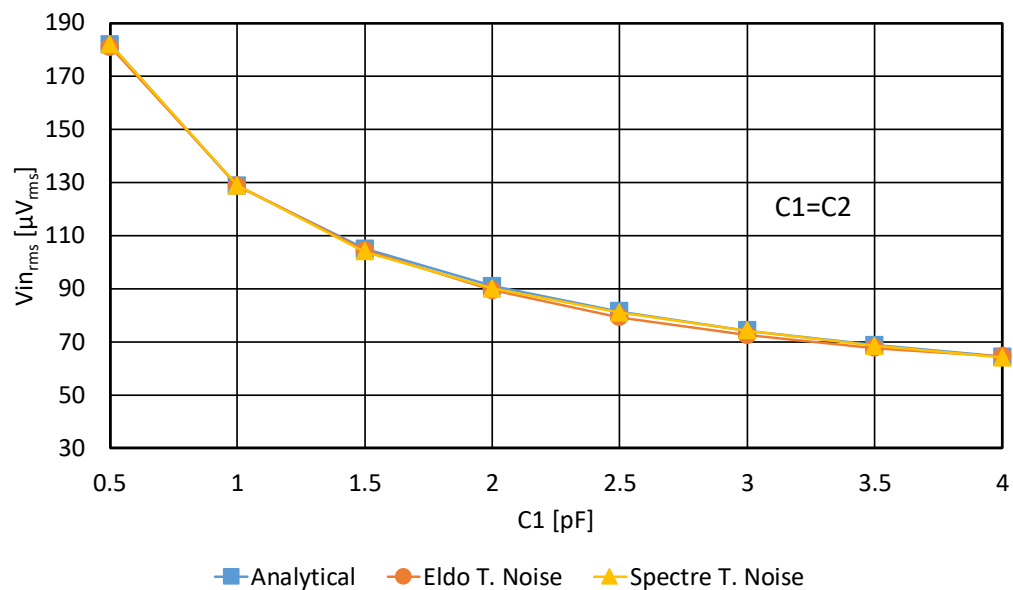


Figure 5.8 – Simulated and calculated RMS noise vs C_1 for CDS1.

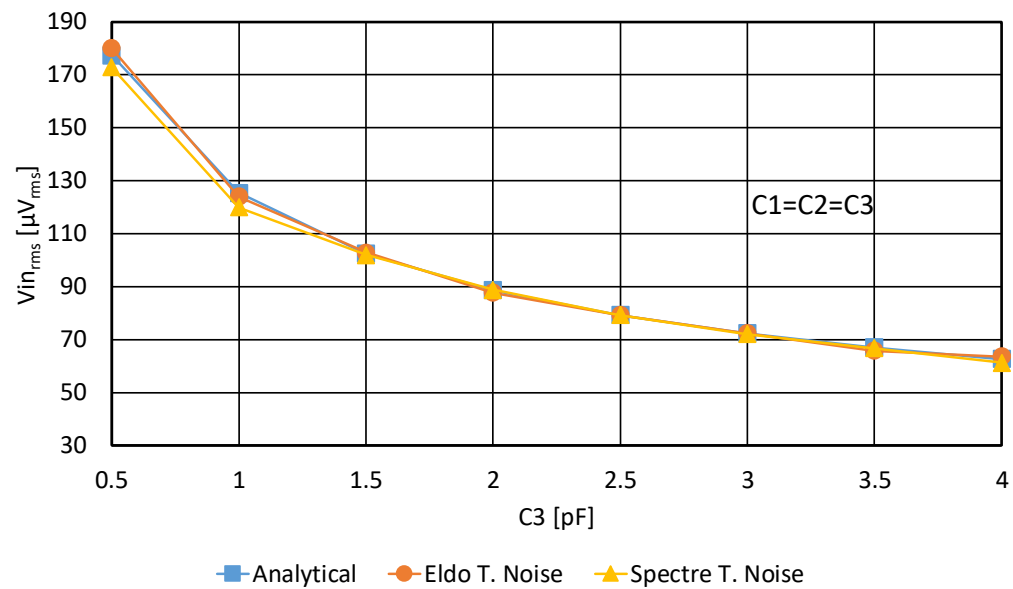


Figure 5.9 – Simulated and calculated RMS noise vs C_3 for CDS2.

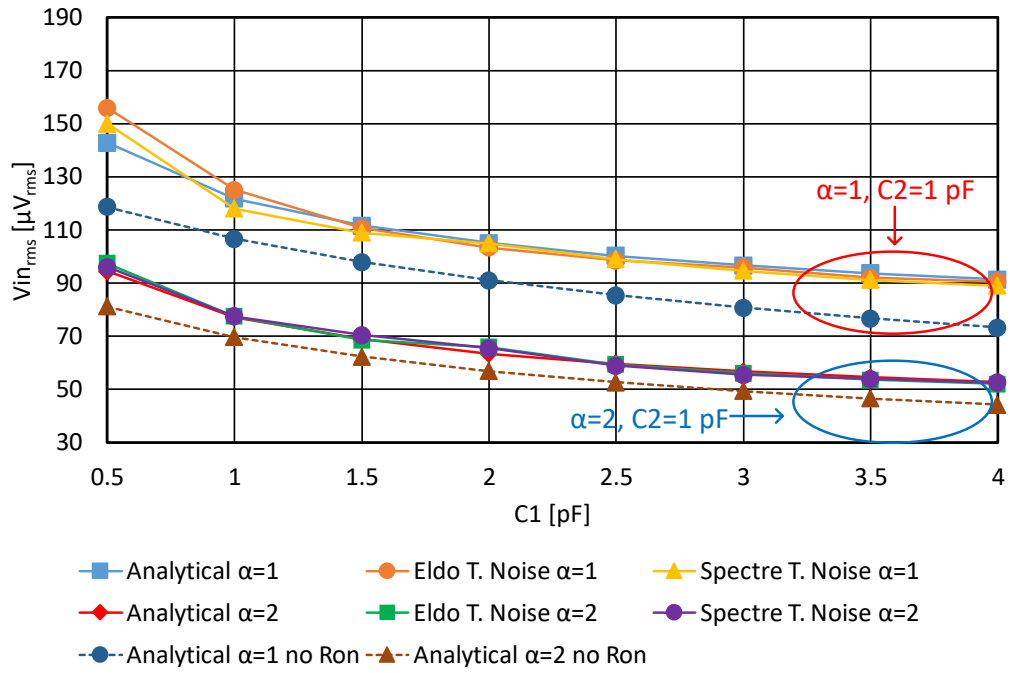


Figure 5.10 – Simulated and calculated RMS noise vs C_1 for CDS3.

the contrary, the amplifier-based CDS3 features an input-referred noise inversely proportional to the gain which depends directly on the size of the input capacitor. Hence, a lower noise is obtained at the cost of a lower input range, larger silicon area and power consumption. The advantage of CDS1 over CDS3 becomes even more obvious for values of γ larger than two. CDS3 remains a good solution for combining amplification with CDS. The voltage buffer-based CDS2 shows roughly the same noise performance than CDS1 at the cost of more power, area and non-linearity.

In addition, the presented analysis highlights the impact of switches on-resistance which are usually neglected. This is even more true whenever the designer needs to minimize as much as possible the noise, γ , due to active elements.

5.3 Beyond the CTIA: the CIS readout chain

In the previous sections, the classic PPG readout chains, as shown in Chapter 4, have been compared in terms of SNR for a given optical power. Specifically, it has been shown in section 5.2.3 that a CTIA-based structure comes with some key advantages in terms of power and noise with respect to the ZTIA-based one. Indeed, in the case of a CTIA, the amplifier output only needs to track the integrated photocurrent, which is much lower in bandwidth than in the ZTIA case. This implies that an amplifier with lower bandwidth and slew rate, and hence lower quiescent current, can be chosen to achieve a given photodetector bandwidth. It has also been highlighted that for a target SNR, both solutions show still an important electronic read noise level, calling for further design (and technology) optimizations. In this regard, it is objective of this section to analyse whether it is possible to go beyond the advantages introduced by the CTIA-based structure, leading to truly low-noise and low-power PPG sensors.

The CMOS image sensors (CIS) started by occupying the market of low cost and low performance image sensors and took advantage of the exploding consumer electronic devices market such as smartphones, tablets and digital cameras. Quickly, CMOS image sensors became the technology of choice with respect to speed, resolution, power consumption and on-chip integration thanks to the introduction and consolidation of the pinned photodiodes (PPDs) technology in CIS. In this section we will first deepen the technology and working principle behind the PPDs and also compare the CTIA-based structure performance with respect to the CIS one (PPD-based) in the PPG application.

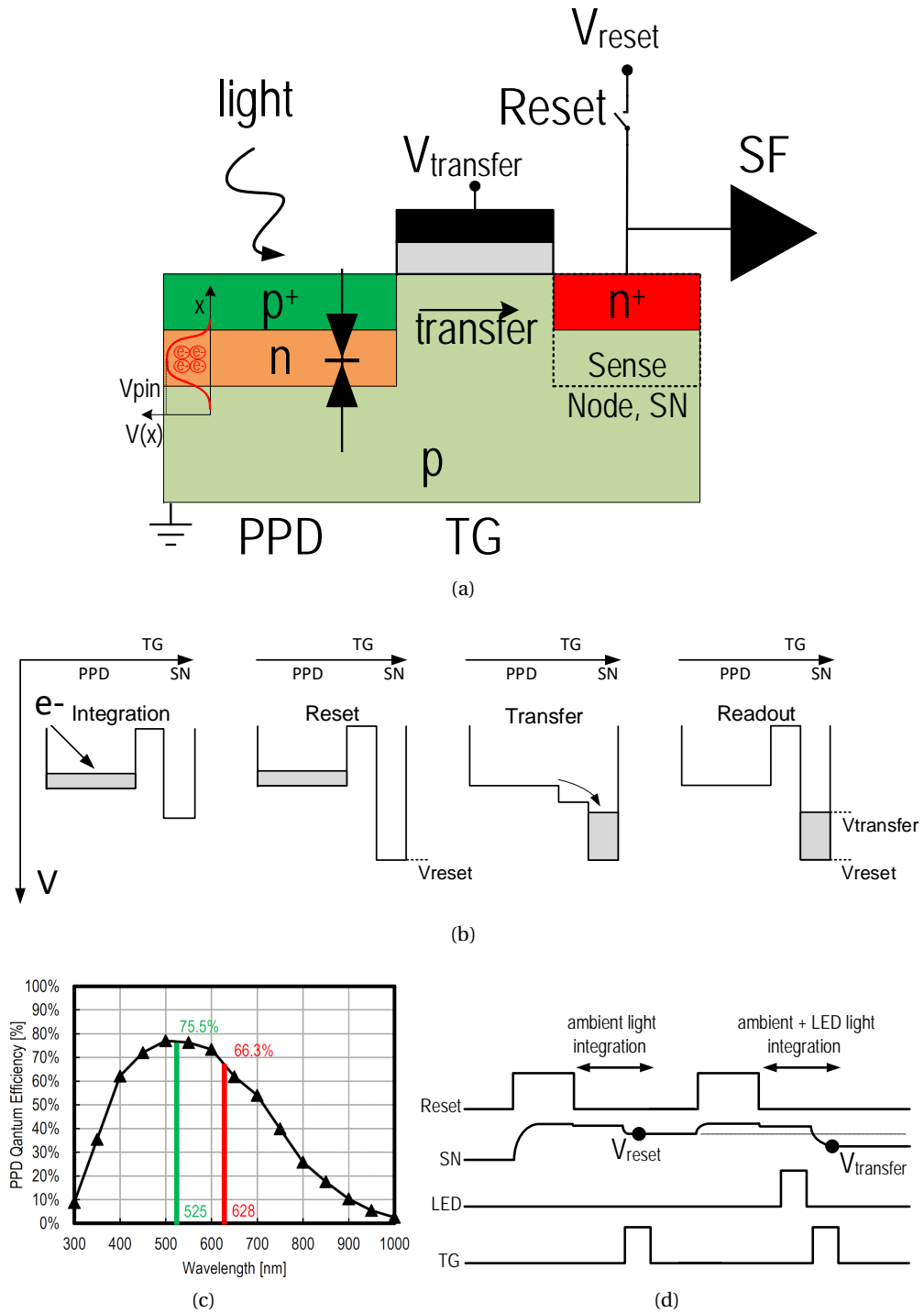


Figure 5.11 – PPD device: (a) PPG cross section, (b) PPD hydraulic equivalent model, (c) PPD QE, (d) Conventional PPD readout timing diagram, (e) PPD timing diagram for PPG.

5.3.1 The pinned photodiode

Historically, PPDs have been first developed for charged-coupled device (CCD) technology for their enhanced performances, such as low dark current and good effective quantum efficiency (EQE), as illustrated in Fig. 5.11c [164]. A PPD consists of a np junction buried under a shallow highly doped p+ thin layer, as sketched in Fig. 5.11a. A PPD behaves as a charge well where the photogenerated electrons can be stored. As shown in Fig. 5.11a the potential across the two junctions takes its maximum (pin voltage, V_{pin}) in the depleted n region. Due to the electric field in the depleted region, the photogenerated electrons are attracted by the maximum potential across the junction. The transfer gate (TG) is used to control the potential barrier at the edge of the PPD and consequently allowing the accumulated charge to move towards the sense node (SN). When the TG voltage is low enough, the potential under the transfer gate is lower than the pin voltage of the PPD, allowing the photogenerated electrons to be integrated in the potential well. Moreover, the TG isolates the SN capacitance from the PPD one, leading to a lower SN capacitance and hence a larger voltage on the SN for the same charge accumulated in the PPD. The SN is simply a n+p junction capacitance. The voltage at the surface of the n+ layer is initially set, during the reset phase, to a high voltage, V_{reset} , in the 2.5 to 3.3 V range creating a depletion at the n+p interface. At first, the reset level is sensed, i.e. V_{reset} . After sensing the reset, the TG voltage is increased creating a depletion layer under the TG. The potential under the TG is larger than V_{pin} , but still lower than V_{reset} . During this time, i.e. transfer, the depletion layers will merge leading to the photogenerated electrons to diffuse towards the larger SN potential. The charge diffusion to the SN causes its voltage to drop from V_{reset} to $V_{transfer}$, with a step proportional to the quantity of photogenerated electrons, i.e. impinging light. This step is processed by the readout circuitry by subtracting the reset level. This operation corresponds to a CDS and not only subtracts the reset level, but as well reduces the low-frequency readout noise and the kTC noise sampled at the level of the sense node during the reset operation, [132, 165], as shown in Chapter 5. The above-mentioned operations, i.e. SN reset, charge integration and transfer, can be described by the hydraulic model as shown in Fig. 5.11b.

Nowadays, PPDs are the key ingredients of CMOS image sensors (CIS), thanks to the lower dark current and a lower noise achieved due to the CDS reference. Several markets including security, scientific imaging and medical are relying today on this technology. The excellent performance of a PPD device makes it particularly suitable for the PPG application. Indeed, an on-chip high sensitivity and low noise PD can significantly reduce the LED power needed to target a specific SNR. Since the LED is the most power hungry part of a PPG chain, this would dramatically enhance the PPG sensor's battery lifetime.

Fig. 5.11d shows the PPD timing diagram properly adapted for the PPG application. It will be shown in Chapter 6 that the same timing diagram can be exploited for efficiently cancelling the ambient light (AL) thanks to the intrinsic CDS mechanism. Referring to Fig. 5.11d, the timing diagram consists of two successive readouts having as light source the AL and the AL+LED, respectively. With respect to Fig. 5.11b, V_{reset} and $V_{transfer}$ are the SN voltages due

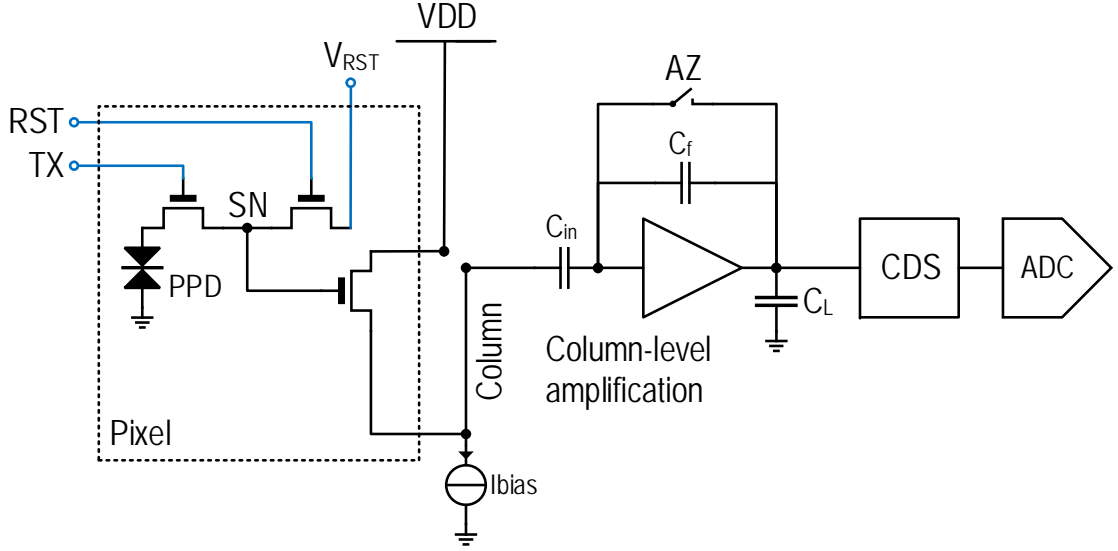


Figure 5.12 – Conventional source follower based CIS readout chain.

to the AL and the AL + LED light integration and transfer, respectively. As discussed above, the CDS scheme will differentiate the two samples leading to an efficient ALC.

5.3.2 The CIS readout chain

Most of the CIS readout chains are based on the in-pixel source follower. This scheme offers a simple design, a high dynamic range and simple reset robust against charge injection [150]. For this reason, this is the most used CIS readout chain. Fig. 5.12 shows the schematic of a conventional CIS readout chain based on a PPD, an in-pixel source follower stage, column level amplification and correlated sampling. It has been shown in [150] that a correlated multiple sampling immediately after the amplifier leads to noise reduction. As far as this analysis is concerned, a correlated double sampling block has been considered.

5.3.3 The CIS readout chain noise analysis

Similarly to the CTIA readout chain, three noise sources have been considered: the shot noise of the light, the thermal noise and the flicker noise. For each noise source, the variance at the output of the readout chain is first calculated and then referred to the input as a noise charge. Hence the pixel conversion gain is a key parameter in the noise analysis. It has been shown in [150] that the pixel conversion gain can be approximated to

$$A_{CG} \approx \frac{1}{C_{SN}}, \quad (5.51)$$

where C_{SN} is the total SN capacitance. Eq. (5.51) neglects the intrinsic and extrinsic capacitance of the in-pixel source follower transistor. Indeed, unlike a classic CIS application, for the

PPG case C_{SN} should be large enough to ensure the correct SNR and dynamic range. In this regard, the design of a PPG sensor should meet at least the SNR requirement of 28.5 dB, to achieve an accuracy within 2% of the peripheral oxygen saturation [117]. Accounting for the light shot noise only, the SNR is equal to

$$SNR = \frac{N_{AC}}{\sqrt{\sigma_{shot}^2}} = \frac{PI \cdot N}{\sqrt{N}}, \quad (5.52)$$

where N is the number of impinging photons and PI the perfusion index. Rounding 28.5 dB to decimal 30 and considering a worst case PI value of 0.2%, (5.52) can be solved for N , leading to $N = 225 \cdot 10^6$. Supposing a SN dynamic equal to V_{SN} , then C_{SN} can be calculated as

$$C_{SN} = \frac{qN}{V_{SN}}, \quad (5.53)$$

where q is the electron charge and N is the minimum number of impinging photons. Supposing $V_{SN} = 1.5V$ and $N = 225 \cdot 10^6$, C_{SN} results equal to 24 pF, whose value is sufficiently large to neglect any extrinsic or intrinsic capacitance.

The shot noise

In the case of a CIS readout chain, two shot noise sources have to be considered. First, the shot noise introduced by the light itself, whose noise variance is simply equal to the mean quantity of photons or photogenerated electrons.

Second, during the readout, the charge transferred to the SN may be corrupted by all the leakage currents through the junctions and gate oxide due to tunnelling. Since these leakage currents are due to barrier control processes, they give rise to shot noise [150]. It has been shown above that the minimum number of photons to cope with the PPG application can be larger than several hundred million. In other words, any leakage current shot noise can be neglected with respect to the shot noise of the light.

The thermal noise

In the CIS readout chain the column level amplifier plays two major roles. First, it controls the bandwidth limiting the thermal noise originating from the in-pixel source follower stage. Second, it introduces a gain large enough to make the contribution of the next stages to the total input-referred noise negligible. Under these assumptions, only two thermal noise sources can be considered: the in-pixel source follower and the column level amplifier. The two dominant pixel and column level noise sources are uncorrelated, thus their noise PSDs add. As detailed in [150], the total input-referred thermal noise charge variance can be calculated

as

$$\overline{Q_{th}^2} = \alpha_{th} \cdot \frac{kT}{A_{col} \cdot C} \left(\frac{\gamma_{SF} G_{m,A} (C_{SN})^2}{G_{m,SF}} + \frac{\gamma_A}{A_{CG}^2} \right) = \alpha_{th} \cdot \frac{kT}{A_{col}} \cdot \frac{C_{SN}^2}{C} \left(\frac{\gamma_{SF} G_{m,A}}{G_{m,SF}} + \gamma_A \right), \quad (5.54)$$

where $C = C_L + \frac{C_{in}}{A_{col} + 1}$. α_{th} is a unitless circuit design parameter reflecting the impact of CDS. It can be calculated numerically and is simply equal to 2, supposing sufficient settling time operations [150].

The flicker noise

It is well-known that the drain current 1/f noise PSD is inversely proportional to the gate area. In CIS readout chains, the transistors located outside the pixel array (e.g. column level amplifier) and fed with a low impedance signal can be designed with gate dimensions much larger than the in-pixel source follower transistor. In this case, source follower transistor becomes the dominant 1/f noise source in the CIS readout chain and the other 1/f noise sources can be neglected. Consequently, in the 1/f noise analysis, we only consider the noise originating from the pixel. As detailed in [150], the total input-referred flicker noise charge variance can be calculated as

$$\overline{Q_{1/f}^2} = \alpha_{1/f} \cdot \frac{K_F C_{SN}^2}{C_{ox}^2 \cdot WL}, \quad (5.55)$$

where $\alpha_{1/f}$ is a unitless circuit design parameter reflecting the impact of the CDS noise reduction on the 1/f noise. Based on the detailed analytical calculation [150], it is simply equal to 4.5, supposing sufficient settling time operations.

CTIA and CIS comparison

As far as the CTIA noise is concerned, the noise equations presented earlier in the chapter will be re-utilised and referred to the input. The quantization noise is supposed to be the same between the two structures and for this reason neglected in the comparison.

Before deepening the comparison between the two structures, it is important to draw the reader's attention on one important point already tipping the balance in favour of the CIS readout. Indeed, unlike a standard PD-based readout chain, such as the CTIA, the intrinsic double sampling readout scheme of the PPDs, like the CCDs, cancels the reset noise (together with an important reduction of the electronic low frequency noise). This is one of the major reason why first the CCDs and then the PPDs have replaced the 3 transistors (3T) pixels. The read noise in 3T pixel is dominated by the reset noise sampled at the SN after the reset resulting into a noise floor standard deviation generally of about a few tens of electrons (e-rms) [150]. Similarly to a 3T-based readout chain, the CTIA readout chain is also limited by the reset noise which corresponds to the noise charges frozen in the PD parasitic capacitance during the

autozeroing of the TIA, as shown in section 5.2.4 in (5.48).

Independently of the readout chain, it has been shown earlier in the chapter that the input referred SNR can be expressed as

$$SNR = 10\log_{10} \frac{S^2}{N^2} = 10\log_{10} \frac{S^2}{\sigma_{sh}^2 + \sigma_{th}^2 + \sigma_{1/f}^2}, \quad (5.56)$$

supposing the noise variances to be uncorrelated. The individual signal and noise variances are reported in Tab. 5.4 both for the CTIA and the CIS-based readout.

The CTIA and CIS readout chains are compared assuming the same signal bandwidth and with respect to the parameters listed in Tab. 5.3. The CIS integration time is set to be equal to the CTIA one, e.g. T_{ON} . The sensitivity of the PD and the PPD is supposed to be the same and so the photosensitive area. It has been decided to compare the two structures for three different PI values, i.e. 0.2%, 1% and 10%, and as well three different PD parasitic capacitances C_{PD} , i.e. 100 pF, 500 pF and 1000 pF. The comparison is shown in Figs. 5.13 to 5.15.

Table 5.3 – Design Parameters

Parameter	Value	Parameter	Value
$G_{m,CTIA} = G_{m,SF}$	10 μS	T_{ON}	100 μs
$G_{m,A}$	3.5 μS	R_L	100 $M\Omega$
$\gamma_{SF} = \gamma_{CTIA}$	1	γ_A	1
R_F	1 $M\Omega$	W	5 μm
C_F	9 pF	L	2 μm
C_L	1 pF	K_F	$10^{-27} C^2$
C_{ox}	8.46 $fF/\mu m^2$	T	300K

Figs. 5.13 to 5.15 report the SNR as by (5.56) versus the photogenerated input electrons, meaning the input optical power. Similarly to the ZTIA/CTIA comparison, the target SNR is set to 28.5 dB which is the minimum value in order to achieve an accuracy within 2% of the peripheral oxygen saturation [117]. Independently of the PI value, Figs. 5.13 to 5.15 show that the CIS based structure features a lower read noise. This results into more shot noise limited operations. This is even more clear, as the PI increases. According to (5.53), the larger the PI, the smaller the SN capacitance has to be, resulting into a lower input referred noise floor. Figs. 5.13 to 5.15 also show that, independently of the PI value, the CIS structure achieves the target SNR with a lower input power level leading to an important LED power reduction. The LED power saving ranges from roughly 2 up to about 40 times, for larger PI values. In this regard, it should be mentioned that a PI value equal to 0.2% corresponds to a quite unrealistic scenario. This means that accounting for a PI of about 1% the CIS structure requires roughly 1 order of magnitude lower LED power with respect to the CTIA-based one.

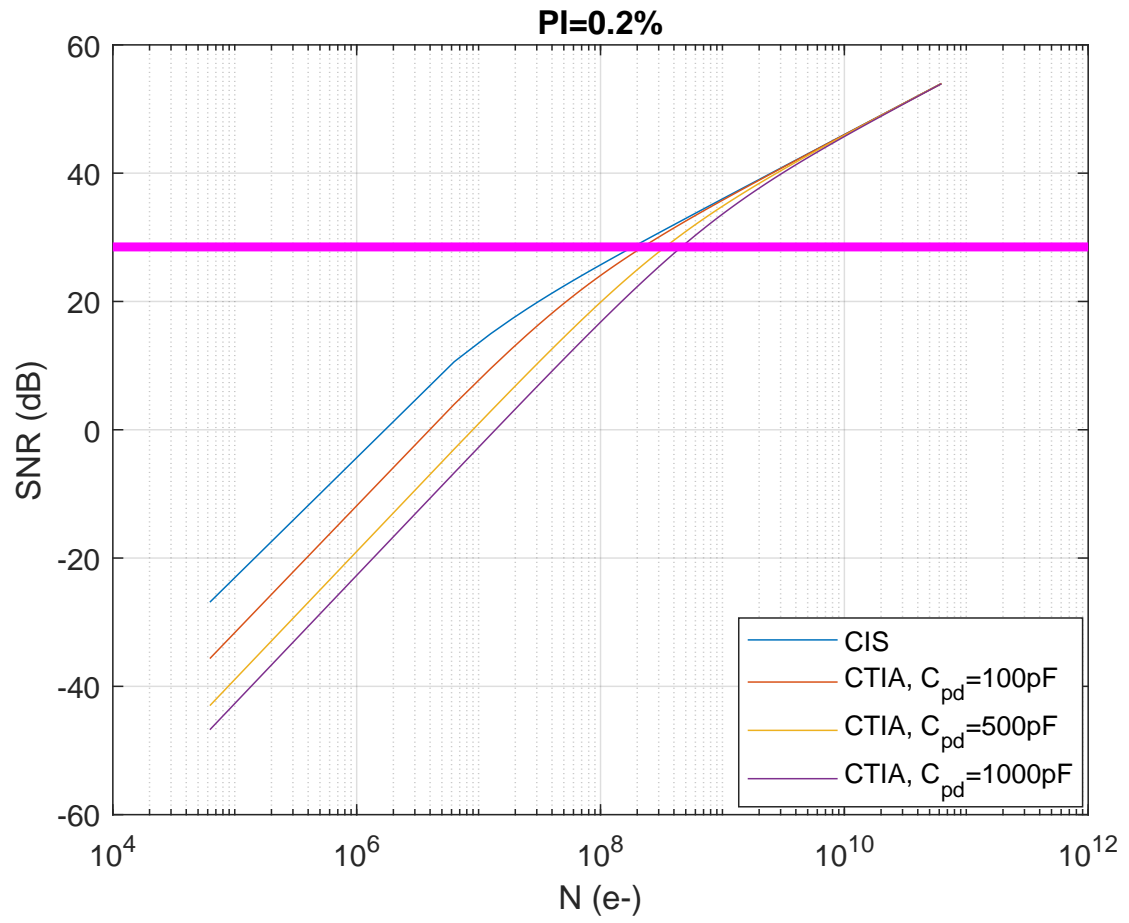


Figure 5.13 – CIS vs CTIA at 0.2% PI and for three different PD parasitic capacitances.

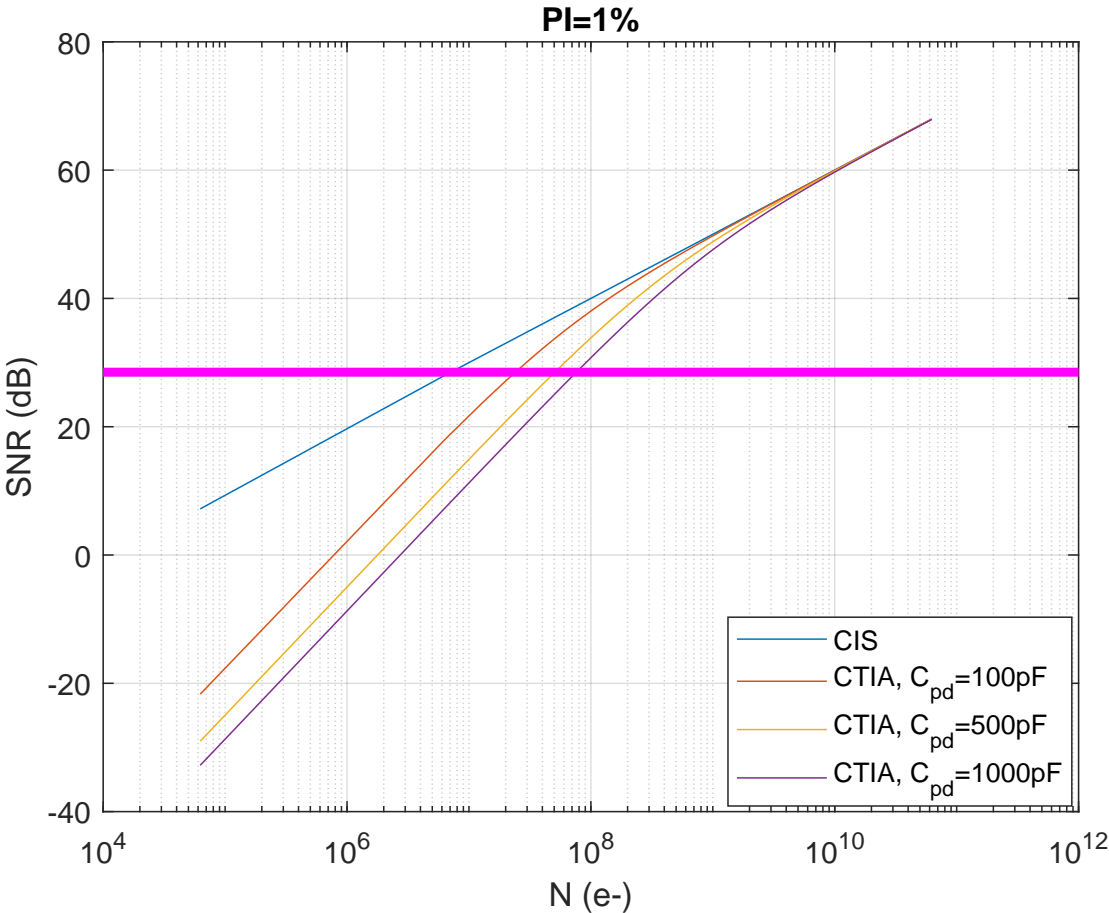


Figure 5.14 – CIS vs CTIA at 1% PI and for three different PD parasitic capacitances.

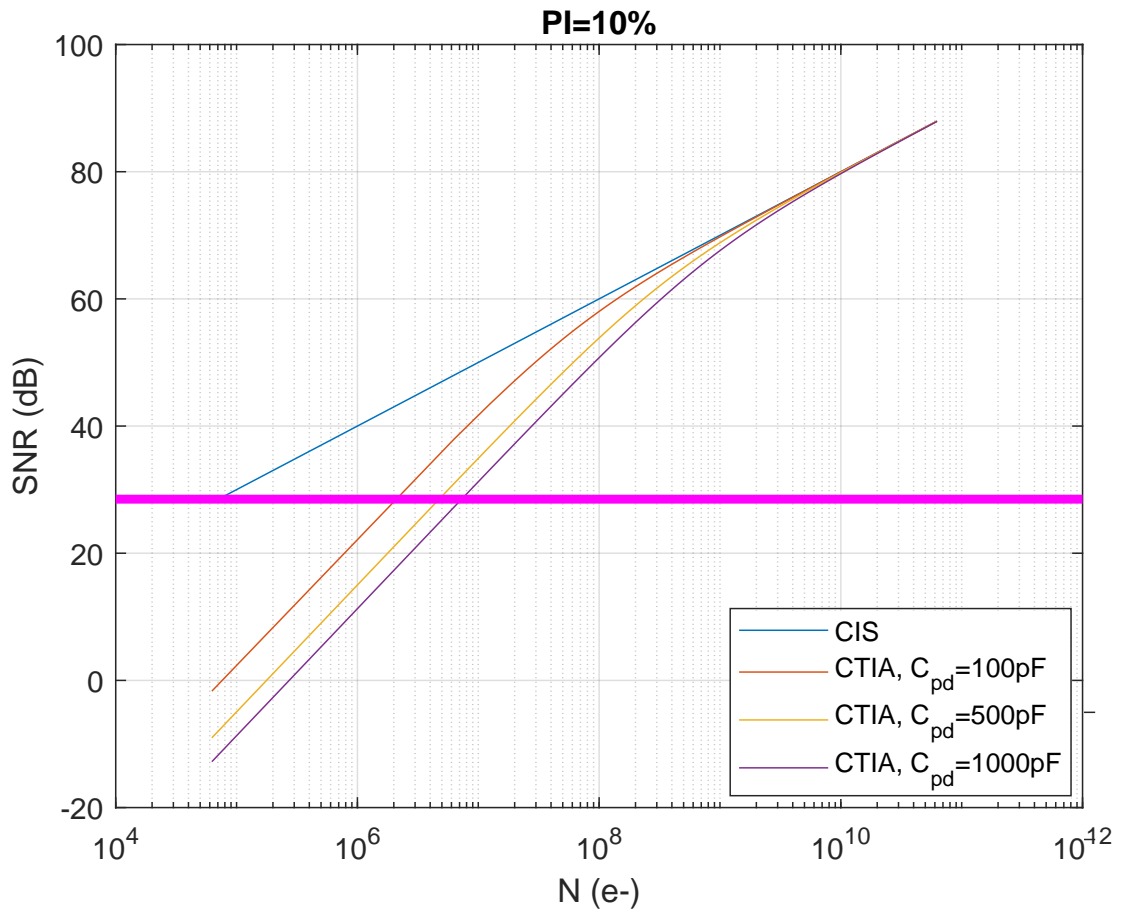


Figure 5.15 – CIS vs CTIA at 10% PI and for three different PD parasitic capacitances.

Table 5.4 – Noise analysis summary comparing CTIA and CIS readout chain.

Readout chain:	CTIA	CIS
Conversion gain	$\frac{1}{C_F}$	$\frac{1}{C_{SN}}$
Signal [e^2 –]	$\left(PI \cdot \frac{T_{ON} I_{ph}}{q}\right)^2 = (PI \cdot N)^2$	$(PI \cdot N)^2$
Input-referred 1/f noise [e_{rms}^2 –]	$\alpha_{1/fCTIA}^2 \cdot \frac{C_F^2}{q^2} \cdot \frac{K_F}{C_{ox}^2} \cdot WL \left(\frac{C_{PD} + C_F}{C_F}\right)^2$	$\frac{\alpha_{1/f}}{q^2} \cdot \frac{K_F C_{SN}^2}{C_{ox}^2 \cdot WL}$
Input-referred thermal noise [e_{rms}^2 –]	$\alpha_{thCTIA}^2 \cdot \frac{C_F^2}{q^2} \cdot \frac{kT}{C_F} \cdot \left(\frac{C_{PD} + C_F}{C_F}\right)^2$	$\frac{\alpha_{th}}{q^2} \cdot \frac{kT}{A_{col}} \cdot \frac{C_{SN}^2}{C} \left(\frac{\gamma_{SF} G_{mA}}{G_{m,SF}} + \gamma_A\right)$
Input-referred sampled thermal noise [e_{rms}^2 –]	$\frac{C_{PD}^2}{q^2} \cdot \left[\frac{\gamma kT}{\alpha C_{PD} + C_L} + \frac{kT}{C_{PD}} \frac{C_L}{C_{PD} + C_L} \right]$	-
Input-referred shot noise [e_{rms}^2 –]	$\frac{\alpha_{shCTIA}}{q} \cdot 2I_{ph} T_{ON} = N$	N

5.4 Artefacts: the motion-induced signal corruption

General types of noises have been presented in the previous sections, all affecting the PPG signal quality. In addition, PPG is known to be particularly susceptible to motion-induced artefacts (MA). Overcoming MA presents one of the most challenging problems while designing a PPG sensor. For this reason, we have decided to dedicate a full section to it.

During a PPG monitoring, various types of motions can distort the PPG signal. MA can be periodic or non-periodic and can present a much larger amplitude than the AC component of the PPG signal [155]. In addition, the MA can fall within the same frequency band as the HR [156]. This ultimately renders linear filtering with fixed cut-off frequency useless. Eventually, additional hardware or advanced signal processing techniques are required to deal with MA. This is particularly important for wearable devices in the wellness and fitness space.

5.4.1 Motion artefacts sources

MA can be the outcome of several sources. First of all, the displacement between the PPG sensor and the skin. This can ultimately corrupt the way the reflected or transmitted light reaches the PD. Any periodic displacement of the PPG sensor with respect to the skin would behave as a mixer for the received light, in other words corrupting its frequency component.

In addition, any motion-induced skin displacement would result into a vascular volume change, ultimately causing noise. This ultimately changes the DC component of the PPG signal and consequently its time and frequency features. The vascular volume change is mainly due to movement of the blood in the vessels. In other words, the emitted light will propagate through a time-varying tissue whose absorbance is not anymore purely static.

The MAs effect on the PPG signal also changes with respect to the body location. For instance, a PPG signal measured on the wrist suffers from more intense MA. This is due to the tissue deformation induced by the large tendons.

Last but not the least, the blood acceleration induced by the body movement is also an additional cause behind the MA. Any body acceleration causes an additional pressure gradient on the blood which is superimposed on the heart's one [157]. This effect is particularly important for large arteries since, according to the Bernoulli's law, their larger section imposes lower pressure gradients. On the contrary, small blood vessels intrinsically undergo larger pressure gradients making them more resilient to the effect induced by the body movements. In other words, the additional pressure gradient due to the body movement has a lower effect on the small blood vessels, which are associated with peripheral sites.

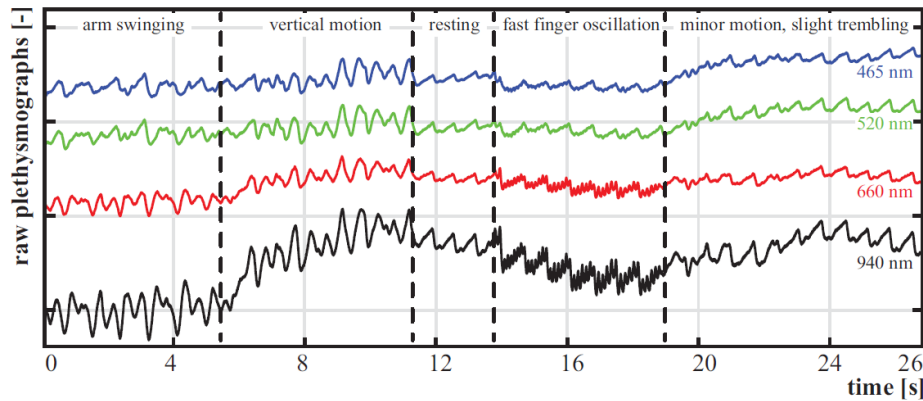


Figure 5.16 – Effect of MAs on simultaneously recorded reflective PPG signals at different wavelengths. The deeper light penetration comes with more pronounced MA [46].

5.4.2 Wavelength dependency

In the previous section several MA sources have been illustrated. Among them, the effect of the body movement on the blood acceleration plays an important role. It has been illustrated that smaller vessels tend to be more resilient to this effect thanks to their intrinsically larger pressure gradient. As explained in Chapter 2, smaller blood vessels are usually associated with both peripheral sites and shallower skin layers (outermost dermis layer, as shown in Fig. 2.6).

As presented in Chapter 2, the green light is often preferred thanks to its lower penetration in the skin. So far, this has been explained as the result of a simpler light tissue interaction and larger photon survival rates. In addition, thanks to its lower penetration, green light tends to shine smaller vessels which are less sensitive to MA. In other words, the green light is also preferred due to its larger resilience from MA, when compared to red or IR [158]. Unlike the green, the extremely limited blue light penetration makes the resulting PPG quite noisy due to the reduced shined blood volume changes [159]. This is the reason why this wavelength is not implemented in PPG sensors.

Fig. 5.16 shows, for different motion types, the effect of MA on simultaneously recorded reflective PPG signals, at different wavelengths [46]. Clearly, the deeper light penetration comes with more pronounced MA, or consequently lower signal-to-motion-ratio (SMR) [155]. The work in [158] has also shown that the least MA effect on the green light PPG sensor takes place at the upper arm, confirming the impact of the body location in MA. Indeed, as mentioned earlier and confirmed in [158], peripheral sites tend to be less resilient to MA. In particular, this applies to the green light and little to the IR, whose SMR doesn't show similar trends along the body.

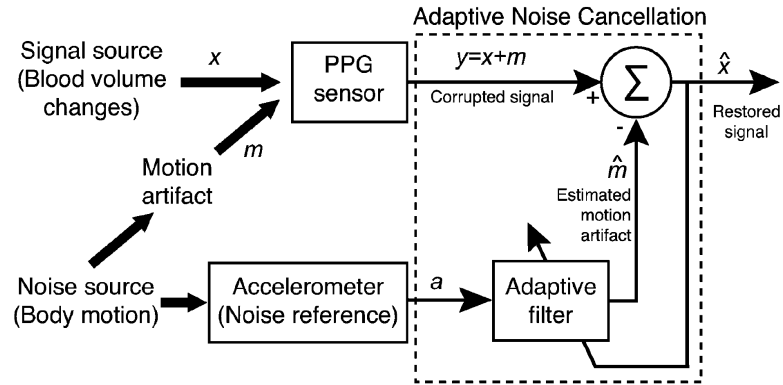


Figure 5.17 – Block diagram of the adaptive noise cancellation (ANC) technique. The noise reference is generated by an accelerometer [156].

5.4.3 Proposed techniques to reduce motion artefacts

Several solutions have been proposed to reduce the effect of MA in PPG sensors. The majority of the motion artefacts cancellation (MAC) techniques rely on the use of an external accelerometers or gyroscopes. These devices are used to provide a motion reference signal which is dynamically used to filter out in-band MA. This technique is called adaptive noise cancellation (ANC) and has been introduced in [160].

Fig. 5.17 shows how the ANC works. The output of the PPG sensor, y , is a combination of the physiological signal, depending on the blood volume change, x , and a motion-induced noise, m . If m is known, then a simple subtractor can recover x out of y . An adaptive filter, whose coefficients are adaptively computed, is in charge of estimating m , so to extract x . This filter requires a MA reference signal that is supposed to show a strong correlation with the MA and the MA-free PPG signal. In other words, the MA is estimated from the MA reference signal, i.e. the accelerometer. Several filter types have been proposed, including finite impulse response (FIR) [156].

A passive MAC has been proposed in [161], which is based on a PPG sensor placed on the superior and posterior auricular skins. The excellent ear perfusion, limited ear MA and a special module design has significantly reduced the MA without the need of any additional hardware or signal processing scheme. Similarly, the work in [162] has proposed to place, with respect to the PD, two sets of LEDs, on the left and the right. This would help minimizing the effect of the skin-probe displacement, above all at the wrist level.

The work in [163] has suggested to perform the MAC by employing two PPG sensors, as shown in Fig. 5.18. The main PPG sensor is in contact with the skin to detect the PPG signal, $d(n)$ in Fig. 5.18, which is corrupted by the MA. The second PPG sensor is not in contact with the skin and placed into a 7.5 mm air gap. This second PPG is intended to detect the MA only, $u(n)$ in Fig. 5.18. Eventually, the MAC takes place thanks to a non-linear adaptive canceller filter exploiting a recursive least square algorithm.

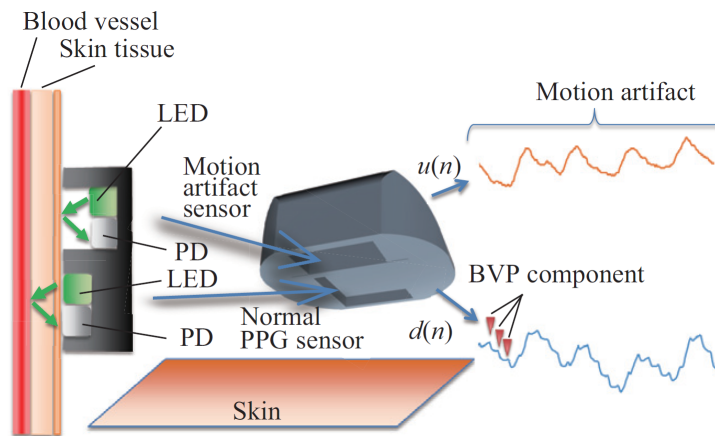


Figure 5.18 – MAC based on two PPG sensor: the first is in contact with the skin and so used to detect the PPG with MA. The PPG signal carries the blood volume pulse (BVP) components. The second PPG sensor is not in contact with the skin and used to evaluate the MA [163].

MA may also result from micromotions, which are not always accurately captured by accelerometers. For instance, slightly moving one finger generates quite low MA which are not easily detectable by an accelerometer positioned on the wrist. On the contrary, such little movement can be large enough to reduce the PPG signal quality. The work in [155] has proposed to replace the accelerometer or gyroscope with a photoelectric motion reference. It has been proposed to use a PPG signal recorded by the green light as the main PPG channel and a second IR PPG channel as the motion reference. Indeed, as mentioned earlier in the chapter, green PPG signals come with at least 10 dB larger SMR than the IR. Seven types of periodic motions have been analysed in order to study the correlation between the MA in the green and in the IR. The proposed solution relies on a 5 steps algorithm implementing continuous wavelet transform and time domain decomposition and reconstruction. The downside of this technique, as pointed out in [155], is the larger power consumption coming from the additional IR PPG channel, since an accelerometer consumes around 10%-20% of the power burnt by the IR PPG channel, and the increased signal processing complexity.

Because of our constraints in terms of power consumption, the sensor proposed in this work cannot afford to embed any ANC technique, which goes beyond this PhD work. On the other hand, as it will be pointed out in the next chapter, all the possible passive methods have been implemented in order to reduce the effect of MA.

Conclusions

Despite the advantages and opportunities behind the PPG technology, today PPG sensors are still limited by noise and artefacts. Indeed, several noise sources should be accounted for when designing a PPG sensor: the shot noise of the photogenerated current, the thermal and flicker noise of the readout chain and the quantization noise of the ADC. Among the different proposed PPG readout chains, discussed in Chapter 4, the one with a TIA, a CDS and an ADC is the most used one, both in academic and commercial solutions. The TIA is often proposed either as a ZTIA or a CTIA. Providing a detailed and comprehensive noise analysis in PPG readout chains is key in order to reduce the LED power. Indeed, the LED power can be reduced provided the noise floor of the readout electronics is decreased proportionally to achieve the same SNR. A classic PPG readout chain has been analysed both in ZTIA and CTIA configurations in terms of SNR and power trade-offs. Assuming the same signal bandwidth between the two compared structures, a ZTIA-based readout chain comes with both larger LED power (8 times more) and a larger G_m , compared to a CTIA-based one. This advantage is attributed to the integration feature of the CTIA. Indeed, the CTIA comes intrinsically with a larger bandwidth than the ZTIA. Comparing the two for the same BW means, in other words, having a larger signal gain for the CTIA than the ZTIA. Moreover, the ZTIA shows a larger read noise than the CTIA, which is, on the contrary, intrinsically more shot noise limited. It should also be noticed that both solutions show still an important electronic read noise level, calling for further design optimizations.

The CMOS image sensors (CIS) is today dominating the exploding consumer electronic devices market such as smartphones, tablets and digital cameras. Quickly, CMOS image sensors became the technology of choice with respect to speed, resolution, power consumption and on-chip integration thanks to the introduction and consolidation of the PPD technology in CIS. The important advantage of PPDs in terms of sensitivity and noise make them a serious candidate in the PPG application to go beyond the CTIA-based structure and the limitations introduced by the off-chips PDs. Assuming a PI equal to 1%, same signal bandwidth and comparable sensitivity between the CTIA and the CIS readouts, the latter achieves the target SNR with more than 1 order of magnitude lower LED power. The advantage introduced by the CIS can also be extended for larger PIs. Indeed, the CIS readout chain shows, no matter the PI value, a lower electronic noise floor resulting into intrinsically more shot noise limited operations.

The CDS is key for reducing the effect of the ambient light, offsets and $1/f$ noise. Despite this, CDS circuits are still limited by circuit non-idealities, including analog switches non-idealities (on and off resistances), charge injection and thermal noise, the latter usually referred to as kTC noise. The sampled noise voltage variance (kT/C) is, by definition, inversely proportional to the capacitance. On the contrary, both power and silicon area are directly proportional to the capacitance, resulting into a noise/power-area trade-off. From a design perspective, it is necessary to be fully aware of the capacitances ultimately limiting the circuit performance. kTC noise analysis of SC circuits is never a simple task, considering that the noise transfer function,

for these circuits, changes in time. Modern CAD simulators are useful in the estimation of the overall noise features, despite they require a very high accuracy set-up, resulting into extremely long simulations. Moreover, they don't provide simple analytical expressions to optimize the SC circuit noise. In this perspective, three possible CDS circuits have been compared analytically and benchmarked in terms of kTC noise. A fully passive CDS is particularly suitable for ultra-low power applications, despite the SNR is affected by the intrinsic signal loss due to the charge sharing mechanism. Moreover, it is not affected by any signal saturation, the latter usually due to active elements. One of the main advantages of this implementation is that the SNR can be improved without limiting the input signal range and only at the cost of more silicon area (larger capacitors).

In addition to the noise, PPG is known to be particularly susceptible to motion artefacts. Overcoming those artefacts presents one of the most challenging problems while designing a PPG sensor. Several solutions have been proposed to reduce the effect of motion in PPG sensors. First of all, motion artefacts are wavelength dependent. Thanks to the shorter penetration of the green light, the latter achieves more resilience to MA with respect to red and IR. Secondly, these artefacts can be reduced by choosing specific body locations. For instance, the ears report less MA with respect to the arms. Other cancellation techniques rely on the use of an external accelerometers, gyroscopes or optical channel. These devices are used to provide a motion reference signal which is dynamically used to filter out in-band motion artefacts. This technique is called adaptive noise cancellation.

6 A micropower PPG sensor

As illustrated in Chapter 4, the design of a PPG sensor, on the AFE side, still follows a quite standard paradigm. Despite few differences, almost all the prior works embed an off-chip PN or PiN-based PD, converting the photogenerated electrons into a current, followed by a TIA, amplifying and translating into a voltage the photogenerated current.

Despite the quality of the engineering solutions presented so far, both in academia or in commercial products, their power consumption is still strongly affected by the few tens of mAs of the LED drivers and we should not expect dramatic improvements unless there are fundamental changes in the PPG sensor technology. This is particularly true for the PD which is limiting the power/noise trade-off due to its rather large capacitance. In this regard, any new PD technology combining high sensitivity and low-noise operations can lead to a dramatic LED power saving, towards truly micropower PPG sensors. Chapter 5 has demonstrated that a pinned photodiode-based readout chain (CIS) can lead to lower noise and lower power PPG operations. The objective of this chapter is to show how a CIS readout can be further optimized for the PPG application leading to truly micropower operations.

6.1 The double TG pinned photodiode structure

As shown in Chapter 5, today PPDs are the key ingredients of CMOS image sensors (CIS), thanks to the lower dark current and a lower noise achieved due to the CDS reference. Several markets including security, scientific imaging and medical are relying today on this technology. The excellent performance of a PPD device makes it particularly suitable for the PPG application. Indeed, an on-chip high sensitivity and low noise PD can significantly reduce the LED power needed to target a specific SNR. Since the LED is the most power hungry part of a PPG chain, this would dramatically enhance the PPG sensor's battery lifetime. A double TG PPD device, as shown in Fig. 6.1a, is the best fit for the PPG application. Indeed, the double TG scheme, i.e. TGsink (TGs) and TGtransfer (TGt), allows to precisely control the amount of charges integrated in the PPD well and eventually reaching the SN for readout. This scheme is actually helpful for any application needing a consistent amount of impinging photons,

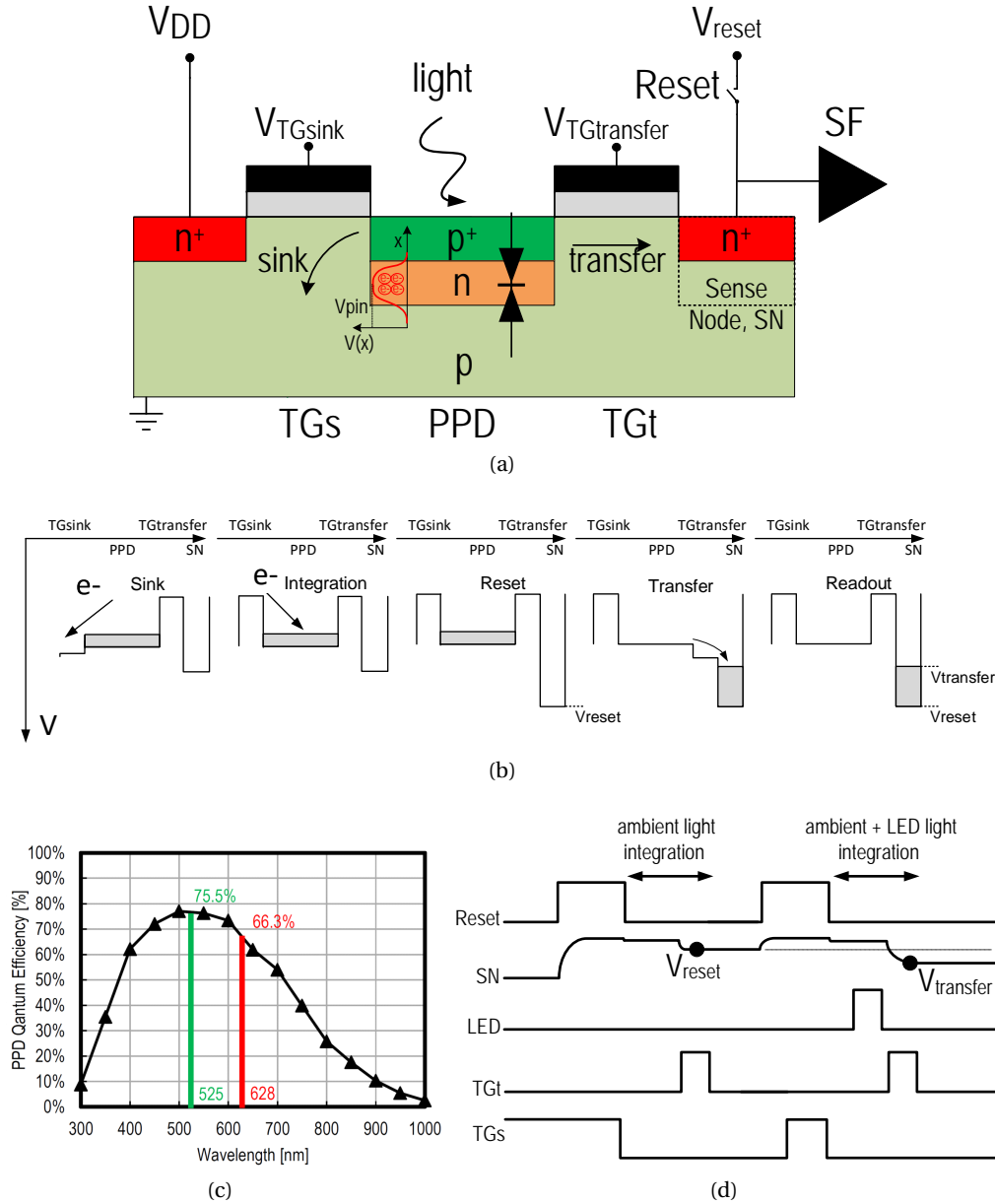


Figure 6.1 – PPD device: (a) double TG PPG cross section, (b) PPD hydraulic equivalent model, (c) PPD EQE, (d) Conventional PPD readout timing diagram, (e) Modified timing diagram for ALC.

to avoid any possible well saturation, like the PPG one. In addition, controlling precisely the photoelectrons' integration means avoiding any possible LED light waste, leading to a power efficient lighting scheme. Another competitive advantage of the double TG scheme is the capability of efficiently cancelling the ambient light (AL) thanks to the CDS. The timing diagram of the ambient light cancellation (ALC) is shown in Fig. 6.1d. As explained above, it consists of two successive readouts having as light source the AL and the AL+LED, respectively. With respect to Fig. 6.1b, V_{reset} and $V_{transfer}$ are the SN voltages due to the AL and the AL

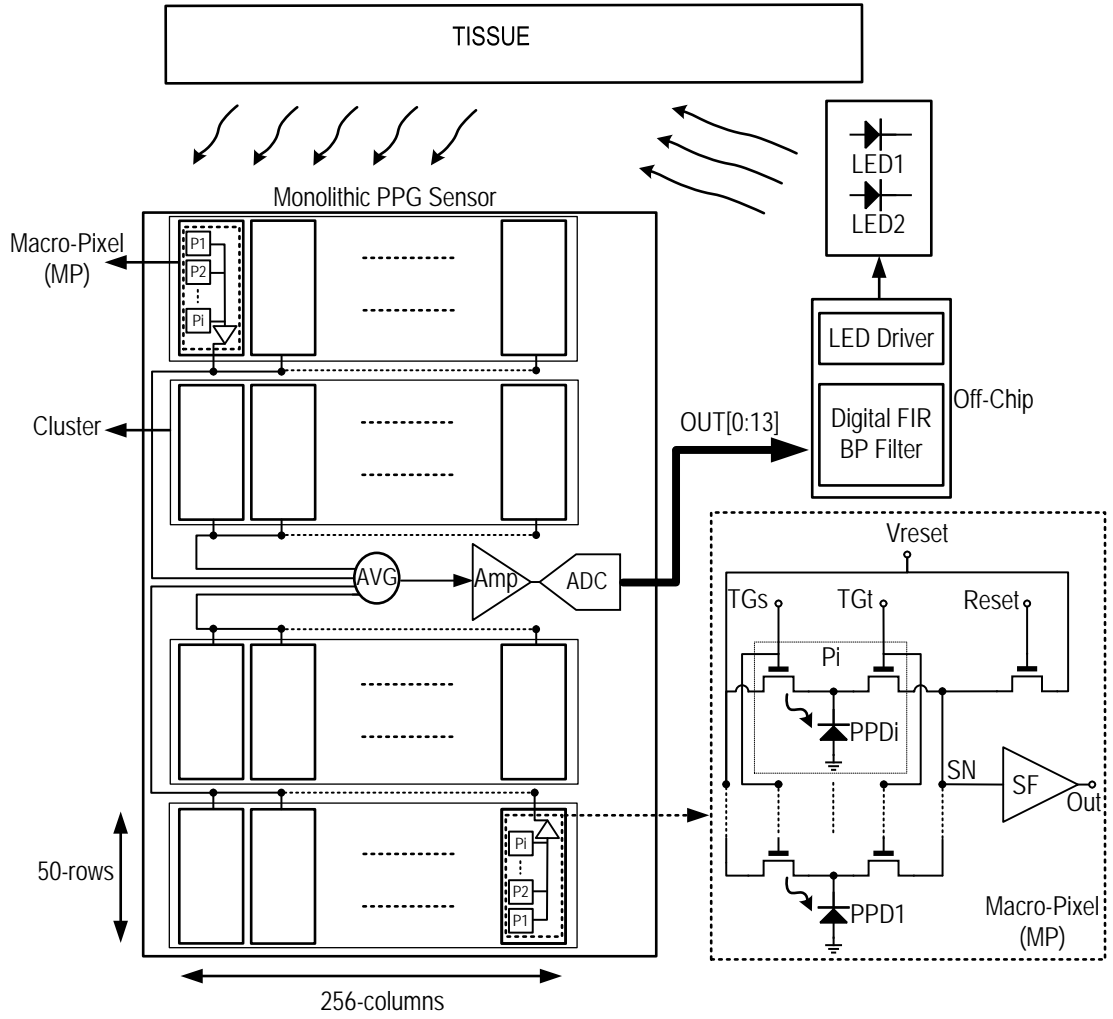


Figure 6.2 – Block diagram of the proposed monolithic PPG sensor. The implemented ASIC consists of an array of macro-pixels, as photosensitive area, an averaging block, an amplifier and an ADC.

+ LED light integration and transfer, respectively. As discussed above, the CDS scheme will differentiate the two samples leading to an efficient ALC. The double TG scheme and the μ s transfer PPD operations guarantee that the AL, both natural and artificial, integrated within the two windows is the same. This will be further detailed in section 6.2.3.

6.2 The micropower PPG sensor architecture

The block diagram of the micropower PPG sensor is shown in Fig. 6.2. The proposed solution consists of a fully integrated chip embedding an array of PPDs, a passive averaging block, a switched-cap (SC) amplifier and an ADC, which will be described in details in the next sections.

6.2.1 Array of PPDs

As discussed in section 6.1, a PPD is intrinsically a diffusion-based device. For this reason, a PPD cannot operate correctly with a pitch size considerably larger than a few hundred μm , not to end up with an inefficient charge transfer and also losing the advantage of having a low dark current, [164, 166, 167]. In addition, a larger pixel comes with a larger parasitic capacitance which ultimately affects the noise performance. With these considerations, an array of double TG PPDs has been designed, as shown in Fig. 6.2. Placing the PPDs into an array eases the engineering trade-off between the possible achievable dynamic range and the overall noise performance. The total number of pixels has been chosen according to the target SNR. Indeed, the design of a PPG sensor should meet at least the SNR requirement of 28.5 dB, to achieve an accuracy within 2% of the peripheral oxygen saturation [117].

Accounting for the light shot noise only, the SNR is equal to

$$SNR = \frac{N_{AC}}{\sqrt{\sigma_{shot}^2}} = \frac{PI \cdot N}{\sqrt{N}}, \quad (6.1)$$

where N is the number of impinging photons and PI the perfusion index. Rounding 28.5 dB to decimal 30 and considering a worst case PI value of 0.2%, (6.1) can be solved for N , leading to $N = 225 \cdot 10^6$. If one considers a PPD well saturation, N_{sat} of $6.4 \cdot 10^3$, as in [164], then the number of pixels needed to cope with the SNR requirement is

$$pixels = \frac{N}{N_{sat}} = \frac{225 \cdot 10^6}{6.4 \cdot 10^3} = 35156. \quad (6.2)$$

Eq. (6.1) considers the shot noise only. Another important noise source is the quantization noise and the electronic readout noise, which modify (6.1) to

$$SNR = \frac{N_{AC}}{\sqrt{\sigma_{shot}^2 + \sigma_{ADC}^2 + \sigma_r^2}} = \frac{PI \cdot N}{\sqrt{N + \frac{\Delta^2}{12} + \sigma_r^2}}, \quad (6.3)$$

where Δ is the quantization step (assuming uniform quantization) which depends on the full-scale range (FSR) and the chosen bit resolution, N_{bit} , and σ_r the read noise standard-deviation (STD). Accounting for these additional noise sources and keeping a margin of some dBs on the SNR requirement, the chosen number of pixels is 51200.

Indeed, the photosensitive area consists of four clusters of 50 rows and 256 columns, meaning 51200 total pixels, as discussed above. The 50 pixels along the i-column are assembled in a macro-pixel (MP), as shown in Fig. 6.2. The pixels of one MP share the same source-follower (SF) saving power while maintaining a reasonably low parasitic capacitance at the shared SN.

The MP consists of an array of PPDs having each two TG, a sink TGs and a transfer gate TGt. TGs sinks the charge cumulated in the PPDs to the reset voltage (V_{RST}), while TGt allows the charge transfer to the SN. The SN is shared between multiple PPDs, which are gated to

either sink or transfer their charge synchronously. This process is also referred to as charge binning. It allows averaging the outputs of the MP PPDs without the need for any additional circuitry. This charge binning presents key advantages when compared to the implementation of a single photodiode as large as the macropixel. Indeed, PPDs may suffer from charge transfer inefficiency due to the slow diffusion charge transfer mechanism or to the presence of a potential barrier under the transfer gate [168]. These non-idealities scale with the size of the photodiode. Hence, such a combination of pixels enables more efficient and faster charge transfer compared to a single large PPD with equivalent area by mitigating the effect of charge transfer non-idealities.

The spatial averaging is done in two steps: first, a charge averaging on the shared SN within the same column and, second, a voltage averaging among the 1024 columns at the SFs output. This leads to a considerable shot and read noise reduction, together with a full pre-filtering of the PPG signal itself. In addition to the noise optimization, the proposed pixel achieves between 66% and 75% EQE for the selected LED wavelengths as shown in Fig. 6.1c, further reducing the LED power needed for achieving the target SNR [117]. It should be mentioned that the full integration of the PPD in silicon offers an excellent EQE within the visible range, but comes at the cost of less sensitivity in the IR region.

Next, the PPG signal is amplified by a low noise programmable gain SC amplifier.

6.2.2 One big pixel versus an array of pixels?

This section aims at deepening the competitive advantage of having an array of pixels versus a single big one. The two embodiments are both possible and shown in Fig. 6.3, for comparison. First of all, as discussed in section 6.2.1, a PPD is intrinsically a diffusion-based device. For this reason, a PPD cannot operate correctly with a pitch size considerably larger than a few hundred μm . As shown in (6.2), the minimum number of pixel needed to cope with the SNR requirements for the peripheral oxygen saturation, if one considers a PPD well saturation, N_{sat} of $6.4 \cdot 10^3$, is more than 35156. Having one single PPD pixel as large as 35156 pixels would result into an inefficient charge transfer and also a larger dark current. If the one big pixel configuration is needed, a regular PN or PiN junction has to be envisaged, with all the consequent power and noise challenges, as explained in Chapter 5.

The MP structure, as explained above, comes with the competitive advantage of spatial averaging, which leads to further noise reduction. Actually, as far as the kTC noise coming after the pixel is concerned, the large pixel may supply charges to one SF, whose output is connected to a capacitor C_{big} , as shown in Fig. 6.3, being 1024 times larger than the one used for the single column, in the array structure. We recall that the array has 1024 columns. In terms of the kTC noise after the pixel the two structures are the same. On the contrary, whatever kTC noise taking place at the level of the pixel would definitely benefit from any averaging process among the 1024 columns. On the other hand, the array enables an important power optimization. Indeed, in the array structure, the SF corresponding to one column is biased in weak inversion

(WI). We should recall that in weak inversion the transconductance is linearly proportional to the current. On the contrary, in the single pixel approach, the large capacitive load and the bandwidth requirements force the SF to be biased in strong inversion (SI). In this case, the SF transconductance scales with the square root of the biasing current. In other words, both the capacitor and the transconductance scale linearly, unlike the biasing current. Fig. 6.4 shows, for the same SF bandwidth, how the ratio of the two SF currents, i.e. I_{big}/I_{array} , scales with respect to both the $(W/L)_{big}$ and the inversion coefficient (IC) of the big pixel SF, i.e. IC_{big} . The proposed comparison has been carried out for a 1024 columns array, considering a CMOS NMOS 180 nm process with the following technological values: $n = 1.2$, $\beta_{SI} = 300 \mu A/V^2$. Moreover, I_{big} has been fixed to 0.5 mA, whose value leads to a reasonable bandwidth, given the large capacitive load. Fig. 6.4a shows that I_{big} is always larger than I_{array} and eventually tends to I_{array} only for the unrealistic value of $(W/L)_{big}$ equal to 1000. In other words, as shown in Fig. 6.4b, this means having the big pixel SF biased in WI, for which IC tends to unity [145]. On the other hand, it is not possible, at the given I_{big} , to bias the big pixel SF in WI since this would require an unrealistically large transistor. The reader should refer to appendix A for further details. The same analysis shows that, for the same bandwidth, the 0.5 mA biasing current in the single pixel corresponds to less than 50 μA biasing current in the array structure, leading to a dramatic power saving thanks to the current efficiency of the WI. It should also be recalled that the weak inversion comes with better thermal noise performance, thanks to the lower generated γ at a given transconductance, and avoids any velocity saturation that is present in minimum length transistors, further degrading the current efficiency [145].

Simulating the two structures in terms of equal SF bandwidth has resulted into the big pixel structure consuming more than 2.5 times larger biasing current than the array one. Since the SF determines the largest part of the micropower PPG sensor power budget and accounting for the above considerations, the array structure has been finally preferred.

6.2.3 Switched-cap averaging and amplifier

Fig. 6.5 shows the analog-front-end (AFE) implementation with the related timing diagram. The sense nodes, shared by 50 PPDs and corresponding to the SFs inputs, are first reset. Meanwhile, each individual PPD starts integrating the impinging light corresponding to the AL. In order to precisely control the light-induced charge integration, the PPDs are first emptied by the sink switch TGs. At the end of the first integration phase, the generated photoelectrons are transferred, via the transfer gate TGt, to the SNs. The capacitance of each SN, shared by the 50 pixels along the same column, converts the integrated photoelectrons into a voltage and performs the charge averaging across the 50 rows. After the transfer is completed the SF output voltages are sampled on capacitors $C1_i$ via $S1_i$. Next, the SNs are reset again and the LED is pulsed on. As above, the PPDs precisely integrate the LED light superimposed to AL, and the related voltage level is sampled on $C2_i$, via $S2_i$, where $C2_i$ and $C1_i$ are made equal to 0.5 pF. The power switch SSF is only closed during this charge transfer and sampling phase for minimal power consumption. By closing $S3_i$ and $S4_i$ all the capacitors $C1_i$ and

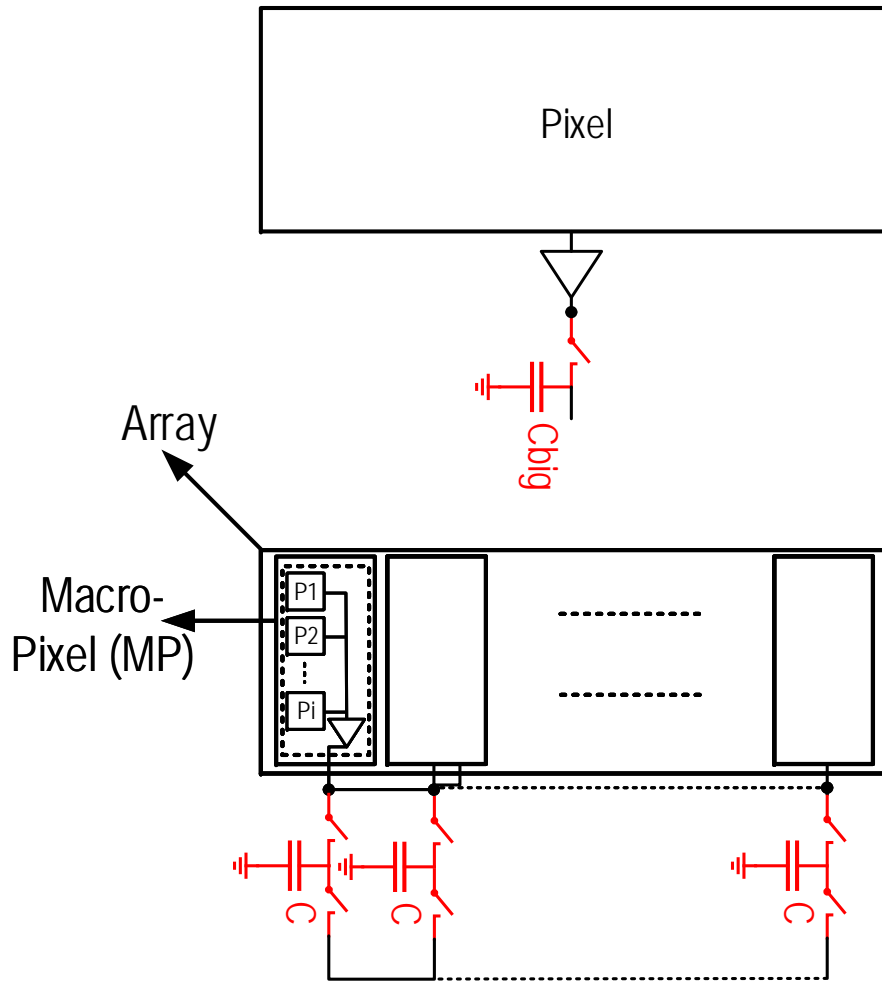


Figure 6.3 – An array of pixels versus a single big pixel.

$C2_i$ related to the same sample are connected in parallel and share their charge, resulting into a voltage equal to the spatial average of the array pixel output samples. In addition, the large capacitor resulting from the parallel connection of multiple column-level capacitors acts as a large hold capacitor for the following stage. The full averaging operation comes with a shot noise variance reduction of 50×1024 and a read noise variance reduction of 1024. In order to extract the difference of the two averaged samples, corresponding to the AL and the AL plus LED light, a SC amplifier is operated as shown in Fig. 6.5. First, the averaged AL sample is stored in $C3$, via $S5$ and SAZ . This phase enables to autozero the amplifier which is key for offset and $1/f$ noise reduction [132]. Then, SAZ is opened and the charge stored in $C3$ (2 pF) is transferred to $C4$. At the closing of $S6$, the amplified difference between the two average values is obtained at the amplifier's output, leading to an efficient AL cancellation. The amplifier embeds a programmable gain (set by the value of $C4$), from 1 to 32 to adapt to different operating conditions. It then drives an incremental ADC, through $SF2$. The power switches S_{amp} and S_{ADC} are only closed at the beginning of the array averaging and opened after the A-to-D conversion.

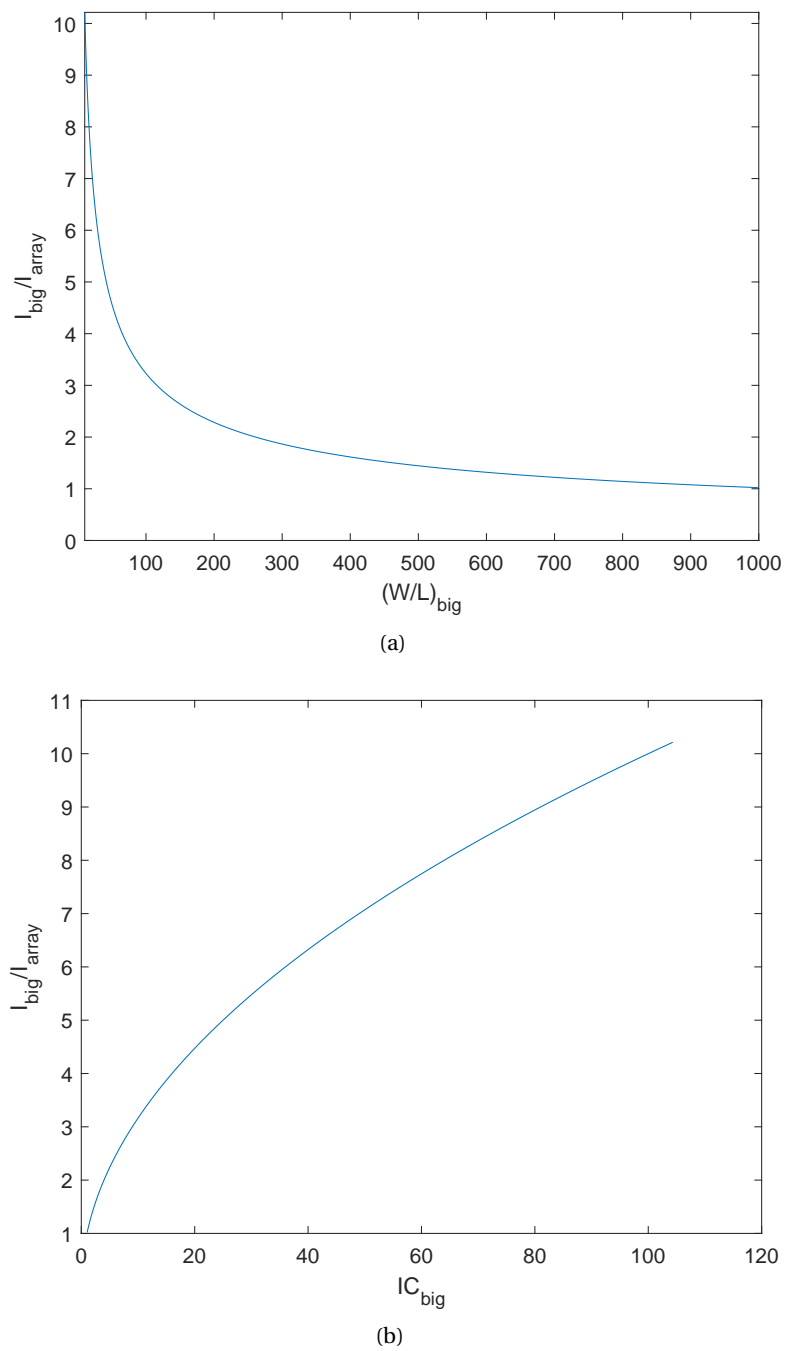


Figure 6.4 – (a) Ratio of the single pixel current and the array one versus the (W/L) of the single pixel SF, (b) Ratio of the currents versus the inversion coefficient of the single pixel SF.

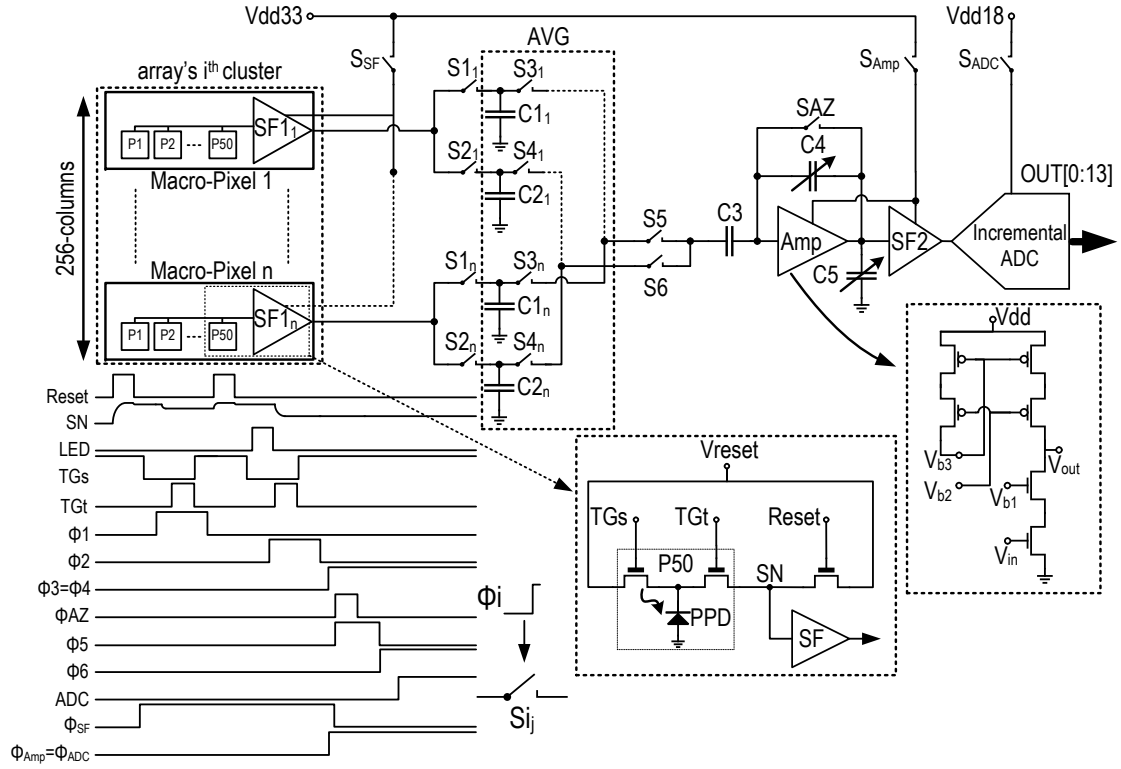


Figure 6.5 – Architecture of the monolithic PPG sensor and detailed schematic of the OTA used in the amplifier, the averaging block, together with the timing diagram.

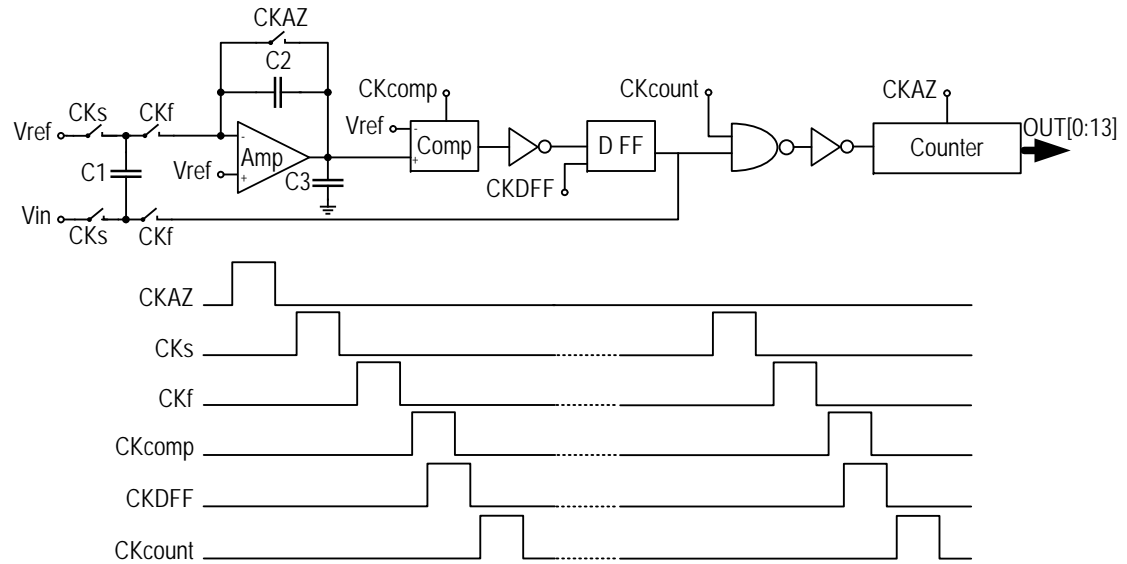


Figure 6.6 – Full schematic of the on-chip incremental ADC with the related timing diagram.

6.2.4 A low-power incremental ADC

The block diagram of the low-power incremental ADC is shown in Fig. 6.6. Incremental ADCs are often the best choice for low frequency and high resolution sensor interface [169]. An

incremental ADC works as a $\Delta\Sigma$ ADC, but with a periodic reset at the end of the conversion cycle. The overall ADC is operated at 1.8 V power supply, except for the four input switches CKs and CKf which are driven at a 3.3 V gate voltage to cope with the amplifier's output that can take values larger than 1.8 V.

The designed ADC consists at first of a passive subtractor (Δ) followed by an OTA-based SC integrator (Σ). At the beginning of the ADC operation, the SC-OTA is autozeroed, during phase CKAZ. In addition, it resets the SC-OTA feedback capacitor and the asynchronous counter, determining the stop condition for the ADC. During the next phase CKs, the output of SF2, V_{in} , is subtracted from the ADC reference voltage, V_{ref} . The difference between the two is integrated by the integrator, during phase CKf. Apart from CKAZ, all the ADC phases happen at 10 MHz frequency. The larger the input subtraction, the faster the SC-OTA output reaches V_{ref} , causing the latched comparator to move from logic state 0 to 1, during phase CKcomp. In CKDFE, a D-Flip Flop (DFF) tracks this new value and, thanks to a feedback loop, imposes to the SC-OTA to revert the direction of integration. The number of times the comparator toggles from 0 to 1 is counted by an asynchronous counter, during phase CKcount. In other words, a small input signal will see the comparator output more often at 0 rather than 1, determining a low final count. On the contrary, a large input signal will immediately make the SC-OTA output reach V_{ref} , determining the comparator output to stay much often at 1 rather than 0, so consequently a large final count.

One of the advantages of this design relies on the tunable ADC resolution. Indeed, a larger resolution is achieved by making the counter count for a longer time. At 10 MHz frequency operations, resetting the counter after 409.6 μ s and 1.6 ms means reaching 12-bits and 14-bits, respectively. The ADC power consumption is dominated by the OTA static current, 12 μ A at 1.8 V supply, which guarantees the correct settling time at the chosen operating frequency.

6.2.5 Micrograph picture and measurement set-up

The objective of this section is to introduce the measurement set-up with which the micropower PPG sensor has been fully characterized.

Testing printed-circuit-board 1.0

The first measurement set-up and the micrograph die photo of the 0.18 μ m chip are shown in Fig. 6.7. The chip measures 4 mm by 5 mm.

The printed-circuit-board (PCB) as in Fig. 6.7a drives the chip, by providing the bias voltages and the clock phases. This is done by the means of a National Instruments PXI e-1082 machine. The same tool handles the data acquisition, whose values are shown on a Labview interface, as in Fig. 6.7b.

The micropower PPG sensor is bonded on a PGA together with 6 RGB LEDs and a resin optical

barrier to avoid any direct optical cross-talk. Visible LEDs have been preferred so to match the maximum EQE of the array, as presented in Fig. 6.1c.

Testing printed-circuit-board 2.0

A second experimental set-up has been also implemented with the aim of getting a portable testing platform. The second experimental set-up is shown in Fig. 6.8. It consists of a field-programmable-gate-array (FPGA) board driving the PPG chip. By means of an universal-asynchronous-receiver-transmitter (UART) protocol, the chip's data are real-time streamed out to a computer, via the FPGA, for displaying or further processing. The chip and the LEDs (all surrounding the chip) are placed on a compact board, shown in Fig. 6.8b. The latter measures 2 cm by 3 cm and allows PPG measurements on different body locations. Two LED families, each one both in green and red, have been chosen and both are mounted on the PCB. Visible LEDs, green and red, have been preferred to match the maximum EQE of the array, as presented in Fig. 6.1c. The LEDs are driven off-chip by the means of discrete current sources and switches. The silicon and the LEDs are protected by a plastic 3D-printed case which has been sealed by a highly-transparent glass. To enhance the quality of the PPG reading and to reduce the impact of any motion artefact, particular attention has been dedicated to the realization of this compact board. Indeed, as already shown in Chapter 2, while engineering a PPG module the direct light cross-talk between the LED and the PD, the PD-LED distance and the LED's height versus the PD's are particularly important variables that can ultimately enhance or deteriorate the PPG readings. Moreover, as presented in section 5.4, the visible LEDs have been preferred since the corresponding PPG signal is more resilient to the effect of motion. In addition, the LEDs within the same family are placed on the left and the right with respect to the PPG sensor. As pointed out in section 5.4, this helps minimizing the effect of the skin-probe displacement, above all at the wrist level.

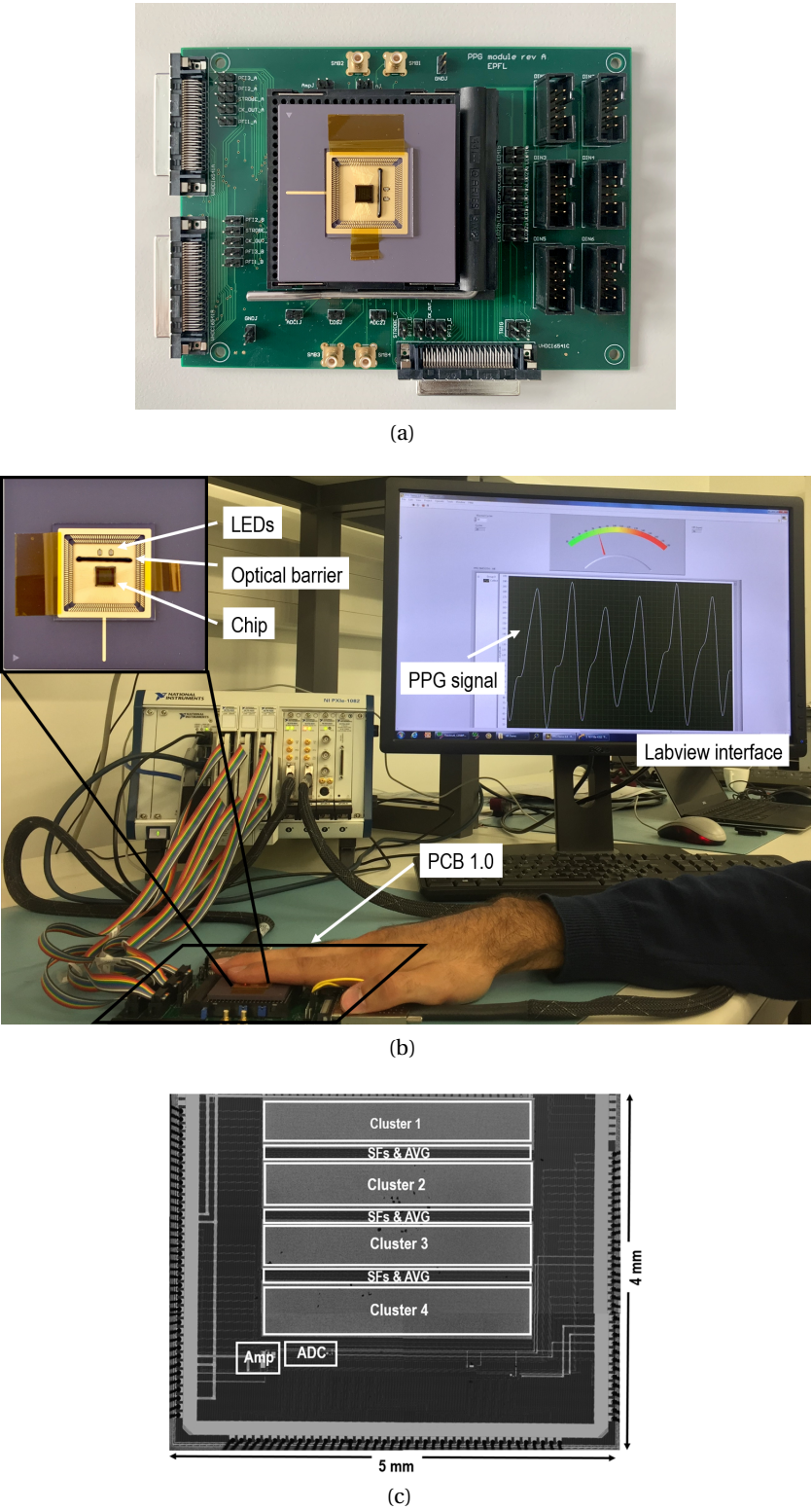


Figure 6.7 – (a) PCB 1.0, (b) PPG set-up and optical signal, highlighting the DC and AC components , (c) Micrograph of the monolithic PPG sensor, 4 mm by 5 mm.

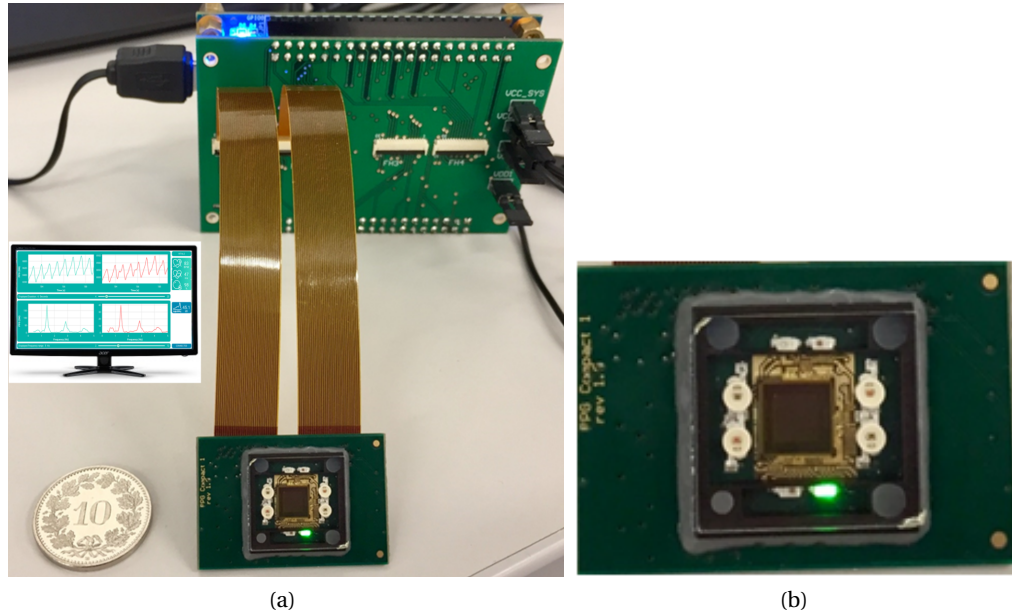


Figure 6.8 – (a) PCB 2.0: measurement set-up consisting of an FPGA device interfacing with an application running on a computer and the monolithic PPG sensor on a compact board, (b) Zoom on the compact evaluation board of 2 cm by 3 cm.

6.2.6 The characterization of the micropower PPG sensor

The objective of this section is to provide the characterization of the micropower PPG sensor. The first part is devoted to the electronic characterization, while the second to the in-vivo PPG acquisition and performance.

Light to digital conversion

The linearity of the light to digital conversion for the micropower PPG chip is shown in Fig. 6.9. The sensor is exposed to an LED shining at increasing driving current and the resulting output digital number is acquired. The programmable amplifier gain has been set to 8 which enables a wide range of emitting light conditions without saturation. With the exception of sub-mA LED operations, the chip shows $\pm 3\%$ non-linearity in the light to digital conversion. Note that this includes all the sources of non-linearity from the LED, the readout chain to the ADC. On the other hand, as described in Chapter 2, the PPG signal consists of a relatively large DC component that can change due to respiration, AL conditions, skin tone and LED-PD distance [26]. Hence, the PPG signal is generally maintained around half of the full dynamic range, which means, with respect to Fig. 6.9, keeping the ADC output around 7000 DN, (Digital Numbers). In this condition, the non-linearity is less than $\pm 1\%$.

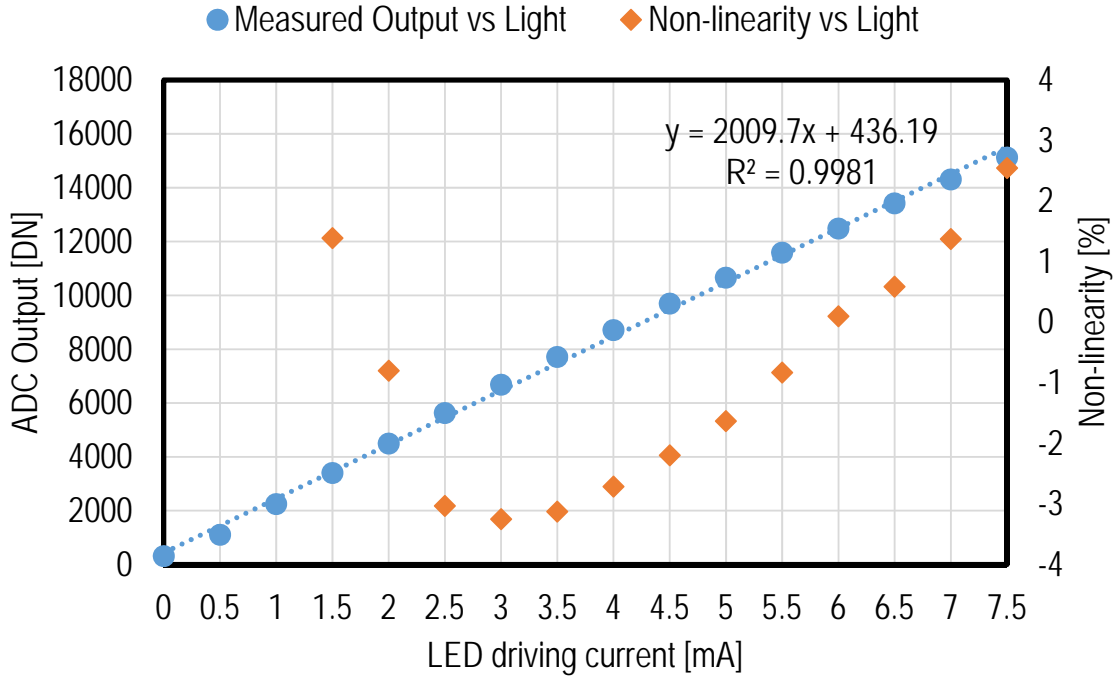


Figure 6.9 – Measured chip light-to-digital conversion linearity.

Total noise

Fig. 6.10 shows the overall sensor's output noise standard deviation (STD). The STD remains constant across the dynamic range, demonstrating the effectiveness of the shot noise reduction by the spatial averaging mechanism, as discussed in section 6.2.1. In other words, the shot noise is maintained negligible in the working conditions. The total noise measured at the output of an off-chip 11 taps FIR low-pass filter is 3.1 DNrms in average corresponding to an input-referred noise as low as 0.68 e-rms per PPD, thanks to the noise shaping introduced by the incremental ADC. Indeed, the noise measured directly at the output of the ADC corresponds to 9.43 DNrms. This accounts for all the noise components including the readout noise, quantization noise, shot noise and LED flicker noise.

Fig. 6.11 shows the impact of the variable analog gain on the overall noise. The output noise STD is reported at the output of the ADC as well as the off-chip digital LPE. The noise obtained at the output of the LPE is referred to the input after normalization with the analog gain. Fig. 6.11 shows that the noise decreases gradually by increasing the gain before reaching a plateau. The plateau represents the noise contribution level of the array and SC circuits preceding the amplifier. The contribution of the amplifier and ADC dominates only when an analog gain below 8 is applied.

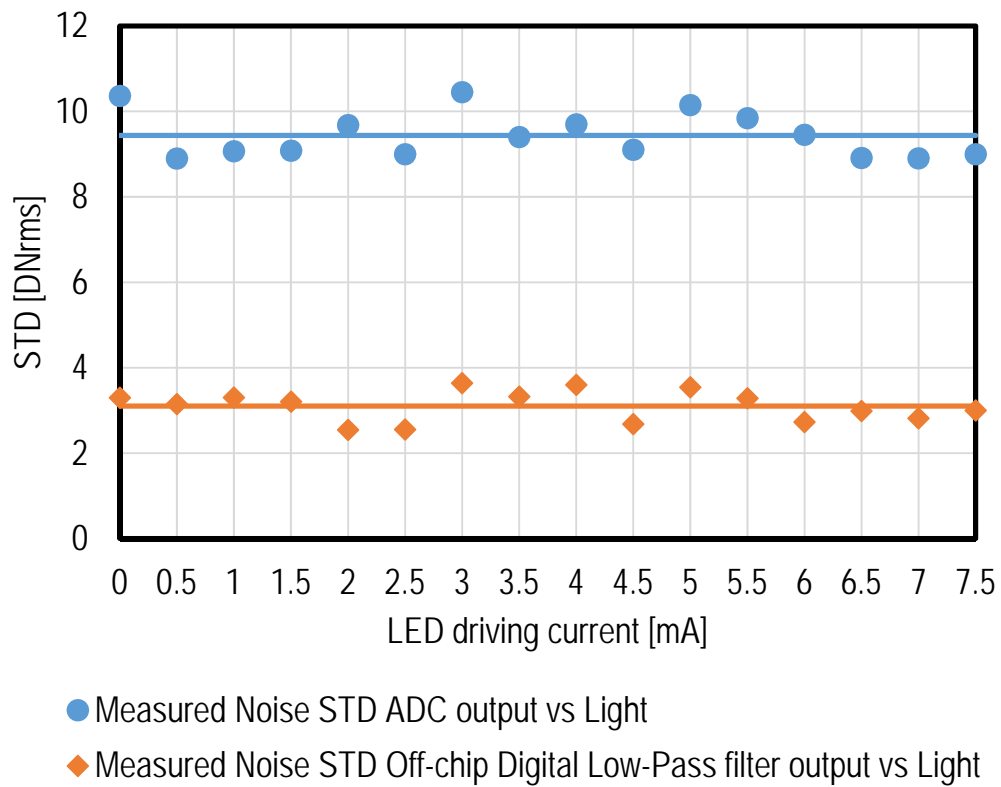


Figure 6.10 – Total noise STD shown both at the output of the ADC and an off-chip 11 taps FIR digital low-pass filter.

Ambient light cancellation

As already shown in Chapter 4, ALC is key in PPG sensors. As it is described in the previous sections, two consecutive samples can be sensed by the PPDs and subtracted thanks to the SC network and amplifier autozeroing. Assuming the ambient light conditions to be static during the two sampling interval, the first sample can sense the ambient light and the second one can have the signal superimposed on the same ambient light level. Hence the subtraction of the two samples leads to ALC. As shown in section 4.2.1, the closest the two samples are, the more efficient the ALC is.

Fig. 6.12 shows the sensor performance for ALC. The sensor is exposed to varying lighting conditions from 500 to 8500 Lux. The sensor is operated in two modes: with and without the ALC. The chip outputs, in each mode, are plotted in Fig. 6.12. The figure shows that the sensor chip, when operating with the ALC, reduces considerably the background light by about 20 dB with respect to the other mode. Note that the light source used in the experiment oscillates at 50 Hz.

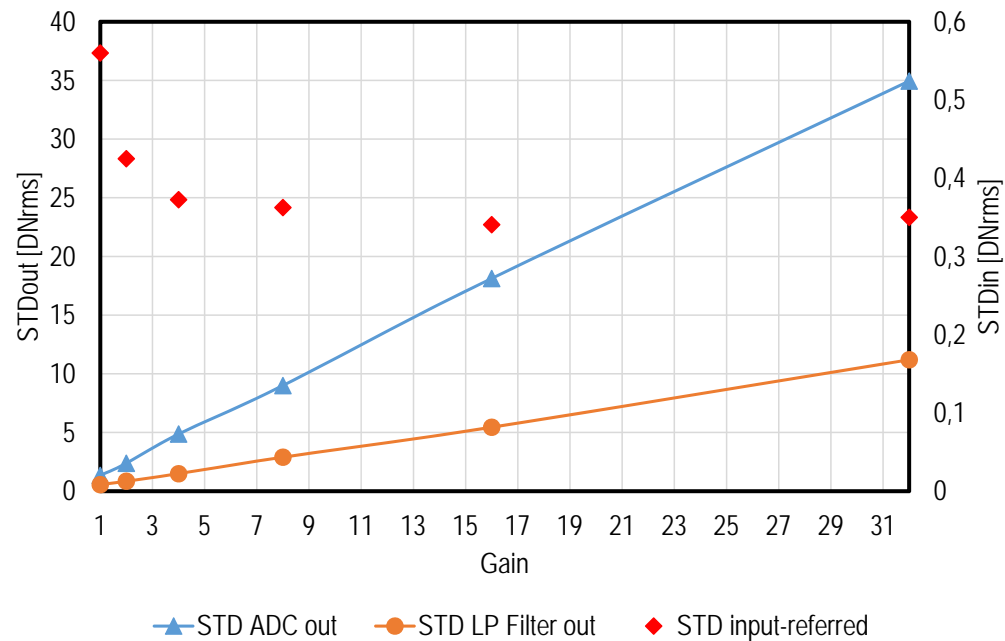


Figure 6.11 – Total noise STD, reported both at the output and input-referred, as a function of the gain.

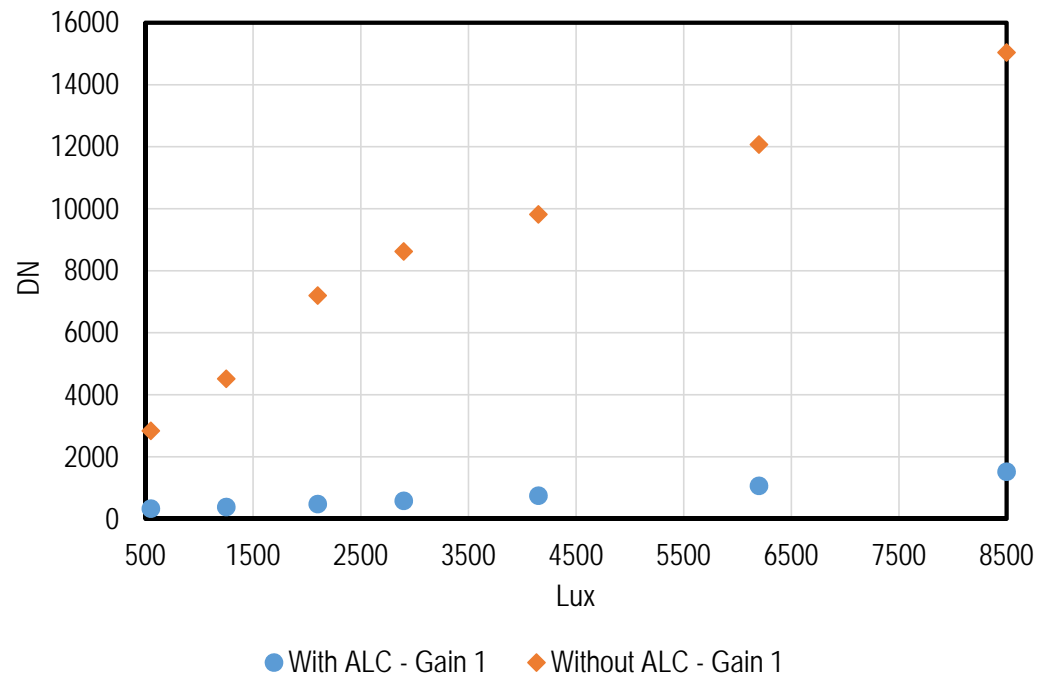


Figure 6.12 – Output DN with and without the ALC vs the AL.

Table 6.1 – ADC characterization

Parameters	[169]	This work		
<i>Technology</i> [nm]	65	180		
<i>ENOB</i> [bit]	14.78	10.44	11.7	12.08
<i>FoM_w</i> [pJ/conv.]	0.76	0.79	1.33	4.09
<i>BW</i> [kHz]	0.25	9.76	2.44	0.61
<i>Area</i> [mm ²]	0.2	0.0089*		
Note	*included a counter-based decimation filter			

ADC

In order to assess our ADC design, the Walden Figure-of-Merit (FoM) defined as

$$FoM_w = \frac{Power}{2^{ENOB} \cdot 2BW}, \quad (6.4)$$

has been considered, where *Power* is the overall ADC power consumption, *ENOB* the effective number of bits, accounting for the Signal-to-Noise-and-Distortion (SINAD), and *BW* the maximum signal bandwidth. The FoM, the lower the better, is expressed in *pJ/conv. – step* [169]. In our design, the maximum signal BW depends on the chosen resolution. Indeed, as shown in section 6.2.4, lower resolutions come with faster conversions and consequently larger allowable signal BW. The results are shown in Tab. 6.1. Our design reaches almost the same FoM as the reference work [169], but at much lower area and larger signal bandwidth, despite a less advanced technology node 180 nm in our case compared to 65 nm in [169]. On the other hand, this is achieved at a lower *ENOB*.

In-vivo PPG measurements

An in-vivo acquisition of PPG has been performed in reflection mode on the index finger. Fig. 6.13 shows a comparison between the HR directly extracted from the sensor output and a commercial ECG chest strap. The comparison features a HR average error and max error of 1.38 bpm and 3 bpm, respectively. These measurements have been taken on three healthy male subjects for a total of 222 measurements. These measurements have been obtained with a sampling frequency of 40 Hz, an average LED driving power of 1.97 μW (red light), at a duty cycle of 0.07%, and a readout (AFE+ADC) average power consumption of 2.63 μW only. This is obtained, referring to Fig. 6.5, by closing SSF for 80 μs and SAmp with SADC for 0.5 *ms*.

In Fig. 6.14 two PPG signals are shown, both recorded on the index finger. The PPG signals are recorded and displayed thanks to an application running on a computer whose interface is shown in Fig. 6.14. The two signals are recorded for a green and red LED and shown both in time and frequency domain. For both the emitting wavelengths, the Fast-Fourier-Transform (FFT) shows a clear signal component with a measured SNR of 45.1 dB for the green channel at a sampling frequency of 25 Hz. Due to the lower tissue absorption encountered by the red light,

the measured PI for the red channel is roughly 4 times lower giving rise to an SNR of about 33 dB. Together with the recorded PPG signals, Fig. 6.14 displays the real-time *HR*, heart rate variability (*HRV*) and S_pO_2 . Indeed, the measured SNR on the two channels clearly overcomes the requirements for a reliable S_pO_2 measurement, as discussed in section 6.2.1. Regarding the S_pO_2 measurement, as shown in section 3.3, the difference in the extinction coefficient of oxygenated and deoxygenated haemoglobin at the green wavelength is comparable with the difference at near-IR (800 nm). Moreover, the choice of the visible range fits best the EQE of our PPD, Fig. 6.1c, further reducing the needed LED power. The measurements as in Fig. 6.14 have been performed at a total power consumption (LED Green+LED Red+AFE+ADC) of 44 μW , out of which only 35 μW are burnt by the LEDs.

Fig. 6.15 displays a real time PPG signal recorded on the wrist for the green channel at a total power consumption (LED+AFE+ADC) of 29 μW , out of which only 20 μW are burnt by the LED. Despite the severe challenges at the wrist location due to the extremely low PI, the recorded SNR of 29.6 dB is sufficient for the strict requirement around the measure of the S_pO_2 . Unlike Fig. 6.13, measurements in Figs. 6.14 and 6.15 have been obtained with a sampling frequency of 25 Hz and a duty cycle of 0.7%. The reported power consumption is obtained, referring to Fig. 6.5, by closing SSF for 400 μs and SAmp with SADC for 2.5 *ms*.

The objective behind Fig. 6.13 is to report the lowest power consumption which is still enough to guarantee reliable HR monitoring versus a gold standard. Figs. 6.14 and 6.15 show, respectively, how much power overhead one has to account while using this sensor for more constrained applications, such as the S_pO_2 , or more challenging body locations, such as the wrist. In all cases, the micropower operations are always guaranteed.

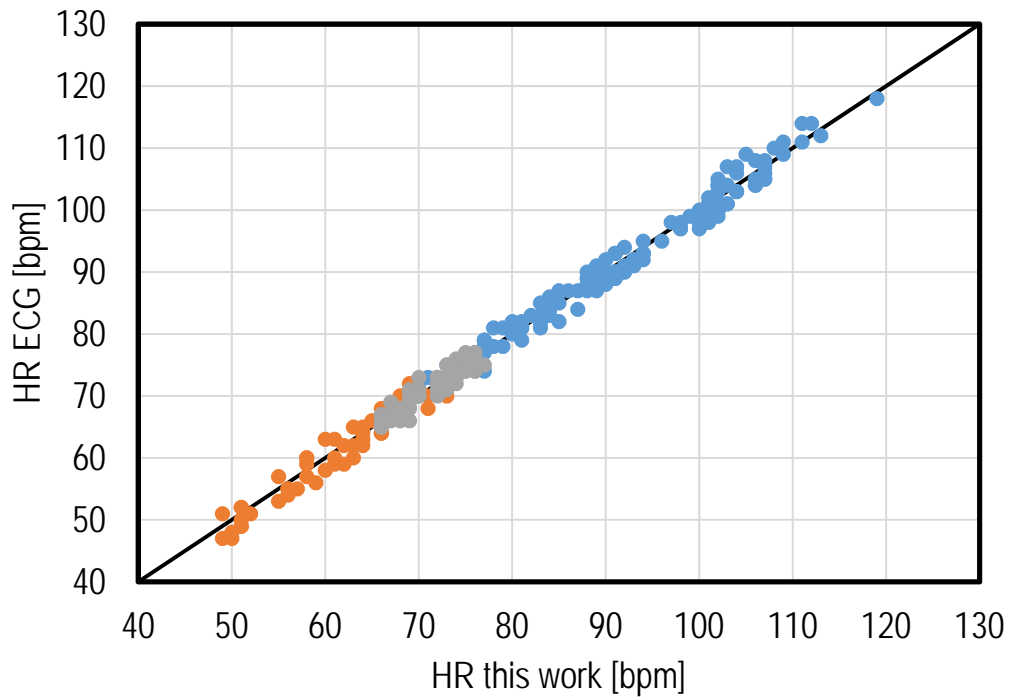


Figure 6.13 – Correlation of HR data between this work and a commercial ECG chest strap. The experiment has been carried out at $4.6 \mu\text{W}$ total power (LED+AFE+ADC) on three healthy individuals (each color representing one person).

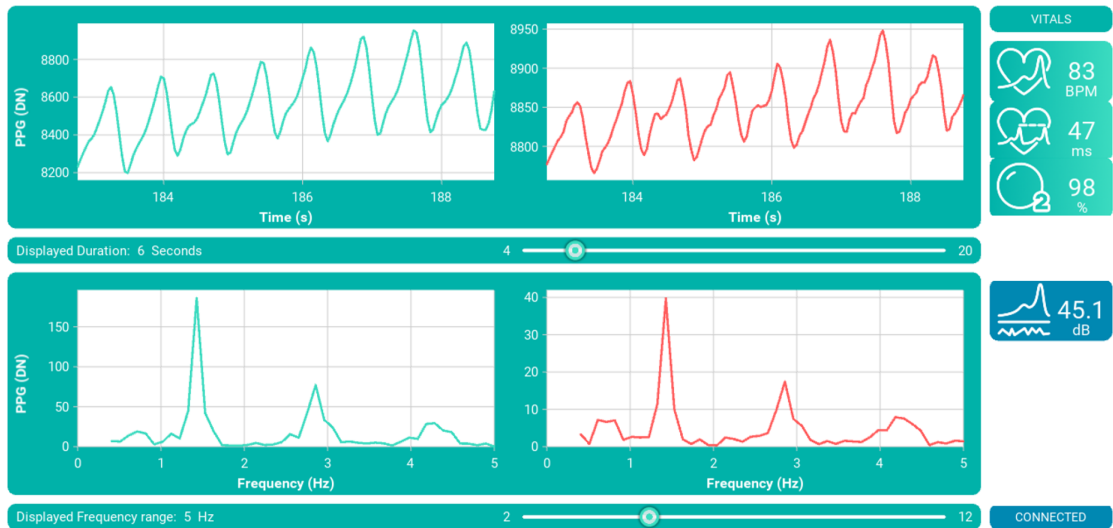


Figure 6.14 – Measured PPG raw signals at the finger for two emitting wavelengths, green and red. The real-time HR , HRV , S_pO_2 are displayed from the top to the bottom, respectively. The measured SNR is related to the green channel.

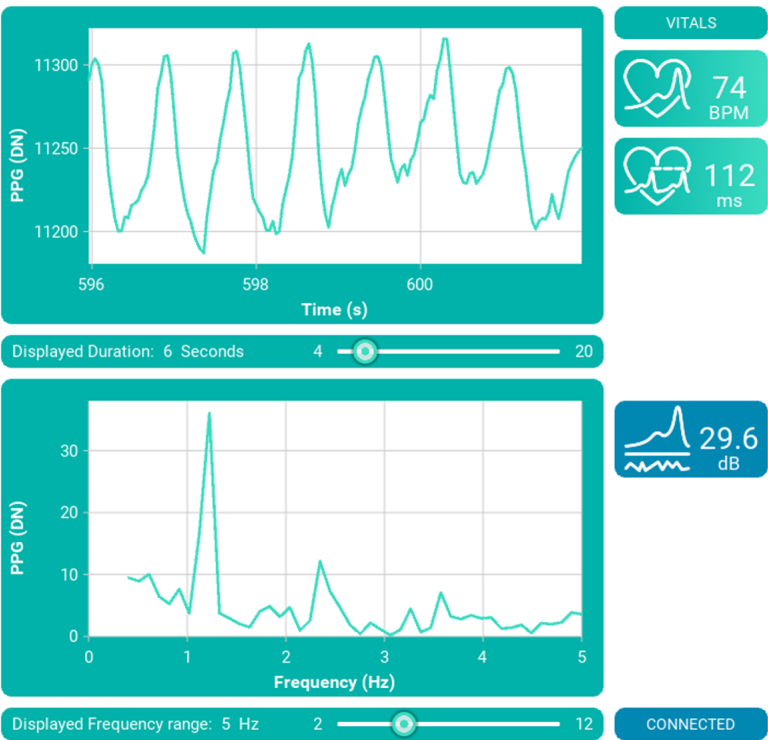
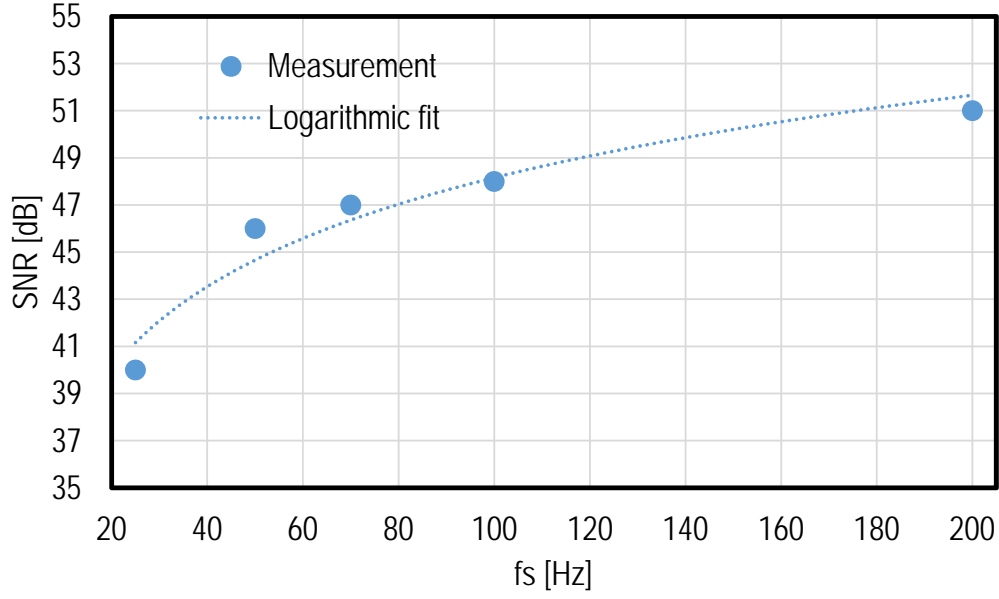


Figure 6.15 – Measured PPG raw signals at the wrist for the green channel. The real-time *HR*, *HRV* and *SNR* are displayed from the top to the bottom, respectively.


 Figure 6.16 – Measured SNR vs f_s and logarithmic fit.

SNR vs sampling frequency

The objective of this section is to show how the measured SNR of the PPG signal changes with respect to the sampling frequency, f_s . The SNR has been measured on the same subject and identical body location, i.e. finger, in order to avoid any possible measurement mismatch. The SNR is evaluated by considering the total PPG AC signal power carried by the fundamental frequency, f_{AC} , and the two harmonics, $2f_{AC}$ and $3f_{AC}$, versus the noise floor, as reported in the following equation

$$SNR_{measured} = 10 \log_{10} \left(\frac{S_{f_{AC}}^2 + S_{2f_{AC}}^2 + S_{3f_{AC}}^2}{N_{floor}^2} \right). \quad (6.5)$$

For the experiment, f_s has been swept from 25 Hz to 200 Hz, whose span guarantees a quite versatile field of use. During the measurement the subject's HR has ranged between 72 bpm and 75 bpm, meaning an f_{AC} of 1.2 Hz and 1.25 Hz, respectively. Obviously, a larger f_s comes with a larger LED and chip power consumption. In order to account for the increased power, a FoM has been introduced

$$FoM = \frac{SNR_{measured}}{Power_{total}}, \quad (6.6)$$

expressed in $dB/\mu W$, which reports the overall sensor efficiency. Fig. 6.16 shows how the measured SNR changes according to f_s . Increasing f_s results into an SNR increase. On the other hand, this translates into a consistent power increase which reduces the sensor efficiency.

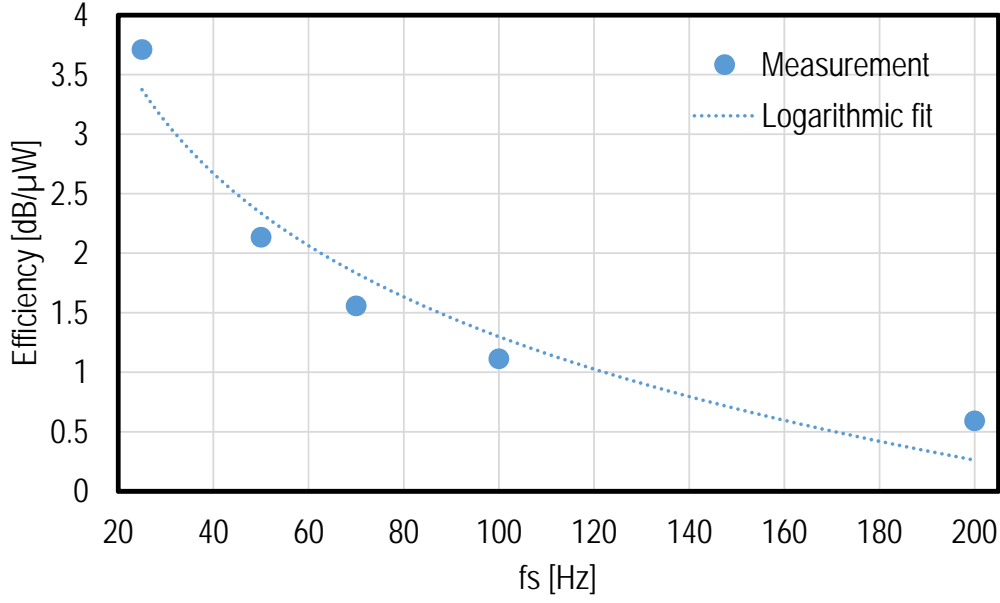


Figure 6.17 – Measured sensor efficiency vs f_s and logarithmic fit.

Indeed, as shown in Fig. 6.17, the maximum sensor efficiency is reached for f_s equal to 25 Hz.

Fig. 6.16 shows that the SNR depends logarithmically on f_s . This can be explained by the effect of the sampling frequency on the noise floor in the Nyquist band. Indeed the PPG signal is sampled without any anti-aliasing filter, which results into aliasing. In the Nyquist band the noise floor is amplified by the undersampling factor [132], which is inversely proportional to f_s . This linear behavior is transposed into a logarithm one by (6.5) which confirms the trends reported in Figs. 6.16 and 6.17. Indeed, as shown in Fig. 6.16, increasing f_s by a factor 4 results into an SNR increase of about $20\log_{10} 4 = 12 \text{ dB}$, which is exactly the measured SNR difference in dB between the 25 Hz and the 200 Hz case.

Discussion and comparison to state-of-the-art

The measurement results of the proposed PPG sensor, presented in the previous sections, are summarized and compared to the most recent and relevant state-of-the-art's work in Tab. 6.2. Tab. 6.2 shows that the proposed new sensor architecture comes with a dramatic power saving. Indeed, the enhanced sensitivity and noise performance of our chosen photodetecting scheme enable a significant power saving leading to the record low level of $4.6 \mu\text{W}$, LED included. This is about 10 to 100 times lower than state-of-the-art [117, 131, 124, 125, 126, 127, 170, 137]. Moreover, this record low power performance doesn't come at the cost of a low SNR. Indeed, the measured SNR, even at low sampling frequency, is larger than the one provided in state-of-the-art which is often lower than 40 dB [117, 131].

The improvements achieved in this work were obtained by carefully re-shaping the photode-

tection scheme and AFE. Indeed, the excellent sensitivity, EQE and noise performance of PPDs enable a consistent reduction of the needed LED power to target a specific SNR. The PPDs have been integrated into an array, this enabling spatial averaging and a consistent noise reduction. The number of PPDs has been carefully chosen based on an SNR and dynamic range analysis. This accounts for both the most important noise sources and the minimum number of impinging photons guaranteeing enough SNR at the fairly low PI of the PPG signal.

The biggest challenge to efficiently reduce the PPG sensor power consumption comes from the LEDs driving current. Indeed, due to the intrinsic limitations coming from the biological tissues [26] the LED driving current should be large enough to ensure enough light reflection. This becomes even more severe in the presence of dark skin tones. State-of-the-art's works have mostly focused on reducing the LED power by heavily duty-cycling the light emission. At first, this has happened at uniform sampling [117, 131], even though the reached total power consumption is still in the order of several hundreds of μW , as shown in Tab. 6.2.

The works in [124, 125] have presented a non-uniform, i.e. compressive, sampling PPG sensor. Indeed, the PPG signal is sparse in the frequency domain and this can be exploited to achieve a strong reduction of the LED duty-cycle and generally speaking of the average sampling frequency. A duty-cycle as low as 0.0125% and an effective sampling frequency of 4 Hz have been obtained, as shown in Tab. 6.2. Although the compressive sampling scheme comes with competitive advantages, on the other hand this is still challenging. Indeed, it requires a tight synchronization of all the system's components and reconstructing the compressive-sampled data requires additional power. Consequently, even for this work, the reached total power consumption is still in the order of several hundreds of μW , as shown in Tab. 6.2.

A heart-beat-locked loop system that significantly reduces the LED power by activating the light emission only during the PPG peaks has been recently demonstrated in [126, 127]. However, this power reduction comes at the cost of more complexity since it requires a non-trivial heart beat prediction scheme and intrinsically hinders the full PPG wave representation.

The proposed solution relying on a PPD array enables the full integration of the photosensitive area together with the AFE. Indeed, an off-chip PD comes with a non-negligible parasitic capacitance, ultimately limiting the noise performance and the speed/power of the AFE. Moreover, it increases the silicon area. The recent work in [137] shows an interesting PPG sensor integrating on silicon an array of PDs with distributed 1b delta-sigma light-to-digital converter. Despite the achieved power consumption is very promising versus the state-of-the-art's work, this doesn't account for the LED driving current which is supposed to be quite large given the fairly high sampling frequency.

Table 6.2 – Summary of the PPG sensor performance with comparison to state-of-the-art.

Reference	This work		[117]	[131]	[124, 125]	[126, 127]	[170]	[137]
Year	2019	2013	2015	2015	2016	2018	2015	2017
Technology [<i>nm</i>]	180	350	180	180	180	180	350	180
Supply Voltage [<i>V</i>]	3.3/1.8 ^a	3.3	1.8	1.2	1.2	3.3	3.3	NA
Sampling Frequency	40	100	165	4	100	10000	10000	160000
[<i>Hz</i>]								
LED Duty Cycle [%]	0.07	3	0.7	0.0125	0.0175	NA	NA	10 ^b
Full Integration ^c	Yes	No	No	No	No	Yes	Yes	Yes
Avg HR Error [<i>bpm</i>]	1.38 ^d	NA	NA	NA	NA	NA	NA	NA
Max HR Error [<i>bpm</i>]	3	NA	NA	10	2.1	NA ^e	NA ^e	NA
LED Power [<i>μW</i>]	1.97-26.6	309-1360	120-1125	43-1200	16-520	NA	NA	NA
AFE+ADC Power	2.63	528	216	172	27.4	NA	NA	13-14.4 ^f
[<i>μW</i>]								
TOT Power [<i>μW</i>] ^g	4.6	837	336	215	43.4	4600 ^h	4600 ^h	NA

^aADC supplied at 1.8 V^bReported data for LED pulsed operations^cPhotosensitive area+AFE+ADC^dMeasured at 4.6 μ W total power vs a commercial ECG chest strap on 222 measurements on three healthy individuals, as in Fig. 6.13^eThe work focuses on the $S_p O_2$ accuracy^fLED Pulsed operations^gBest case from the given data for the HR mode^hSupposed to be dominated by the digital processing unit

6.3 AC/DC ratio enhancement

As already mentioned earlier in this manuscript, the extremely low PI of a PPG signal, makes the dynamic-range (DR) a key constraint in PPG sensors design. As shown in Chapter 4, the DR ultimately determines, for instance, the resolution with which the S_pO_2 can be measured. The tight link between the required DR, the S_pO_2 and the PI has been shown in Fig. 4.5. For the worst PI case, i.e. 0.2%, a receiver DR larger than 90 dB is needed to ensure an accuracy within 0.2% of the S_pO_2 in the 70%-100% range.

State-of-the-art works have tried to solve the DR challenge in PPG analog front-end (AFE) either by the means of logarithmic amplifiers [133] or thanks to feedback loops which subtract a variable DC current from the AFE input [46, 117, 131, 126]. All the above-mentioned solutions rely on additional circuitry at the cost of more complexity, power consumption and silicon area. Another possibility, as shown in Chapter 2, relies on increasing the PD to LED distance, at the cost of a larger LED power [26].

This chapter shows an extremely low-power PPG sensor taking advantage of the high sensitivity of PPDs together with an ultra-low noise and low power AFE. Moreover, the PD area is implemented as an array of double TG PPDs. The double TG structure allows to precisely control the integrated charges and to efficiently cancel the AL. The double TG structure mentioned above can also be exploited to enhance the PI of the PPG signal at the device level consequently relaxing the DR requirements on the AFE. Measurement results show that by tuning the TG control voltage and the transfer time, the PPG PI can be enhanced by a factor 5 without any signal loss or additional circuitry.

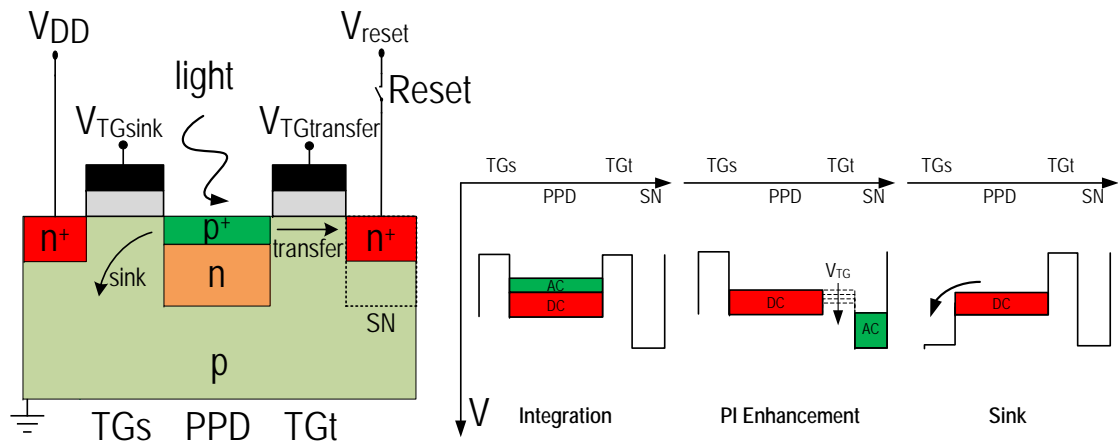


Figure 6.18 – The double TG PPD device and the three most important phases: Integration, PI Enhancement and Sink. The PI Enhancement illustrates a PPD readout in which only a part of the integrated photo-generated electrons reaches the SN.

6.3.1 Working principle

As shown in section 6.1, a PPD consists of a np junction buried under a shallow highly doped p+ thin layer. It behaves as a charge well where the photo-generated electrons are stored. The TG controls the potential barrier at the edge of the PPD. The two transfer-gates structure, a sink gate (TGs) and a transfer gate (TGt), allows to precisely control the charge integrated into the well and eventually reaching the sense-node (SN). TGt allows only the part of the charge corresponding to the AC component of the PPG signal to reach the SN, whereas TGs dumps the remaining DC charge. The work in [168] shows that the potential barrier encountered by the photo-generated electrons while diffusing towards the SN is modulated by the TG control voltage, V_{TG} . The amount of diffusing charge depends exponentially on V_{TG} , while logarithmically on the transfer time, $t_{transfer}$. Hence, V_{TG} and $t_{transfer}$ can be used to set the proportion of the diffusing charge towards the SN with respect to the one remaining in the PPD. This mechanism can be efficiently exploited to improve the PI of the PPG signal. Indeed, during the integration phase, assuming the PPD is far from saturation, the PPD stores both the DC and AC components of the PPG wave, as shown in Fig. 6.18. By tuning both V_{TG} and $t_{transfer}$, the PI can be enhanced by transferring only the AC-related charge, leaving the DC part in the well. The double TG scheme enables, thanks to the sink phase, to empty the PPD well from this remaining DC-related charge. Transferring only the AC-related charge to the SN relaxes the DR constraints on the AFE and hence reduces its power consumption.

6.3.2 Measurements results

The idea described above is validated using the micropower PPG sensor described earlier in this chapter. The PPG signal is emulated by a green LED shining at 525 nm which is continuously driven by a sinusoidal current oscillating at 0.8 Hz (corresponding to an HR of 48 bpm), superimposed onto a DC current in order to mimic a PPG wave featuring a PI equal to 10 %. It should be mentioned that the proposed method works throughout the full possible PPG frequency range (up to 4 Hz), as long as the PPD integration time remains shorter than the maximum frame rate. The green LED is chosen since usually preferred in a PPG sensor for its intrinsic larger PI, as shown in Chapter 2. On the other hand, the proposed method can be implemented even for different emitting wavelengths, i.e. red. The measures have been performed at 50 Hz sampling frequency. The proposed set-up guarantees no artefacts coming from measurements on human beings. Indeed, factors such as the displacement between the body location and the PPG sensor or specific metabolic conditions may have introduced incoherent measurement results.

The measurement results are shown in Figs. 6.19 to 6.21. Fig. 6.19 shows the transferred DC and AC components of the emulated PPG signal versus V_{TG} , ranging from 0.3 V to 3 V and for different $t_{transfer}$, ranging between 100 ns and 1 μ s, at steps of 100 ns. In Fig. 6.19 the trade-off between V_{TG} and $t_{transfer}$ is illustrated. For the longest $t_{transfer}$ equal to 1 μ s almost all the DC charge is transferred for V_{TG} larger than 2.5 V. Whereas, for the shortest $t_{transfer}$ equal to

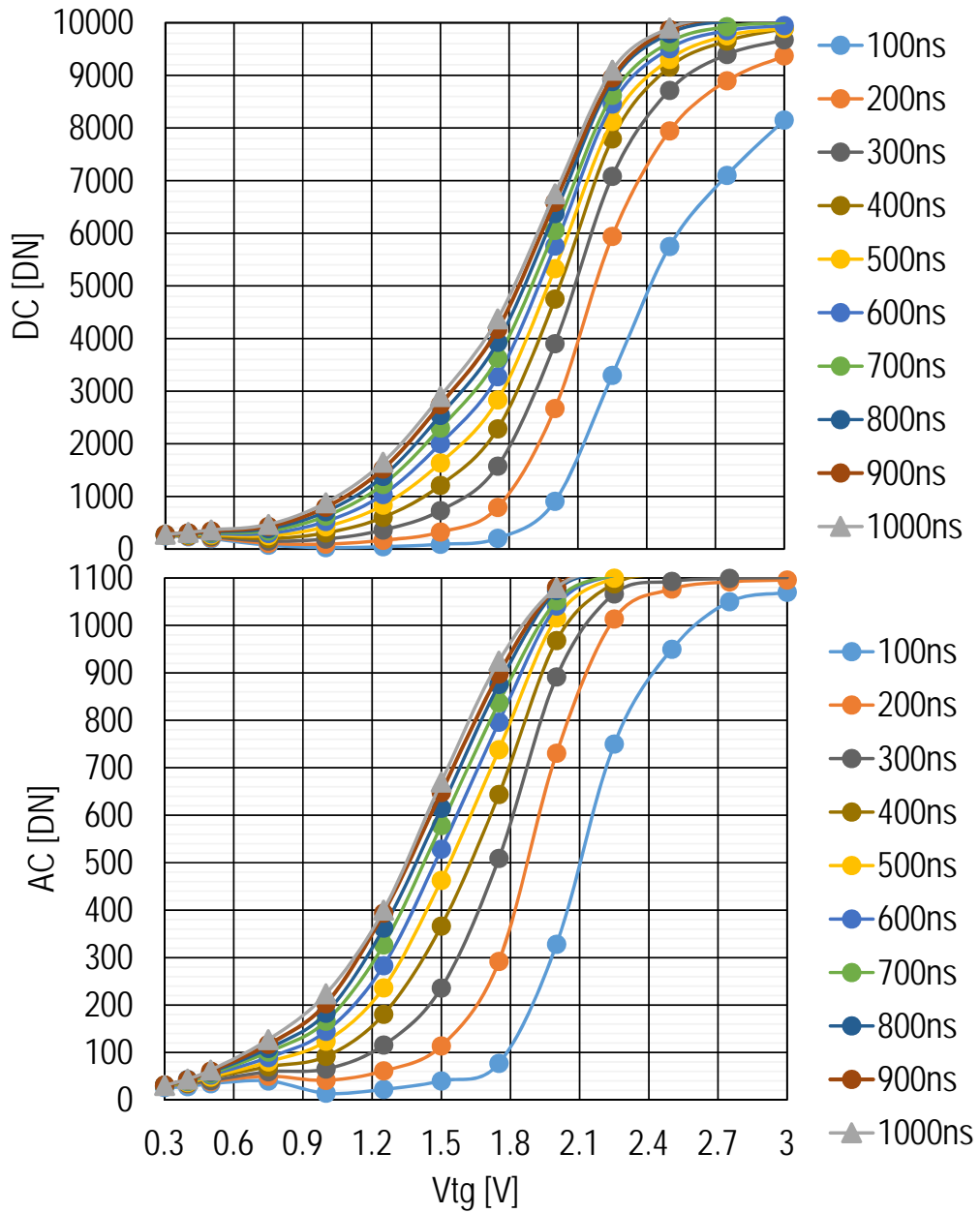


Figure 6.19 – Measured DC and AC components of the emulated PPG wave vs the TG control voltage for several transfer times.

100 ns only 80% of the DC charge is transferred even at the maximum V_{TG} .

Regarding the AC component, as expected, the full scale of the AC signal is roughly 10% of the DC one. Unlike the DC component, a complete AC transfer already happens at V_{TG} equal to 2 V for the longest $t_{transfer}$. Fig. 6.19 illustrates that transferring the same fraction of charges requires less V_{TG} for the AC component than the DC one. This property can be exploited to enhance the PI of the PPG signal as demonstrated in Fig. 6.20. Fig. 6.20 shows the PI computed from the measured signals of Fig. 6.19 versus V_{TG} , for the same values of $t_{transfer}$. For all the

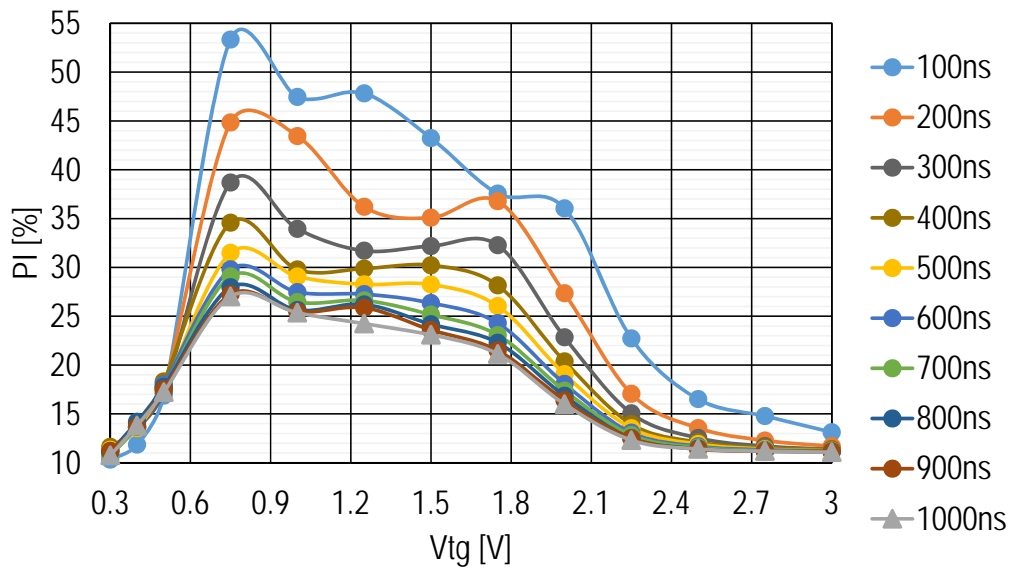


Figure 6.20 – Measured PI vs the TG control voltage for several transfer times.

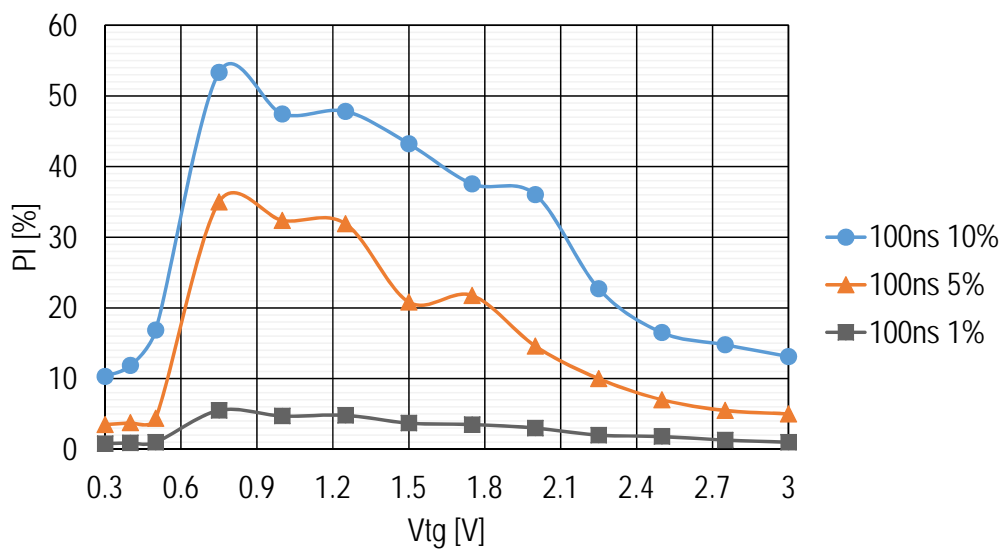


Figure 6.21 – Measured PI vs the TG control voltage at three different emulated PPG PI, 10%, 5% and 1%, for $t_{transfer}$ of 100 ns.

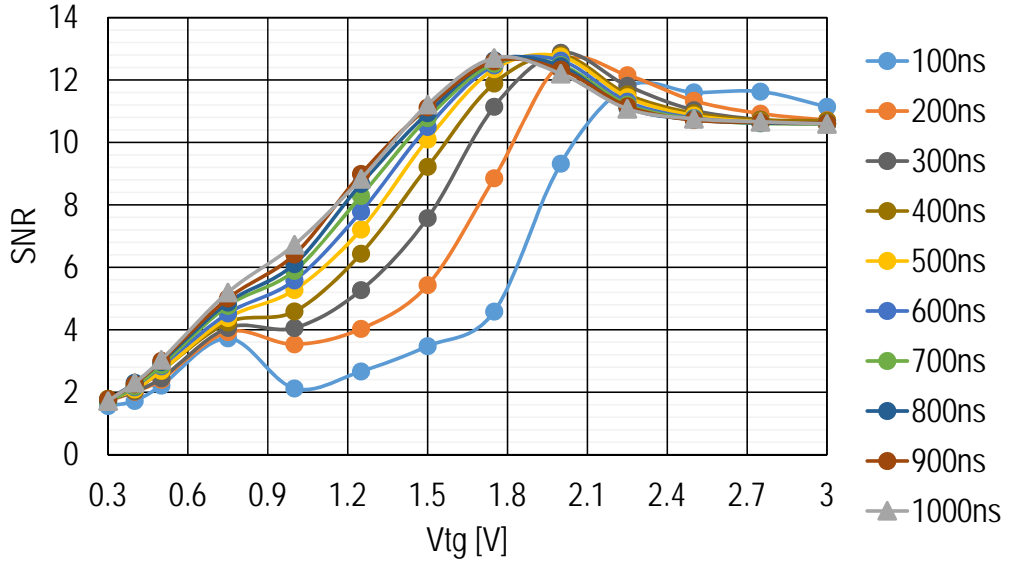


Figure 6.22 – Measured SNR vs the TG control voltage for several transfer times.

proposed $t_{transfer}$, reducing V_{TG} down to a certain value comes with a significant increase in the measured PI, as explained above. A maximum PI has been measured between 0.75 V and 1 V. Below these values, the increasing potential barrier encountered by the photo-generated electrons comes with a consistent PI reduction. In addition to V_{TG} , $t_{transfer}$ represents a second degree of freedom. Indeed, Fig. 6.20 also shows that even for the optimal V_{TG} , as above, shortening the transfer time is beneficial to enhance the PI. In particular, $t_{transfer}$ and V_{TG} equal to 100 ns and 0.75 V, respectively, show the best measured PI. Unlike the standard way of operating a PPD, $t_{transfer}$ and V_{TG} larger than 1 μ s and 2.75 V, respectively, the proposed configuration enhances the PI by more than a factor 5. Fig. 6.21 shows the impact of the proposed PI enhancement technique for three different emulated PI cases, 10%, 5% and 1% for $t_{transfer}$ of 100 ns. It confirms that this technique can also adapt to PPG signals with different PIs.

6.3.3 Discussion on the AC/DC ratio enhancement technique

As shown in Fig. 6.19, thanks to the PI enhancement, the DC component drops from 10000 DN to 80 DN. This relaxes the DR constraints on the readout chain by 42 dB. On the other hand, the AC component is also reduced. Hence, analysing the effect of the proposed PI enhancement technique on the SNR is also important. In PPG applications the best achievable SNR is limited by the shot noise related to the charge transfer mechanism, whose standard deviation corresponds to $\sqrt{DC + AC}$. The maximum SNR can then be expressed as $AC/\sqrt{DC + AC}$. Fig. 6.22 shows the impact of the PI enhancement technique on the SNR. For the 100 ns $t_{transfer}$ case, the SNR can be maintained constant up to V_{TG} equal to 2.1 V. In this case, for the same SNR, the DR is relaxed by more than 15 dB.

Conclusions

This chapter demonstrates that a PPD device is an excellent alternative to conventional PN or PiN-based PD for PPG applications. Indeed, the extremely low noise and high sensitivity performance of PPD devices accompanied by an ultra low noise and low power AFE represent the two key ingredients for reducing the LED power consumption.

The PPG sensor presented in this chapter integrates an array of PPDs, a SC AFE and an ADC. Placing the PPDs into an array eases the engineering trade-off between the possible achievable dynamic range and the overall noise performance. The total number of pixels has been chosen according to the target SNR to achieve an accuracy within 2% of the peripheral oxygen saturation. The photosensitive area consists of four clusters of 50 rows and 256 columns, meaning 51200 total pixels. The 50 pixels along the i-column are assembled in a macro-pixel (MP). The pixels of one MP share the same source-follower, so saving power while maintaining a reasonably low parasitic capacitance at the shared SN.

Each pixel within the MP embeds a double TG structure: a sink TGs and a transfer gate TGt . The double TG structure allows to precisely control the charge integrated into the PPD well and eventually reaching the SN for processing. Specifically, TGs sinks the charge cumulated in the PPDs to the reset voltage, while TGt allows the charge transfer to the SN. The SN is shared between multiple PPDs, which are gated to either sink or transfer their charge synchronously. This process is also referred to as charge binning. It allows averaging the outputs of the MP PPDs without the need for any additional circuitry. This charge binning also enables more efficient and faster charge transfer compared to a single large PPD with equivalent area by mitigating the effect of charge transfer non-idealities.

Compared to recent state-of-the-art this work comes with the lowest power consumption. Moreover, among the most relevant state-of-the-art's works, this is the only solution featuring a full integration of the photosensitive area together with the AFE and the ADC at an extremely low power consumption, i.e. smaller than $10\ \mu\text{W}$, this accounting both for the LED and the AFE+ADC.

The double TG structure, within the MP, can also be exploited for enhancing the PI of a PPG signal, without any power or silicon overhead, by properly tuning the TG control voltage and the charge transfer time. TGt can allow only the part of the integrated charge corresponding to the AC component of the PPG signal to reach the SN. Whereas, TGs can dump the remaining DC charge. In this regards, this work further illustrates the trade-off between the TG control voltage and the charge transfer time. It points out that a larger fraction of the AC signal is transferred at a lower TG control voltage with respect to the DC one. This translates into a maximum PI occurring at TG control voltage around 1 V, for charge transfer time ranging between 100 ns and $1\ \mu\text{s}$. A maximum PI enhancement of a factor 5 is reached for TG control voltage and charge transfer time equal to 1 V and 100 ns, respectively. In addition, the PI can also be increased considerably without any impact on the SNR for optimal transfer parameters.

Compared to state-of-the-art PI enhancement techniques, this work comes without any circuit power consumption or silicon area overhead. Indeed, the PPG PI is corrected right at the level of the PPD by properly tuning the TG control voltage and the charge transfer time.

It should be recalled that, despite the great potential behind the PPG technology, the fairly large power burnt by the LEDs still represent a serious challenge towards truly continuous PPG operations. In this perspective, the proposed micropower PPG sensor represents a turning point. The extremely low power consumption and excellent signal quality combined with the possibility of PI enhancement makes this solution a serious answer to the increasing demand of continuous and reliable health monitoring devices, especially when the body location makes the PPG recording suffer from a particularly low PI.

7 A low-power and mm-resolution 1D ToF sensor

In the ever expanding field of consumer electronics and wearable devices, light sensing is playing a key role in closing the loop between the user, his environment and the electronic device. Devices such as smartphones, smartwatches or wrist bands embed photonic sensors for imaging, display control, user recognition, proximity sensing and even health monitoring involving measurements of the light intensity, photons time-of-flight (ToF) or spectroscopy.

Increasing the interest for portable consumer electronics relies on two conflicting factors which are the miniaturization and the battery lifetime on one side, and enhancing the applications and interaction possibilities on the other side. Hence, integrating more and more sensors is becoming one of the key challenges in the smartphone and smartwatch industry especially for photonic sensors that require specific constraints such as being all located at the surface of the device.

One question rises when addressing this problem: would it be possible to converge several photonic applications in a single sensor? The move of some semiconductor market leaders towards this direction supports the relevance of this question [171].

7.1 Towards "all-in-one" photonic sensors

One of the challenges facing this "all-in-one" trend resides at the early front-end of each light sensing readout chain: the photosensitive device. Indeed, today large junction photodiodes are used for ALS [151], CMOS PPDs are used for imaging [172], single photon avalanche photodiodes (SPADs) are used for direct ToF [173] and so on. Each of these sensors originate from a different mainstream technology making it complicated to integrate all of them on a same chip.

The PPD [174] presents a great opportunity in this regard. PPDs are perfectly integrated into CMOS processes with even advanced technology nodes [175] [176]. The performance proven in the last decade at the level of noise, sensitivity and dynamic range makes the PPDs ultimately suitable for high precision light sensing [177, 178, 166, 164, 179]. In addition, the

fast gating of these devices offers the possibility of addressing time resolved applications such as ToF [180, 181, 182]. Last but not least, the compatibility of PPDs with CMOS processes [175] reduces dramatically the cost for large volume production.

In this chapter we aim at answering the question raised above: is it possible to design a PPD based sensor chip suitable for a variety of applications related to mobile and wearable devices with key features such as ultra-low power, high sensitivity and ultra-low noise?

In Chapter 6 we have demonstrated that the PPDs are excellent alternatives to standard PDs in the emerging digital health domain. Their enhanced performance, in terms of both noise and sensitivity, accompanied by an ultra low-power and low-noise AFE leads to a truly micropower PPG sensor design, reducing the total power consumption from one to two order of magnitude with respect to the state-of-the-art.

The objective of this section is to demonstrate that the same chip can be also used for ToF distance measurements, at low-power and mm resolutions operations.

7.2 Direct and indirect ToF operations

ToF devices are active illumination system consisting of a laser, usually a vertical-cavity surface-emitting laser (VCSEL) and a sensor. The laser emits the light towards a target, which is, partially, reflected back to the sensor. The time needed for the light to travel back-and-forth from the target, i.e. ToF, is measured and translated into a distance. The travelled distance is the product of the speed of light with the half of the measured time.

Historically, there are two ways of measuring the ToF: by the means of direct or indirect operations, as shown in Fig. 7.1. In the direct mode, the time difference (delay) between the emitted pulse and the received signal is evaluated. In other words, the VCSEL sends a light pulse and a counter measures how long it takes for this pulse to reach the sensor back from the target. This is usually called "stop-watch" approach. On the contrary, the indirect approach modulates the emitted light at a certain frequency and measures the ToF by evaluating the phase difference between the modulated laser emission and the incoming signal from the target.

Direct ToF systems usually embed SPADs. By knowing the speed of light, TDCs are used to measure the time between the incident and the reflected light, exploiting the excellent sensitivity of SPADs. Despite direct ToF camera are nowadays the key elements behind the LiDAR (light-detection-and-ranging), especially in the automotive business where the range requirements are usually in the hundred of meters, they show some limits at sub-mm resolutions. Indeed, achieving 1 mm resolution means being capable, on the electronics side, to discriminate 6.7 ps, which relies on excellent timings.

Indirect ToF systems usually embed demodulation pixels (2 taps, 4 taps), including PPDs. Indirect ToF operations are today preferred for small range 3D imaging applications, since

less constrained by the usually longer required integration time, with respect to the LiDAR applications. For indirect operations, the modulation frequency determines the maximum measurable distance. Indeed, given a modulation frequency f_m , the maximum range is the speed of light divided by two times f_m . Beyond this value, the modulated laser emission and the incoming signal become indistinguishable. The indirect ToF range imagers can be sub-classified depending on the light source. Indeed, the laser can be either modulated by a sinusoidal wave (continuous wave) or by a square wave (pulsed illumination). Pulsed illuminations require simpler distance evaluation. On the contrary, continuous wave stimulation usually requires quadrature sampling techniques to evaluate the phase delay.

The objective of this chapter is to explore whether an indirect PPD-based ToF system can become a serious alternative to SPADs in LiDAR applications.

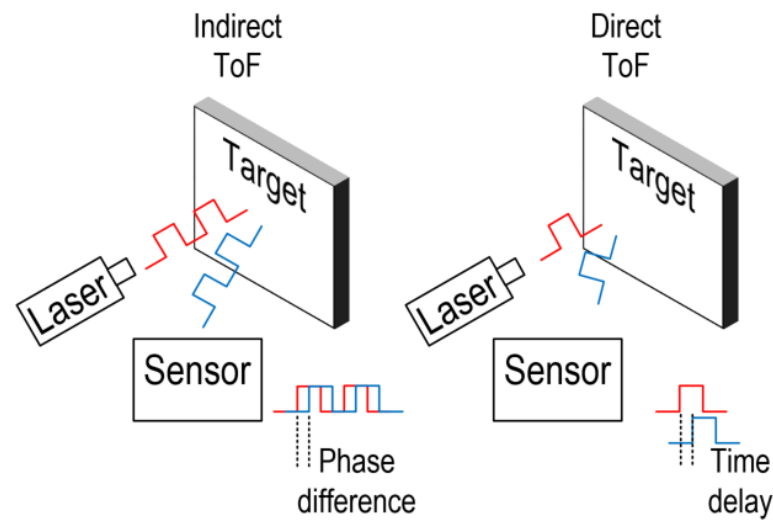


Figure 7.1 – Indirect and direct ToF operations.

7.3 A low-power 1D indirect ToF sensor

For the sake of clearness, the chip architecture is re-proposed in Fig. 7.2. Indeed, this is the same as in Chapter 6.

1D ToF distance ranging is key in several applications from consumer electronics to industrial metrology. For portable applications such as drones, cameras and smartphones, safety and power consumption constraints make ToF sensors suffer from a generally poor signal reflected back from the scene featuring a small contrast with ambient light. This section shows how the micropower PPG sensor presented in Chapter 6 is used to perform single point ToF distance measurement while addressing the aforementioned issues. In the following, it is demonstrated how high fill factor and ultra-low noise featured by the presented sensor enable the reduction of both the light source and the sensor power consumption to cope with the constraints of portable applications.

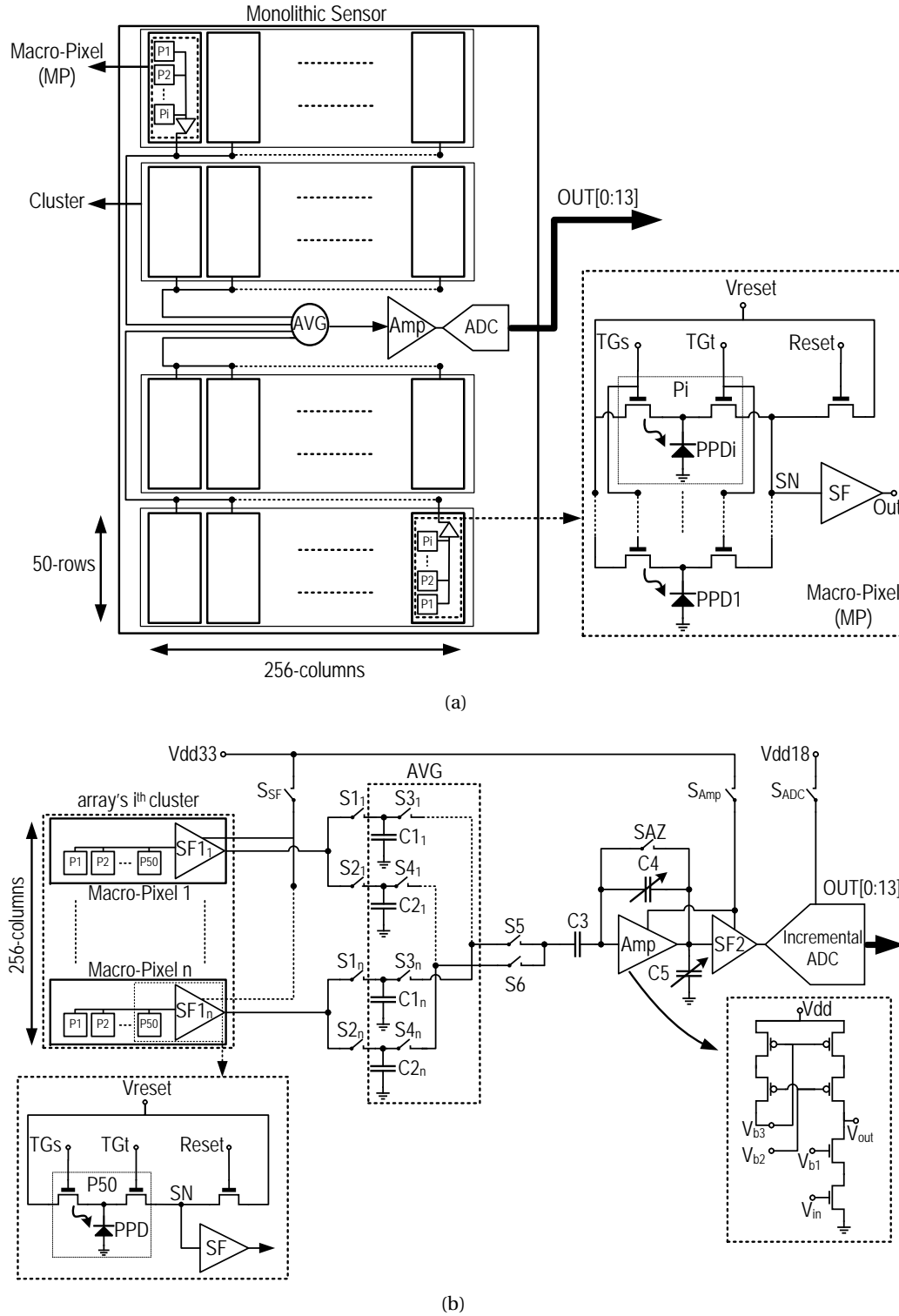


Figure 7.2 – The PPD-based sensor: (a) block diagram of the proposed sensor, (b) Architecture of the sensor and detailed schematic of the OTA, used in the amplifier, and the averaging block.

Fig. 7.3 shows how the circuit of Fig. 7.2 is driven to perform an indirect ToF measurement. As shown in Figs. 7.3b and 7.3c, the source is modulated at the same frequency as the TGs and TGt . The readout operation as shown in Fig. 7.3a is repeated twice.

For the first readout, TGs and TGt are operated as shown in Fig. 7.3b. At the end of the phase Φ_1 a first voltage proportional to a charge Q_1 is sampled and held in capacitors $C1_{1...n}$. The

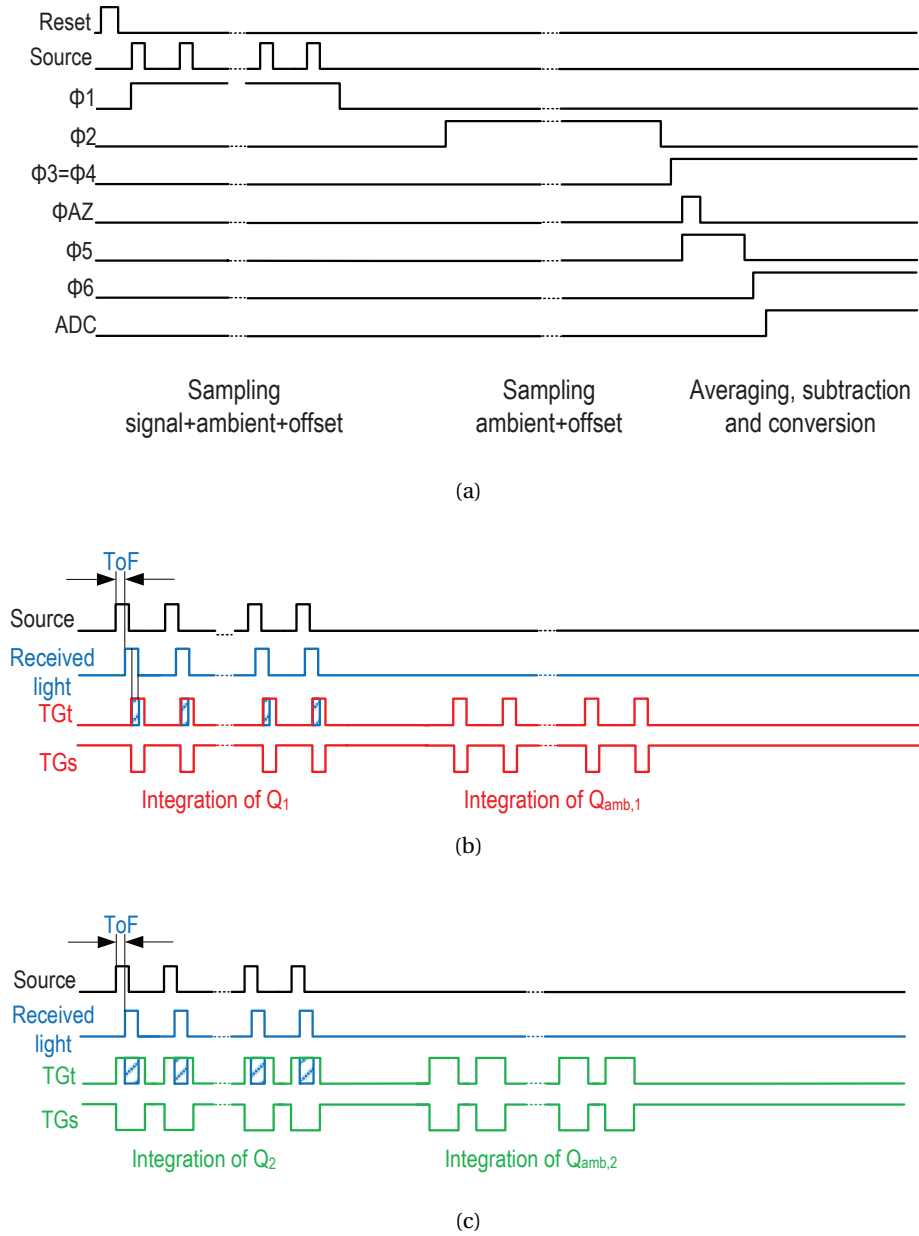


Figure 7.3 – PPG timing diagram related to Fig. 7.2b. (a) Readout chain, (b) Transfer gates and source control for first acquisition and (c) second acquisition.

charge Q_1 can be expressed roughly as

$$Q_1 = \alpha \cdot ToF \cdot Q + Q_{amb,1} + cte, \quad (7.1)$$

where Q is the charge corresponding to the total light emitted by the source, α is the attenuation depending on the distance and reflectivity of the object, $Q_{amb,1}$ is the charge corresponding to the ambient light and ToF is the time that light needs to travel from the source to the sensor. Indeed, the longer ToF the more emitted light gets integrated within the exposure windows. In the phase Φ_2 , the same operation is repeated without pulsing on the source in order to integrate only the charge related to ambient light $Q_{amb,1}$. A voltage proportional to this charge is sampled and held on capacitors $C2_{1...n}$. Thanks to the switched capacitor amplifier, the two samples are subtracted, leading to a first sample proportional to $Q_1 - Q_{amb,1}$. A second readout is then performed with TGs and TGt operated as shown in Fig. 7.3c. At the end of the phase Φ_1 , a first voltage proportional to a charge Q_2 is sampled and held in capacitors $C1_{1...n}$. The charge Q_2 can be expressed roughly as

$$Q_2 = \alpha \cdot Q + Q_{amb,2} + cte, \quad (7.2)$$

where $Q_{amb,2}$ is the charge corresponding to the ambient light. Indeed, in this phase, the integration window is large enough to integrate the total amount of charge $\alpha \times Q$. In the phase Φ_2 the same operation is repeated without pulsing on the source in order to integrate only the charge related to ambient light $Q_{amb,2}$. In the same way as above the two samples are subtracted leading to a second sample proportional to $Q_2 - Q_{amb,2}$.

Thanks to the two separated readouts the ToF can be calculated as

$$ToF = \frac{Q_1 - Q_{amb,1}}{Q_2 - Q_{amb,2}} + cte, \quad (7.3)$$

where cte is a calibration parameter depending on the offset and time windows characteristics. The ratio used to calculate ToF is a normalization which makes the ToF measure insensitive to the source power and the target colour.

7.3.1 Characterization of the low-power 1D ToF sensor

The performance of the proposed 1D ToF sensor has been characterized with the testing set-up, as shown in Fig. 7.4. It is the same as the one presented in Fig. 6.7a, for the PPG application, with the only difference of an external 10 mW 650 nm VCSEL. Like the PPG application, the data acquisition has been performed by means of the National Instruments PXI e-1082 machine. A Labview interface is used for computing the ratio given by (7.3) and displaying the measured distance.

The chip characterization for the ToF operations has started with the assessment of the pertinence of the sensor itself for time-resolved applications. In this regard, the sensor has been directly exposed to a VCSEL without any intermediate optical system. All the measurements

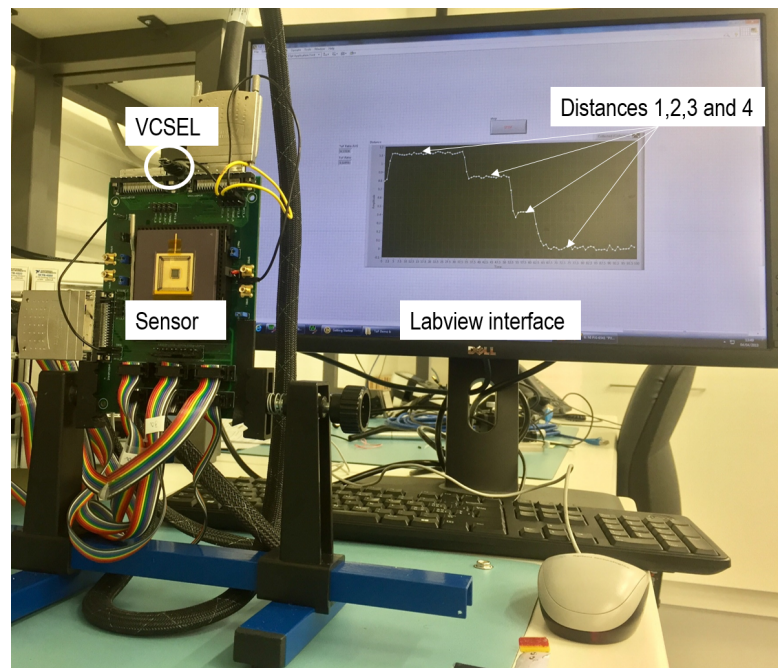


Figure 7.4 – ToF measurement set-up showing the sensor and the VCSEL without any lenses and the labview interface displaying the real time measured distance.

have been performed at room temperature. The source is duty cycled to generate, during the exposure time of $6\ \mu\text{s}$, 144 consecutive pulses of 16 ns duration with a period of 40 ns, as shown in Figs. 7.3b and 7.3c. The average (accounting for the duty cycle) current consumption during the exposure is as small as $6\ \mu\text{A}$ with a driving voltage of 2.1 V. The delay between the source pulses and the transfer windows is swept in order to characterize the way the output of the sensor follows the laser pulse delay. Fig. 7.5a shows how linearly the sensor output follows the delay generated, first in steps of 100 ps and then is steps of 1 ns. The cumulative measured error standard deviation accounting for non-linearity, noise and source noise is less than 10 ps. This demonstrates that this architecture is suitable for time-resolved applications requiring 10 ps timing resolution without having to use any on-chip or off-chip high speed circuits. Applications like fluorescence lifetime imaging can strongly benefit from such a timing resolution.

With less than 10 ps timing resolution, the sensor is expected to be capable of achieving mm range resolution in a ToF set-up. The VCSEL is oriented towards the scene as well as the sensor without any focusing lenses or light filters. Only a small fraction of the VCSEL pulse light gets reflected back to the sensor from the target. The sensor is set for an exposure of $640\ \mu\text{s}$ during which the VCSEL emits pulses of 16 ns with a frequency of 12.5 MHz, while the transfer windows last for 40 ns following the scheme shown in Fig. 7.3. The VCSEL average current consumption during the exposure is less than 2 mA. The target is then moved away from the sensor and the VCSEL with steps of 1 cm up to 35 cm and then with steps of 10 cm up to 170 cm. The maximum range of 170 cm is not an absolute limit, since extendible by increasing the

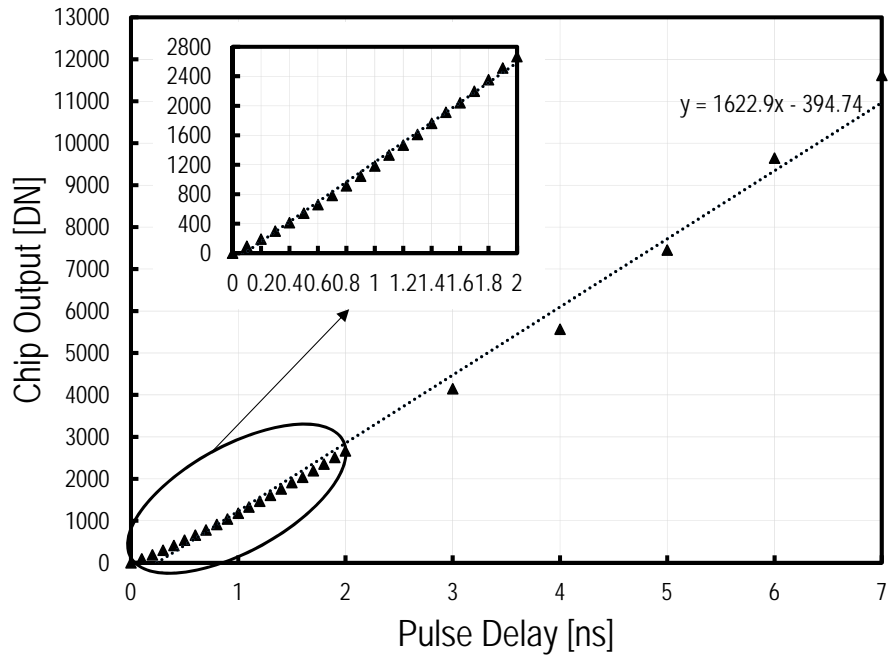
Table 7.1 – ToF Sensor Performance

Parameter	Value
Process	180 nm CIS
Voltage supply	3.3/1.8 V
Array size	1024(H) × 50(V)
Frame Rate	500 Hz
ADC resolution	14 bits
Integration time	640 μ s with a 2 mA current supply VCSEL
Fill factor	80%
Repetition Frequency	12.5 MHz
Emitter	650 nm VCSEL
Sensor current consumption	3 μ A
Emitter current consumption	2 mA
Optical set-up	No lenses for emitter and sensor
Measurable range	1.7 m
Range resolution	2 mm @50Hz

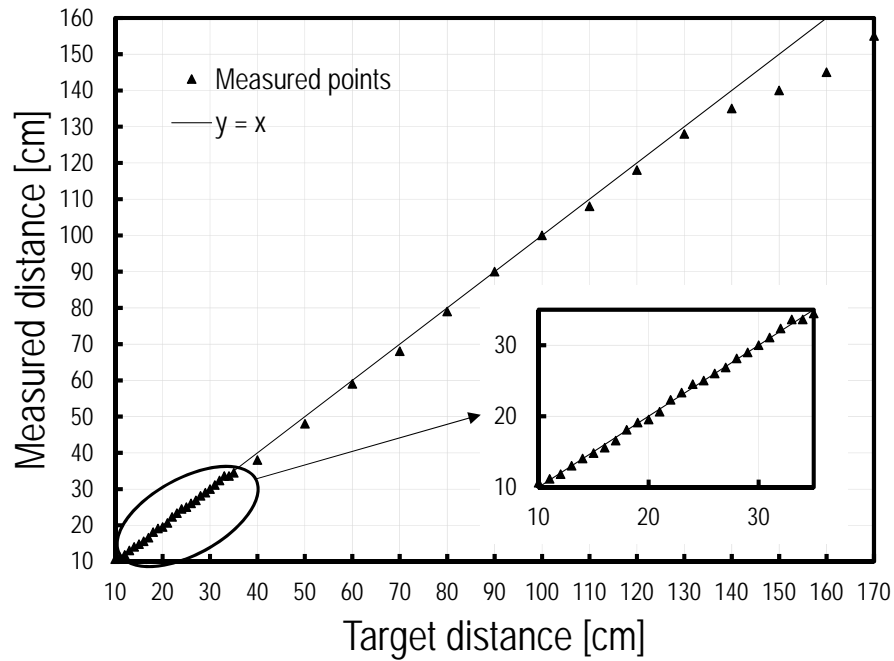
VCSEL power and by changing its modulation frequency. The two ambient-light-free samples corresponding to Q_1 and Q_2 , as shown in Fig. 7.3, are processed and converted into the digital domain by the on-chip ADC. The ratio of the two samples and the extraction of the measured distance thanks to a linear fit obtained with a first calibration is calculated off-chip. Fig. 7.5b shows the measured versus target distance when sweeping the target from 10 to 170 cm under an ambient light level of 3000 Lux and averaging 10 consecutive frames to mitigate the set-up noise. Since the sensor operates at 500 Hz, the effective measurement frame rate is 50 Hz. The inset of Fig. 7.5b shows a focus on positions between 10 and 35 cm where the sweep step is only 1 cm. By measuring the standard deviation of the difference between the measured and target distances, an RMS value of 2 mm is obtained. The ToF sensor performance are summed up in Tab. 7.1.

7.4 Discussion and comparison to the state-of-the-art

For the ToF application, the sensor performance is compared with two commercial product just released by market leading companies active in the field of ToF sensors [183, 184]. The comparison is summarized in Tab. 7.2. Both products used for comparison implement SPAD technology. Indeed SPADs are suitable for direct ToF or wave front detection [185], but such devices still present several design and industrialization challenges [186]. Indeed, SPADs require significant CMOS process optimization to cope with the large voltages needed for biasing the photodiodes close to their breakdown limit. At the design level, as mentioned earlier, direct ToF requires highly precise timing with jitters below 10 ps and suffers from small fill factors, the latter reducing the EQE. The exploitation of the indirect operations makes the architecture of the presented chip more relaxing in terms of timing constraints. Indeed, a ToF system embedding this architecture would operates at 40 ns transfer time.



(a)



(b)

Figure 7.5 – (a) Sensor output versus source pulse delay steps of 100 ps up to 2 ns and 1 ns after with a zoom onto the 100 ps steps. (b) The target versus measured distance with steps of 1 cm up to 35 cm and 1 cm after measured with the sensor chip and light emitted from a VCSEL and reflected back from the target.

Table 7.2 – ToF Sensing Comparison Table

Parameter	This work	[184]	[183]
Process	180 nm CIS	NA	NA
Pixel technology	PPD	SPAD	SPAD
Voltage supply	3.3/1.8 V	2.8 V	3.3 V
Sensor size	4×5 mm ² without VC-SEL	4.4×2.4 mm ² with VC-SEL	2.2×3.6 mm ² with VC-SEL
Frame Rate	50 Hz	33 Hz	60 Hz
ADC resolution	14-bits	8-bits	NA
Emitter and sensor average consumption	2 mA	19 mA	NA
Optical set-up	No lenses	with lenses	with lenses
Measurable range	130 cm	120 cm	60 cm
Range resolution	2 mm	48 mm	30 mm

The high fill factor of this sensor together with the high EQE of PPDs and the low noise of the readout chain enable the sensor to operate with lower integration time and lower VCSEL light intensity. Compared to [183, 184], this sensor features one order of magnitude better precision with one order lower emitter light, at a larger covered distance range. Indeed, the sensor requires less than 2 mA average current dissipation in the VCSEL during exposure and only 10 μ W power dissipation at the level of the sensor when operating at 50 Hz, eventually enabling a 2 mm resolution for 130 cm range.

Last, but not the least, it should also be recalled that the proposed sensor, as in Fig. 7.2, has been primarily designed for the PPG application. Indeed, the number of PPDs involved in the sensor, as described in section 6.2.1, has been chosen based on the dynamic range and SNR constraints of the PPG application. A second version of the chip, tailored for the ToF application, would result into even better performance.

Conclusions

The increasing demand for embedding more and more light sensors in portable and wearable devices is calling for higher integration and reuse of the sensor interface electronics.

In this chapter, it is shown that the same chip used for the PPG can also be used for realizing a low-power ToF distance ranging device thanks to the double TG structure in the pixel. The sensor requires less than 2 mA average current in the VCSEL during exposure and only 10 μ W for the sensor chip when operating at 50 Hz enabling a 2 mm resolution for 130 cm range.

Moreover, the presented architecture is implemented in a standard CIS process which presents a considerable advantage for large volume consumer applications and for miniaturization. The CMOS implementation also allows the integration of digital processing or machine learning for specific applications on the same die opening the way for edge computing.

Eventually, the sensor architecture presented in this work not only offers the advantage of covering ALS, PPG and ToF using the same device, but it also brings significant performance improvement in each application field. As mentioned above, for single point ToF distance ranging, the resolution and emitter (VCSEL) power consumption are reduced by more than one order of magnitude as well. This architecture represents a promising step towards all-in-one miniaturized photonic sensors.

8 Conclusions

PPG sensors are nowadays integral parts of wearable devices. The importance of PPG for medical monitoring is proven by the number of primary vital signs directly or indirectly recordable out of it, such as the heart rate, the respiration rate and the blood pressure. Nowadays, specific factors such as the increase of CVDs, as a consequence of increased obesity and population ageing, are changing the modern healthcare needs and already impacting on the countries' budgets. In this perspective, any technology leading to efficient and remote health monitoring would represent a societal breakthrough. In this regard, the PPG technology is a serious candidate to lead the digital health revolution. Today, the popularity of PPG sensors in smartwatches, smartphones or smartrings is largely due to the convenience and low cost of these devices. Despite this, accurately estimating people's vitals by the means of these devices still remains challenging and we should not expect dramatic improvements in reliability unless there are fundamental changes in the sensor technology. On the other hand, thanks to the "readiness" of such sensors into wearable platforms, any fundamental change in the today PPG sensor technology leading to better sensing would be simply welcomed as a serious game changer.

A PPG signal consists of a tiny AC component, fully synchronous with respect to the cardiac period, which is superimposed on a large quasi-static baseline. The majority of the medical information are brought by the AC component. For this reason, it is key to build PPG sensors maximizing the AC part of the PPG signal. The physics behind a PPG signal is the Beer-Lambert law which describes the attenuation of monochromatic light travelling through an uniform medium containing an absorbing substance. On the other hand, despite the Beer-Lambert law gives a good understanding of how a PPG signal is generated, the interaction of light with biological tissues is more complex than what is described by the Beer-Lambert law. Indeed, such interaction includes the optical processes of scattering, reflection, transmission and fluorescence. In this regard, building a performing PPG sensor requires some attention. For instance, the choice of the light wavelength has implications on the light-tissue interaction and generated artefacts. Moreover, the distance from the PD and the LED (and relative height) is key in enhancing the AC component of the PPG signal.

So far, the PPG technology has been extensively used to monitor several physiological measurements such as the heart rate and the blood oxygen saturation. On the other hand, a PPG signal carries additional information ultimately related to stress, respiration rate and blood pressure. In this perspective, several works in literature have very promising methods for extracting as many vitals as possible from a PPG sensor. For instance, some of them have exploited the variability of the heart rate to predict the atrial fibrillation. Among the vitals that can be detected from a PPG signal, the blood pressure has a key role. Hypertension is the major cause of premature death worldwide: it causes more than 7.5 million deaths, about 13% of the total death and an estimated 1.13 billion people worldwide have hypertension. For this reason, it is essential that the blood pressure is measured regularly and continuously. A PPG signal carries several information that are directly or indirectly linked to hypertensive pathologies. The advent of artificial intelligence through machine learning and deep learning is changing the paradigm increasing the probability of seeing fully wearable and non-invasive blood pressure monitoring systems.

Designing a good PPG sensor undergoes several bottlenecks and engineering trade-offs. The LED power, due to its few tens of mAs driving current, is still the largest power hungry element. In the last 10 years, we have seen the PPG circuits power scaling down at an almost constant LED power. This ultimately limits the applicability of PPG sensors in platforms for continuous monitoring. One possible solution relies on reducing as much as possible the LED duty cycle to values well below 1%. The downside of this is the increased complexity of the analog front-end. Indeed, in order to cope with those very short pulse, the AFE has to be capable of settling within a short amount of time. From a design perspective, this means a larger bandwidth and consequently more power consumption and larger (thermal) noise. Additional complexity may also come from sub-Nyquist sampling operations which effectively reduce the duty cycle and the sampling frequency at the cost of more processing power. Reducing the LED duty cycle also means distributing the signal power over a very large number of harmonics so increasing the needed bandwidth to recover the signal power. For this reason, wideband TIAs are often chosen, followed by analog or digital filters.

Despite a PPG sensor always comes with an optical shielding, handling the ambient light is not easy. The large IR power of the natural light can saturate the front-end due to the large IR penetration in the skin. The artificial light often comes with large order of harmonics whose effect cannot be easily cancelled by CDS blocks, otherwise using a large sampling frequency which increases the LED and circuit power consumption. The extremely low PI of a PPG signal makes the design of a PPG sensor even more complicated. First of all, the DC has to be properly corrected at the input by the means of feedback loops, bringing power and area overheads. Secondly, for applications requiring strict resolutions, such as the oxygen saturation, the extremely low PI imposes a minimum dynamic range at the front-end, which is usually larger than 90 dB in the worst PI conditions. Designing a PPG sensor for a large dynamic range, low noise and low power operations is not an easy task and very often requires some engineering trade-offs. For instance, the dynamic range can be traded versus the power for applications, such as the heart rate, not requiring a strict resolution or a large SNR.

Despite the advantages and opportunities behind the PPG technology, today PPG sensors are still limited by noise and artefacts. Indeed, several noise sources should be accounted for while designing a PPG sensor: the shot noise of the photogenerated current, the thermal and the flicker noise of the readout chain and the quantization noise of the ADC. Among the different proposed PPG readout chains, as presented in Chapter 4, the one with a TIA, a CDS and an ADC is the most used one, both in academic and commercial solutions. The TIA is often proposed either as a ZTIA or a CTIA. Providing a detailed and comprehensive noise analysis in PPG readout chains is key in order to reduce the LED power. Indeed, the LED power can be reduced provided the noise floor of the readout electronics is decreased proportionally to achieve the same SNR. A classic PPG readout chain has been analysed both in ZTIA and CTIA configurations in terms of SNR and power trade-offs. Assuming the same signal bandwidth between the two compared structures, a ZTIA-based readout chain comes with both larger LED power (8 times more) and a larger G_m , compared to a CTIA-based one. This advantage is attributed to the integration feature of the CTIA. Indeed, the CTIA comes intrinsically with a larger bandwidth than the ZTIA. Comparing the two for the same BW means, in other words, having a larger signal gain for the CTIA than the ZTIA. Moreover, the ZTIA shows a larger read noise than the CTIA, which is, on the contrary, intrinsically more shot noise limited. It should also be noticed that both solutions show still an important electronic read noise level, calling for further design optimizations.

The CMOS image sensors (CIS) is today dominating the exploding consumer electronic devices market such as smartphones, tablets and digital cameras. Quickly, CMOS image sensors became the technology of choice with respect to speed, resolution, power consumption and on-chip integration thanks to the introduction and consolidation of the PPD technology in CIS. The important advantage of PPDs in terms of sensitivity and noise make them a serious candidate in the PPG application to go beyond the CTIA-based structure and the limitations introduced by the off-chips PDs. Assuming a PI equal to 1%, same signal bandwidth and comparable sensitivity between the CTIA and the CIS readouts, the latter achieves the target SNR with more than 1 order of magnitude lower LED power. The advantage introduced by the CIS can also be extended for larger PIs. Indeed, the CIS readout chain shows, no matter the PI value, a lower electronic noise floor resulting into intrinsically more shot noise limited operations.

The CDS is key for reducing the effect of the ambient light, offsets and $1/f$ noise and, for this reason, it is widely used in PPG circuits. Despite this, CDS circuits are still limited by circuit non-idealities, including analog switches non-idealities (on and off resistances), charge injection and thermal noise, the latter usually referred to as kTC noise. The sampled noise voltage variance (kT/C) is, by definition, inversely proportional to the capacitance. On the contrary, both power and silicon area are directly proportional to the capacitance, resulting into a noise/power-area trade-off. From a design perspective, it is necessary to be fully aware of the capacitances ultimately limiting the circuit performance. kTC noise analysis of SC circuits is never a simple task, considering that the noise transfer function, for these circuits, changes in time. Modern CAD simulators are useful in the estimation of the overall noise features, despite

they require a very high accuracy set-up, resulting into extremely long simulations. Moreover, they don't provide simple analytical expressions to optimize the SC circuit noise. In this perspective, three possible CDS circuits have been compared analytically and benchmarked in terms of kTC noise. A fully passive CDS is particularly suitable for ultra-low power applications, despite the SNR is affected by the intrinsic signal loss due to the charge sharing mechanism. Moreover, it is not affected by any signal saturation, the latter usually due to active elements. One of the main advantages of this implementation is that the SNR can be improved without limiting the input signal range and only at the cost of more silicon area (larger capacitors).

In addition to the noise, PPG is known to be particularly susceptible to motion artefacts. Overcoming those artefacts presents one of the most challenging problems while designing a PPG sensor. Several solutions have been proposed to reduce the effect of motion in PPG sensors. First of all, motion artefacts are wavelength dependent. Thanks to the shorter penetration of the green light, the latter achieves more resilience to MA with respect to red and IR. Secondly, these artefacts can be reduced by choosing specific body locations. For instance, the ears report less MA with respect to the arms. Other cancellation techniques rely on the use of an external accelerometers, gyroscopes or optical channel. These devices are used to provide a motion reference signal which is dynamically used to filter out in-band motion artefacts. This technique is called adaptive noise cancellation and goes beyond the scope of this work.

The majority of PPG sensors, both in academia and in commercial products, still utilize off-chip PDs, mostly PN or PiN junctions. The parasitic capacitance of those devices degrades the speed and noise performance of the front-end. For this reason, some few works have proposed to integrate the PD together with the processing chains for better performance. Integrating the PD would also result into lower costs in production.

Today, PPDs are the key ingredients of CMOS image sensors, thanks to the lower noise and enhanced sensitivity. Several markets including security, scientific imaging and medical are relying today on this technology. The excellent performance of a PPD device makes it particularly suitable for the PPG application. Indeed, an on-chip high sensitivity and low noise PD can significantly reduce the LED power needed to target a specific SNR. Since the LED is the most power hungry part of a PPG chain, this would dramatically enhance the PPG sensor's battery lifetime.

The PPG sensor presented in this work integrates an array of PPDs, a SC AFE and an ADC. Placing the PPDs into an array eases the engineering trade-off between the possible achievable dynamic range and the overall noise performance. The total number of pixels has been chosen according to the target SNR to achieve an accuracy within 2% of the peripheral oxygen saturation. The photosensitive area consists of four clusters of 50 rows and 256 columns, meaning 51200 total pixels. The 50 pixels along the i-column are assembled in a macro-pixel (MP). The pixels of one MP share the same source-follower, so saving power while maintaining a reasonably low parasitic capacitance at the shared sense node (SN).

Each pixel within the MP embeds a double TG structure: a sink TGs and a transfer gate TGt . The double TG structure allows to precisely control the charge integrated into the PPD well and eventually reaching the SN for processing. Specifically, TGs sinks the charge cumulated in the PPDs to the reset voltage, while TGt allows the charge transfer to the SN. The SN is shared between multiple PPDs, which are gated to either sink or transfer their charge synchronously. This process is also referred to as charge binning. It allows averaging the outputs of the MP PPDs without the need for any additional circuitry. This charge binning also enables more efficient and faster charge transfer compared to a single large PPD with equivalent area by mitigating the effect of charge transfer non-idealities. Compared to recent state-of-the-art this work comes with the lowest power consumption. Moreover, among the most relevant state-of-the-art's works, this is the only solution featuring a full integration of the photosensitive area together with the AFE and the ADC at an extremely low power consumption, i.e. smaller than $10\ \mu W$, this accounting both for the LED and the AFE+ADC.

The double TG structure, within the MP, can also be exploited for enhancing the PI of a PPG signal, without any power or silicon overhead, by properly tuning the TG control voltage and the charge transfer time. TGt can allow only the part of the integrated charge corresponding to the AC component of the PPG signal to reach the SN. Whereas, TGs can dump the remaining DC charge. In this regards, this work further illustrates the trade-off between the TG control voltage and the charge transfer time. It points out that a larger fraction of the AC signal is transferred at a lower TG control voltage with respect to the DC one. This translates into a maximum PI occurring at TG control voltage around 1 V, for charge transfer time ranging between 100 ns and 1 μs . A maximum PI enhancement of a factor 5 is reached for TG control voltage and charge transfer time equal to 1 V and 100 ns, respectively. In addition, the PI can also be increased considerably without any impact on the SNR for optimal transfer parameters. Compared to state-of-the-art PI enhancement techniques, this work comes without any circuit power consumption or silicon area overhead. Indeed, the PPG PI is corrected right at the level of the PPD by properly tuning the TG control voltage and the charge transfer time.

It should be recalled that, despite the great potential behind the PPG technology, the fairly large power burnt by the LEDs still represent a serious challenge towards truly continuous PPG operations. In this perspective, the proposed micropower PPG sensor represents a turning point. The extremely low power consumption and excellent signal quality combined with the possibility of PI enhancement makes this solution a serious answer to the increasing demand of continuous and reliable health monitoring devices, especially when the body location makes the PPG recording suffer from a particularly low PI.

Last but not the least, the increasing demand for embedding more and more light sensors in portable and wearable devices is calling for higher integration and reuse of the sensor interface electronics. Inspired by this need, this work has investigated whether the micropower PPG sensor could have been used for a different application, taking advantage of its low power, low noise and high sensitivity features. It has been shown that the same chip used for the PPG can also be used for realizing a low-power 1D indirect ToF distance ranging device thanks to the

double TG structure in the pixel. The sensor requires less than 2 mA average current in the VCSEL during exposure and only 10 μ W for the sensor chip when operating at 50 Hz enabling a 2 mm resolution for 130 cm range.

Moreover, the presented architecture is implemented in a standard CIS process which presents a considerable advantage for large volume consumer applications and for miniaturization. The CMOS implementation also allows the integration of digital processing or machine learning for specific applications on the same die opening the way for edge computing. Eventually, the sensor architecture presented in this work not only offers the advantage of covering ALS, PPG and ToF using the same device, but it also brings significant performance improvement in each application field. As mentioned above, for single point ToF distance ranging, the resolution and the laser power consumption are reduced by more than one order of magnitude as well. This architecture represents a promising step towards all-in-one miniaturized photonic sensors.

8.1 Future perspectives

The sensor architecture presented in this PhD work offers the advantage of covering several possible applications with significant performance improvement in each of them. For this reason, possible future works may go in multiple directions. Nevertheless, in the following some of these directions are highlighted.

- 1) the number of pixel as presented in Chapter 6 can be decreased by roughly 30%, leading to an important saving on the silicon area. This is particularly important in the perspective of re-utilizing this device in commercial applications.
- 2) this PhD work has mostly focused on the power and signal quality optimization at the level of the PPG sensor, without any system level consideration. The quality of the PPG signal and the incredibly low power consumption make this micropower PPG sensor a key element of whatever monitoring system. In this regard, it would be interesting to utilize the saved silicon area from the reduced array to integrate on silicon the LED drivers, the clock generation and a communication protocol.
- 3) in the perspective of developing a system out of the micropower PPG sensor, special attention should be devoted to the effect of motion artefacts. In particular, as presented in section 5.4, an active motion artefacts cancellation technique has to be implemented. Eventually, the integration of an accelerometer would be beneficial.
- 4) the excellent SNR and signal morphology, at the extremely low power budget, obtained from the micropower PPG sensor make it particularly interesting in the perspective of extracting as many as possible vitals from the PPG signal. In particular, as presented in Chapter 3, blood pressure represents today a hot topic. A PPG signal carries several information that are directly or indirectly linked to hypertensive pathologies. On one hand, the excellent PPG signal morphology would make those information easily visible. On

the other hand, the micropower operation can give rise to a truly continuous PPG monitoring, eventually generating more observation data. This, combined with the advent of artificial intelligence through machine learning and deep learning, would represent the first step towards a fully wearable and non-invasive blood pressure monitoring systems.

Publications note

The content of Chapter 5 has been published in:

- 1 **A. Caizzone**, C. Enz, and A. Boukhayma, “Comprehensive Noise Analysis in PPG Readout Chains,” 2017 International Conference on Noise and Fluctuations (ICNF), June 2017, DOI: 10.1109/ICNF.2017.7985971.
- 2 **A. Caizzone**, C. Enz, and A. Boukhayma, “An Accurate kTC Noise Analysis of CDS Circuits,” in 2018 16th IEEE International New Circuits and Systems Conference (NEWCAS), June 2018, DOI: 10.1109/NEWCAS.2018.8585674.

The content of Chapters 6 and 7 has been published in:

- 1 **A. Caizzone**, A. Boukhayma, and C. Enz, “A 2.6 μ W Monolithic CMOS Photoplethysmographic Sensor Operating with 2 μ W LED Power,” in 2019 IEEE International Solid State Circuits Conference - (ISSCC), February 2019, DOI: 10.1109/ISSCC.2019.8662404, pp. 290–291.
- 2 **A. Caizzone**, A. Boukhayma, and C. Enz, “A 2.6 μ W Monolithic CMOS Photoplethysmographic (PPG) Sensor Operating with 2 μ W LED Power for Continuous Health Monitoring,” IEEE Transactions on Biomedical Circuits and Systems, pp. 1243–1253, vol. 13, n. 6, December 2019, DOI: 10.1109/TBCAS.2019.2944393. *invited journal to the ISSCC special issue*
- 3 **A. Caizzone**, A. Boukhayma, and C. Enz, “AC/DC Ratio Enhancement in Photoplethysmography Using a Pinned Photodiode,” IEEE Electron Device Letters, pp. 1828–2831, vol. 40, n. 11, November 2019, DOI: 10.1109/LED.2019.2940063.
- 4 A. Boukhayma*, **A. Caizzone***, and C. Enz, “An Ultra-Low Power PPG and mm-Resolution ToF PPD-Based CMOS Chip Towards All-in-One Photonic Sensors,” IEEE Sensors Journal, pp. 11858–11866, vol. 19, n. 24, December 2019, DOI: 10.1109/JSEN.2019.2939479.
**equally contributing authors*

Chapter 8. Conclusions

- 5 A. Boukhayma, **A. Caizzone**, R. Capoccia, and C. Enz, “Design and Optimization of Low Power and Low Light Sensor,” accepted at the 2020 IEEE Custom Integrated Circuits Conference - (CICC). *invited paper*
- 6 **A. Caizzone**, A. Boukhayma, and C. Enz, “Health Monitoring Device,” Patent number: WO2019016191 (A1), 2019.

A Appendix

Chapter 4

In Chapter 3 we have seen that the relationship between the oxygen saturation and the R coefficient is the following

$$SO_2 \% = \frac{\epsilon_{Hb}(\lambda_1) - \epsilon_{Hb}(\lambda_2)R}{\epsilon_{Hb}(\lambda_1) - \epsilon_{HbO_2}(\lambda_1) + [\epsilon_{HbO_2}(\lambda_2) - \epsilon_{Hb}(\lambda_2)]R} \cdot 100, \quad (A.1)$$

being ϵ the extinction coefficients at a given emitting wavelength for the oxygenated and deoxygenated hemoglobin. Taking advantage of the extinction coefficients of Tab. A.1, (A.1) can be rewritten as

$$S_aO_2 \% = \frac{1.61 - 20.23R}{1.45 + 2.88R} \cdot 100. \quad (A.2)$$

Inverting (A.2) results in R equal to

$$R = \frac{161 - 1.45S_aO_2\%}{2023 + 2.88S_aO_2\%}. \quad (A.3)$$

The minimum dynamic range for a given oxygen level depends on the PI, but as well on the maximum acceptable error on the R parameter. The maximum acceptable error of R in terms of oxygen saturation can be derived by differentiating (A.3) as following

$$\frac{\Delta R}{R} \leq \frac{\Delta S_aO_2}{R} \frac{dR}{dS_aO_2} = \frac{2}{R} \frac{dR}{dS_aO_2} = -\frac{2 \cdot 3397}{(161 - 1.45S_aO_2\%)(2023 + 2.88S_aO_2\%)}, \quad (A.4)$$

where $\Delta S_aO_2 = 2$ since a maximum error of 2 digits is required in the oxygen saturation measurements [117]. Eq. (A.4) shows that for larger saturation levels, larger errors are acceptable without compromising the goodness of the oxygen saturation. This is one of the reason why oxygen saturation measurements below a certain value (70%) are not reliable anymore, since requiring stricter tolerances.

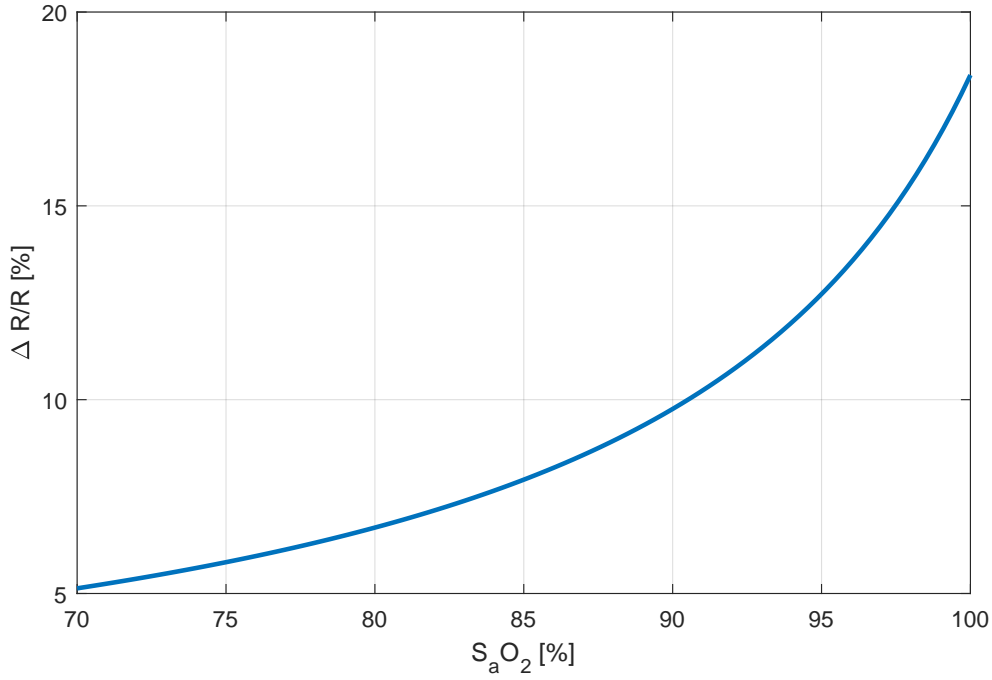


Figure A.1 – Maximum acceptable ratio of R for the oxygen saturation. Larger oxygen levels are more robust to errors.

Table A.1 – Extinction coefficients of Hb and HbO2 in the visible range.

Wavelength [nm]	Extinction coefficient [$l \cdot mmol^{-1} \cdot cm^{-1}$]	
	Hb	HbO2
λ_2 540	20.23	23.11
λ_1 650	1.61	0.16

The dynamic range is defined as following

$$DR = 20 \log_{10} \left(\frac{DC}{noise\ floor} \right) = 20 \log_{10} \left(\frac{DC}{AC \frac{\Delta AC}{AC}} \right). \quad (A.5)$$

In (A.5), the noise floor is expressed in terms of the AC component. Indeed, the ratio between the AC component and the noise floor should always be larger than 30 to guarantee the maximum error of 2 digits in the oxygen saturation measurements [117].

Eq. (A.4) can be rewritten in terms of the maximum tolerable error on the AC component as following

$$\frac{\Delta R}{R} \approx \sqrt{2} \frac{\Delta AC}{AC}. \quad (A.6)$$

This takes into account that, first, for the oxygen saturation two wavelengths are needed,

meaning two AC components are calculated and, second, the variation on the DC component is supposed to be negligible.

Eventually, taking advantage of (A.5), (A.6), the minimum dynamic range accounting for the maximum error on R is equal to

$$DR = 20\log_{10} \left(\frac{\sqrt{2}DC/AC}{abs(\frac{\Delta R}{R})_{max}} \right) = 20\log_{10} \left(\frac{\sqrt{2}PI^{-1}}{abs(\frac{\Delta R}{R})_{max}} \right). \quad (A.7)$$

Chapter 6

As introduced in section 6.2.2, the assumption of equal bandwidth between the single pixel structure and the array means

$$\frac{Gm_{column}}{C_{column}} = \frac{Gm_{big}}{C_{big}}, \quad (A.8)$$

where

$$C_{big} = N \cdot C_{column}, \quad (A.9)$$

being N the number of the columns in the array, i.e. 1024 in our case. In other words, taking advantage of (A.9), (A.8) can be rewritten as

$$N \cdot Gm_{column} = Gm_{big}, \quad (A.10)$$

Supposing the single column SF in WI and the big pixel one in SI leads to

$$N \cdot \frac{I_{column}}{nU_t} = \frac{I_{array}}{nU_t} = \sqrt{\frac{2I_{big}\beta}{n}}, \quad (A.11)$$

where n is the slope factor, U_t the thermal voltage and $\beta = \mu \cdot C_{ox} \cdot (W/L)$. Eventually, (A.11) can be rewritten as

$$I_{array} = U_t \sqrt{2nI_{big}\beta}. \quad (A.12)$$

Taking advantage of the EKV formalism [145], we can rewrite (A.11) in terms of the inversion coefficient, IC_{big} , of the big pixel SF. We recall that

$$IC_{big} = \frac{I_{big}}{2 \cdot n \cdot \beta \cdot U_t^2}. \quad (A.13)$$

Fixing I_{big} equal to \bar{I}_{big} , i.e. 0.5 mA as in section 6.2.2, and taking advantage of (A.13) means

$$\frac{\bar{I}_{big}}{I_{array}} = \sqrt{IC_{big}}. \quad (A.14)$$

This means that I_{array} will always be smaller than \bar{I}_{big} and eventually it becomes equal to \bar{I}_{big} for IC_{big} equal to 1, corresponding to the big pixel SF biased in WI. As already pointed out in section 6.2.2, at the given \bar{I}_{big} , it is not possible to bias the big pixel SF in WI since this would require an unrealistically large transistor, i.e. $(W/L)_{big} \gg 100$. On the other hand, the WI is always possible for the big pixel SF at the price of reduced bandwidth and larger silicon area.

Fig. A.2 shows, for the same SF bandwidth, how the big pixel SF current scales with respect to

the array one. The proposed comparison has been carried out accounting for a $(W/L)_{big}$ equal to 10. Fig. A.2 demonstrates that the same bandwidth can be achieved with $48\ \mu\text{A}$ biasing current in the array structure versus $0.5\ \text{mA}$ in the single pixel, ultimately leading to a dramatic power saving.

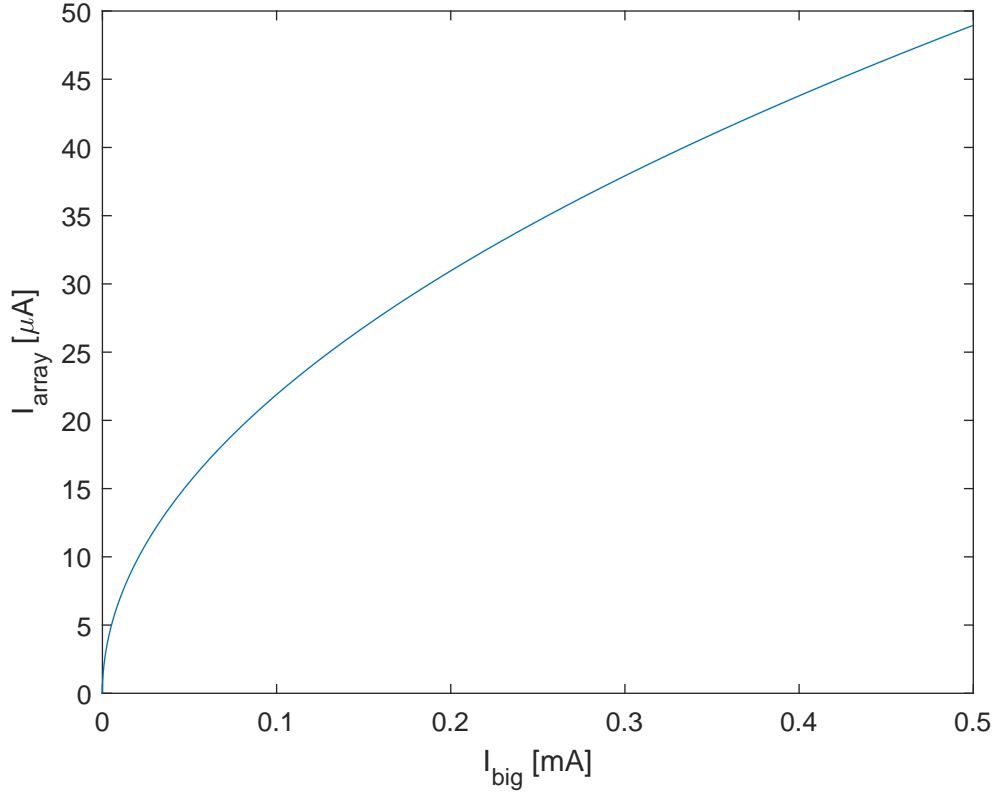


Figure A.2 – Single pixel current consumption versus the array one, at the same SF bandwidth.

Chapter 5

Simple Thermal Noise Estimation of Switched Capacitor Circuits Based on OTAs – Part I: Amplifiers with Capacitive Feedback

Christian Enz *Fellow, IEEE*, Antonino Caizzzone *Member, IEEE*, Assim Boukhayma *Member, IEEE*,
and François Krummenacher

Abstract—This paper presents a simple method for estimating the thermal noise voltage variance in passive and active switched-capacitor (SC) circuits using operational transconductance amplifiers (OTA). The proposed method is based on the Bode theorem for passive network which is extended to active circuits based on OTAs with capacitive feedback. It allows for a precise estimation of the thermal noise voltage variance by simple inspection of three equivalent circuits avoiding the calculation of any transfer functions nor integrals. In this Part I, the method is applied to SC amplifiers and track & hold circuits and successfully validated by means of transient noise simulations. Part II extends the application of the method to integrators and active SC filters.

Index Terms—thermal noise, kTC, Bode theorem, amplifier.

I. INTRODUCTION

SWITCHED-CAPACITOR (SC) circuits were invented in the 70's as a way to perform analog signal processing on-chip using the capacitors, switches and amplifiers available in MOS technologies [1], [2]. They take advantage of the fact that the circuit characteristic only depends on capacitance ratios which turn out to be very accurate thanks to the excellent matching of capacitors. Additionally the frequency response of SC filters can be tuned by changing the clock frequency [3]. SC circuits have then been used broadly for various circuits including analog-to-digital and digital-to-analog converters [4]. They are increasingly used in many more applications like radio frequency (RF) circuits [5]–[7] or sensor front-end circuits [8]–[10] to perform various analog signal processing operations such as sampling, amplification or filtering.

The analysis of SC circuits has received considerable attention in the 80's in particular for the computation of the noise [11]–[17]. With the application of SC circuits to a wider range of analog and RF circuits, new computation techniques have also been proposed more recently [18]–[20]. Today, modern circuit simulators allow to compute noise for example in the time domain using transient noise analysis [21]. However all of these techniques remain complex and are mostly focused on an efficient numerical computation of the PSD by dedicated EDA tools. They cannot be used for the derivation of simple analytical expressions of the noise voltage variance.

The performance of SC circuits is ultimately limited by the thermal and flicker noise (or $1/f$ noise) generated by the amplifiers and by the thermal noise coming from the switches. Since SC circuits are sampled-data systems, the broadband thermal noise is aliased into the Nyquist band, resulting in an increase of the noise power spectral density (PSD) by a factor equal to the ratio of the equivalent noise bandwidth to the Nyquist frequency which is usually much larger than one [14], [22], [23]. The $1/f$ noise contribution can therefore usually be neglected and if it still remains important, the amplifier $1/f$ noise and offset can be reduced by increasing the transistor gate areas or eventually eliminated thanks to circuit techniques like auto-zeroing [23]–[26] or chopper stabilization [23], [27], [28]. Under such conditions, the sampled thermal noise remains the dominant noise source particularly when minimal capacitance values are used, since the sampled noise voltage variance is inversely proportional to the capacitance.

Since the power consumption and silicon area are proportional to the capacitance [29], whereas the noise voltage variance is inversely proportional to the capacitance, it is crucial to identify which capacitances are setting the noise voltage variance. Unfortunately, the derivation of the noise PSD and variance is not easy because SC circuits are periodically time-varying circuits. The noise is therefore cyclostationary and usually characterized by the power spectral density (PSD) averaged over one period [30].

The optimization of SC circuits for achieving at the same time low-noise operation at low-power requires an accurate estimation of the noise variance. The latter is traditionally calculated for each phase in the frequency domain by first evaluating the transfer functions from all the noise sources to the node where the noise needs to be evaluated. The total noise PSD is then integrated over frequency to provide the noise variance. This approach is however quite tedious and impractical [31] and for large networks, it becomes extremely cumbersome to get an analytical expressions [32].

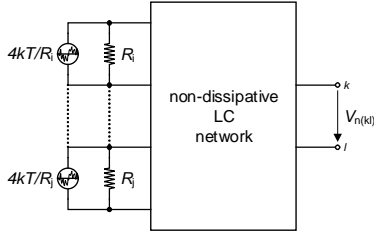
This work proposes a simple method for estimating the thermal noise voltage variance at any port of passive and active circuits made of operational transconductance amplifiers (OTA) with capacitive feedback as found in SC circuits [33]. The proposed method, based on the Bode theorem [34], allows the calculation of the thermal noise voltage variance across any capacitor by simple inspection of several equivalent schematics made of capacitors only, avoiding the evaluation of complex transfer functions and cumbersome integrals.

Manuscript submitted August 15, 2019.

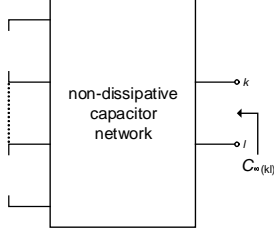
Corresponding author: C. Enz (email: christian.enzepfl.ch).

C. Enz, A. Caizzzone and A. Boukhayma are with the Integrated Circuits Lab (ICLAB), Micro-engineering Institute, School of Engineering, EPFL.

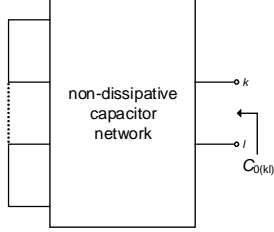
F. Krummenacher is with the Electrical Engineering Institute, School of Engineering, EPFL.



(a) Thermal noise voltage variance in a passive RLC network.



(b) Circuit for calculating C_∞ .



(c) Circuit for calculating C_0 .

Part I is dedicated to the derivation of the extended Bode theorem and its application to SC amplifiers and track & hold circuits. Part II is focused on the application of the extended Bode theorem to SC filters. Section II of this first Part starts by recalling the Bode theorem, which is at the heart of the proposed method. Section III then presents an extension of this theorem to OTAs with capacitive feedback as found in SC circuits. The method is then illustrated in Section IV by two simple examples, namely a SC amplifier and a SC track & hold circuit. The calculated noise in each case is compared to transient noise simulations results showing an excellent match. Conclusions are then given in Section V

II. THE BODE THEOREM FOR PASSIVE NETWORKS

The Bode theorem [34]–[36] is a very efficient method to calculate the noise voltage variance at any port of an RLC circuit and particularly of capacitive networks. However, this method is limited to passive RLC networks.

In linear circuits, the noise analysis is traditionally performed by integrating the noise PSD. This requires the calculation of the transfer functions from each uncorrelated noise source to the node where the noise has to be evaluated (for example at the circuit output) and then adding the obtained uncorrelated contributions. In case of a passive RLC network, the thermal noise is generated in the resistors while the rest of the circuit made of ideal capacitors and inductors is noiseless. The circuit can then be represented as shown in Fig. 1a where all resistors are modeled by a noiseless resistor in parallel with a noisy current source with power spectral density

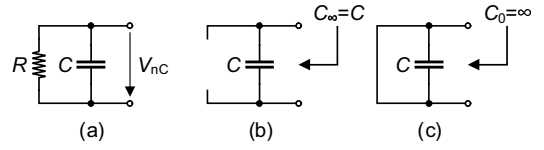


Fig. 2: Example of a 1st-order low-pass passive filter.

$4k_B T/R$. The thermal noise variance between any nodes k and l of the passive RLC circuit can be calculated using the Bode theorem without the need for computing any integral by simple inspection of two equivalent circuits. The thermal noise voltage variance at any port is simply given by [34]–[36]

$$V_n^2 = k_B T \cdot \left(\frac{1}{C_\infty} - \frac{1}{C_0} \right), \quad (1)$$

where k_B is the Boltzmann constant and T the absolute temperature. Capacitance C_∞ is defined as

$$\frac{1}{C_\infty} = \lim_{s \rightarrow +\infty} sZ(s), \quad (2)$$

which corresponds to the capacitance obtained when looking into the port after having removed all resistances from the circuit (or set them to infinity) as illustrated in Fig. 1b. Capacitance C_0 is defined as

$$\frac{1}{C_0} = \lim_{s \rightarrow 0} sZ(s), \quad (3)$$

which corresponds to the capacitance obtained when looking into the port after having replaced all resistances by a short circuit (or set them to zero) as illustrated in Fig. 1c.

The simplest example of the application of the Bode theorem to a passive RC circuit is the 1st-order low-pass filter illustrated in Fig. 2a. As shown in Fig. 2b, capacitance C_∞ is obtained after removing the resistance and is therefore equal to C . Capacitance C_0 is obtained from (3) after replacing the resistance by a short resulting in $1/C_0 = 0$. Applying the Bode theorem (1), the noise voltage variance is then simply equal to the well-known formula $V_n^2 = k_B T/C$.

III. EXTENSION OF THE BODE THEOREM TO TRANSCONDUCTANCE AMPLIFIERS WITH CAPACITIVE FEEDBACK

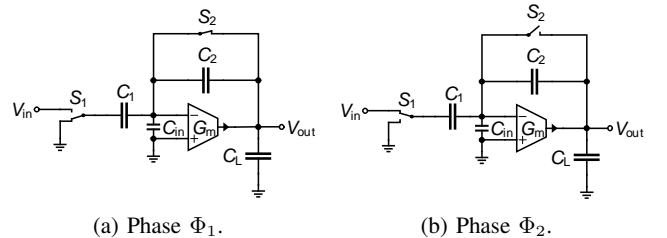


Fig. 3: SC autozero (AZ) amplifier.

This Section presents an extension of the Bode theorem to be used for calculating the thermal noise voltage variance seen at any port of an OTA-based SC circuit during a given phase.

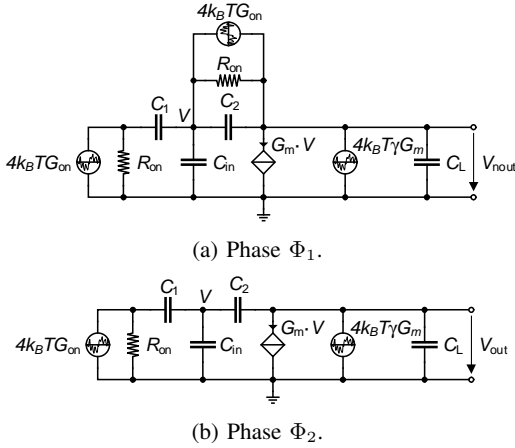


Fig. 4: Small-signal equivalent circuit of Fig. 3 for the calculation of the output noise voltage.

The Bode theorem presented above strictly applies only for the calculation of the thermal noise voltage variances of passive networks. However, it will be shown below that it can be extended to estimate the thermal noise voltage variance of amplifiers implemented with transconductance stages having a capacitive feedback. The simplest of such amplifier is the capacitive feedback amplifier shown in Fig. 3, where the amplifier is a differential OTA [3], [37]. Note that the amplifier can also represent a single-ended transconductance stage as simple as a single transistor or cascoded transistor for improved dc gain [38]. For more power-efficient implementation, the single-ended amplifier can be implemented by a simple inverter to take advantage of its current reuse feature [39]. In the following discussion, the OTA is assumed to be ideal (infinite DC gain, offset free, no saturation) and can be modelled by a voltage controlled current source (VCCS).

The amplifier operates with two non overlapping phases: the autozero (AZ) phase Φ_1 , followed by the amplification phase Φ_2 . During phase Φ_1 , shown in Fig. 3a, the amplifier output is connected to its input, discharging the feedback capacitor C_2 . Assuming the DC gain of the OTA is infinite, capacitors C_1 and C_{in} are then also discharged. In the amplification phase Φ_2 , switch S_1 is connected to the input, amplifying the input voltage. The voltage gain between the input and output voltage is simply equal to $A_v = -C_1/C_2$. Note that this amplifier is called autozero amplifier because it strongly reduces the OTA offset and flicker noise [23]. It can be shown that the residual input-referred offset of the amplifier is equal to the OTA original offset divided by the amplifier voltage gain A_v (assuming again that the OTA has an infinite DC gain). It can also be shown that the amplifier equivalent input-referred noise is free from the original OTA flicker noise and increased due to the aliasing of the broadband thermal noise due to the sampling process [23].

We are interested in the output noise variance at the end of the amplification phase Φ_2 , when the signal is actually read at the output. As mentioned above, thanks to the AZ process, the flicker noise of the OTA is strongly reduced [23] and hence the noise at the amplifier output during phase Φ_2 is dominated by

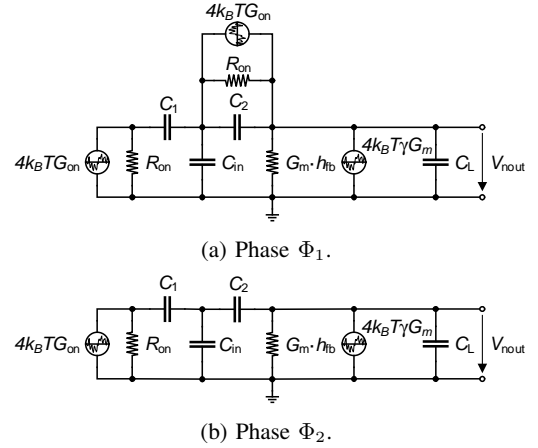


Fig. 5: Equivalent circuit replacing the VCCS of Fig. 4 by a resistance with conductance $G_m \cdot h_{fb}$ for the calculation of the output thermal noise voltage.

the thermal noise coming from the OTA and from the switches. The noise voltage variance at the output can be calculated in a classical way by integrating the output noise voltage PSD over frequency or calculating the equivalent noise bandwidth. An additional noise component needs to be accounted for at the end of phase Φ_2 , namely the noise that is generated across capacitor C_1 during phase Φ_1 . This noise is sampled as a noise charge on C_1 when the switch S_1 opens at the end of phase Φ_1 and then transferred to the feedback capacitor C_2 during phase Φ_2 . The variance of this output noise voltage is obtained by first calculating the variance of the noise voltage across C_1 during phase Φ_1 by calculating the noise voltage PSD across C_1 and integrating it over frequency. This noise voltage variance corresponds to a frozen charge that is then transferred to the feedback capacitor during phase Φ_2 . Assuming that the OTA DC gain is infinite, the voltage across C_2 is equal to the output voltage. The output noise voltage variance due to the noise sampled on C_1 at the end of phase Φ_1 is simply equal to the noise voltage variance across C_1 multiplied by the square of the voltage gain A_v . Now, although the procedure is straightforward, it is actually not always possible to get simple analytical expressions for the noise voltage variances mentioned above. Of course the latter can always be calculated numerically using a simple .NOISE simulation, but for circuit optimization it is useful to have analytical expressions showing the dependence of the noise to the various components. The Bode theorem can unfortunately not be used because we now have an active component. However, we will show below that the noise voltage variances can be estimated by extending the original Bode theorem to circuits including amplifiers implemented as transconductance amplifiers with a capacitive feedback.

For the noise analysis, it is reasonable to use a small-signal analysis. The small-signal equivalent circuit of the amplifier of Fig. 3 used to calculate the output noise voltage is shown in Fig. 4, where the noise current sources across resistances R_{on} represent the thermal noise of the switches having a PSD $4k_B T G_{on}$, where $G_{on} = 1/R_{on}$, whereas the noise current

source across the VCCS represents the OTA thermal noise referred to the output with a PSD $4k_B T \gamma G_m$, where γ is the thermal noise excess factor close to unity for a single transistor and usually larger than 2 for a differential OTA.

In both phases Φ_1 and Φ_2 , neglecting the current noise sources, the voltage at the transconductance amplifier virtual ground is only a function of the output voltage

$$V = h_{fb} \cdot V_{out}, \quad (4)$$

where $h_{fb} \triangleq V/V_{out}$ is the feedback voltage gain. During phase Φ_1 it is simply equal to unity, whereas during phase Φ_2 it is given by

$$h_{fb} = \frac{C_2}{C_1 + C_2 + C_{in}}. \quad (5)$$

The circuits of Fig. 4 can therefore be simplified by replacing the VCCS by a simple resistance having a conductance equal to $G_m \cdot h_{fb}$ resulting in the simplified circuits shown in Fig. 5. The later circuits can now be considered as passive and can be represented as in Fig. 6a. However, the Bode theorem cannot be applied directly because the noise current source corresponding to the conductance $h_{fb} \cdot G_m$ is not equal to $4k_B T h_{fb} G_m$ like for the noise sources associated to the switch resistances. In order to apply the Bode theorem, the OTA noise current source PSD $4k_B T \gamma G_m$ can be split into the sum of $4k_B T h_{fb} G_m$ and a term $4k_B T (\gamma - h_{fb}) G_m$ that includes the OTA thermal noise excess. The circuit of Fig. 6a can hence be decomposed into two circuits, the circuit shown in Fig. 6b, where all the conductances have the same noise temperature T , and the circuit of Fig. 6c, where the switches are considered noiseless and the noise source corresponding to conductance $h_{fb} \cdot G_m$ is considered to have a noise temperature equal to $(\gamma/h_{fb} - 1) \cdot T$. The variance of the noise voltage $V_{n(kl)}^2$ between any node k and l of the circuit of Fig. 6a can then be calculated using the superposition of the noise sources as the sum of the noise voltage variance $V_{n1(kl)}^2$ of the circuit shown in Fig. 6b, where all the conductances have the same noise temperature T , and noise voltage variance $V_{n2(kl)}^2$ of the circuit shown in Fig. 6c, corresponding to the excess noise in the equivalent conductance of the OTA with a noise temperature $(\gamma/h_{fb} - 1) \cdot T$

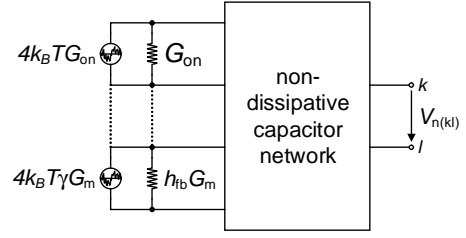
$$V_{n(kl)}^2 = V_{n1(kl)}^2 + V_{n2(kl)}^2. \quad (6)$$

The Bode theorem for passive networks can then be applied to the circuit shown in Fig. 6b to calculate the noise voltage variance $V_{n1(kl)}^2$ as

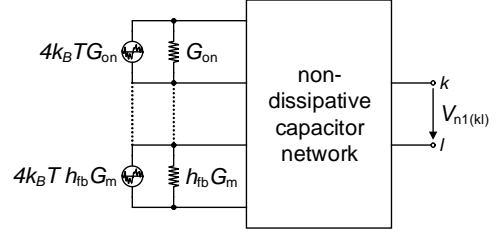
$$V_{n1(kl)}^2 = k_B T \cdot \left(\frac{1}{C_{\infty(kl)}} - \frac{1}{C_{0(kl)}} \right), \quad (7)$$

where $C_{\infty(kl)}$ corresponds to the capacitance seen when looking between the nodes k and l when all the switches and transconductance amplifiers are removed, and $C_{0(kl)}$ corresponds to the capacitance obtained looking between the nodes k and l when the switches are replaced by short-circuits and all OTAs have their output shorted to ground.

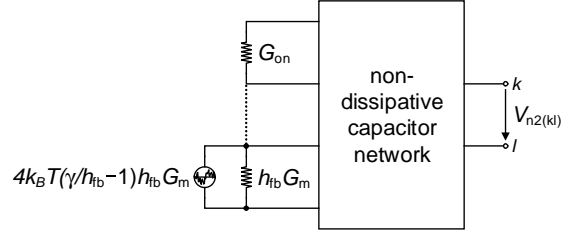
The circuit of Fig. 6c can be further simplified considering that usually $G_{on} \gg h_{fb} \cdot G_m$ and hence the on-conductances of the switches can be replaced by short-circuits resulting in



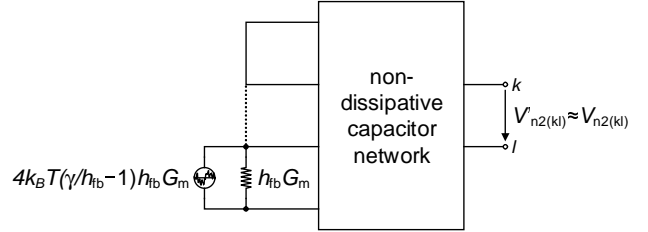
(a) transconductance amplifier-based SC circuit in one phase represented as a passive RC network.



(b) Circuit of Fig. 6a with all conductances having the same noise temperature T .



(c) Circuit of Fig. 6a without the switch noise sources and accounting for the excess noise of the transconductance amplifier with a noise temperature $(\gamma/h_{fb} - 1) \cdot T$.



(d) Simplification of the circuit of Fig. 6c accounting for the fact that usually $G_{on} \gg h_{fb} \cdot G_m$.

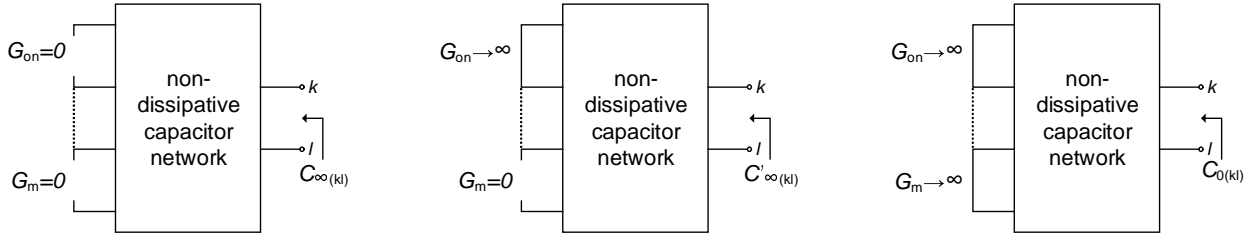
Fig. 6: Simplified schematic of transconductance amplifiers-based circuit [33].

the circuit shown in Fig. 6d. The noise voltage variance $V_{n2(kl)}^2$ accounting for the OTA excess noise temperature can therefore be estimated by applying the Bode theorem to the circuit of Fig. 6d resulting in

$$V_{n2(kl)}^2 \cong k_B T \cdot \left(\frac{\gamma}{h_{fb}} - 1 \right) \cdot \left(\frac{1}{C'_{\infty(kl)}} - \frac{1}{C_{0(kl)}} \right), \quad (8)$$

where $C'_{\infty(kl)}$ corresponds to the capacitance seen between the nodes k and l when all the switches are replaced by short-circuits and the transconductance amplifiers are removed.

The total thermal noise voltage variance seen between nodes



(a) Equivalent circuit used for the calculation of $C_{\infty(kl)}$: all switches and OTAs of the SC circuit are removed. (b) Equivalent circuit used for the calculation of $C'_{\infty(kl)}$: all switches that are closed during the clock phase in consideration are replaced by short-circuits and all OTAs of the SC circuit are removed. (c) Equivalent circuit used for the calculation of $C_{0(kl)}$: all switches that are closed during the clock phase in consideration are replaced by short-circuits and all OTAs of the SC circuit have their output shorted to ground.

Fig. 7: Capacitances calculation for the extended Bode theorem [33].

k and l is then given by summing (7) and (8), resulting in

$$V_{n(kl)}^2 = k_B T \cdot \left[\frac{1}{C_{\infty(kl)}} + \frac{\gamma/h_{fb} - 1}{C'_{\infty(kl)}} - \frac{\gamma/h_{fb}}{C_{0(kl)}} \right]. \quad (9)$$

Eq. (9) is central to this calculation method. It shows that the computation of $V_{n(kl)}^2$, for example at the amplifier output, only requires the evaluation of the three capacitances $C_{\infty(kl)}$, $C'_{\infty(kl)}$ and $C_{0(kl)}$. The latter can easily be calculated by inspection of the three equivalent circuits depicted in Fig. 7 which are each composed only of capacitors.

The extension of the Bode theorem presented in this Section will now be illustrated and validated by transient noise simulations for various SC circuits in the next Section.

IV. PRACTICAL EXAMPLES OF THERMAL NOISE ESTIMATION IN OTA-BASED SC CIRCUITS

A. SC Amplifier

1) *Analysis:* Let's now get back to the SC amplifier shown in Fig. 3 and apply the extended Bode theorem to calculate the noise voltage variances. We start calculating the noise voltage variance across the sampling capacitor C_1 during phase Φ_1 $V_{nC_1}^2|_{\Phi_1}$. To this purpose, we need to calculate the three capacitances seen across C_1 , namely $C_{\infty(C_1)}$, $C'_{\infty(C_1)}$ and $C_{0(C_1)}$ during phase Φ_1 . They can easily be calculated from the equivalent circuits shown in Fig. 8, resulting in

$$C_{\infty(C_1)} = C_1, \quad (10a)$$

$$C'_{\infty(C_1)} = C_1 + C_{in} + C_L, \quad (10b)$$

$$C_{0(C_1)} = \infty. \quad (10c)$$

Recognizing that the feedback gain during phase Φ_1 is simply equal to unity, the noise voltage variance across C_1 during phase Φ_1 can be evaluated from (9) as

$$V_{nC_1}^2|_{\Phi_1} = \frac{k_B T}{C_1 + C_{in} + C_L} \cdot \left(\gamma + \frac{C_{in} + C_L}{C_1} \right). \quad (11)$$

Eq. (11) is actually identical to the result derived analytically in Appendix VI-A by calculating the noise contributions from each of the noise sources shown in Fig. 4a, namely the two switches and the OTA. Each contribution is obtained by first calculating the transfer function from each noise source to the voltage across capacitor C_1 and integrating the corresponding

noise PSD over frequency. The noise voltage variances due to each of the noise source assuming that the switch resistances are negligible compared to $1/G_m$ (i.e. $G_m R_{on} \ll 1$) are given in Table II. The total noise voltage variance is obtained by summing these three variances resulting in the result shown in the last row of Table II which is identical to (11). Note that when setting $C_{in} = 0$ in (11), we also get the same result than found in [40] which has been computed using the equivalent noise bandwidth approach. As expected, (11) does not depend on C_2 since the latter is short-circuited. This happens even though the individual contributions of each switch depends on C_2 as shown in Table II, but their sum does not depend on C_2 anymore.

To this noise voltage variance corresponds a noise charge sampled on C_1 at the end of phase Φ_1 and having a variance

$$Q_{nC_1}^2|_{\Phi_1} = C_1^2 \cdot V_{nC_1}^2|_{\Phi_1}. \quad (12)$$

This charge is then injected to the virtual ground at the beginning of phase Φ_2 and transferred to the feedback capacitor C_2 during phase Φ_2 thanks to the action of the OTA. Assuming that the latter has an infinite DC gain and a zero offset voltage, the output voltage is equal to the voltage across C_2 . The output noise voltage variance due to the noise sampled on C_1 at the end of phase Φ_1 is then given by

$$\begin{aligned} V_{nout}^2|_{\Phi_1} &= \frac{Q_{nC_1}^2|_{\Phi_1}}{C_2^2} = \left(\frac{C_1}{C_2} \right)^2 \cdot V_{nC_1}^2|_{\Phi_1} \\ &= \left(\frac{C_1}{C_2} \right)^2 \cdot \frac{k_B T}{C_1 + C_{in} + C_L} \cdot \left(\gamma + \frac{C_{in} + C_L}{C_1} \right). \end{aligned} \quad (13)$$

The variance of the output noise voltage during phase Φ_2 is simply evaluated using (9) which requires the calculation of the three capacitances $C_{\infty(out)}$, $C'_{\infty(out)}$ and $C_{0(out)}$ seen from the output. The latter can be calculated from the equivalent schematics shown in Fig. 9 resulting in

$$C_{\infty(out)} = C_L + \frac{C_2 C_{in}}{C_2 + C_{in}}, \quad (14a)$$

$$C'_{\infty(out)} = C_L + \frac{C_2 (C_1 + C_{in})}{C_1 + C_2 + C_{in}}, \quad (14b)$$

$$C_{0(out)} = \infty. \quad (14c)$$

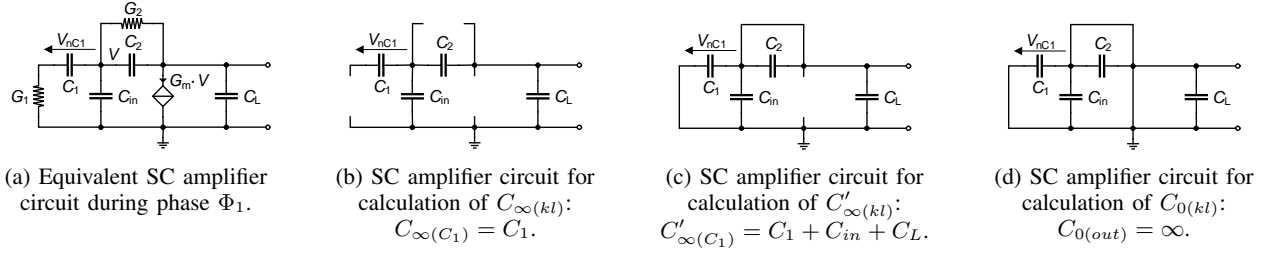


Fig. 8: SC amplifier equivalent circuit schematics for phase Φ_1 .

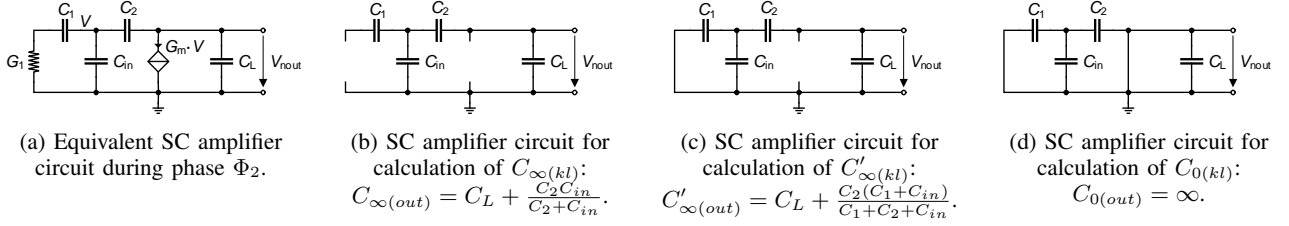


Fig. 9: SC amplifier equivalent circuit schematics for phase Φ_2 .

Eq. (9) also requires the feedback gain h_{fb} which during phase Φ_2 is given by

$$h_{fb}|_{\Phi_2} = \frac{C_2}{C_1 + C_2 + C_{in}}. \quad (15)$$

The output noise voltage variance during phase Φ_2 can now be evaluated from (9) leading to

$$V_{nout}^2|_{\Phi_2} = \frac{k_B T}{C_2} \cdot (\gamma \cdot \beta_{ota}|_{\Phi_2} + \beta_{sw}|_{\Phi_2}), \quad (16)$$

where

$$\beta_{ota}|_{\Phi_2} = \frac{(C_1 + C_2 + C_{in})^2}{B}, \quad (17a)$$

$$\beta_{sw}|_{\Phi_2} = \frac{C_1 C_2^3}{(C_2 C_{in} + C_2 C_L + C_{in} C_L) \cdot B}, \quad (17b)$$

with

$$B = C_1 C_2 + C_2 C_{in} + C_1 C_L + C_2 C_L + C_{in} C_L. \quad (18)$$

Note that (16) is identical to the result derived in Appendix VI-A using the classical approach described above and given in the last row of Table IV.

Eq. (17a) and (17b) can be rewritten as

$$\beta_{ota}|_{\Phi_2} = \frac{(|A_v| + \alpha_{in} + 1)^2}{D}, \quad (19a)$$

$$\beta_{sw}|_{\Phi_2} = \frac{|A_v|}{(\alpha_{in} + \alpha_L + \alpha_{in} \alpha_L) \cdot D}, \quad (19b)$$

$$D = \frac{B}{C_2^2} = |A_v| + \alpha_L \cdot (|A_v| + \alpha_{in} + 1) + \alpha_{in}, \quad (19c)$$

where $|A_v| \triangleq C_1/C_2$, $\alpha_{in} \triangleq C_{in}/C_2$ and $\alpha_L \triangleq C_L/C_2$.

Assuming that $|A_v| \gg 1$, $\alpha_{in} < 1$ and $\alpha_L < 1$, $D \cong |A_v| \cdot (\alpha_L + 1)$ and equations (19a) and (19b) simplify to

$$\beta_{ota}|_{\Phi_2} \cong \frac{|A_v|}{\alpha_L + 1}, \quad (20a)$$

$$\beta_{sw}|_{\Phi_2} \cong \frac{1}{(\alpha_{in} + \alpha_L + \alpha_{in} \alpha_L)(\alpha_L + 1)}, \quad (20b)$$

Before calculating the total noise voltage variance at the output, we can rewrite (13) as

$$V_{nout}^2|_{\Phi_1} = \frac{k_B T}{C_2} \cdot (\gamma \cdot \beta_{ota}|_{\Phi_1} + \beta_{sw}|_{\Phi_1}), \quad (21)$$

where

$$\beta_{ota}|_{\Phi_1} = \frac{|A_v|^2}{|A_v| + \alpha_{in} + \alpha_L} \cong |A_v|, \quad (22a)$$

$$\beta_{sw}|_{\Phi_1} = \frac{|A_v| \cdot (\alpha_{in} + \alpha_L)}{|A_v| + \alpha_{in} + \alpha_L} \cong \alpha_{in} + \alpha_L. \quad (22b)$$

The total output noise voltage variance at the end of phase Φ_2 is then given by summing (21) and (16), resulting in

$$V_{nout}^2 = V_{nout}^2|_{\Phi_1} + V_{nout}^2|_{\Phi_2} = \frac{k_B T}{C_2} \cdot (\gamma \cdot \beta_{ota} + \beta_{sw}), \quad (23)$$

where

$$\beta_{ota} = \beta_{ota}|_{\Phi_1} + \beta_{ota}|_{\Phi_2} \cong |A_v| \cdot \frac{\alpha_L + 2}{\alpha_L + 1}, \quad (24a)$$

$$\begin{aligned} \beta_{sw} &= \beta_{sw}|_{\Phi_1} + \beta_{sw}|_{\Phi_2} \cong \\ &\cong \alpha_{in} + \alpha_L + \frac{1}{(\alpha_{in} + \alpha_L + \alpha_{in} \alpha_L)(\alpha_L + 1)}. \end{aligned} \quad (24b)$$

It can be shown that the effect of C_{in} is negligible as long as the DC gain of the OTA is infinite. The switch contribution given by (24b) can be further simplified by setting $C_{in} = 0$ (or $\alpha_{in} = 0$) resulting in

$$\beta_{sw} \cong \alpha_L + \frac{1}{\alpha_L(\alpha_L + 1)}. \quad (25)$$

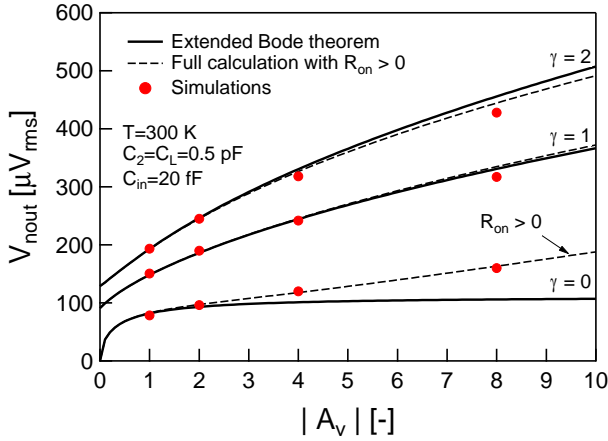


Fig. 10: Output noise rms voltage versus the amplifier gain $|A_v|$ for $\gamma = 0, 1, 2$.

2) *Simulations*: The above results for the SC amplifier have been verified by transient noise simulation [21] in ELDO[®]. The simulations are performed on a circuit where the OTA is modeled by a simple VCCS and the switches are modelled by an ideal switch in series with a noisy resistor of resistance $R_{on} = 5 \text{ k}\Omega$. The noise of the OTA is generated by a noisy resistor of value γ/G_m and injected at the OTA output by means of a VCCS with a unity transconductance. The sampling period has been chosen equal to $1 \mu\text{s}$ and the temperature is set to $T = 300 \text{ K}$.

Fig. 10 shows the output noise rms voltage versus the gain $|A_v|$ for different values of the OTA excess noise factor $\gamma = 0, 1, 2$. The simulations have been performed for different gains $|A_v| = 1, 2, 4, 8$ by changing the value of C_1 keeping $C_2 = C_L = 0.5 \text{ pF}$. When increasing capacitance C_1 , it also increases the effective load capacitance $C_{out} = C_L + (1-\beta)C_2$ with $\beta = C_2/(C_1 + C_2 + C_{in})$ and the settling time $t_{set} = C_{eq}/G_m$ where $C_{eq} = C_{out}/\beta$. The VCCS transconductance G_m has therefore been chosen to keep a constant settling time $t_{set} = T_s/10 = 100 \text{ ns}$ for each values of C_1 and hence of $|A_v|$. Note that the influence of the input capacitance C_{in} is negligible and the later has been set to a realistic value of $C_{in} = 20 \text{ fF}$. The simulation results for $\gamma = 1$ and $\gamma = 2$ are very close to the estimation computed from (23). However, a small deviation is observed for the case where $\gamma = 0$ which corresponds to the noise generated by the switches only. The simulation results are slightly larger than the values predicted by (23), particularly for the maximum gain $|A_v| = 8$. The reason for this is that larger gains require larger G_m resulting in the product $G_m \cdot R_{on}$ increasing to about 0.27 which does no more fulfill the assumption of $G_m \cdot R_{on} \ll 1$ used in the Bode theorem derivation. The impact of a non-zero $G_m \cdot R_{on}$ has been checked using the full analytical expressions obtained from the classical analysis detailed in Appendix VI-A¹. The results are plotted in Fig. 10 by dashed lines which are very

¹Note that, for the sake of compactness, the analytical expressions including the effect of a non-zero $G_m \cdot R_{on}$ could not be included in the Appendix VI-A because they are rather large expressions.

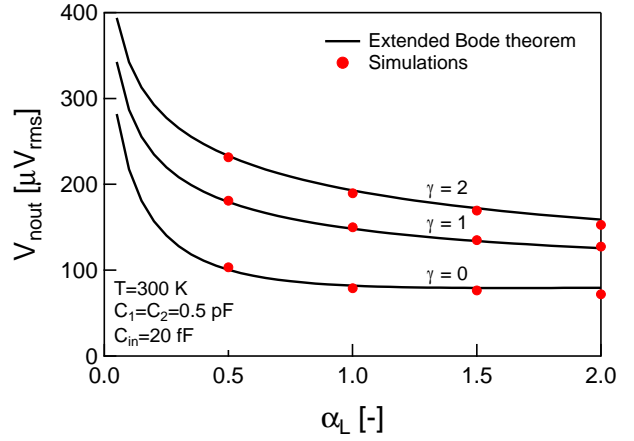


Fig. 11: Output noise rms voltage versus α_L for $\gamma = 0, 1, 2$.

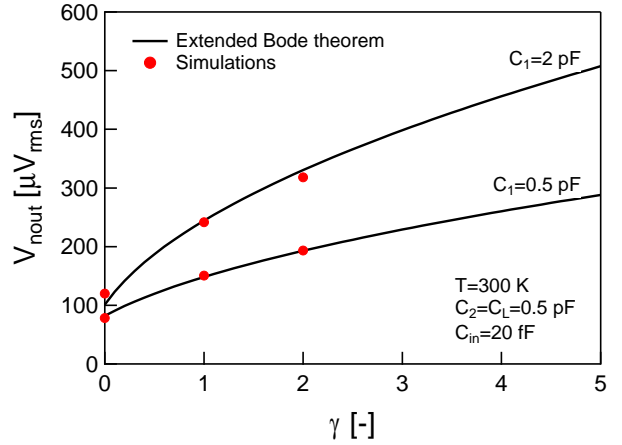


Fig. 12: Output noise voltage versus γ for $C_1 = 0.5 \text{ pF}$ and $C_1 = 1 \text{ pF}$.

close to the simulation results, confirming the origin of the deviation.

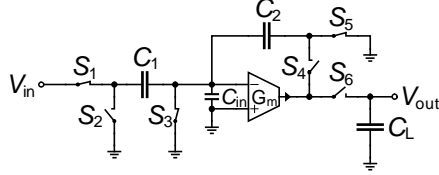
Fig. 11 shows the output noise rms voltage versus α_L for $\gamma = 0, 1, 2$ and for a unity voltage gain $|A_v| = 1$ ($C_1 = C_2 = 0.5 \text{ pF}$). The noise simulation results are very close to the estimation using (23).

Finally, Fig. 12 shows the output noise rms voltage versus the OTA noise excess factor γ for two different values of C_1 ($C_1 = 0.5 \text{ pF}$ and $C_1 = 2 \text{ pF}$ corresponding to a voltage gain $|A_v| = 1$ and $|A_v| = 4$, respectively). As expected from (23), $V_{nout,rms}$ increases as $\sqrt{\beta_{ota} \cdot \gamma + \beta_{sw}}$. The simulation results fall again very close to the value predicted with (23).

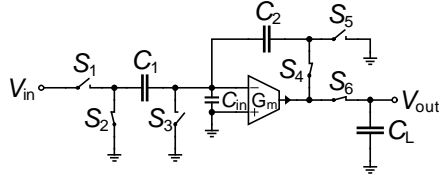
B. SC Track & hold

Fig. 13 shows the schematic of a basic SC track & hold (TH) circuit which can operate either as a TH or as a SC amplifier featuring a voltage gain set by the capacitance ratio C_1/C_2 . This circuit operates in two phases as shown in Fig. 13. During phase Φ_1 , shown in Fig. 13a, the sampling capacitor C_1 samples the input signal V_{in} . During this phase, the feedback capacitor C_2 is shorted to be reset, while the capacitor C_L

holds the charge that has been sampled at the end of phase Φ_2 of the previous switching period. During phase Φ_2 , shown in Fig. 13b, the charge sampled in C_1 is transferred to the feedback capacitor C_2 . The output voltage seen across C_L is then simply equal to $C_1/C_2 \cdot V_{in}$. This voltage is then sampled and held on C_L at the end of phase Φ_2 .



(a) SC track & hold circuit during phase Φ_1 .



(b) SC track & hold circuit during phase Φ_2

Fig. 13: SC Track & hold circuit.

1) *Analysis:* The output voltage is read during phase Φ_1 from the hold capacitor C_L and the sampled output noise must therefore be calculated at the end of phase Φ_2 . As in the example above, this circuit presents two non-overlapping phases for which the equivalent linear circuits are depicted in Fig. 14a and Fig. 15a, respectively.

The capacitors sampling a noise charge at the end of phase Φ_1 are C_1 , C_2 as well as the parasitic capacitance at the OTA input C_{in} . The sum of these noise charges is injected into the virtual ground during phase Φ_2 and transferred to the feedback capacitor C_2 . This noise charge on capacitor C_2 results in a noise voltage at the OTA output which will be sampled on C_L at the end of phase Φ_2 .

The extended Bode theorem is used to calculate the noise voltage variances across capacitors C_1 , C_2 and C_{in} for phase Φ_1 . The calculations of capacitors C_∞ , C'_∞ and C_0 for each capacitor C_1 , C_2 and C_{in} during phase Φ_1 is done using the equivalent circuits shown in Fig. 14. The resulting voltage variances based on (9) are then given by

$$V_{nC_1}^2|_{\Phi_1} = k_B T \cdot \left[\frac{1}{C_1} + 0 - 0 \right] = \frac{k_B T}{C_1}, \quad (26a)$$

$$V_{nC_2}^2|_{\Phi_1} = k_B T \cdot \left[\frac{1}{C_2} + 0 - 0 \right] = \frac{k_B T}{C_2}, \quad (26b)$$

$$V_{nC_{in}}^2|_{\Phi_1} = k_B T \cdot \left[\frac{1}{C_{in}} + 0 - 0 \right] = \frac{k_B T}{C_{in}}. \quad (26c)$$

The total noise charge generated during phase Φ_1 and injected into the virtual ground is then given by

$$\begin{aligned} Q_n^2|_{\Phi_1} &= C_1^2 \cdot V_{nC_1}^2|_{\Phi_1} + C_2^2 \cdot V_{nC_2}^2|_{\Phi_1} + C_{in}^2 \cdot V_{nC_{in}}^2|_{\Phi_1} \\ &= k_B T \cdot (C_1 + C_2 + C_{in}). \end{aligned} \quad (27)$$

The charge $Q_n^2|_{\Phi_1}$ is subsequently transferred to capacitor C_2 during phase Φ_2 . Assuming again that the OTA has an

infinite DC gain and a zero offset voltage, the output voltage is equal to the voltage across C_2 and the variance of the noise voltage seen at the output of the OTA resulting from this charge is hence given by

$$V_{nC_L}^2|_{\Phi_1} = V_{nC_2}^2|_{\Phi_1} = \frac{Q_n^2|_{\Phi_1}}{C_2^2} = \frac{k_B T}{C_2} \cdot \beta_{sw}|_{\Phi_1}. \quad (28)$$

where

$$\beta_{sw}|_{\Phi_1} = A_v + \alpha_{in} + 1, \quad (29)$$

with $A_v \triangleq C_1/C_2$, $\alpha_{in} \triangleq C_{in}/C_2$.

For phase Φ_2 , the noise charge held on capacitor C_L can be directly calculated using the extended Bode theorem applied at the output. Fig. 15 shows the equivalent circuit schematics used for the noise voltage variance calculation using (9), which additionally also requires the feedback gain h_{fb} given by

$$h_{fb} = \frac{V}{V_{out}} = \frac{1}{A_v + \alpha_{in} + 1}. \quad (30)$$

The variance of the noise voltage generated across C_L during phase Φ_2 is then given by

$$V_{nC_L}^2|_{\Phi_2} = \frac{k_B T}{C_2} \cdot (\gamma \cdot \beta_{ota}|_{\Phi_2} + \beta_{sw}|_{\Phi_2}). \quad (31)$$

where

$$\beta_{ota}|_{\Phi_2} = \frac{(A_v + \alpha_{in} + 1)^2}{D}, \quad (32a)$$

$$\beta_{sw}|_{\Phi_2} = \frac{1}{\alpha_L} \cdot \frac{A_v + \alpha_{in}}{D}, \quad (32b)$$

where D is given by (19c) and $\alpha_L \triangleq C_L/C_2$. The first term in (31) corresponds to the contribution of the OTA during phase Φ_2 and is actually identical to the expression (19a) obtained for the SC amplifier. This not surprising since, assuming the inputs are grounded and the switches are ideal (zero resistance and hence noiseless), the circuit of Fig. 13b is identical to that of the SC amplifier shown in Fig. 3a. The second term in (31) corresponds to the contribution of the switches.

In this circuit, none of the capacitors is holding a noise charge from one switching period to the next. Indeed, capacitor C_2 is reset during phase Φ_1 , capacitors C_1 and C_{in} are reset during phase Φ_2 by the action of the OTA, while capacitor C_L is connected to the OTA output during phase Φ_2 to sample the new value. Consequently, at the end of each switching period, the noise variance of the output voltage corresponds to the sum of the noise injected from phases Φ_1 and Φ_2 without any contributions from the previous switching periods. The variance of the total noise voltage sampled on C_L can hence be expressed as

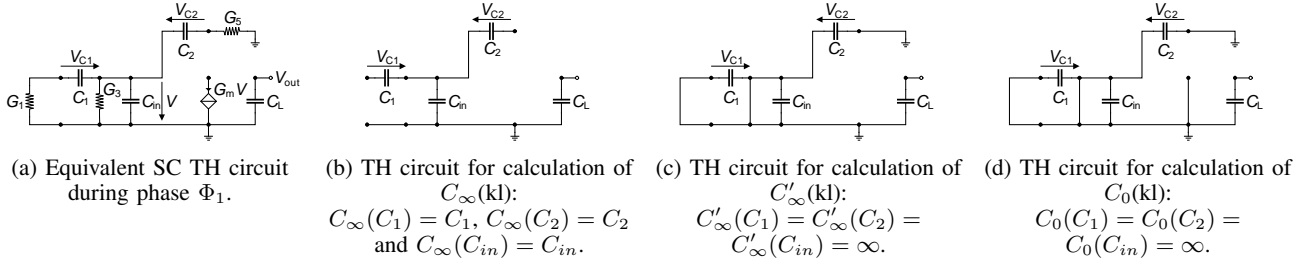
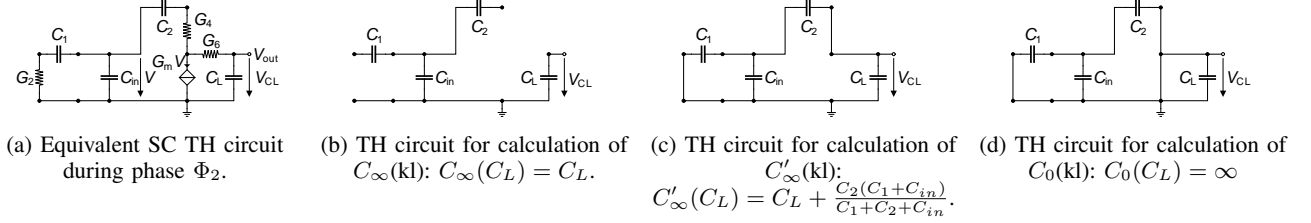
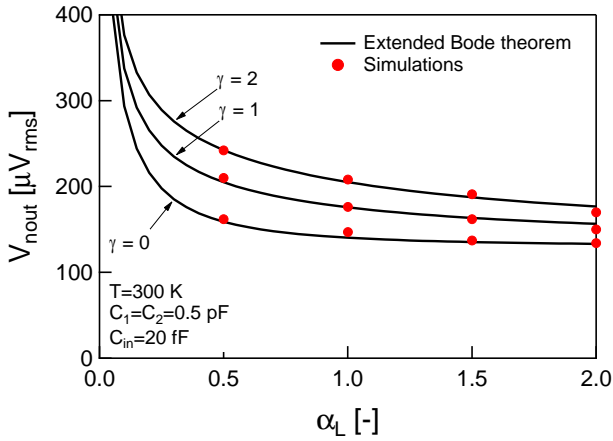
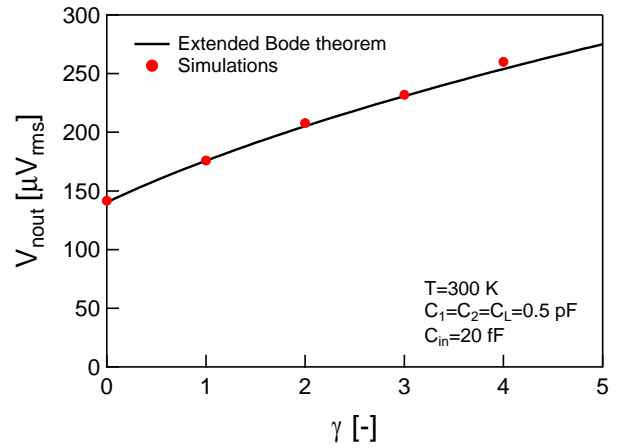
$$V_{nC_L}^2 = V_{nC_L}^2|_{\Phi_1} + V_{nC_L}^2|_{\Phi_2} = \frac{k_B T}{C_2} \cdot (\gamma \cdot \beta_{ota} + \beta_{sw}), \quad (33)$$

where

$$\beta_{ota} = \beta_{ota}|_{\Phi_2}, \quad (34a)$$

$$\beta_{sw} = \beta_{sw}|_{\Phi_1} + \beta_{sw}|_{\Phi_2}, \quad (34b)$$

The first term in brackets of (33) is the noise contribution coming from the OTA, which only contributes during phase


 Fig. 14: TH equivalent circuit schematics for phase Φ_1 .

 Fig. 15: TH equivalent circuit schematics for phase Φ_2 .

 Fig. 16: Output noise rms voltage versus α_L for $\gamma = 0, 1, 2$.

 Fig. 17: Output noise voltage versus γ for $C_1 = 0.5$ pF.

V. CONCLUSION

Φ_2 , while the second term is due to the noise coming from the switches during phases Φ_1 and Φ_2 . Note that (33) matches the result presented in [41] except for the second term $\beta_{sw}|_{\Phi_2}$ in (34b) which corresponds to the contribution of the switches in phase Φ_2 and which is omitted in [41]. This is reasonable since this term is usually small and can be neglected for the TH circuit because in general $C_{in} \ll C_1 = C_2$ ($A_v = 1$).

2) *Simulations*: The results obtained for the SC TH have also been validated by transient noise simulation for a gain $A_v = 1$ with the same sampling period and temperature as for the SC amplifier. The output noise rms voltage is plotted versus α_L in Fig. 16 for 3 different values of $\gamma = 0, 1, 2$. Fig. 17 shows the output rms noise voltage versus the OTA thermal noise excess factor γ for $C_1 = C_2 = C_L = 0.5$ pF. In both cases, the simulation results are very close to the theoretical results predicted from the extended Bode theorem (23).

The optimization of SC circuits for achieving at the same time low-noise operation at low-power requires an accurate estimation of the integrated noise at the circuit output. Part I of this paper presents a simple method to obtain an analytical expression of the thermal noise voltage variance at any port of an active SC circuit made of OTAs with a capacitive feedback. The thermal noise variance is derived by simple inspection of three different circuits avoiding the laborious calculation of the noise transfer functions and integrals. It is based on an extension of the original Bode theorem which allows the exact calculation of the thermal noise voltage variance but only in passive circuits [34]. In Part I, the proposed method is applied to a SC amplifier and a SC track & hold circuit and is successfully validated by transient noise simulations. Part II of the paper will illustrate how this method can be extended to the calculation of thermal noise voltage variances in SC filters.

VI. APPENDICES

A. SC Amplifier Noise Calculation

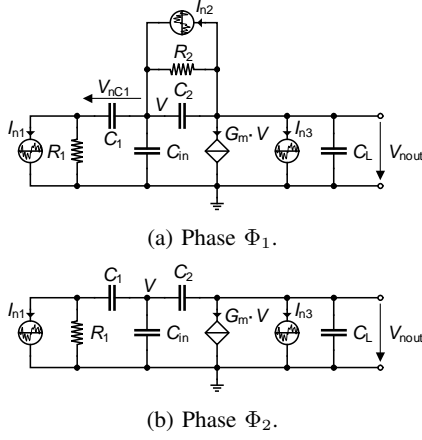


Fig. 18: Small-signal equivalent circuit of Fig. 3 for the calculation of the output noise voltage.

The noise of the SC amplifier of Fig. 3 can be calculated in a classical way. The noise voltage variance across capacitor C_1 during phase Φ_1 can be calculated from the equivalent small-signal circuit shown in Fig. 18a using

$$V_{nC1}^2|_{\Phi_1} = \sum_{i=1}^3 V_{nC1,i}^2|_{\Phi_1}, \quad (35)$$

and

$$V_{nC1,i}^2|_{\Phi_1} = \int_0^{+\infty} |R_{m,i}(f)|^2 \cdot S_{I_{n,i}} \cdot df, \quad (36)$$

where $R_{m,i}$ are the noise transfer functions (NTF) (actually transresistances) from the current noise sources $I_{n,i}$ to the voltage across C_1 and $S_{I_{n,i}}$ are the PSD of the thermal noise current sources $I_{n,i}$ given by $S_{I_{n,1}} = S_{I_{n,2}} = 4k_B T / R_{on}$ and $S_{I_{n,3}} = 4k_B T \gamma G_m$. The NTF $R_{m,i}$ are given by

$$R_{m,i} \triangleq \frac{V_{nC1}}{I_{n,i}} = R_i \cdot \frac{n_2 s^2 + n_1 s + n_0}{d_3 s^3 + d_2 s^2 + d_1 s + d_0} \quad (37)$$

where the scaling factors R_i and the coefficients of $R_{m,i}$ for $i = 1, 2, 3$ are given in Table I. For thermal noise, the PSD $S_{I_{n,i}}$ are constant and the noise voltage variance can be calculated using the equivalent noise bandwidth $B_{n,i}$ as

$$V_{nC1,i}^2|_{\Phi_1} = |R_{m,i}(0)|^2 \cdot 4k_B T \cdot S_{I_{n,i}} \cdot B_{n,i}. \quad (38)$$

In the case of the SC amplifier in phase Φ_1 , the NTF are of 3rd-order. The noise bandwidth and variances can then be obtained by using the expression (22) in [32]. The resulting noise voltage variances for each noise source assuming that the switch resistances are negligible ($G_m R_{on} \ll 1$) are given in Table II. The total noise voltage variance is obtained by summing the 3 contributions, leading to the result shown in the last row of Table II. Note that even though the individual contributions of the switch noise sources $I_{n,1}$ and $I_{n,2}$ given in Table II both contain capacitance C_2 , when summing both contributions, as expected, the result becomes independent of C_2 as shown in the fourth row of Table II.

The same approach can be used to calculate the noise voltage variance at the amplifier output during phase Φ_2 using the small-signal schematic of Fig. 18b. The coefficients of the 2nd-order NTF are given in Table III. Using the technique presented in [32] we get the noise voltage variances at the amplifier output during phase Φ_2 due to noise sources $I_{n,1}$ and $I_{n,3}$ given in Table IV. The total output noise voltage variance is then given by summing these two contributions, leading to the result shown in the last row of Table IV.

TABLE I: Coefficients of the NTF for the SC-Amplifier in phase Φ_1 .

Term	$R_{m,1}$	$R_{m,2}$	$R_{m,3}$
R_i	R_{on}	$\frac{1}{G_m}$	$-\frac{1}{G_m}$
n_2	$\frac{R_{on}(C_2C_{in}+C_2C_L+C_{in}C_L)}{G_m}$	0	0
n_1	$\frac{C_2G_mR_{on}+C_{in}+C_L}{G_m}$	$R_{on}C_L$	$R_{on}C_2$
n_0	1	0	1
d_3	$\frac{C_1R_{on}^2(C_2C_{in}+C_2C_L+C_{in}C_L)}{G_m}$		
d_2	$\frac{R_{on}(C_1C_2G_mR_{on}+C_1C_2+C_1C_{in}+2C_1C_L+C_2C_{in}+C_2C_L+C_{in}C_L)}{G_m}$		
d_1	$\frac{C_1G_mR_{on}+C_1+C_2G_mR_{on}+C_{in}+C_L}{G_m}$		
d_0	1		

 TABLE II: Contributions of the various noise sources to $V_{nC_1}^2$ during phase Φ_1 .

Noise source	Corresponding noise voltage variance across C_1	
$I_{n,1}$	$V_{nC_1,1}^2$	$\frac{k_B T (C_1 (C_2(C_{in}+C_L)+C_{in}^2+3C_{in}C_L+C_L^2)+(C_{in}+C_L)(C_2(C_{in}+C_L)+C_{in}C_L))}{C_1(C_1+C_{in}+C_L)(C_1(C_2+C_{in}+2C_L)+C_2(C_{in}+C_L)+C_{in}C_L)}$
$I_{n,2}$	$V_{nC_1,2}^2$	$\frac{C_L^2 k_B T}{(C_1+C_{in}+C_L)(C_1(C_2+C_{in}+2C_L)+C_2(C_{in}+C_L)+C_{in}C_L)}$
$I_{n,3}$	$V_{nC_1,3}^2$	$\frac{\gamma k_B T}{C_1+C_{in}+C_L}$
Switches only	$V_{nC_1,1}^2 + V_{nC_1,2}^2$	$\frac{k_B T (C_{in}+C_L)}{C_1(C_1+C_{in}+C_L)}$
Total	$V_{nC_1}^2$	$\frac{k_B T}{C_1+C_{in}+C_L} \cdot \left(\gamma + \frac{C_{in}+C_L}{C_1} \right)$

 TABLE III: Coefficients of the NTF for the SC-Amplifier in phase Φ_2 .

Term	$R_{m,1}$	$R_{m,3}$
R_i	$\frac{R_{on}C_1}{C_2}$	$-\frac{C_1+C_2+C_{in}}{G_mC_2}$
n_1	$-\frac{C_2}{G_m}$	$\frac{R_{on}C_1(C_2+C_{in})}{C_1+C_2+C_{in}}$
n_0	1	1
d_2	$\frac{R_{on}C_1(C_2C_{in}+C_2C_L+C_{in}C_L)}{G_mC_2}$	
d_1	$\frac{C_1C_2+C_2C_{in}+C_1C_L+C_2C_L+C_{in}C_L+G_mR_{on}C_1C_2}{G_mC_2}$	
d_0	1	

 TABLE IV: Contributions of the various noise sources to V_{nout}^2 during phase Φ_2 .

Noise source	Corresponding noise voltage variance at the amplifier output	
$I_{n,1}$	$V_{nout,1}^2$	$\frac{k_B T C_1 C_2^2}{(C_2(C_{in}+C_L)+C_{in}C_L)(C_1(C_2+C_L)+C_2(C_{in}+C_L)+C_{in}C_L)}$
$I_{n,3}$	$V_{nout,3}^2$	$\frac{\gamma k_B T (C_1+C_2+C_{in})^2}{C_2(C_1(C_2+C_L)+C_2(C_{in}+C_L)+C_{in}C_L)}$
Total	V_{nout}^2	$\frac{k_B T}{C_2} \frac{1}{C_{in}C_L+C_1(C_2+C_L)+C_2(C_{in}+C_L)} \left((C_1+C_2+C_{in})^2 \cdot \gamma + \frac{C_1C_2^3}{C_{in}C_L+C_2(C_{in}+C_L)} \right)$

REFERENCES

- [1] W. Poschenrieder, "Frequenzfilterung durch Netzwerke mit periodisch gesteuerten Schaltern," in *Proc. NTG-Symp. Analyse und Synthese von Netzwerken*, Stuttgart, 1966, pp. 221–237.
- [2] D. L. Fried, "Analog Sample-data filters," *IEEE Journal of Solid-State Circuits*, vol. 7, no. 4, pp. 302–304, Aug. 1972.
- [3] R. Gregorian and G. C. Temes, *Analog MOS Integrated Circuits for Signal Processing*. Wiley, 1986.
- [4] J. L. McCreary and P. R. Gray, "All-MOS Charge Redistribution Analog-to-digital Conversion Techniques - Part I," *IEEE Journal of Solid-State Circuits*, vol. 10, no. 6, pp. 371–379, Dec. 1975.
- [5] M. Darvishi, R. v. d. Zee, and B. Nauta, "Design of Active N-Path Filters," *IEEE Journal of Solid-State Circuits*, vol. 48, no. 12, pp. 2962–2976, 2013.
- [6] A. Ghaffari, E. A. M. Klumperink, M. C. M. Soer, and B. Nauta, "Tunable High-Q N-Path Band-Pass Filters: Modeling and Verification," *IEEE Journal of Solid-State Circuits*, vol. 46, no. 5, pp. 998–1010, May 2011.
- [7] Y. Xu and P. R. Kinget, "A Switched-Capacitor RF Front End With Embedded Programmable High-Order Filtering," *IEEE Journal of Solid-State Circuits*, vol. 51, no. 5, pp. 1154–1167, May 2016.
- [8] A. Boukhayma, A. Peizerat, and C. Enz, "A Sub-0.5 Electron Read Noise VGA Image Sensor in a Standard CMOS Process," *IEEE Journal of Solid-State Circuits*, vol. 51, no. 9, pp. 2180–2191, Sept. 2016.
- [9] A. Boukhayma, A. Dupret, J.-P. Rostaing, and C. Enz, "A Low-noise CMOS THz Imager Based on Source Modulation and an In-pixel High-Q Passive Switched-capacitor n-path Filter," *Sensors*, vol. 16, no. 3, March 2016.
- [10] A. Boukhayma, A. Peizerat, and C. Enz, "A Correlated Multiple Sampling Passive Switched Capacitor Circuit for Low Light CMOS Image Sensors," in *2015 International Conference on Noise and Fluctuations (ICNF)*, June 2015, pp. 1–4.
- [11] M. Liou and Y.-L. Kuo, "Exact analysis of switched capacitor circuits with arbitrary inputs," *IEEE Transactions on Circuits and Systems*, vol. 26, no. 4, pp. 213–223, April 1979.
- [12] J. Vandewalle, H. D. Man, and J. Rabaey, "The adjoint switched capacitor network and its application to frequency, noise and sensitivity analysis," *International Journal of Circuit Theory and Applications*, vol. 9, no. 1, pp. 77–88, Jan. 1981.
- [13] J. H. Fischer, "Noise sources and calculation techniques for switched capacitor filters," *IEEE Journal of Solid-State Circuits*, vol. 17, no. 4, pp. 742–752, 1982.
- [14] C. A. Gobet and A. Knob, "Noise Analysis of Switched Capacitor Networks," *IEEE Trans. on Circuits and Systems*, vol. 30, no. 1, pp. 37–43, Jan. 1983.
- [15] J. Goette and C. A. Gobet, "Exact Noise Analysis of SC Circuits and an Approximate Computer Implementation," *IEEE Trans. on Circuits and Systems*, vol. 36, no. 4, pp. 508–521, April 1989.
- [16] L. Toth and K. Suyama, "Exact noise analysis of 'ideal' SC networks," in *1991, IEEE International Symposium on Circuits and Systems*, 11–14 June 1991 1991, pp. 1585–1588 vol.3.
- [17] L. Toth, I. Yusim, and K. Suyama, "Noise analysis of ideal switched-capacitor networks," *IEEE Transactions on Circuits and Systems I: Fundamental Theory and Applications*, vol. 46, no. 3, pp. 349–363, March 1999.
- [18] O. Oliaei, "Numerical algorithm for noise analysis of switched-capacitor networks," *IEEE Transactions on Circuits and Systems I: Fundamental Theory and Applications*, vol. 50, no. 7, pp. 865–876, July 2003.
- [19] V. Vasudevan, "A time-domain technique for computation of noise-spectral density in linear and nonlinear time-varying circuits," *IEEE Transactions on Circuits and Systems I: Regular Papers*, vol. 51, no. 2, pp. 422–433, 2004.
- [20] V. Vasudevan and M. Ramakrishna, "Computation of the average and harmonic noise power-spectral density in switched-capacitor circuits," *IEEE Transactions on Circuits and Systems I: Regular Papers*, vol. 51, no. 11, pp. 2165–2174, Nov. 2004.
- [21] P. Bolcato and R. Poujois, "A New Approach for Noise Simulation in Transient Analysis," in *Proc. of the IEEE International Symposium on Circuits and Systems (ISCAS)*, vol. 2, May 1992, pp. 887–890.
- [22] C. A. Gobet, "Spectral Distribution of a Sampled 1st-order Lowpass Filtered White Noise," *Electronics Letters*, vol. 17, no. 19, pp. 720–721, Sept. 1981.
- [23] C. C. Enz and G. C. Temes, "Circuit Techniques for Reducing the Effects of Op-amp Imperfections: Autozeroing, Correlated Double Sampling, and Chopper Stabilization," *Proceedings of the IEEE*, vol. 84, no. 11, pp. 1584–1614, Nov. 1996.
- [24] R. C. Yen and P. R. Gray, "A MOS Switched-capacitor Instrumentation Amplifier," *IEEE Journal of Solid-State Circuits*, vol. 17, no. 6, pp. 1008–1013, Dec. 1982.
- [25] F. Krummenacher, "Micropower Switched Capacitor Biquadratic Cell," *IEEE Journal of Solid-State Circuits*, vol. 17, no. 3, pp. 507–512, June 1982.
- [26] C. Enz, "Analysis of low-frequency noise reduction by autozero technique," *Electronics Letters*, vol. 20, no. 23, pp. 959–960, 1984.
- [27] K.-C. Hsieh, P. R. Gray, D. Senderowicz, and D. G. Messerschmitt, "A low-noise chopper-stabilized differential switched-capacitor filtering technique," *IEEE Journal of Solid-State Circuits*, vol. 16, no. 6, pp. 708–715, Dec. 1981.
- [28] C. C. Enz, E. A. Vittoz, and F. Krummenacher, "A CMOS chopper amplifier," *IEEE Journal of Solid-State Circuits*, vol. 22, no. 3, pp. 335–342, June 1987.
- [29] R. Castello and P. Gray, "Performance Limitations in Switched-capacitor Filters," *IEEE Transactions on Circuits and Systems*, vol. 32, no. 9, pp. 865–876, Sept. 1985.
- [30] W. A. Gardner, *Introduction to Random Processes: With Applications to Signals and Systems*. New York, 1989.
- [31] R. Schreier, J. Silva, J. Steensgaard, and G. C. Temes, "Design-oriented Estimation of Thermal Noise in Switched-capacitor Circuits," *IEEE Transactions on Circuits and Systems I: Regular Papers*, vol. 52, no. 11, pp. 2358–2368, Nov. 2005.
- [32] A. Dastgheib and B. Murmann, "Calculation of Total Integrated Noise in Analog Circuits," *IEEE Transactions on Circuits and Systems I*, vol. 55, no. 10, pp. 2988–2993, Nov. 2008.
- [33] C. Enz, F. Krummenacher, and A. Boukhayma, "Simple Thermal Noise Estimation of OTA-based Switched-capacitor Filters," in *2015 International Conference on Noise and Fluctuations (ICNF)*, June 2015, pp. 1–4.
- [34] H. W. Bode, *Network Analysis and Feedback Amplifier Design*. New York: van Nostrand Company, 1945.
- [35] H. Weinrichter, "Equivalent Noise Sources of Switched-Capacitor Elements," in *Proc. of the IEEE International Symposium on Circuits and Systems (ISCAS)*, Rome, May 1982, pp. 38–41.
- [36] B. Furrer, "Rauschen von Filtern mit geschalteten Kapazitäten," PhD, ETHZ, Date 1983, no. 7284.
- [37] F. Krummenacher, "High voltage gain CMOS OTA for micropower SC filters," *Electronics Letters*, vol. 17, no. 4, pp. 160–162, 1981.
- [38] P. R. Gray, P. J. Hurst, S. H. Lewis, and R. G. Meyer, *Analysis and Design of Analog Integrated Circuits*, 5th ed. Wiley, 2009.
- [39] F. Krummenacher, E. Vittoz, and M. Degrauwe, "Class AB CMOS amplifier micropower SC filters," *Electronics Letters*, vol. 17, no. 13, pp. 433–435, 1981.
- [40] A. Caizzone, A. Boukhayma, and C. Enz, "An Accurate kTC Noise Analysis of CDS Circuits," in *2018 16th IEEE International New Circuits and Systems Conference (NEWCAS)*, June 2018, pp. 22–25.
- [41] B. Murmann, "Thermal Noise in Track-and-Hold Circuits: Analysis and Simulation Techniques," *IEEE Solid-State Circuits Magazine*, vol. 4, no. 2, pp. 46–54, Spring 2012.



Christian Enz (M'84, S'12) received the M.S. and Ph.D. degrees in Electrical Engineering from the EPFL in 1984 and 1989 respectively. He is currently Professor at EPFL, Director of the Institute of Micro-engineering and head of the IC Lab. Until April 2013 he was VP at the Swiss Center for Electronics and Microtechnology (CSEM) in Neuchâtel, Switzerland where he was heading the Integrated and Wireless Systems Division. Prior to joining CSEM, he was Principal Senior Engineer at Conexant (formerly Rockwell Semiconductor Systems), Newport Beach,

CA, where he was responsible for the modeling and characterization of MOS transistors for RF applications. His technical interests and expertise are in the field of ultralow-power analog and RF IC design, wireless sensor networks and semiconductor device modeling. Together with E. Vittoz and F. Krummenacher he is the developer of the EKV MOS transistor model. He is the author and co-author of more than 250 scientific papers and has contributed to numerous conference presentations and advanced engineering courses. He is an individual member of the Swiss Academy of Engineering Sciences (SATW). He has been an elected member of the IEEE Solid-State Circuits Society (SSCS) AdCom from 2012 to 2014. He is also the Chair of the IEEE SSCS Chapter of Switzerland.



François Krummenacher received the M.S. and Ph.D. degrees in electrical engineering from the Swiss Federal Institute of Technology (EPFL) in 1979 and 1985 respectively. He has been with the Electronics Laboratory of EPFL since 1979, working in the field of low-power analog and mixed analog/digital CMOS IC design, as well as in deep sub-micron and high-voltage MOSFET device compact modeling. Dr. Krummenacher is the author or co-author of more than 120 scientific publications in these fields. Since 1989 he has also been working

as an independent consultant, providing scientific and technical expertise in IC design to numerous local and international industries and research labs.



Antonino Caizzzone Antonino Caizzzone was born in Milazzo, Italy, in 1991. He received his bachelor degree in electronic engineering from the University of Catania (Italy) in 2013 and two masters in Micro & Nano Technologies from INPG Grenoble (France) and Polytechnique of Turin (Italy), respectively, in 2015. He is currently working toward the Ph.D. at the Ecole Polytechnique Federale de Lausanne (EPFL), under the supervision of Prof. Enz and Dr. Boukhayma, on the subject of ultra-low noise and low power sensors for healthcare. Between 2012 and

2013 he worked in STMicroelectronics as an intern on the design of analog electronics on plastic substrate. In 2014, he worked at Georgia Tech. (USA) as visiting researcher on the subject of energy harvesters. .



Assim Boukhayma received the graduate engineering degree (D.I.) in information and communication technology and the M.Sc. in microelectronics and embedded systems architecture from Institut Mines Telecom (IMT Atlantique), France, in 2013. He was awarded with the graduate research fellowship for doctoral studies from the French atomic energy commission (CEA) and the French ministry of defense (DGA). He received the Ph.D. from EPFL in 2016 on the topic of Ultra Low Noise CMOS Image Sensors. In 2017, he was awarded the Springer Theses

prize in recognition of outstanding Ph.D. research. He is currently a scientist at EPFL ICLAB, conducting research in the areas of image sensors and noise in circuits and systems. From 2012 to 2015, he worked as a researcher at Commissariat à l'Energie Atomique (CEA-LETI), Grenoble, France. From 2011 to 2012, he worked with Bouygues-Telecom as a Telecommunication Radio Junior Engineer.

Bibliography

- [1] Statista, *Internet of things connected devices installed base worldwide from 2015 to 2025 (billions)*. Consumer Electronics, 2016.
- [2] Safeatlast, *IoT STATISTICS (INFOGRAPHIC)*. Ana Bera for Safeatlast, 2019.
- [3] United Nations, *World Population Prospects: 2019*. Department of Economic and Social Affairs United Nations, 2019.
- [4] K. Atkinson and D. Mabey, *Revolutionizing Tropical Medicine: Point-of-Care Tests, New Imaging Technologies and Digital Health*. John Wiley and Sons Inc., 2019.
- [5] MarketsandMarkets, *IoT Healthcare Market by Component, Application, End User, and Region - Global Forecast to 2022*. MarketsandMarkets, 2016.
- [6] McKinsey, *Big data: The next frontier for innovation, competition and productivity*. McKinsey Global Institute, 2011.
- [7] World Health Organization, *Cardiovascular diseases (CVDs)*, 2017.
- [8] American Heart Associations, *Heart Disease and Stroke Statistics-2019 At-a-Glance*, 2019.
- [9] G. Eknoyan, “Adolphe Quetelet (1796–1874)—the average man and indices of obesity,” *Nephrology Dialysis Transplantation*, vol. 23, pp. 57–41, September 2017.
- [10] BMI, *Body mass index*. Wikipedia english, 2015.
- [11] A. Keys, F. Fidanza, M. Karvonen, N. Kimura, and H. Taylor, “Indices of relative weight and adiposity,” *Journal of Chronic Diseases*, vol. 25, pp. 329–343, 1972.
- [12] World Health Organization, *Obesity and Overweight*, 2018.
- [13] OECD, *Obesity Update 2017*. Organisation for Economic Co-operation and Development (OECD), 2017.
- [14] D. Haslam and W. James, “Obesity,” *The Lancet (Review)*, Elsevier Ltd., vol. 366, pp. 1197–1209, October 2015.

Bibliography

- [15] United Nations, *World Population Prospects: The 2010 revision*. Adapted from Global Health & Aging, World Health Organization, 2011.
- [16] Deloitte, *2019 Global health care outlook*. Shaping the future, 2019.
- [17] J. Peake, G. Kerr, and J. Sullivan, "A Critical Review of Consumer Wearables, Mobile Applications, and Equipment for Providing Biofeedback, Monitoring Stress, and Sleep in Physically Active Populations," *frontiers in Physiology*, June 2018.
- [18] MordorIntelligence, *Optical Pulse Sensor Market - Growth, Trends, and Forecast (2019-2024)*. Mordor Intelligence, 2018.
- [19] J. Allen, "Photoplethysmography and its application in clinical physiological measurement," *PHYSIOLOGICAL MEASUREMENT*, pp. 1–39, February 2007.
- [20] A. Challoner, "Photoelectric plethysmography for estimating cutaneous blood flow," *Non-Invasive Physiological Measurements*, vol. 1, pp. 125–151, 1979.
- [21] A. Hertzman, "The blood supply of various skin areas as estimated by the photoelectric plethysmograph," *Am. J. Physiol.*, vol. 125, pp. 328–340, 1938.
- [22] T. Aoyagi, M. Kiahi, K. Yamaguchi, and S. Watanabe, "Improvement of the earpiece oximeter," *Abstracts of the 13th Annual Meeting of the Japanese Society of Medical Electronics and Biological Engineering*, pp. 90–91, 1974.
- [23] J. Allen and A. Murray, "Similarity in bilateral photoplethysmographic peripheral pulse wave characteristics at the ears, thumbs and toes," *Physiological Measurement*, vol. 21, no. 3, pp. 369–377, aug 2000. [Online]. Available: <https://doi.org/10.1088/0967-3334/21/3/03>
- [24] W. Cui, L. E. Ostrander, and B. Y. Lee, "In vivo reflectance of blood and tissue as a function of light wavelength," *IEEE Transactions on Biomedical Engineering*, vol. 37, no. 6, pp. 632–639, June 1990.
- [25] P. D. Mannheimer, J. R. Cascini, M. E. Fein, and S. L. Nierlich, "Wavelength selection for low-saturation pulse oximetry," *IEEE Transactions on Biomedical Engineering*, vol. 44, no. 3, pp. 148–158, March 1997.
- [26] J. G. Webster, *Design of Pulse Oximeters*. Bristol, PA, USA: Philadelphia: Institute of Physics Pub., 1997.
- [27] M. R. Grubb, B. R. Hayes-Gill, J. A. Crowe, D. Sharkey, N. Marlow, and N. J. Miles, "Towards forehead reflectance photoplethysmography to aid delivery room resuscitation in newborns," in *4th European Conference of the International Federation for Medical and Biological Engineering*, J. Vander Sloten, P. Verdonck, M. Nyssen, and J. Haueisen, Eds. Berlin, Heidelberg: Springer Berlin Heidelberg, 2009, pp. 1053–1056.

-
- [28] W. Karlen, S. Raman, J. M. Ansermino, and G. A. Dumont, "Multiparameter respiratory rate estimation from the photoplethysmogram," *IEEE Transactions on Biomedical Engineering*, vol. 60, no. 7, pp. 1946–1953, July 2013.
 - [29] M. Nitzan, A. Babchenko, D. Shemesh, and J. Alberton, "Influence of thoracic sympathectomy on cardiac induced oscillations in tissue blood volume," *Medical and Biological Engineering and Computing*, vol. 39, no. 5, pp. 579–583, Sep 2001. [Online]. Available: <https://doi.org/10.1007/BF02345149>
 - [30] U. Schultz-Ehrenburg and V. Blazek, "Value of Quantitative Photoplethysmography for Functional Vascular Diagnostics," *Skin Pharmacology and Physiology*, vol. 14, pp. 316–323, March 2001.
 - [31] V. Shusterman, K. P. Anderson, and O. Barnea, "Spontaneous skin temperature oscillations in normal human subjects," *American Journal of Physiology-Regulatory, Integrative and Comparative Physiology*, vol. 273, no. 3, pp. R1173–R1181, 1997, PMID: 9321901. [Online]. Available: <https://doi.org/10.1152/ajpregu.1997.273.3.R1173>
 - [32] S.-H. Tseng, P. Bargo, A. Durkin, and N. Kollias, "Chromophore concentrations, absorption and scattering properties of human skin in-vivo," pp. 14 599–14 617, Aug 2009. [Online]. Available: <http://www.opticsexpress.org/abstract.cfm?URI=oe-17-17-14599>
 - [33] R. Klabunde, *Cardiovascular Physiology Concepts*. Lippincott Williams & Wilkins, 2012,, 2012.
 - [34] R. Anderson and J. Parrish, "The optics of human skin," *The Journal of Investigative Dermatology*, vol. 77, 1981.
 - [35] A. Murray and D. Marjanovic, "Optical assessment of recovery of tissue blood supply after removal of externally applied pressure," *Medical and Biological Engineering and Computing*, vol. 35, no. 4, pp. 425–427, Jul 1997. [Online]. Available: <https://doi.org/10.1007/BF02534102>
 - [36] Y. Maeda, M. Sekine, and T. Tamura, "The advantages of wearable green reflected photoplethysmography," *Journal of Medical Systems*, vol. 35, no. 5, pp. 829–834, Oct 2011. [Online]. Available: <https://doi.org/10.1007/s10916-010-9506-z>
 - [37] H.-O. Teichmann, T. Herrmann, and T. Bach, "Technical aspects of lasers in urology," *World journal of urology*, vol. 25, pp. 221–5, 07 2007.
 - [38] <https://science4fun.info/skin/>, .
 - [39] P. Costas, "Light-tissue interaction," *Course given at the Univeristy of Cyprus, Biomedical Imaging and Applied Optics Laboratory*, 2015.
 - [40] V. Roberts, "Photoplethysmography- fundamental aspects of the optical properties of blood in motion," *Transactions of the Institute of Measurement and Control*, vol. 4, no. 2, pp. 101–106, April 1982.

Bibliography

- [41] J. T. B. Moyle, *Pulse Oximeters*. London: BMJ, 1994.
- [42] V. Twersky, "Multiple scattering of waves and optical phenomena," *Journal Optical Society*, vol. 52, pp. 145–171, 1962.
- [43] —, "Interface effects in multiple scattering by large, low refracting, absorbing particles," *Journal Optical Society*, vol. 60, pp. 908–914, 1970.
- [44] —, "Absorption and multiple scattering by biological suspensions," *Journal Optical Society*, vol. 60, pp. 1084–1093, 1970.
- [45] S. Chatterjee, S. Phillips, and Kyriacou, "Monte carlo investigation of the effect of blood volume and oxygen saturation on optical path in reflectance pulse oximetry," *Biomedical Physics and Engineering Express*, vol. 2, no. 6, 2016.
- [46] P. Schönle, "A power efficient spectrophotometry & ppg integrated circuit for mobile medical instruments," *PhD Dissertation ETHZ*, 2017.
- [47] <https://www.vectorstock.com/royalty-free-vector/human-skin-layered-epidermis-with-hair-follicle-vector-21642351>, .
- [48] M. J. C. Van Gemert, S. L. Jacques, H. J. C. M. Sterenborg, and W. M. Star, "Skin optics," *IEEE Transactions on Biomedical Engineering*, vol. 36, no. 12, pp. 1146–1154, Dec 1989.
- [49] Y. Kao, P. C. . Chao, and C. Wey, "Design and validation of a new ppg module to acquire high-quality physiological signals for high-accuracy biomedical sensing," *IEEE Journal of Selected Topics in Quantum Electronics*, vol. 25, no. 1, pp. 1–10, Jan 2019.
- [50] OSRAM, *BIOFY Opto-mechanical integration of the SFH 7070*. Application Note No.AN113, 2018.
- [51] P. A. Kyriacou, S. Powell, R. M. Langford, and D. P. Jones, "Esophageal pulse oximetry utilizing reflectance photoplethysmography," *IEEE Transactions on Biomedical Engineering*, vol. 49, no. 11, pp. 1360–1368, Nov 2002.
- [52] E. Tur, M. Tur, H. I. Maibach, and R. H. Guy, "Basal perfusion of the cutaneous microcirculation: Measurements as a function of anatomic position," *Journal of Investigative Dermatology*, vol. 81, no. 5, pp. 442 – 446, 1983. [Online]. Available: <http://www.sciencedirect.com/science/article/pii/S0022202X15432312>
- [53] V. Fuster, A. Wayne, and R. O'Rourke, *Hurst's the heart*. New York, N.Y. : McGraw-Hill, 2011.
- [54] J. Webster, *Medical Instrumentation Application and Design*. Fourth edition, John Wiley & Sons, Hoboken, NJ, 2010, 2010.
- [55] T. Opthof, "The normal range and determinants of the intrinsic heart rate in man," *Cardiovascular Research*, vol. 45, no. 1, pp. 177–184, January 2000.

- [56] A. Tarniceriu, J. Harju, A. Vehkaoja, J. Parak, R. Delgado-Gonzalo, P. Renevey, A. Yli-Hankala, and I. Korhonen, "Detection of beat-to-beat intervals from wrist photoplethysmography in patients with sinus rhythm and atrial fibrillation after surgery," in *2018 IEEE EMBS International Conference on Biomedical Health Informatics (BHI)*, March 2018, pp. 133–136.
- [57] D. Q. Feild, S. H. Zhou, E. D. Helfenbein, R. E. Gregg, and J. M. Lindauer, "Technical challenges and future directions in lead reconstruction for reduced-lead systems," *Journal of Electrocardiology*, vol. 41, no. 6, pp. 466 – 473, 2008. [Online]. Available: <http://www.sciencedirect.com/science/article/pii/S0022073608002677>
- [58] HR, *Heart Rate*. Wikipedia english, 2015.
- [59] A. Uusitalo, T. Mets, K. Martinmäki, S. Mauno, U. Kinnunen, and H. Rusko, "Heart rate variability related to effort at work," *Applied Ergonomics*, vol. 42, no. 6, pp. 830 – 838, 2011. [Online]. Available: <http://www.sciencedirect.com/science/article/pii/S0003687011000147>
- [60] A. Schäfer and J. Vagedes, "How accurate is pulse rate variability as an estimate of heart rate variability?: A review on studies comparing photoplethysmographic technology with an electrocardiogram," *International Journal of Cardiology*, vol. 166, no. 1, pp. 15 – 29, 2013. [Online]. Available: <http://www.sciencedirect.com/science/article/pii/S0167527312003269>
- [61] P. K. Stein, A. A. Ehsani, P. P. Domitrovich, R. E. Kleiger, and J. N. Rottman, "Effect of exercise training on heart rate variability in healthy older adults," *American Heart Journal*, vol. 138, no. 3, pp. 567 – 576, 1999. [Online]. Available: <http://www.sciencedirect.com/science/article/pii/S0002870399701626>
- [62] P. Dehkordi, A. Garde, W. Karlen, D. Wensley, J. M. Ansermino, and G. A. Dumont, "Pulse rate variability compared with heart rate variability in children with and without sleep disordered breathing," in *2013 35th Annual International Conference of the IEEE Engineering in Medicine and Biology Society (EMBC)*, July 2013, pp. 6563–6566.
- [63] J. Harju, A. Tarniceriu, J. Parak, A. Vehkaoja, A. Yli-Hankala, and I. Korhonen, "Monitoring of heart rate and inter-beat intervals with wrist plethysmography in patients with atrial fibrillation," in *Physiological Measurements*, vol. 39, no. 6, June 2018.
- [64] S. Arberet, M. Lemay, P. Renevey, J. Solà, O. Grossenbacher, D. Andries, C. Sartori, and M. Bertschi, "Photoplethysmography-based ambulatory heartbeat monitoring embedded into a dedicated bracelet," in *Computing in Cardiology 2013*, Sep. 2013, pp. 935–938.
- [65] E. Gil, M. Orini, R. Bailon, J. Vergara, L. Mainardi, and P. Laguna, "Photoplethysmography pulse rate variability as a surrogate measurement of heart rate variability during non-stationary conditions," in *Physiological Measurements*, vol. 31, Aug. 2010.

- [66] Y. Chiu, P. W. Arand, S. G. Shroff, T. Feldman, and J. D. Carroll, "Determination of pulse wave velocities with computerized algorithms," *American Heart Journal*, vol. 121, no. 5, pp. 1460 – 1470, 1991. [Online]. Available: <http://www.sciencedirect.com/science/article/pii/0002870391901539>
- [67] S. Nemati, M. M. Ghassemi, V. Ambai, N. Isakadze, O. Levantsevych, A. Shah, and G. D. Clifford, "Monitoring and detecting atrial fibrillation using wearable technology," in *2016 38th Annual International Conference of the IEEE Engineering in Medicine and Biology Society (EMBC)*, Aug 2016, pp. 3394–3397.
- [68] M. Malik, "Heart rate variability. standards of measurement, physiological interpretation, and clinical use," in *Circulation*, vol. 93, 1996, pp. 1043–1065.
- [69] N. D. Giardino, P. M. Lehrer, and R. Edelberg, "Comparison of finger plethysmograph to ecg in the measurement of heart rate variability," *Psychophysiology*, vol. 39, no. 2, pp. 246–253, 2002. [Online]. Available: <https://onlinelibrary.wiley.com/doi/abs/10.1111/1469-8986.3920246>
- [70] V. Pamula, C. Van Hoof, and M. Verhlest, *Analog-and-Algorithm- Assisted Ultra-low Power Biosignal Acquisition Systems*. Springer, 2019.
- [71] A. Go *et al.*, "Heart disease and stroke statistics2014 update: a report from the american heart association." *Circulation*, 2013. [Online]. Available: <https://onlinelibrary.wiley.com/doi/abs/10.1111/1469-8986.3920246>
- [72] L. Friberg and L. Bergfeldt, "Atrial fibrillation prevalence revisited," in *Journal of Internal Medicine*, vol. 274, no. 5, 2013, pp. 461–468.
- [73] Y. Miyasaka *et al.*, "Secular trends in incidence of atrial fibrillation in olmsted county, minnesota, 1980 to 2000, and implications on the projections for future prevalence," in *Circulation*, vol. 114, no. 2, 2006, pp. 119–125.
- [74] <https://mobilmed.com.tr/atrial-fibrillation/>, .
- [75] J. Lee, B. A. Reyes, D. D. McManus, O. Mathias, and K. H. Chon, "Atrial fibrillation detection using a smart phone," in *2012 Annual International Conference of the IEEE Engineering in Medicine and Biology Society*, Aug 2012, pp. 1177–1180.
- [76] Y. Shen, M. Voisin, A. Aliamiri, A. Avati, A. Hannun, and A. Ng, "Ambulatory Atrial Fibrillation Monitoring Using Wearable Photoplethysmography with Deep Learning," in *Proceedings of the 25th ACM SIGKDD International Conference on Knowledge Discovery & Data Mining*, 2019, pp. 1909–1916.
- [77] A. Rosengren *et al.*, "Association of psychosocial risk factors with risk of acute myocardial infarction in 11119 cases and 13648 controls from 52 countries (the interheart study): case control study," in *The Lancet*, vol. 364, no. 9438, 2004, pp. 953 – 962.

-
- [78] P. Charlton, P. Celka, B. Farukh, P. Chowienczyk, and J. Alastruey, "Assessing mental stress from the photoplethysmogram: a numerical study," in *Physiological Measurement*, vol. 39, May 2018.
- [79] C. Lochner, Y. Khan, A. Pierre, and A. Arias, "All-organic optoelectronic sensor for pulse oximetry," *Nature Communications*, vol. 5, p. 5745, Dec 2014.
- [80] A. Caizzzone, A. Boukhayma, and C. Enz, "A 2.6 μ W Monolithic CMOS Photoplethysmographic (PPG) Sensor Operating with 2 μ W LED Power for Continuous Health Monitoring," *IEEE Transactions on Biomedical Circuits and Systems*, pp. 1–1, 2019.
- [81] L. Lindberg, H. Ugnell, and P. Öberg, "Monitoring of respiratory and heart rates using a fibre-optic sensor," in *Medical and Biological Engineering and Computing*, vol. 30, no. 5, Sep 1992, pp. 533–537.
- [82] J. Penaz, "Mayer waves history and methodology," in *Automedica*, vol. 2, no. 3, 1978, pp. 135–142.
- [83] P. A. Leonard, J. G. Douglas, N. R. Grubb, D. Clifton, P. S. Addison, and J. N. Watson, "A fully automated algorithm for the determination of respiratory rate from the photoplethysmogram," *Journal of Clinical Monitoring and Computing*, vol. 20, no. 1, pp. 33–36, Feb 2006. [Online]. Available: <https://doi.org/10.1007/s10877-005-9007-7>
- [84] W. Karlen, S. Raman, J. M. Ansermino, and G. A. Dumont, "Multiparameter respiratory rate estimation from the photoplethysmogram," *IEEE Transactions on Biomedical Engineering*, vol. 60, no. 7, pp. 1946–1953, July 2013.
- [85] A. Fusco, D. Locatelli, F. Onorati, G. C. Durelli, and M. D. Santambrogio, "On how to extract breathing rate from ppg signal using wearable devices," in *2015 IEEE Biomedical Circuits and Systems Conference (BioCAS)*, Oct 2015, pp. 1–4.
- [86] W. H. O. (World Health Organization), *Hypertension*, 2019.
- [87] J. Solà and R. Delgado-Gonzalo, *The Handbook of Cuffless Blood Pressure Monitoring: A Practical Guide for Clinicians, Researchers, and Engineers*. Springer, 2019.
- [88] D. A. Calhoun and S. M. Harding, "Sleep and hypertension," *CHEST*, vol. 138, no. 2, pp. 434–443, Aug 2010.
- [89] J. Solà, "Continuous non-invasive blood pressure estimation," *PhD Dissertation ETHZ*, 2011.
- [90] E. Winokur, "Single-site, noninvasive, blood pressure measurements at the ear using ballistocardiogram (bcg), and photoplethysmogram (ppg), and a low-power, reflectance-mode ppg soc," *PhD Dissertation MIT*, 2014.

Bibliography

- [91] A. M. Carek and O. T. Inan, "Robust sensing of distal pulse waveforms on a modified weighing scale for ubiquitous pulse transit time measurement," *IEEE Transactions on Biomedical Circuits and Systems*, vol. 11, no. 4, pp. 765–772, Aug 2017.
- [92] R. Mukkamala, J. Hahn, O. T. Inan, L. K. Mestha, C. Kim, H. Töreyin, and S. Kyal, "Toward ubiquitous blood pressure monitoring via pulse transit time: Theory and practice," *IEEE Transactions on Biomedical Engineering*, vol. 62, no. 8, pp. 1879–1901, Aug 2015.
- [93] S. Martin *et al.*, "Weighing scale-based pulse transit time is a superior marker of blood pressure than conventional pulse arrival time," *Nature Scientific Reports*, vol. 6, no. 39273, December 2016.
- [94] L. Peter, N. Noury, and M. Cerny, "A review of methods for non-invasive and continuous blood pressure monitoring: Pulse transit time method is promising?" *IRBM*, vol. 35, no. 5, pp. 271 – 282, 2014. [Online]. Available: <http://www.sciencedirect.com/science/article/pii/S1959031814000803>
- [95] P. Fung, G. Dumont, C. Ries, C. Mott, and M. Ansermino, "Continuous noninvasive blood pressure measurement by pulse transit time," in *The 26th Annual International Conference of the IEEE Engineering in Medicine and Biology Society*, vol. 1, Sep. 2004, pp. 738–741.
- [96] C. Vlachopoulos, M. O'Rourke, and W. Nichols, *McDonald's Blood Flow in Arteries: Theoretical, Experimental and Clinical Principles*. London, U.K.: Hodder Arnold, 2011.
- [97] P. B. Dobrin and A. A. Rovick, "Influence of vascular smooth muscle on contractile mechanics and elasticity of arteries," in *American Journal of Physiology*, vol. 217, no. 6, Dec. 1969, pp. 1644–1651.
- [98] R. D. Latham *et al.*, "Regional wave travel and reflections along the human aorta: a study with six simultaneous micromanometric pressures," in *Circulation*, vol. 72, 1985, pp. 1257–1269.
- [99] M. C. Baruch *et al.*, "Pulse decomposition analysis of the digital arterial pulse during hemorrhage simulation," in *Nonlinear Biomedical Physics*, vol. 5, no. 1, 2011.
- [100] G. Zhang *et al.*, "Pulse arrival time is not an adequate surrogate for pulse transit time as a marker of blood pressure," in *Journal of Applied Physiology*, vol. 111, 2011, pp. 1681–1686.
- [101] S. Hoeksle, J. Jansen, J. Blom, and J. Schreuder, "Detection of dicrotic notch in arterial pressure signals," in *Journal Clinical Monitoring*, vol. 13, 1997, pp. 309–316.
- [102] P. Chowienczyk, R. Kelly, and H. MacCallum, "Photoplethysmographic assessment of pulse wave reflection: blunted response to endothelium-dependent beta2-adrenergic vasodilation in type ii diabetes mellitus," in *Am Coll Cardiol*, vol. 34, 1999, pp. 2007–2014.

-
- [103] M. Elgendi, "On the analysis of fingertip photoplethysmogram signals," in *Current Cardiology Reviews*, vol. 8, 2012, pp. 14–25.
- [104] M. Ghamari, C. Soltanpur, S. Cabrera, R. Romero, R. Martinek, and H. Nazeran, "Design and prototyping of a wristband-type wireless photoplethysmographic device for heart rate variability signal analysis," in *2016 38th Annual International Conference of the IEEE Engineering in Medicine and Biology Society (EMBC)*, Aug 2016, pp. 4967–4970.
- [105] R. Couceiro *et al.*, "Assessment of cardiovascular function from multi-gaussian fitting of a finger photoplethysmogram," in *Physiological Measurement*, Aug 2015.
- [106] L. Dazhou *et al.*, "A new representation of photoplethysmography signal," in *International Conference on Wireless Algorithms, Systems, and Applications*, 2014.
- [107] S. Millasseau *et al.*, "Contour analysis of the photoplethysmographic pulse measured at the finger," in *Journal of Hypertension*, vol. 24, 2006, pp. 1449–1456.
- [108] K. Takazawa *et al.*, "Assessment of vasocative agents and vascular aging by the second derivative of photoplethysmogram waveform," in *Hypertension*, vol. 32, 1998, pp. 365–370.
- [109] I. Imanaga *et al.*, "Correlation between wave components of the second derivative of plethysmogram and arterial distensibility," *Japanese Heart Journal*, vol. 39, no. 6, pp. 775–784, 1998.
- [110] H. Lax *et al.*, "Studies of the arterial pulse wave and its modification in the presence of human arteriosclerosis," in *Journal of Chronic Diseases*, vol. 3, 1956, pp. 618–631.
- [111] T. Dawber *et al.*, "Characteristics of the dicrotic notch of the arterial pulse wave in coronary heart disease," in *Angiology*, vol. 24, 1973, pp. 244–255.
- [112] W. Yan, R. Peng, Y. Zhang, and D. Ho, "Cuffless continuous blood pressure estimation from pulse morphology of photoplethysmograms," *IEEE Access*, vol. 7, pp. 141 970–141 977, 2019.
- [113] S. Homma *et al.*, "Relationship between accelerated plethysmogram, blood pressure and anterior elasticity," *The Japanese Society of Physical Fitness and Sport Medicine*, vol. 41, pp. 98–107, 1992.
- [114] Y. Kurylyak, F. Lamonaca, and D. Grimaldi, "A neural network-based method for continuous blood pressure estimation from a ppg signal," in *2013 IEEE International Instrumentation and Measurement Technology Conference (I2MTC)*, May 2013, pp. 280–283.
- [115] F. Rundo, A. Ortis, S. Battiato, and S. Conoci, "Advanced bio-inspired system for noninvasive cuff-less blood pressure estimation from physiological signal analysis," *Computation*, vol. 6, no. 3, 2018. [Online]. Available: <https://www.mdpi.com/2079-3197/6/3/46>

Bibliography

- [116] J. Dey, A. Gaurav, and V. N. Tiwari, "Instabp: Cuff-less blood pressure monitoring on smartphone using single ppg sensor," in *2018 40th Annual International Conference of the IEEE Engineering in Medicine and Biology Society (EMBC)*, July 2018, pp. 5002–5005.
- [117] K. N. Glaros and E. M. Drakakis, "A Sub-mW Fully-Integrated Pulse Oximeter Front-End," *IEEE Transactions on Biomedical Circuits and Systems*, vol. 7, no. 3, pp. 363–375, June 2013.
- [118] K. Glaros, "Low-power pulse oximetry and transimpedance amplifiers," *PhD Dissertation Imperial College London*, 2011.
- [119] A. Sedra and K. Smith, *Microelectronic Circuits, Seventh Edition*. Oxford University Press, 2015.
- [120] A. Caizzzone, C.ENZ, and A. Boukhayma, "Comprehensive Noise Analysis in PPG Read-out Chains," *2017 International Conference on Noise and Fluctuations (ICNF)*, pp. 1–4, June 2017.
- [121] J. Graeme, *Photodiode Amplifiers: Op Amp Solutions*. McGraw-Hill, 1996.
- [122] P. Schönle, S. Fateh, T. Burger, and Q. Huang, "A power-efficient multi-channel ppg asic with 112db receiver dr for pulse oximetry and nirs," in *2017 IEEE Custom Integrated Circuits Conference (CICC)*, April 2017, pp. 1–4.
- [123] A. K. Y. Wong, K. Pun, Y. Zhang, and K. N. Leung, "A low-power cmos front-end for photoplethysmographic signal acquisition with robust dc photocurrent rejection," *IEEE Transactions on Biomedical Circuits and Systems*, vol. 2, no. 4, pp. 280–288, Dec 2008.
- [124] P. V. Rajesh, J. M. Valero-Sarmiento, L. Yan, A. Bozkurt, C. Van Hoof, N. Van Helleputte, R. F. Yazicioglu, and M. Verhelst, "A 172 μ W compressive sampling photoplethysmographic readout with embedded direct heart-rate and variability extraction from compressively sampled data," *2016 IEEE International Solid-State Circuits Conference (ISSCC)*, pp. 386–387, Jan 2016.
- [125] V. R. Pamula, J. M. Valero-Sarmiento, L. Yan, A. Bozkurt, C. V. Hoof, N. V. Helleputte, R. F. Yazicioglu, and M. Verhelst, "A 172 μ W Compressively Sampled Photoplethysmographic (PPG) Readout ASIC With Heart Rate Estimation Directly From Compressively Sampled Data," *IEEE Transactions on Biomedical Circuits and Systems*, vol. 11, no. 3, pp. 487–496, June 2017.
- [126] D. Jang and S. Cho, "A 43.4 μ W photoplethysmogram-based heart-rate sensor using heart-beat-locked loop," *2018 IEEE International Solid - State Circuits Conference - (ISSCC)*, pp. 474–476, Feb 2018.
- [127] J. Lee, D. Jang, S. Park, and S. Cho, "A low-power photoplethysmogram-based heart rate sensor using heartbeat locked loop," *IEEE Transactions on Biomedical Circuits and Systems*, vol. 12, no. 6, pp. 1220–1229, Dec 2018.

-
- [128] S. V. Gubbi and B. Amrutur, "Adaptive pulse width control and sampling for low power pulse oximetry," *IEEE Transactions on Biomedical Circuits and Systems*, vol. 9, no. 2, pp. 272–283, April 2015.
- [129] Q. Lin, J. Xu, S. Song, A. Breeschoten, M. Konijnenburg, M. Chen, C. Van Hoof, F. Tavernier, and N. Van Helleputte, "A $196\mu\text{W}$, reconfigurable light-to-digital converter with 119db dynamic range, for wearable ppg/nirs sensors," in *2019 Symposium on VLSI Circuits*, June 2019, pp. C58–C59.
- [130] J. A. C. Patterson, D. C. McIlwraith, and G. Yang, "A flexible, low noise reflective ppg sensor platform for ear-worn heart rate monitoring," in *2009 Sixth International Workshop on Wearable and Implantable Body Sensor Networks*, June 2009, pp. 286–291.
- [131] E. S. Winokur, T. O'Dwyer, and C. G. Sodini, "A Low-Power, Dual-Wavelength Photoplethysmogram (PPG) SoC With Static and Time-Varying Interferer Removal," *IEEE Transactions on Biomedical Circuits and Systems*, vol. 9, no. 4, pp. 581–589, Aug 2015.
- [132] C. C. Enz and G. C. Temes, "Circuit techniques for reducing the effects of op-amp imperfections: autozeroing, correlated double sampling, and chopper stabilization," *Proceedings of the IEEE*, vol. 84, no. 11, pp. 1584–1614, Nov 1996.
- [133] M. Tavakoli, L. Turicchia, and R. Sarpeshkar, "An ultra-low-power pulse oximeter implemented with an energy-efficient transimpedance amplifier," *IEEE Transactions on Biomedical Circuits and Systems*, vol. 4, no. 1, pp. 27–38, Feb 2010.
- [134] M. Tavakoli, "An analog vlsi front end for pulse oximetry," *PhD Dissertation MIT*, 2006.
- [135] E. A. Pelaez and E. R. Villegas, "Led power reduction trade-offs for ambulatory pulse oximetry," in *2007 29th Annual International Conference of the IEEE Engineering in Medicine and Biology Society*, Aug 2007, pp. 2296–2299.
- [136] Y. Liang, M. Elgendi, Z. Chen, and R. Ward, "An optimal filter for short photoplethysmogram signals," in *Nature Scientific Data*, vol. 5, May 2018.
- [137] H. Kim and D. Jee, "A $<25\mu\text{W}$ cmos monolithic photoplethysmographic sensor with distributed 1b delta-sigma light-to-digital convertor," in *ESSCIRC 2017 - 43rd IEEE European Solid State Circuits Conference*, Sep. 2017, pp. 55–58.
- [138] Texas-Instruments, *AFE4403 Ultra-Small, Integrated Analog Front-End for Heart Rate Monitors and Low-Cost Pulse Oximeters*. AFE4403 datasheet, 2014.
- [139] A. Caizzzone, A. Boukhayma, and C. Enz, "A $2.6\mu\text{W}$ Monolithic CMOS Photoplethysmographic Sensor Operating with $2\mu\text{W}$ LED Power," in *2019 IEEE International Solid-State Circuits Conference - (ISSCC)*, Feb 2019, DOI: 10.1109/ISSCC.2019.8662404, pp. 290–291.
- [140] AMS AG, *Biosensor*. AS7026GG datasheet, 2017.

Bibliography

- [141] Maxim Integrated, *Best-in-Class Optical Pulse Oximeter and Heart-Rate Sensor for Wearable Health*. MAX86140 datasheet, 2017.
- [142] Rohm semiconductor, *Optical Sensor for Heart Rate Monitor IC*. BH1790GLC datasheet, 2017.
- [143] B. Razavi, *Design of Integrated Circuits for Optical Communications*. New York: McGraw-Hill, 2003.
- [144] Khoman Phang and D. A. Johns, "A cmos optical preamplifier for wireless infrared communications," *IEEE Transactions on Circuits and Systems II: Analog and Digital Signal Processing*, vol. 46, no. 7, pp. 852–859, July 1999.
- [145] C. Enz and E. Vittoz, *Charge based MOS transistor modeling, The EKV Model for Low-power And RF IC design*. Wiley, 2006.
- [146] A. Papoulis, *Probability, Random Variables, and Stochastic Processes*. Mc-Graw Hill, 1984.
- [147] A. McWhorter, *Semiconductor surface physics*, ser. Series in physics, R. Kingston, Ed. University of Pennsylvania Press, 1957.
- [148] F. N. Hooge, "1/f noise sources," *IEEE Transactions on Electron Devices*, vol. 41, no. 11, pp. 1926–1935, Nov 1994.
- [149] C. Enz and A. Boukhayma, "Recent trends in low-frequency noise reduction techniques for integrated circuits," in *2015 International Conference on Noise and Fluctuations (ICNF)*, June 2015, pp. 1–6.
- [150] A. Boukhayma, "Ultra low noise cmos image sensors," *PhD Dissertation EPFL*, 2016.
- [151] T. I. (Data-Sheet), "ADS111x Ultra-Small, Low Power, I²C-Compatible, 860-SPS, 16-Bit ADCs."
- [152] C. Enz, A. Caizzone, A. Boukhayma, and F. Krummenacher, "Simple Thermal Noise Estimation of Switched Capacitor Circuits Based on OTAs – Part I: Amplifiers with Capacitive Feedback," 2019.
- [153] H. W. Bode, *Network Analysis and Feedback Amplifier Design*. New York: van Nostrand Company, 1945.
- [154] P. Bolcato and R. Poujois, "A new approach for noise simulation in transient analysis," *[Proceedings] 1992 IEEE International Symposium on Circuits and Systems*, vol. 2, pp. 887–890 vol.2, May 1992.
- [155] Y. Zhang, S. Song, R. Vullings, D. Biswas, N. Simões-Capela, N. van Helleputte, C. van Hoof, and W. Groenendaal, "Motion artifact reduction for wrist-worn photoplethysmograph sensors based on different wavelengths," *Sensors*, vol. 19, no. 3, 2019. [Online]. Available: <https://www.mdpi.com/1424-8220/19/3/673>

- [156] M. Poh, N. C. Swenson, and R. W. Picard, "Motion-tolerant magnetic earring sensor and wireless earpiece for wearable photoplethysmography," *IEEE Transactions on Information Technology in Biomedicine*, vol. 14, no. 3, pp. 786–794, May 2010.
- [157] P. Chaturani and A. W. Isaac, "Blood flow with body acceleration forces," *International Journal of Engineering Science*, vol. 33, no. 12, pp. 1807 – 1820, 1995. [Online]. Available: <http://www.sciencedirect.com/science/article/pii/002072259500027U>
- [158] Y. Maeda, M. Sekine, and T. Tamura, "Relationship between measurement site and motion artifacts in wearable reflected photoplethysmography," *Journal of Medical Systems*, vol. 35, no. 5, pp. 969–976, Oct 2011. [Online]. Available: <https://doi.org/10.1007/s10916-010-9505-0>
- [159] J. Lee, K. Matsumura, K. Yamakoshi, P. Rolfe, S. Tanaka, and T. Yamakoshi, "Comparison between red, green and blue light reflection photoplethysmography for heart rate monitoring during motion," in *2013 35th Annual International Conference of the IEEE Engineering in Medicine and Biology Society (EMBC)*, July 2013, pp. 1724–1727.
- [160] B. Widrow, J. R. Glover, J. M. McCool, J. Kaunitz, C. S. Williams, R. H. Hearn, J. R. Zeidler, J. Eugene Dong, and R. C. Goodlin, "Adaptive noise cancelling: Principles and applications," *Proceedings of the IEEE*, vol. 63, no. 12, pp. 1692–1716, Dec 1975.
- [161] L. Wang, B. P. Lo, and G. Yang, "Multichannel Reflective PPG Earpiece Sensor With Passive Motion Cancellation," *IEEE Transactions on Biomedical Circuits and Systems*, vol. 1, no. 4, pp. 235–241, Dec 2007.
- [162] A. Alzahrani, S. Hu, V. Azorin-Peris, L. Barrett, D. Esliger, M. Hayes, S. Akbare, J. Achart, and S. Kuoch, "A multi-channel opto-electronic sensor to accurately monitor heart rate against motion artefact during exercise," *Sensors*, vol. 15, no. 10, pp. 25 681–25 702, 2015. [Online]. Available: <https://www.mdpi.com/1424-8220/15/10/25681>
- [163] T. Shimazaki and S. Hara, "Breathing motion artifact cancellation in PPG-based heart rate sensing," in *2015 9th International Symposium on Medical Information and Communication Technology (ISMICT)*, March 2015, pp. 200–203.
- [164] A. Boukhayma, A. Peizerat, and C. Enz, "A Sub-0.5 Electron Read Noise VGA Image Sensor in a Standard CMOS Process," *IEEE Journal of Solid-State Circuits*, vol. 51, no. 9, pp. 2180–2191, Sep. 2016.
- [165] A. Caizzone, C. Enz, and A. Boukhayma, "An Accurate kTC Noise Analysis of CDS Circuits," in *2018 16th IEEE International New Circuits and Systems Conference (NEWCAS)*, June 2018, pp. 22–25.
- [166] A. Boukhayma, C. Enz, and A. Peizerat, "Temporal Readout Noise Analysis and Reduction Techniques for Low-Light CMOS Image Sensors," *IEEE Transactions on Electron Devices*, vol. 63, no. 1, pp. 72–78, Jan 2016.

Bibliography

- [167] A. Boukhayma, A. Peizerat, and C. Enz, "Noise Reduction Techniques and Scaling Effects Towards Photon Counting CMOS Image Sensors." *Sensors*, vol. 16, no. 4, p. 514, April 2016.
- [168] R. Capoccia, A. Boukhayma, F. Jazaeri, and C. Enz, "Compact Modeling of Charge Transfer in Pinned Photodiodes for CMOS Image Sensors," *IEEE Transactions on Electron Devices*, vol. 66, no. 1, pp. 160–168, Jan 2019, DOI: 10.1109/TED.2018.2875946.
- [169] C.-H. Chen, Y. Zhang, T. He, and G. C. Temes, *Micropower Incremental Analog-to-Digital Converter*. Springer International Publishing Switzerland, Efficient Sensor Interfaces, Advanced Amplifiers, 2016.
- [170] D. He, S. P. Morgan, D. Trachanis, J. Van Hese, D. Drogoudis, F. Fummi, F. Stefanni, V. Guarnieri, and B. R. Hayes-Gill, "A Single-Chip CMOS Pulse Oximeter with On-Chip Lock-In Detection," *Sensors*, vol. 15, no. 7, pp. 17 076–17 088, 2015. [Online]. Available: <http://www.mdpi.com/1424-8220/15/7/17076>
- [171] STMicroelectronics, *All-in-one proximity and ambient light sensing module*. [Online]. Available: <https://www.st.com/en/mems-and-sensors/proximity-sensors.html>
- [172] R. Fontaine, "Innovative technology elements for large and small pixel cis devices," in *International Image Sensors Workshop*, June 2013.
- [173] J. Kvam, *Time of Flight: Principles, Challenges, and Performance*. [Online]. Available: https://www.st.com/content/dam/technology-tour-2017/session-1_track-4_time-of-flight-technology.pdf
- [174] N. Teranishi, A. Kohono, Y. Ishihara, E. Oda, and K. Arai, "No image lag photodiode structure in the interline ccd image sensor," in *1982 International Electron Devices Meeting*, Dec 1982, pp. 324–327.
- [175] E. R. Fossum and D. B. Hondongwa, "A review of the pinned photodiode for ccd and cmos image sensors," *IEEE Journal of the Electron Devices Society*, vol. 2, no. 3, pp. 33–43, May 2014.
- [176] STMicroelectronics, *Imaging Technologies*. [Online]. Available: https://www.st.com/content/st_com/en/about/innovation---technology/imaging.html
- [177] J. Ma, D. Starkey, A. Rao, K. Odame, and E. Fossum, "Characterization of quanta image sensor pump-gate jots with deep sub-electron read noise," *Electron Devices Society, IEEE Journal of the*, vol. 3, no. 6, pp. 472–480, Nov 2015.
- [178] M. Seo, S. Kawahito, K. Kagawa, and K. Yasutomi, "A 0.27e-rms read noise 220- μ v/e-conversion gain reset-gate-less cmos image sensor with 0.11- μ m cis process," *IEEE Electron Device Letters*, vol. 36, no. 12, pp. 1344–1347, Dec 2015.
- [179] A. Boukhayma, *Ultra Low Noise CMOS Image Sensors*. Springer, 2018.

-
- [180] S. Kim, S. Han, B. Kang, K. Lee, J. D. K. Kim, and C. Kim, "A three-dimensional time-of-flight cmos image sensor with pinned-photodiode pixel structure," *IEEE Electron Device Letters*, vol. 31, no. 11, pp. 1272–1274, Nov 2010, DOI: 10.1109/LED.2010.2066254.
- [181] M. Seo, K. Kagawa, K. Yasutomi, T. Takasawa, Y. Kawata, N. Teranishi, Z. Li, I. A. Halin, and S. Kawahito, "11.2 a 10.8ps-time-resolution 256×512 image sensor with 2-tap true-cds lock-in pixels for fluorescence lifetime imaging," in *2015 IEEE International Solid-State Circuits Conference - (ISSCC) Digest of Technical Papers*, Feb 2015, pp. 1–3.
- [182] S. Han, T. Takasawa, K. Yasutomi, S. Aoyama, K. Kagawa, and S. Kawahito, "A time-of-flight range image sensor with background canceling lock-in pixels based on lateral electric field charge modulation," *IEEE Journal of the Electron Devices Society*, vol. 3, no. 3, pp. 267–275, May 2015.
- [183] ams AG, *World's smallest 1D Time-of-Flight*. TMF8701 datasheet, 2019.
- [184] STMicroelectronics, *World's smallest Time-of-Flight ranging and gesture detection sensor*. VL53L0X datasheet, 2019.
- [185] E. A. G. Webster, J. A. Richardson, L. A. Grant, D. Renshaw, and R. K. Henderson, "A single-photon avalanche diode in 90-nm cmos imaging technology with 44% photon detection efficiency at 690 nm," *IEEE Electron Device Letters*, vol. 33, no. 5, pp. 694–696, May 2012, DOI: 10.1109/LED.2012.2187420.
- [186] D. P. Palubiak and M. J. Deen, "Cmos spads: Design issues and research challenges for detectors, circuits, and arrays," *IEEE Journal of Selected Topics in Quantum Electronics*, vol. 20, no. 6, pp. 409–426, Nov 2014, DOI: 10.1109/JSTQE.2014.2344034.



Antonino Caizzone



20th March 1991



Chemin de la Goutte d'Or 10
Bôle, Switzerland



+41 779867664



<https://www.linkedin.com/in/antonino-caizzone-30710964>



antonino@senbiosys.com
antonino.caizzone@epfl.ch

Skills

Cadence Spectre-Virtuoso

Matlab, Simulink, Mathematica

VHDL - FPGA

Labview

3D Printing - ThinkerCad

Comsol

PCB - Altium

Oscilloscopes, Sig-Gens, Multimeters

Clean Room-related Works (Process)

Office Tools

(*)[The skill scale is from 0 (Fundamental Awareness) to 6 (Expert).]

About me

I am a 28-years old passionate entrepreneur with 4+ years of international experience in developing new health-related devices. I have a broad know-how on these sensors and particularly on the PPG one. I strongly believe that the digital health is the next Big Thing and want to take part to this actively. People describe me as determined, resilient and good at communicating to the general public. I can take a project from scratch and lead it to its future success.

Work Experience

01.18 -	Senbiosys SA <i>Co-Founder & CTO</i>	Neuchâtel, CH
04.16-	EPFL <i>PhD - An Ultra Low-Noise Micropower PPG sensor</i>	Neuchâtel, CH
09.15-04.16	EPFL <i>Scientific Assistant - Wearable Devices for Healthcare in the IoT framework</i>	Neuchâtel, CH
06.14-08.14	Georgia-Tech <i>Visiting Researcher - Modeling of piezo-electric materials</i>	Atlanta, USA
10.12-03.13	STMicroelectronics <i>Analog Designer Intern - Designing an RFID receiver on a plastic substrate</i>	Catania, I

Education

2017	CTI, Switzerland CTI Entrepreneurship Training: Business Concept (Federal Program)	5.25/6
2016-2017	Mead Education SA, Switzerland Techniques on Handling Noise and Variabilites & Advanced Analog CMOS Design & Ultra Low Power RF	
2015	INPG Grenoble, France Master in Micro & Nanotechnologies for Integrated Systems - double master	Trés Bien
2015	Polytechnic of Turin, Italy Master in Micro & Nanotechnologies for Integrated Systems - double master	110 cum laude/110
2012	University of Catania, Italy Bachelor in Electronic Engineering	110/110

Patents

2017	Health Monitoring Device - WO2019016191 (A1)
2019	Non-disclosable Information

Languages

Italian [Native]; English [C1]; French [C1]; German [A1]

Interests

Sports (Skiing, Cycling, Hiking); Reading; Cooking; Travelling

Other information

- A, B CH-driving licenses
- CH B-resident permit valid until March 2021

Publications

- | | |
|------|----------------------------------------------------------------------------------------------------------------------------------------------------------------------------------------------------------------------------|
| 2020 | Design and Optimization of Low Power and Low Light Sensor,
- IEEE Custom Integrated Circuits Conference 2020 (CICC) |
| 2019 | A 2.6 μ W Monolithic CMOS Photoplethysmographic (PPG)
Sensor Operating with 2 μ W LED Power for Continuous
Health Monitoring, - IEEE Transactions on Biomedical Circuits
and Systems (impact factor 4.25) |
| 2019 | AC/DC Ratio Enhancement in Photoplethysmography Using a
Pinned Photodiode, - IEEE Electron Device Letters
(impact factor 3.75) |
| 2019 | An Ultra-Low Power PPG and mm-Resolution ToF PPD-Based
CMOS Chip Towards All-in-One Photonic Sensors,
- IEEE Sensors (impact factor 3.07) |
| 2019 | A 2.6 μ W Monolithic CMOS Photoplethysmographic Sensor
Operating with 2 μ W LED Power,
- IEEE International Solid State Circuits Conference 2018
(ISSCC) (leading conference) |
| 2018 | An Accurate kTC Noise Analysis of CDS Circuits,
- IEEE NEWCAS 2018 |
| 2017 | Comprehensive Noise Analysis in PPG Read-out Chains,
- IEEE ICNF 2017 |

update March, 4th 2020